AIR SYSTEM SUMMER FIELD STUDY IN THE AOSERP STUDY AREA, JUNE 1977

by

F. FANAKI, R. HOFF, L. BARRIE, R. MICKLE, M. LUSIS,
K. ANLAUF, A. GALLANT, J. KOVALICK,
F. FROUDE, J. MARKES, J. ARNOLD,
S. MELNICHUK, D. BRYMER,
A. GAUDENZI, A. MOSER,
D. BAGG

Environment Canada
Atmospheric Environment Service

for

ALBERTA OIL SANDS ENVIRONMENTAL RESEARCH PROGRAM

Projects AS 1.5.3 and AS 3.5.2

August 1979

TABLE OF CONTENTS

TABLE OF CONTENTS (CONTINUED)

TABLE OF CONTENTS (CONCLUDED)

LIST OF TABLES

LIST OF TABLES (CONCLUDED)

LIST OF FIGURES

LIST OF FIGURES (CONTINUED)

LIST OF FIGURES (CONTINUED)

LIST OF FIGURES (CONTINUED)

LIST OF FIGURES (CONTINUED)

LIST OF FIGURES (CONCLUDED)

LIST OF FIGURES (CONCLUDED)

ABSTRACT

The third in a series of Atmospheric Environment Service Field Studies in the Alberta Oil Sands Study Area was carried out during June 16-27, 1977. The study was designed to cover the same objectives as those of the previous two studies but for summer conditions. As a consequence, the AES experimental program was similar to the previous experiments. In addition, the program was extended to include observations of particulate dispersion in the Great Canadian Oil Sands (GCOS) plume, using a mobile laser radar (LIDAR). Solar irradiance was also measured at several solar elevations during this study.

To examine the temperature structure of the atmospheric boundary layer at the AOSERP study area, two acoustic sounders were used at Lower Syncrude site and the Camp site. The sounders rendered interesting data that agree well with the meteorological sondes.

The predictive capability of the plume rise formulae were assessed in this study. The formulae used were the same as those applied for winter conditions. A few cases of interest that describe the behaviour of the GCOS plume are described.

Numerous ground traverses of SO_2 under the GCOS plume using a COSPEC were made. Selected days of data were chosen for case studies. All cases describe the behaviour of the GCOS plume under summer conditions.

The particulate plume from the GCOS power plant was observed using LIDAR. Thirteen Eulerian average cross-sections were obtained from which the horizontal and vertical dispersion coefficients, plume rise and plume bearing were derived. A comparison with Gaussian plume formulae shows valley effects and wind shear under stable regimes to be important for this region.

The rate of SO_2 oxidation to sulphates in the GCOS power plant plume was studied using a filter pack apparatus mounted in a helicopter. An SO_2 and O_3 analyser was also flown. Oxidation rates were found to be low prior to 0700, typically, less than $0.5\%\cdot h^{-1}$. Later in the day, appreciable conversion rates were observed

(0.9 - 3.3%·h^{-1}), and a buildup of ozone was noted in the plume on several occasions. The results suggest that heterogeneous processes were unimportant for the atmospheric conditions studied even though the emitted particulate matter contains several potential catalysts in a size range that could remain airborne for long periods of time. On the other hand, homogeneous reactions involving SO_2 and nitrogen oxides in the plume, plus low-level hydrocarbon emissions from the tar sands processing plant, play an important role during the daytime.

Solar radiance and irradiance (300-510 nm) was measured at several solar elevations on two consecutive days (24 and 25 July 1977) under cloudless conditions. This report presents general background information on the topic, summarizes the measurement technique, and presents the solar radiation data in graphical form.

An investigation of the ambient concentration and deposition rate of sulphur compounds and metals in atmospheric particulates was conducted around the GCOS oil extraction plant. Air was sampled 10 km from the source and a network of fifteen deposition collectors was set up in the area. Peak 4 h average gaseous and particulate sulphur concentrations were 14 and 2.3 µg $s.m^{-3}$, respectively. Of the elements Al, Ca, K, Mg, Mn, Sc, Ti, S, and V, only the last two were predominantly of anthropogenic origin. The rest have strong wind blown dust components. This finding was confirmed by the deposition patterns of the various elements about the source. Deposition rates of Al, Ca, Mg, Mn, Part-S, Ti, and V were measured and are related to ambient concentrations by deposition velocities.

ACKNOWLEDGEMENTS

The authors are appreciative of the funds and support provided by the Alberta Oil Sands Environmental Research Program (AOSERP) to carry out this field study. Particular thanks are deserved by the AOSERP staff, in particular A. Mann for his assistance and co-operation and D. Hadler, who provided us with a comfortable home during our stay at the AOSERP camp.

We wish to thank M. Strosher (Alberta Environment) and W. Cary (GCOS), who supplied us with excellent emission data, without which our conclusions would not have been valid; the staff of AES Western Region involved in this study for their valuable assistance and support; AOSERP and Alberta Environment for assistance with vehicles and associated supplies; Wells Horton for preparing and operating the COSPEC boat; and Syncrude Ltd., Environmental Affairs Department for the loan of the Sign-X SO_2 monitor. The authors wish to thank M. Millan for his invaluable advice and assistance; and A. Smith for photographic work. Thanks are due to C. Matthias and H. Martin for reviewing part of this report; D. Crawford for assistance with the collection and analysis of samples; J. Puttock for information on particle size distributions; and R. Portelli for the calculations with the Gaussian-plume dispersion model. We are grateful to J. Hancock of the University of Toronto and F. Philbert of the Canada Centre for Inland Waters for carrying out the neutron activation and atomic absorption analyses of the plume particulate matter; and K. Puckett and E. Finegan for analysing the deposition data.

This research project (AS 1.5.3 and AS 3.5.2) was funded by the Alberta Oil Sands Environmental Research Program, a joint Alberta-Canada research program established to fund, direct, and co-ordinate environmental research in the Athabasca Oil Sands area of northeastern Alberta.

1. INTRODUCTION

Industrial plumes disperse and change their chemical composition as they travel in the atmosphere. The mechanisms of dispersion and chemical change within the plume are functions of local meteorological parameters (e.g., wind speed, wind direction, and temperature), topography, and the chemical composition of both the plume and the atmosphere. The effects on the air quality of the area are numerous, as has been demonstrated in the previous winter field studies. In order to examine the effects of the changes under summer conditions, a third field study was carried out during June 1977 in the Alberta Oil Sands Environmental Research Program (AOSERP) study area (Figure 1). The study had the following specific objectives:

1. To obtain detailed information on wind flow and temperature of the atmospheric boundary layer during the summer conditions;
2. To obtain information on the rise of the Great Canadian Oil Sands (GCOS) plumes, and on the dispersal and concentration of their particulates;
3. To examine the air quality of the area and to measure the deposition of heavy metal and sulphur-bearing particles; and
4. To determine the rate of SO_2 oxidation and its photochemical aspects.

The basic Atmospheric Environment Service (AES) experimental program was similar to the one in the previous studies (Fanaki 1978). In addition, the program included measurements of the GCOS emissions by the AES Laser Radar (LIDAR) and measurements of solar irradiance.

During June the sun rises at 0430 and sets at 2230, giving 18 h of daylight in that area. Consequently, the activities of observations were divided to cover two periods, A and B (Table 1). Period A covered the hours just before sunrise to 1500, while B covered the hours 1400 to 2300. Emphasis was put on period A,

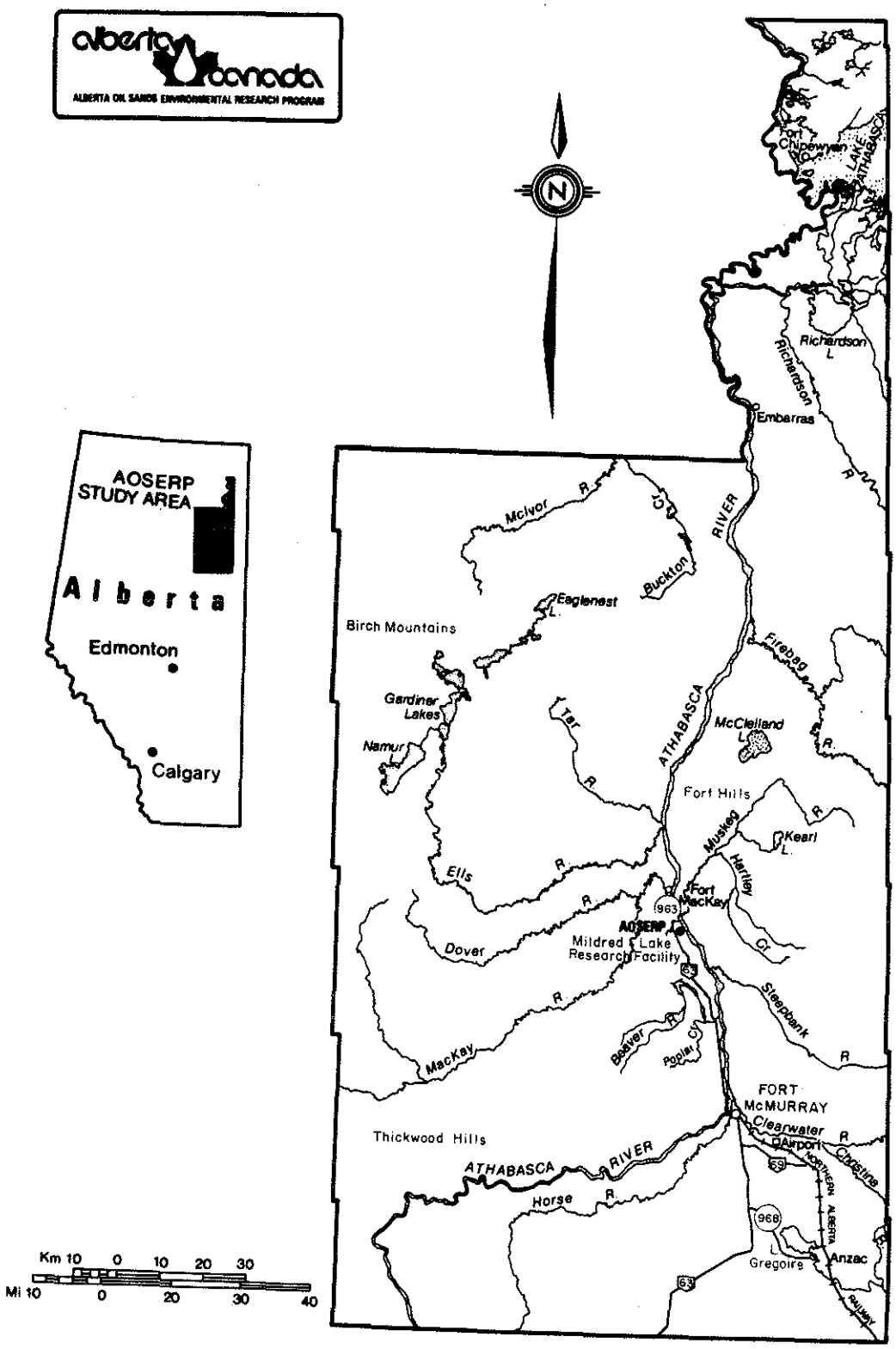

Figure 1. Map of the AOSERP study area.

TABLE 1. AES activities in the AOSERP Study Area for the period 15 to 27 June, 1977.
(LS = Lower Syncrude, MS = Syncrude Mine)

Type of Activities			A	A	A	A	A	B	A	A	B		
Set-Up and Packing	—											—	—
Minisonde Releases I													
Location		LS	LS	LS	LS	LS	LS	LS	LS	LS	LS	LS	
Minisonde Releases II													
Location		RL	RL	RL	RL,FM	FM	RL,FM	RL	RL,MS	MS	MS	MS	
Radiosonde Releases													
Tethersonde Studies			—	—	—	—	—	—	—	—	—		
Location			LS	LS	LS	LS	LS	MS	MS	MS	MS		
Bivane Studies				—	—	—	—	—	—	—	—		
Acoustic Sounder		—	—	—	—	—	—	—	—	—	—	—	
Plume Rise Studies													
LIDAR Studies			—	—			—	—	—				
Aerial Plume Studies			—	—	—	—	—	—	—	—		—	
COSPEC Studies			—	—	—	—	—	—	—	—			
Deposition Studies	—	—	—	—	—	—	—	—	—	—	—	—	
Time (MST)	12	12	12	12	12	12	12	12	12	12	12	12	12
Date June	15	16	17	18	19	20	21	22	23	24	25	26	27

because during that period the plumes from the GCOS plant were relatively good for observations. Only two days were spent in period B type of observations.

A description of the topography of the AOSERP experimental site and of the physical structure of the industrial source (GCOS) was given earlier (Fanaki 1978; Fanaki et al. 1979). Emission parameters from the Power Plant of GCOS for the period of observations are tabulated in Appendix 11.1.

2. METEOROLOGICAL CONDITIONS

Thermal and wind field information, as required to support other aspects of the program, was determined from a series of observations of vertical profiles of wind and temperature. As in previous field studies (Fanaki 1978; Fanaki et al. 1979) profiles were obtained using minisonde, radiosonde, and tethersonde systems, and wind variability was monitoried with a bivane mounted on the permanent 150 m meteorological tower at Lower Syncrude throughout the study period. The thermal structure was further examined using acoustic sounders at two locations. Detailed descriptions of the systems used are contained in earlier reports (Turner and Markes 1974; Fanaki 1978; Fanaki et al. 1979), and the sequence of observations is summarized in Table 1.

A day-by-day description of the weather during the study is included in Appendix 11.2.

2.1 MINISONDE AND RADIOSONDE MEASUREMENTS

During this study atmospheric soundings were obtained from four sites whose locations are identified in Figure 2 in relation to the source, the GCOS plant.

Radiosondes were flown only from the Lower Syncrude Site; they were used to provide humidity information required as part of the GCOS plume study. Minisonde information was used to define thermal structure required in modelling and other studies. As in other field studies, minisondes were flown simultaneously from two different locations in the oil sands area, Lower Syncrude being the base station and a second site being selected to be downwind from the GCOS plant whenever possible. When practicable there were six soundings per day. The minisonde data for this period are available through the AOSERP management office of Alberta Environment.

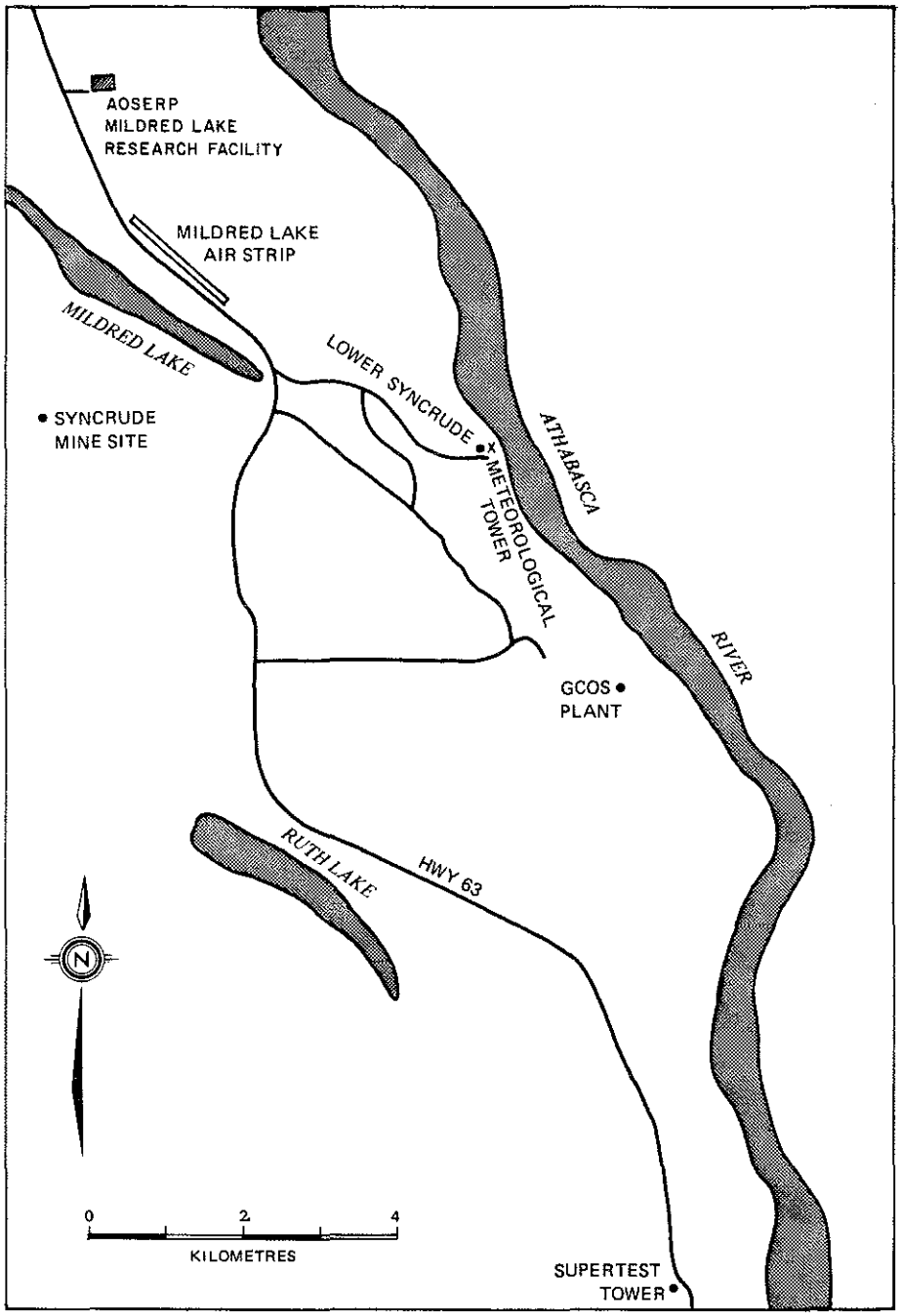

Figure 2. Map of Mildred Lake and vicinity showing the location of the GCOS plant and of the meteorological soundings.

2.2 BIVANE MEASUREMENTS

During this study a project was undertaken to establish the feasibility of using a bivane Gill anemometer to calculate the dispersion coefficients of the GCOS plume. The location of the bivane was the same as that of the February study at Lower Syncrude (Fanaki et al. 1979).

The measurement procedures and a description of the equipment were given in the previous AOSERP Report (Fanaki et al. 1979). The topography surrounding the bivane was also described in the same report.

In a homogeneous field of atmospheric turbulence, the diffusive spread of a plume (σ_y and σ_z) from a continuous elevated point source depends on the standard deviations of wind azimuth (σ_ϕ) and elevation (σ_θ). Hay and Pasquill (1959) indicated that σ_y and σ_z are related to σ_ϕ and σ_θ respectively by the following relation:

$$\sigma_{y,z} = \left[\sigma_{\phi,\theta}\right]_{\tau,S} x \qquad (1)$$

where x is the downwind distance and τ is the total sampling period. S describes the period over which the fixed-point measurements were smoothed to obtain Eulerian time statistics equivalent to Lagrangian Statistics. S is given as

$$S = \frac{X}{\beta \bar{U}}$$

Here $\bar{U}$ is the average wind speed and β is the ratio of the Lagrangian and Eulerian time scales. The value of β ranges from 1.1 to 8.5 (Hay and Pasquill 1959). Pasquill (1976) indicated that $\beta = 4$ was satisfactory for most atmospheric observations.

The bivane data were recorded continuously on a three-channel chart recorder as well as on a tape recorder. The tape recorder was used in this study to simplify the analysis.

The data collected represent 80 h of observation taken from 18 to 24 June during the daytime. The data were divided into

sampling periods τ of 30 min. The smallest smoothing, or averaging, time S was chosen to be 5 s, over which the wind vector u, wind elevation angle θ, and wind azimuth angle ϕ were scaled by using a PDP 11 minicomputer. By applying the same procedure as in the previous field study (Fanaki et al. 1979; see also Gifford 1960; and Munn 1964), we computed variances of wind speed, elevation, and azimuth from running means. The computer grouped the 5 s bivane readings into running means, etc. to yield standard deviations (σ_u, σ_θ, and σ_ϕ) for smoothing times S of 10, 25, 50, 100 s etc. The tabulated values of σ_u, σ_θ, and σ_ϕ are available through the AOSERP Management office, Alberta Environment.

In the application of Equation (1), the limit of S depends on the length of the bivane record. In order to examine this relationship, a typical variation of the wind direction variance σ_ϕ^2 with S is shown in Figure 3, which illustrates the decrease of σ_ϕ^2 with the increase of S for two sets of data. The data were taken at two different times on the same day. The decrease is relatively slow from S = 5 s to 100 s. For S >100 s, σ_ϕ^2 decreases rapidly to near zero. This is as expected; when S increases to 200 s the averaging technique will cut off all microscale fluctuations above 0.005 Hz and leave little to contribute to σ_ϕ^2. In this study only values of σ for S >50 s were used.

The values of σ_y and σ_z obtained using Equation (1) were compared with the observed values obtained by the LIDAR (Sec. 4) and the COSPEC (Sec. 5) and by photography (Sec. 3). The result of the comparison is shown in Figures 4 and 5. As in the previous AOSERP study, Equation (1) underestimates the vertical spread of the plume at various downwind distances. This observation substantiates the conclusions that were drawn from the winter study regarding the use of a bivane to determine the spread of the plume. It appears that the bivane measurements describe wind fluctuations at a different level and location than that of the plume. The disagreement could also be due to the dynamic effects of the plume at the source. The

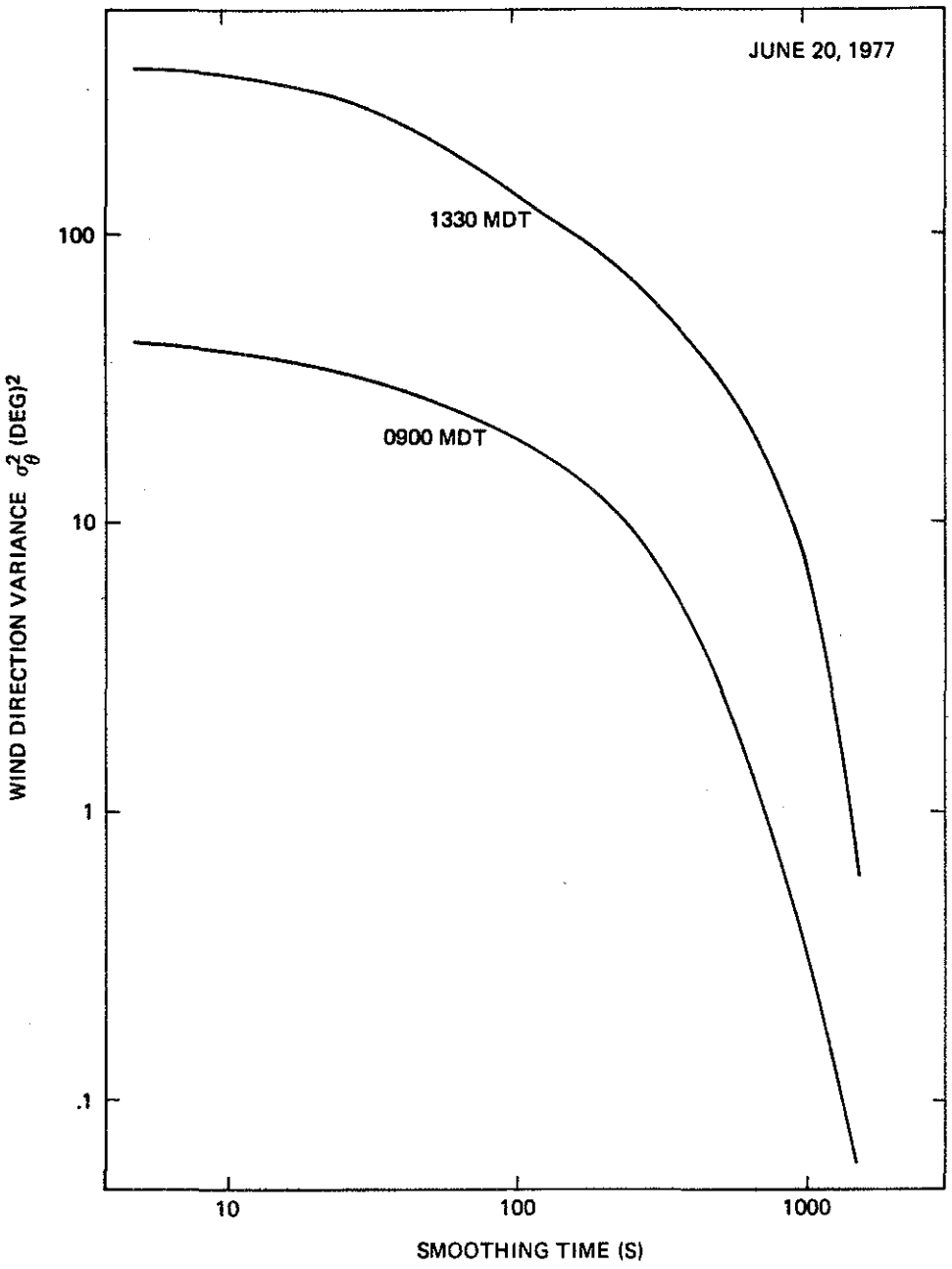

Figure 3. Variations of the wind direction variance with smoothing time for 20 June 1977 at 1330 and 1900 Mountain Daylight Time (MDT).

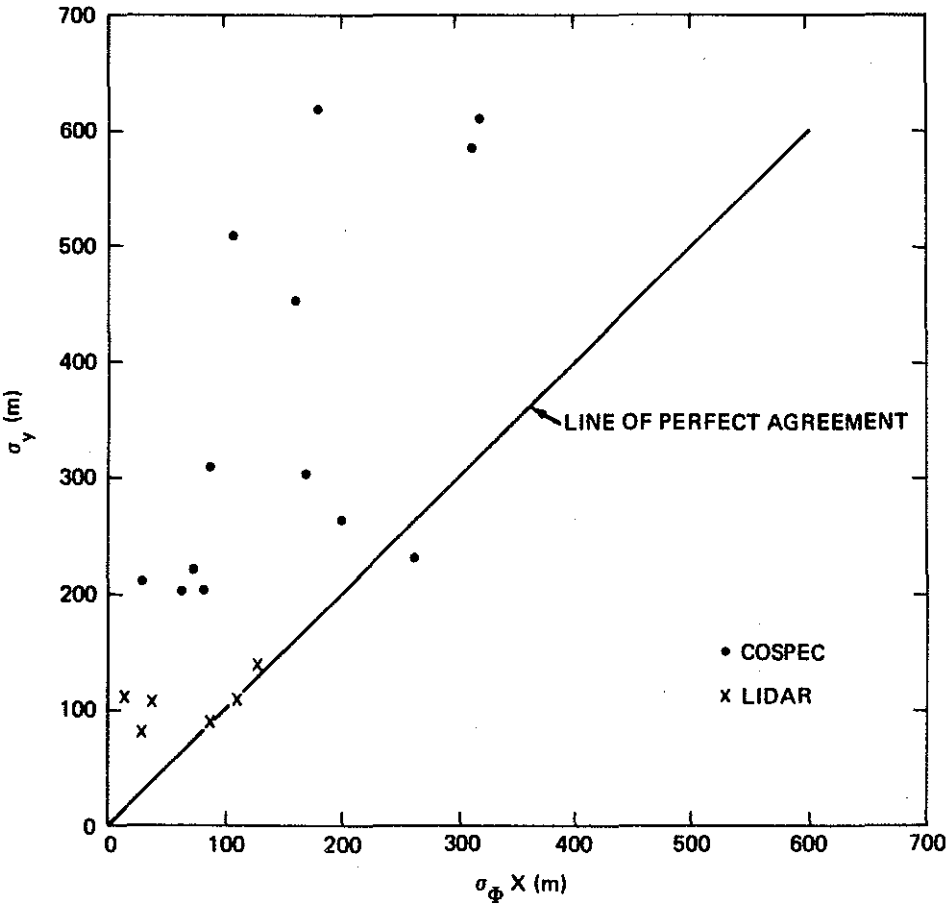

Figure 4. Comparison of predicted versus observed horizontal dispersion coefficients.

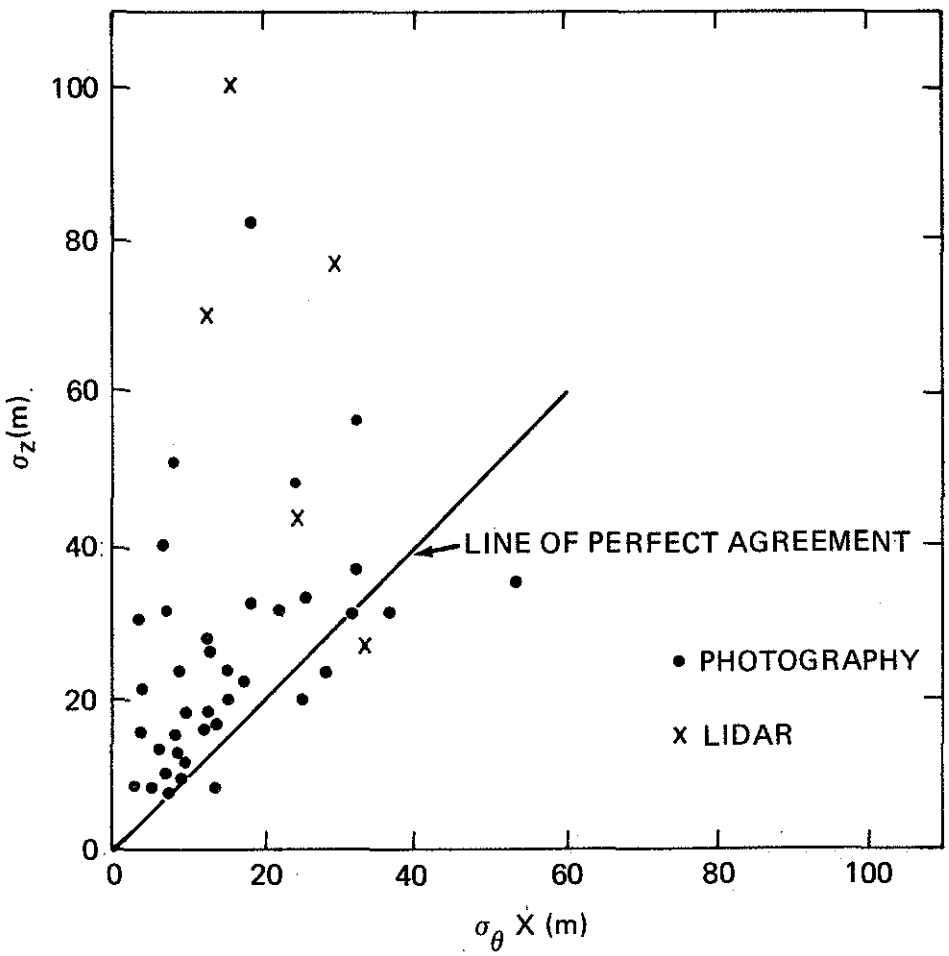

Figure 5. Comparison of predicted versus observed vertical dispersion coefficients.

turbulence initiated by the plume at the source tends to increase the dispersion mechanism. One other reason that may be considered is the assumption that β was equal to 4. This value should be checked by independent measurements of turbulent intensities in the study area.

Some interesting observations may be made regarding the behaviour of σ_θ and σ_ϕ and the standard deviations of the vector wind speed σ_u. Daily variability of σ, while not strictly following the rule, generally increases with the time of day (Figures 6 and 7). They are at a maximum during the afternoon period (1400 to 2000). The increase of σ_ϕ and σ_ϕ may be attributed to the increase in turbulent intensity induced by increased insolation. σ_ϕ and σ_θ fall to a minimum in the morning except on two of the days, 23 and 24 June. On these two days, σ_ϕ and σ_θ reached a value greater than 15°. These days were characterized by weak wind and by large fluctuations in the wind azimuth and elevation in the morning. A sample of the recorded data illustrating these large fluctuations is shown in Figure 8.

Measurements by the minisonde indicated that the wind speed was about 4 $m \cdot s^{-1}$ during that time for both days. The days were characterized by a passage of an occluded front that was linked to an Aleutian low. The flow was southeasterly on 23 June and southwesterly on 24 June. The winds aloft were strong, about 10 $m \cdot s^{-1}$.

The early morning inversion conditions changed to lapse conditions at noon. Surface wind veered and aligned with the valley direction. Heating of the underlying ground lifted the inversion layer to the 800 m level. It is believed that the increase of σ_θ and σ_ϕ during that time was due to the increase in thermal turbulence.

σ_u correlated well with σ_θ and σ_ϕ expect on 25 June (Figure 9). On 25 June there was a slight increase of σ_θ corresponding to the large values of σ_u. σ_ϕ retained its relatively low value during that time. As a sample, Figure 10 shows a plot of σ_u as a function

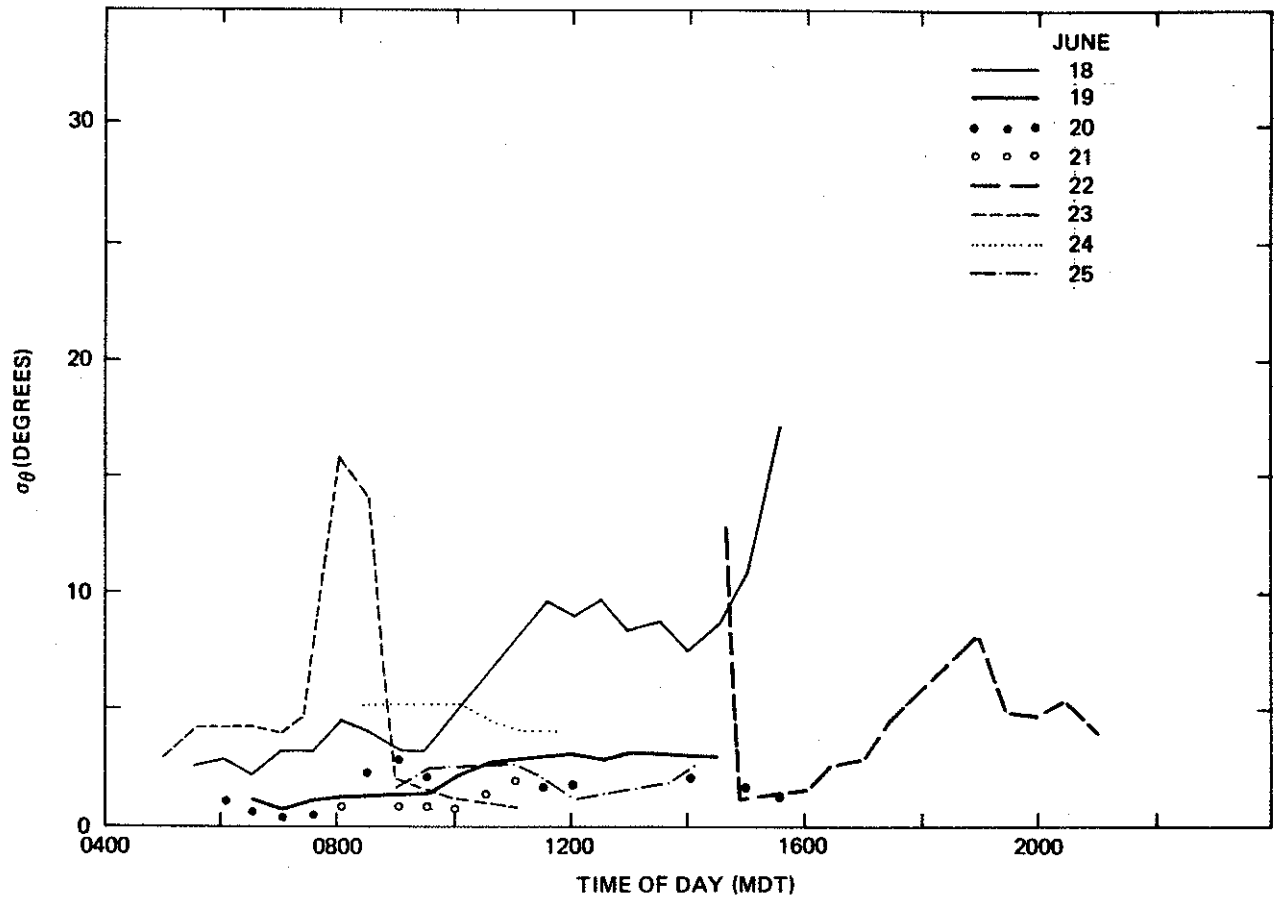

Figure 6. Variation of standard deviation of elevation angle with the time of day.

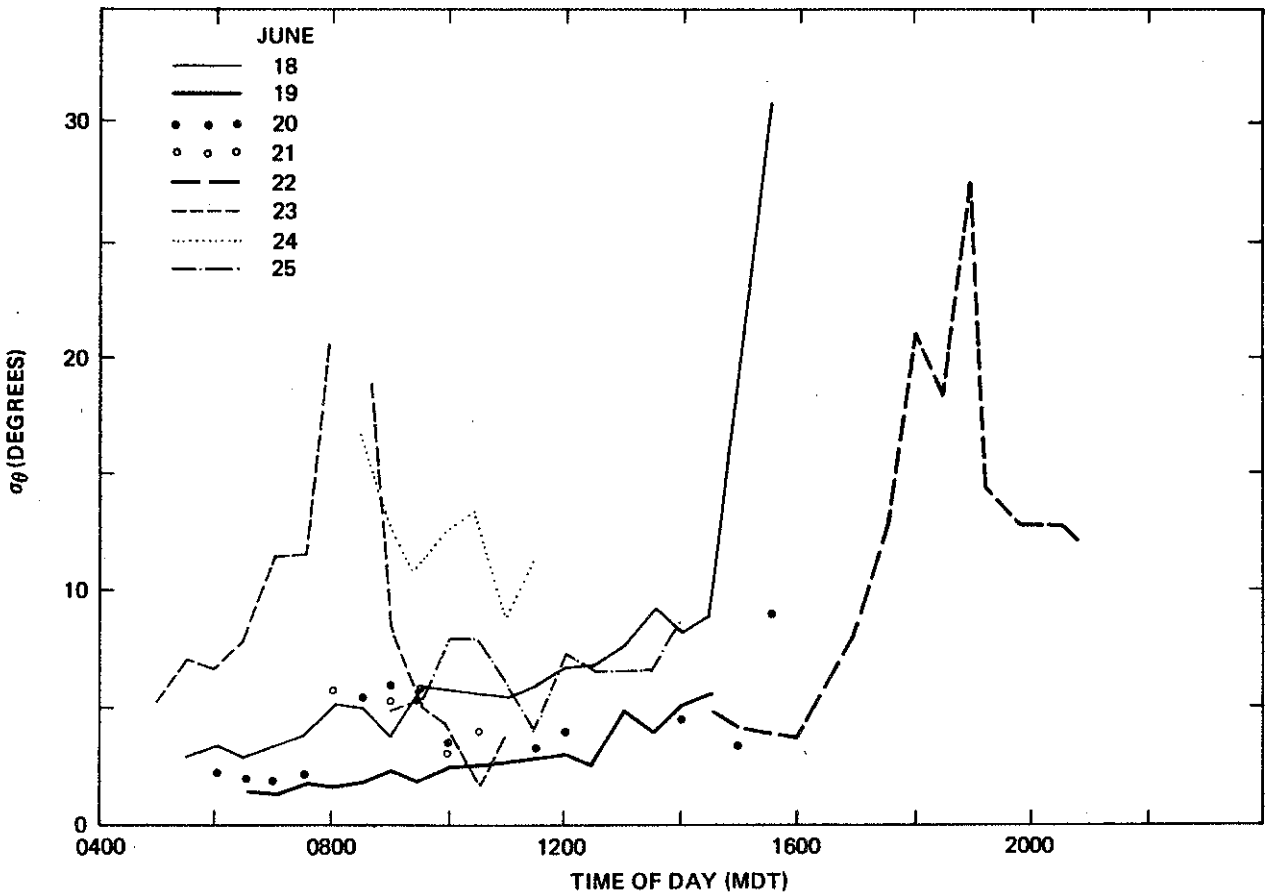

Figure 7. Variation of standard deviation of azimuth angle with the time of day.

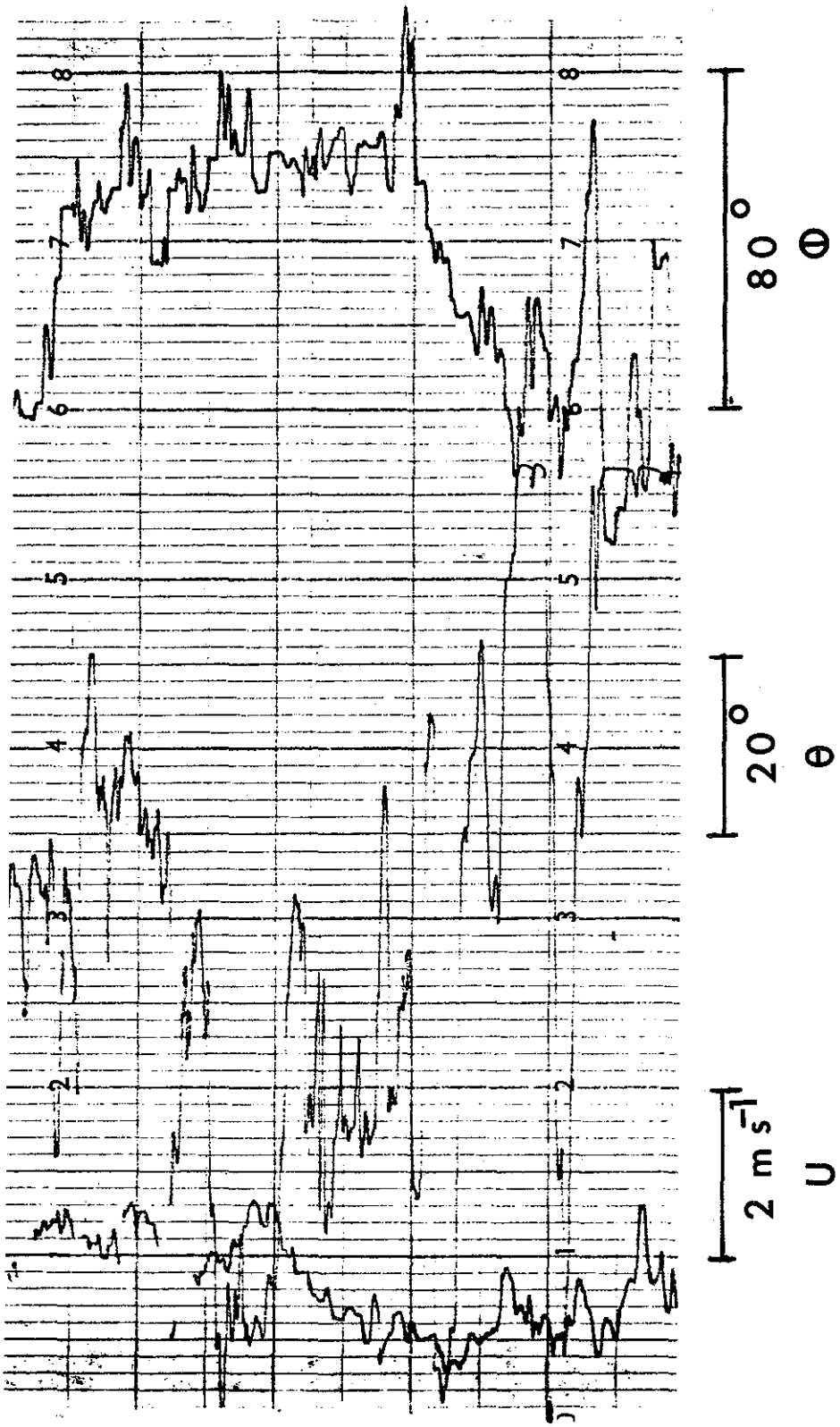

Figure 8. Sample of the bivane record for a 5-min period on 23 June 1977 at the Lower Syncrude site.

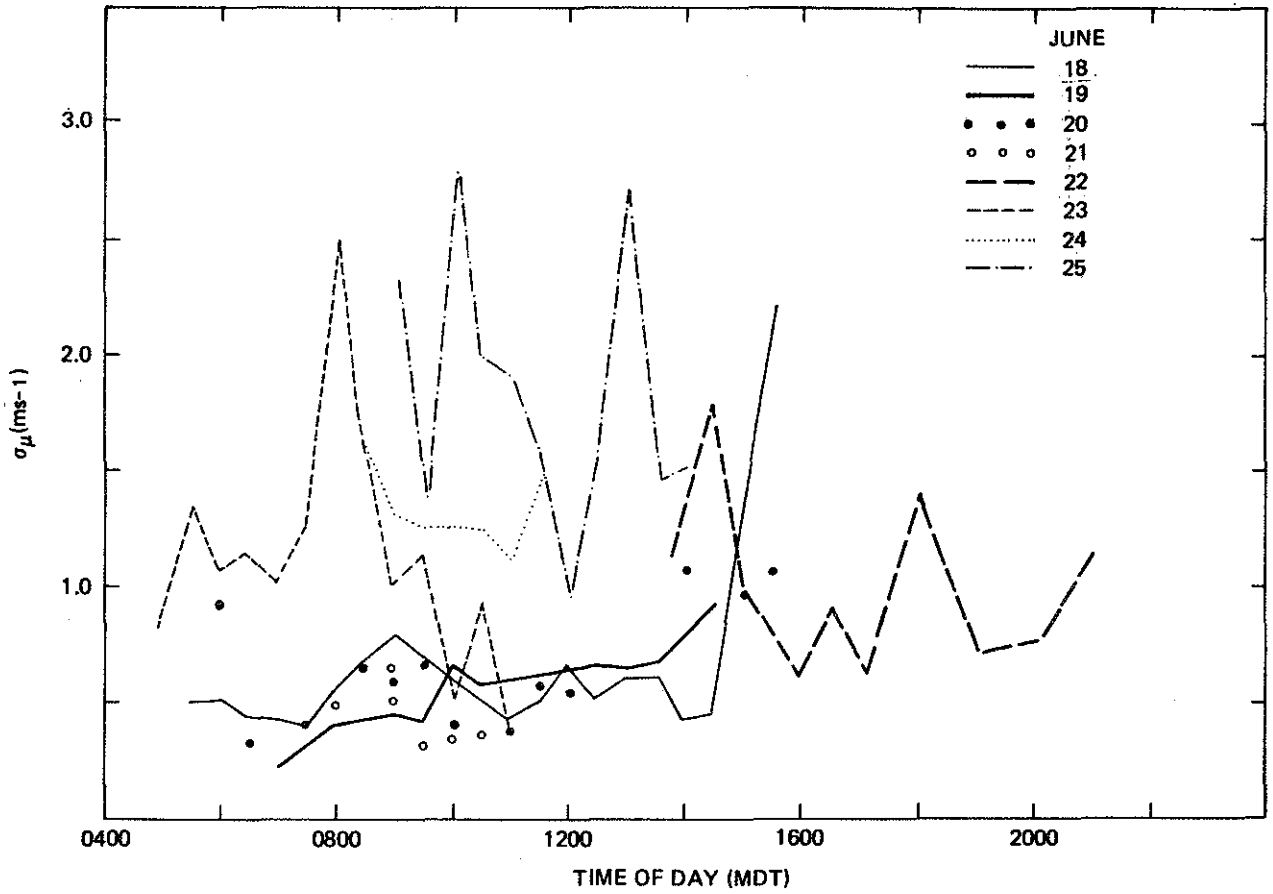

Figure 9. Variation of the standard deviation of vector wind speed with the time of day.

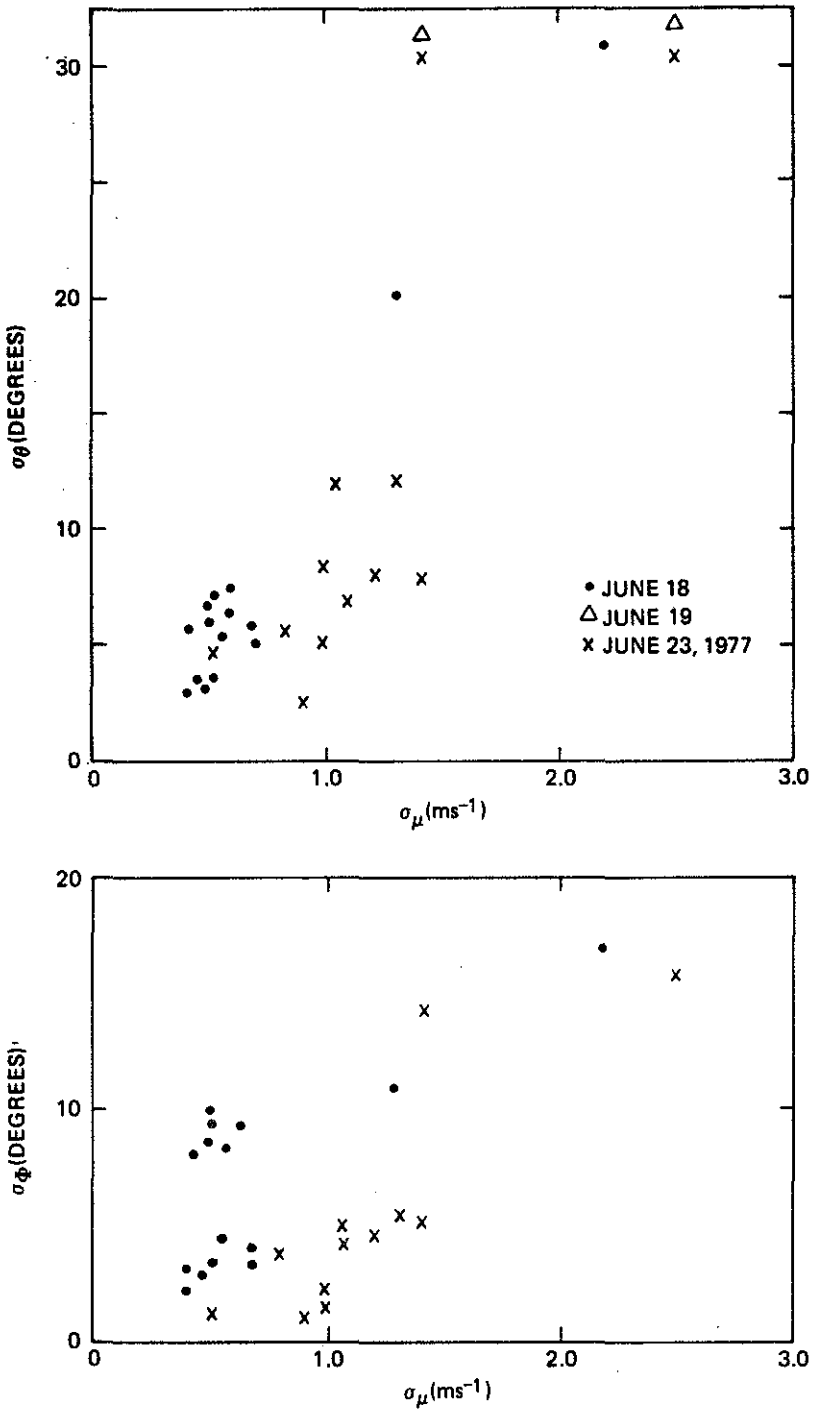

Figure 10. Variation of σ_θ and σ_ϕ with σ_u for 18, 19, and 23 June 1977 at the Lower Syncrude Site.

of σ_θ and σ_ϕ respectively for two days of data. Both σ_θ and σ_ϕ tend to increase with an increase in σ_u. The rate of the increase is larger with σ_θ than with σ_ϕ. σ_u was examined in relation to the mean wind ($\bar{u}$) speed at the bivane level (Figure 11). In spite of the scatter of the points, it may be seen that σ_u increased with an increase in $\bar{u}$. There are also occasionally large values of σ_u under light wind conditions. This perhaps was due to the thermal instability that increases under light wind conditions and high insolation.

Similar to the previous study, Equation (1) disagrees with the observed data. Hence, extrapolation of models similar to Equation (1) to the AOSERP study area must be examined carefully. Further, care would be necessary in the selection of the location of the bivane, since the spectrum of turbulence and the topography differ from one location to another. The use of a tape recorder in collecting the bivane data is recommended because it facilities the analysis.

2.3 TETHERSONDE MEASUREMENTS

The June 1977 tethersonde study was undertaken primarily to study the transition from early morning inversion to mid-day lapse conditions, particularly as related to the wind field. The instrument flown was the same package used in previous studies. Both the Lower Syncrude (17 to 21 June) and the Syncrude Mine (22 to 24 June) sites were used.

The profiles from this study, with ambient temperature (°C), vertical temperature (°C), relative humidity (%), total horizontal wind speed ($m \cdot s^{-1}$) and wind direction (° Magnetic North) being plotted as a function of height above ground level are available through the AOSERP management office of Alberta Environment. The height of the valley walls is indicated on the U/D graph with flow down to valley associated with 124° Magnetic, while the flow up the valley is from 304° Magnetic.

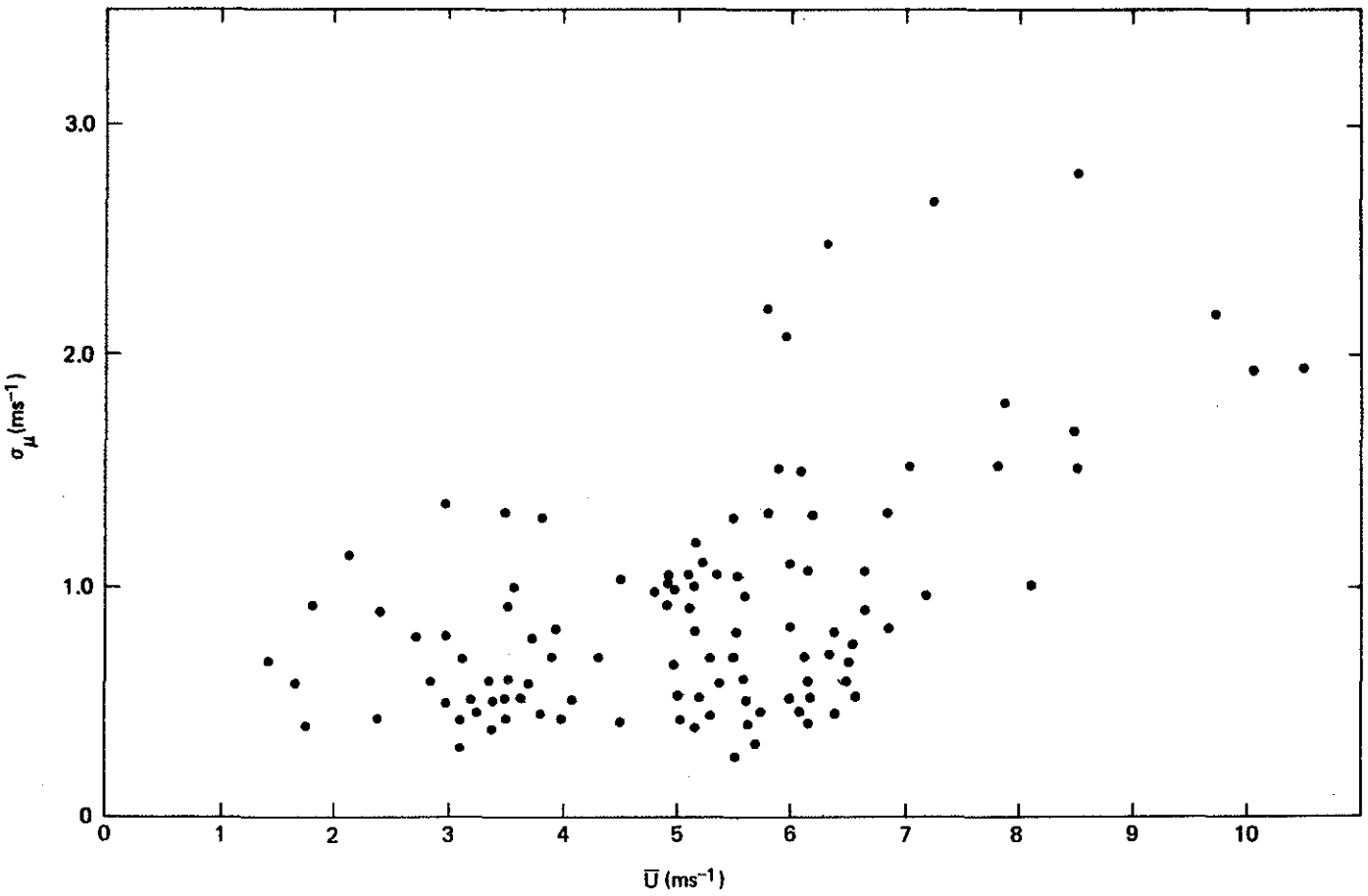

Figure 11. Variation of σ_u with the average vector wind speed at the bivane level.

2.3.1 Discussion of Data

Unfortunately, during the experiment the tethersonde compass malfunctioned periodically, thus limiting quite severely the data set for analysis. However, the series of profiles for 17 June is a good example of the transition from early morning inversion to midafternoon lapse conditions as observed at the Lower Syncrude site. The 0429 profile indicates a layered surface inversion to at least 350 m. Associated with the inversion was a decoupled wind field in the valley with a directional shear of approximately 200° just above the valley walls. Above the minimum associated with this veering layer the wind speed increased constantly to the top of the profile; by 0514 the valley tended to lapse conditions with a strong inversion capping it. As in previous studies, this capping led to a moist air mass being trapped within the valley. With the sharp inversion just above the valley, the veering layer became shallower although the extent of veering did not change. As the day progressed, surface heating tended to weaken and destroy the surface inversion. During this period, the top of the veer layer tended to rise with the rising inversion so that by 0942 the top had reached approximately 400 m. By this time the lower part of the boundary layer was only weakly stable, capped by a more stable layer near 500 m. It can be seen that the region of maximum wind veer is associated with the base of the elevated inversion. It is also worth noting that the wind field below this capping inversion is relatively constant at about 2 $m \cdot s^{-1}$. These light winds had been associated with flow beneath the rising inversion since 0500. By 1030, the upper inversion tended to stall at just above 400 m, giving a classic example of a well-mixed layer capped by an elevated inversion. The typical constant wind field with strong wind veer at the inversion base can be observed. By 1300, the lowest 400 m still exhibited a lapse rate with a slight backing in the wind field and no apparent coupling to the valley direction.

On 24 June at the Syncrude Mine site, a similar situation was observed with multiple stable layering and associated wind veering at 0600. As in previous studies under these situations, the surface winds were aligned with the valley direction. By 1120, the inversion

had lifted to about 500 m with a mixed layer beneath. Through the inversion the wind speed tended to increase by about a factor of two from the constant speed in the mixed layer.

2.3.2 Conclusions

Two case studies made during this field trip showed the formation of a lifting inversion with associated modification of the wind field. By mid-day the inversion had stabilized near 500 m, capping a mixed layer. During the early morning stable conditions the surface winds were detached from winds aloft, as was observed during the winter studies. It is suggested that these conditions would tend to alias wind directions from surface towers along the valley direction.

2.4 ACOUSTIC SOUNDER MEASUREMENTS

As in the AOSERP winter field study (Fanaki et al. 1979), two acoustic sounders[1] were used to study the temperature structure of the planetary boundary layer. A description of the basic acoustic sounding and the characteristics of the sounders was given earlier (Fanaki 1978; Fanaki et al. 1979). The sounders operated simultaneously at two different locations. One sounder was placed at the Lower Syncrude site and the second at the AOSERP camp site (AOSERP Mildred Lake Research Facility) (Figure 2). The second site was selected for convenience and for its low background noise in comparison with the Mildred Lake Air Strip Site that had been used in the previous study. Both sounder antennas were shielded by bales of hay which acted as an acoustically absorbing shield, to reduce the background and wind-generated noise. At the camp site, the location was somewhat noisy when strong winds moved the leaves of the surrounding trees. The noise was temporary and did not affect the analysis of the data.

---

[1] One of the sounders was on loan from Alberta Environment, Edmonton.

In most of the morning observations, several discrete layers of turbulence exist within the deep morning inversion. Figures 12 and 13 show two photographs of the acoustic sounder record for 22 June from 2400 to 0900 Mountain Daylight Time (MDT) at two different locations.

At both locations the inversion layers persist all night and into the early hours of the morning. At the Lower Syncrude Site at 0500 MDT, the inversion layer extends to a height of 300 m above the ground. As the day progresses the layer rises gradually to the 500 m level. At 0800 the top of the inversion layer drops to 250 m within an hour.

The same general features are observed at the camp site (Figure 13). The level of the inversion layer is less than that observed at Lower Syncrude. Since the two sounders are at different elevations, both record different heights for the same thermal turbulent atmospheric structure. More comparisons of sounder records from two different locations at the AOSERP study are have been discussed in a previous report (Fanaki et al. 1979).

The sounder echo at the camp site does not follow the same pattern as that of other site at 0800. During the early hours of the day heating of the underlying surface increases the convective activities, which dissipate the inversion layer.

On occasion at the Lower Syncrude Site, however, the inversion also has been observed to descend to a lower level than the one that occurred on 22 June. A similar type of descending inversion had been observed on 17 June (Figure 14). The inversion layer dropped from 400 m to 50 m between 0800 and 0930. At 0930 the sounder echo was reduced to a minimum. The rate of descent was steady and approximately equal to 250 $m \cdot h^{-1}$.

Lower Syncrude minisonde observations (Figure 15) indicate a rise in temperature in the lower 200 m layer of the atmosphere during that time. The temperature of the underlying surface increased by 14°C between 0400 and 1100. The temperature profile changes from stable to near adiabatic. Weak winds in the valley (2 $m \cdot s^{-1}$) increase with height to 8 $m \cdot s^{-1}$.

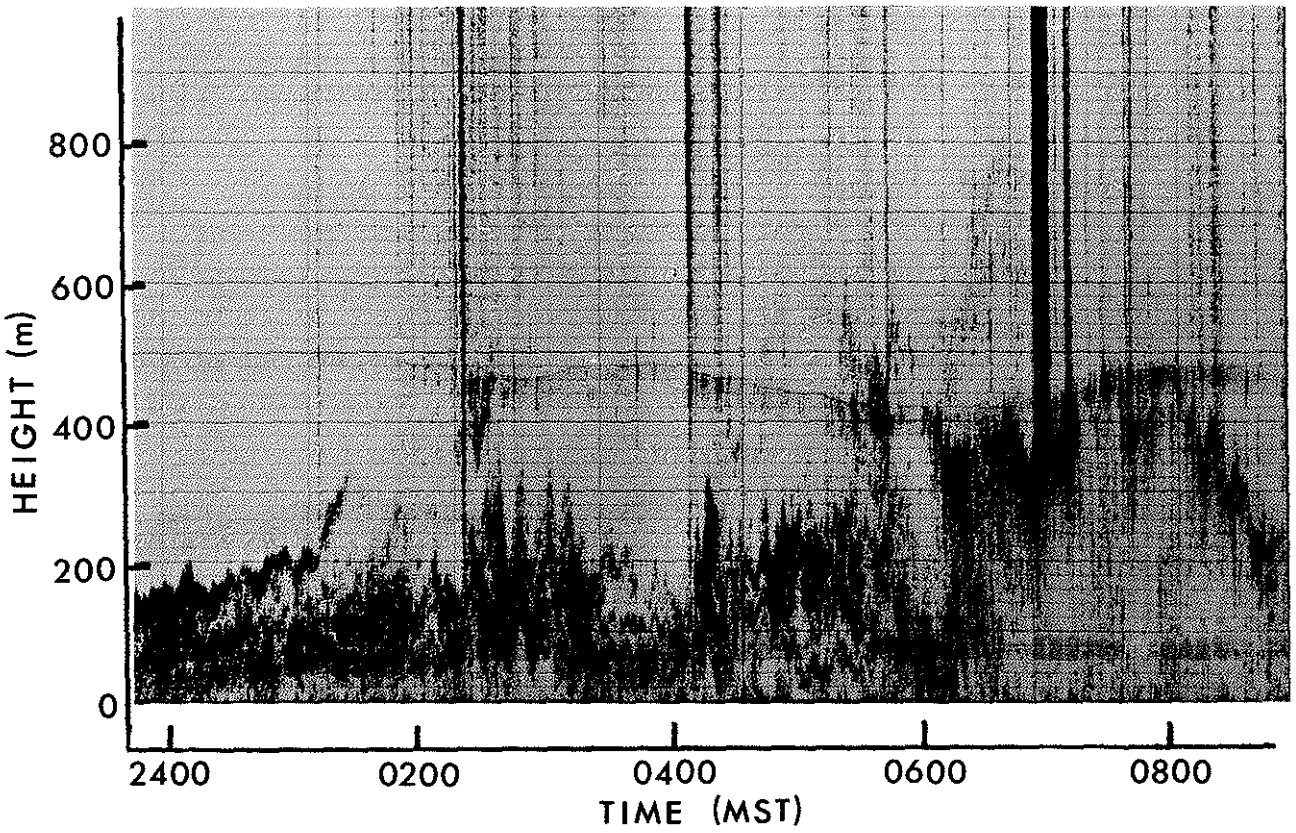

Figure 12. Variation of height of inversion layer with time at the Lower Syncrude site for 22 June 1977.

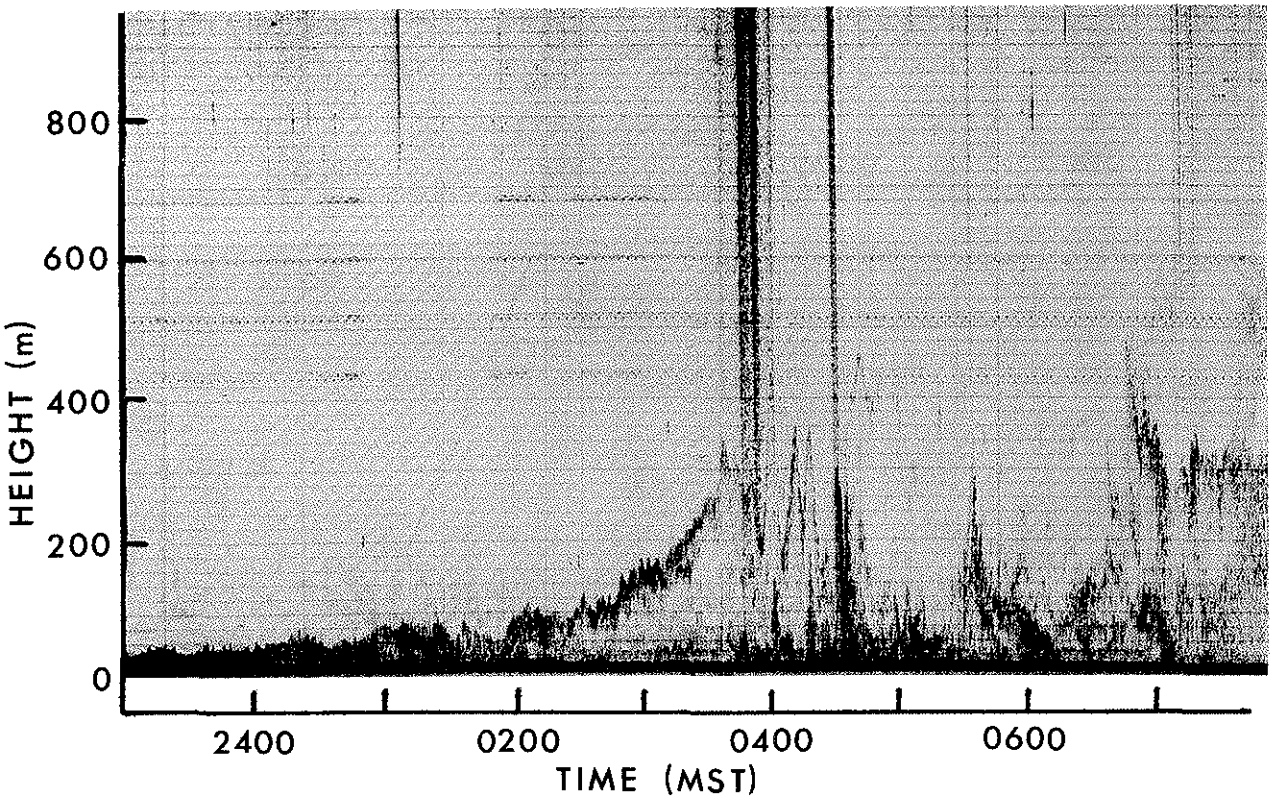

Figure 13. Variation of height of inversion layer with time at the camp site for 22 June 1977.

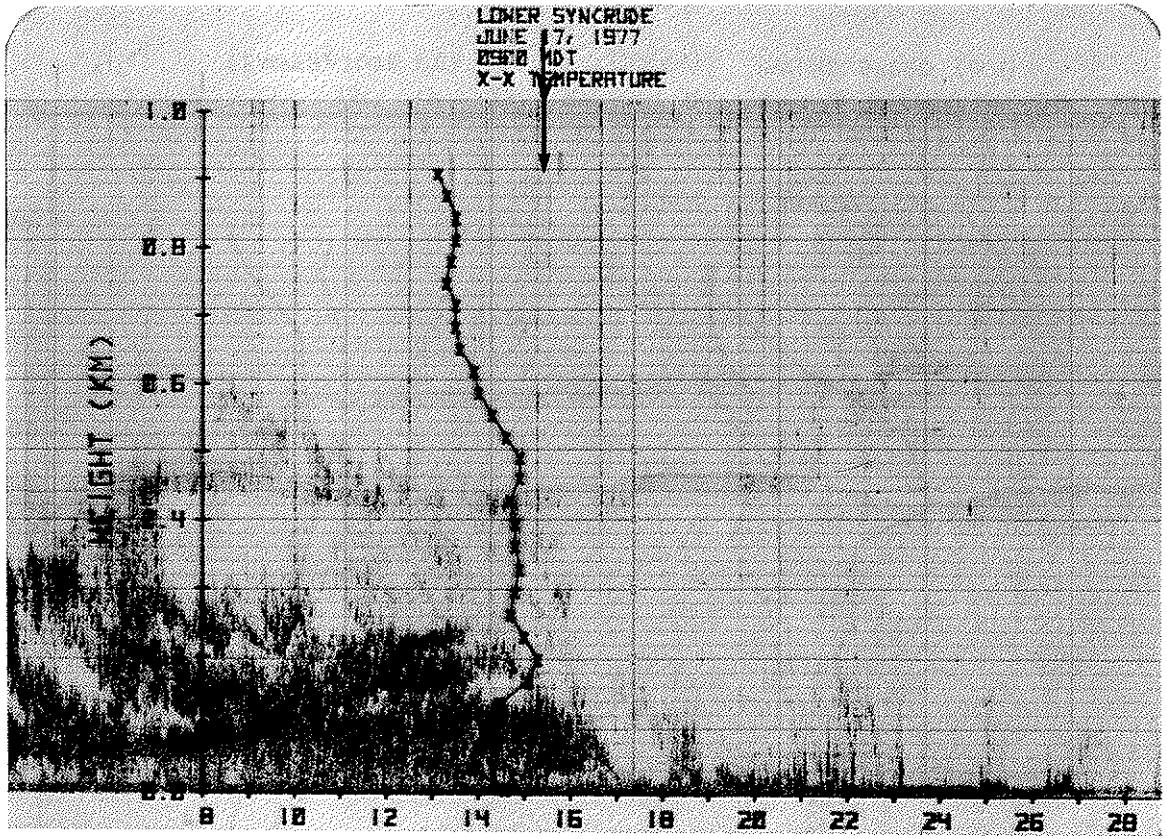

Figure 14. Photograph of the acoustic sounder record for 17 June 1977 at 0900 MDT. The arrow indicates the time at which the temperature profile was taken.

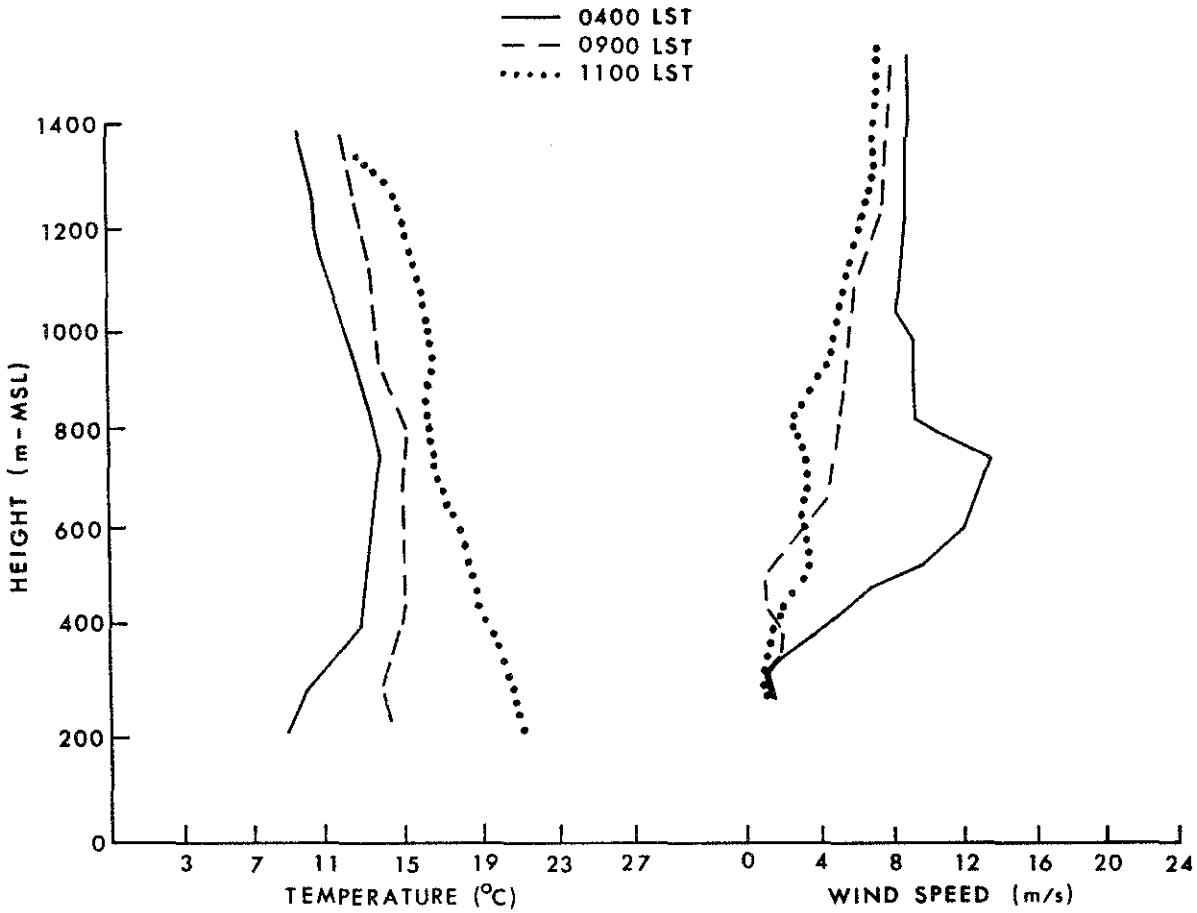

Figure 15. Profiles of temperature and wind speed at the Syncrude Site for 17 June 1977 at different times.

Whiteman and McKee (1977) observed in their study on the structure of inversion layers in a valley that the top of the inversion layer descends after sunrise. Due to the heating of the valley by insolation a thin superadiabatic layer develops that initiates convective plumes that penetrate into the stable layer above. An upslope motion develops that carries out the air above the stable air. Consequently, the inversion layer at the top descends to replace the air removed from below. Continuous mixing of that nature will eventually dissipate the inversion layer. Whiteman and McKee (1977) found that the rate of descent was steady but slower (120 $m \cdot h^{-1}$) than the descent observed in this study.

In order to relate the actual temperature inversion height to the sounder records, the inversion layer top, as recorded by the sounder, was compared to that obtained using the minisonde temperature profiles. A sample of this comparison is shown in Figure 16. In this analysis the inversion layer top as recorded by the sounder was determined and is plotted against the inversion height as given by the minisonde. No attempt is made to calculate the error of the minisonde data and in the acoustic sounder. Eighteen cases of observations are compared in Figure 17, which includes the data obtained during the last AOSERP winter study. The results show good agreement between the two systems of soundings, which implies that the acoustic sounder can be used successfully to measure the inversion height in the AOSERP study area.

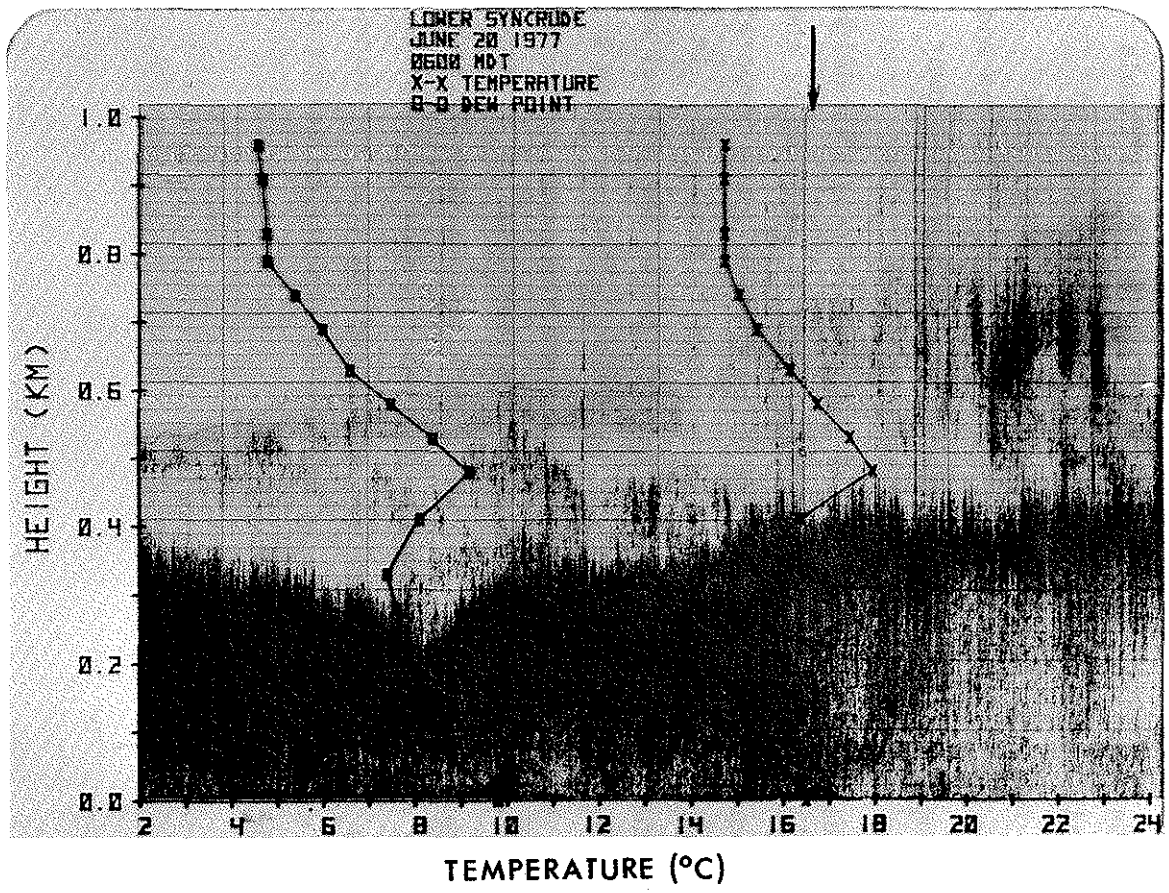

Figure 16. Comparison between the top of an elevated inversion layer and temperature profile at the Lower Syncrude Site for 20 June 1977 at 0600 MDT.

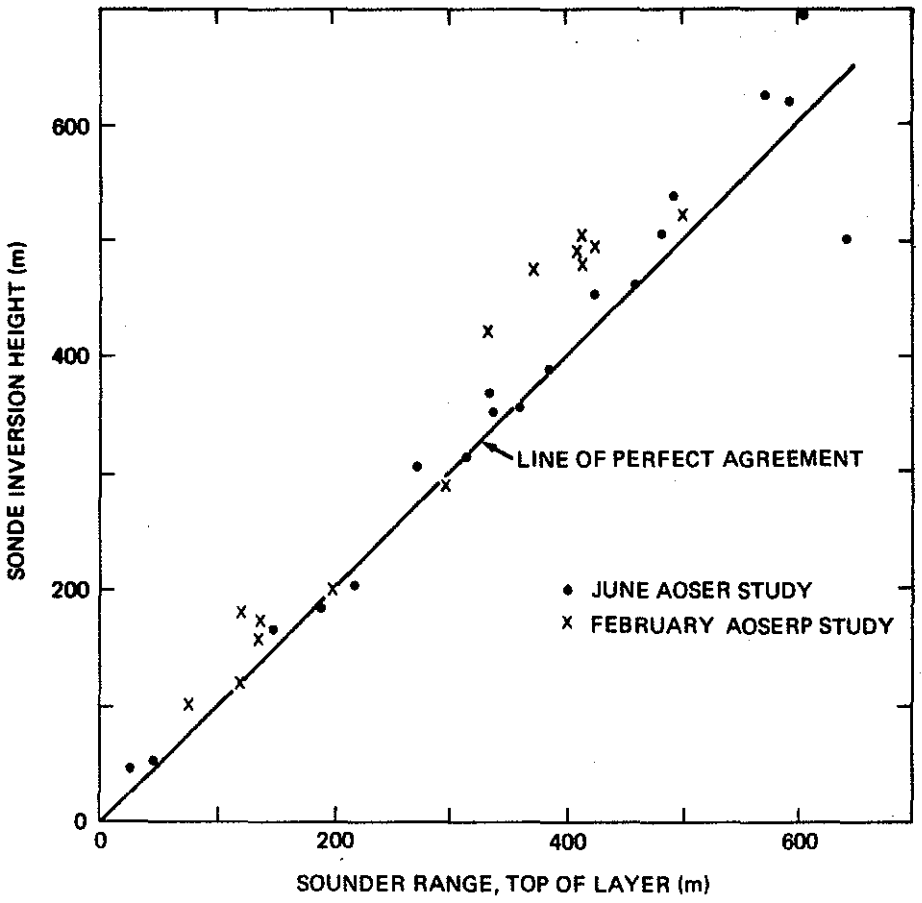

Figure 17. Comparison of predicted inversion height using sonde profiles versus observed using acoustic sounder.

3. PLUME RISE AND PLUME DISPERSION COEFFICIENT STUDY

3.1 PLUME RISE MEASUREMENTS

The technique of photographing the plume in order to determine its rise has been described previously (Fanaki 1978). The camera set-up and associated equipment used in this study were the same as those used in the analysis of the plume photography as discussed in detail by Halitsky (1961) and Fanaki and Lesins (1975). The sources of errors in applying this technique were examined in detail in the first AOSERP report (Fanaki 1978). The total error is estimated to be about 10%.

In this study only the plume from the GCOS power plant stack was studied. The plume was photographed every 30 s over a period of 10 min. The photographs were taken from different locations depending on the wind direction and at different times of day, during the period 16 to 26 June 1977 (see Table 1).

By superimposing the photographs that were taken during the 10 min period and tracing the plume outlines, a time-mean path of the plume was obtained. Table 2 shows the mean plume rise (Δh) above the stack top as a function of the downwind distance. In calculating Δh, the plume was assumed to reach its final rise when its rate of rise was minimum (Montgomery et al. 1971). On the average, Δh was approximately the same magnitude as those obtained during the winter AOSERP studies.

The predictive capability of the plume rise formulae described previously (Fanaki 1978; Fanaki et al. 1979) were examined using the data of this study. This was done by comparing the observed plume rise with the predicted value. Figures 18 to 23 show the result of this comparison. Supporting meteorological parameters (e.g., wind speed and temperature) were obtained from the soundings that were made at Lower Syncrude. The parameters were averaged from the stack top to the top of the plume before they were used.

Table 2. Plume rise as a function of downwind distance for June 1977.

Date	Time	Downwind Distance (m) 0	200	400	600	800	1000	1200	1400	1600
June 16	1120	494	784	827						
	1500	0	106	172	204	223	235	251	255	274
17	0530	0	161	172	172					
	0930	144	368	380	376	384	380	380	390	
	1015	0	396	494	541	561	561	580	584	
	1100	0	137	161	176	176	188			
	1300	0	169	290	353	380	392	404	408	
	1440	0	67	82	94	102	118	129	131	
18	0500	0	192	274	314	357	384	388		
	0600	0	161	235	274	302	314	329	333	
	0655	0	286	368	416	435	470	502		
	0930	0	149	274	384	466	529	561	592	600
	1030	0	145	176	290	408	494	557	627	666
	1130	0	98	192	231	263	282	298	306	
19	0500	0	90	114	137	165	184	188		
	0930	0	98	145	161	200	216	235		
	1030	0	74	106	129	118	122	122	129	137
	1115	0	43	71	86	94	90	98	90	94
	1345	0	74	133	161	231	290	361	392	396
	1430	0	51	67	82	94	106	125		
20	0500	0	59	78	90	90	94	106	106	110
	0600	0	55	102	122	137	145	157		
	0900	0	118	125	133	145	153	157		
	1000	0	78	106	118	125	137	149		

Continued . . .

Table 2. Concluded.

Date	Time	Downwind Distance (m) 0	200	400	600	800	1000	1200	1400	1600
20	1100	0	63	98	123	149	157	161	165	172
	1340	0	51	74	118	137	157	180	200	223
	1430	0	43	63	98	165	184	188	188	196
21	0545	0	106	169	227	274	314	325	345	365
	1400	0	533	584	698	792	941			
22	1430	0	43	012	129	172	188	204	220	231
	1515	0	67	129	161	188	231	243		
	1630	0	67	149	141	133	141	165		
	1730	0	90	141	145	141	149	149	157	
	2030	0	63	110	129	141	157	188	223	255
	2130	0	51	71	98	118	133	145	149	
23	0500	0	63	94	118	129	137	149		
	0600	0	118	122	137	129	141	145		
	0900	0	106	204	267	310	337	368	380	392
	1330	0	27	90	102	106				
24	0430	0	129	172	196	208	216	216	220	
	0600	0	125	180	220	247	255	263	270	274
	1000	0	122	192	227	239	251			
	1100	0	118	172	200	212	223	231	231	235
25	2030	0	82	157	227	263	294	298	310	
	2130	0	31	47	47	63	63	63	67	71
26	1000	0	51	67	82	98	102			
	1100	0	39	43	51	55	55			

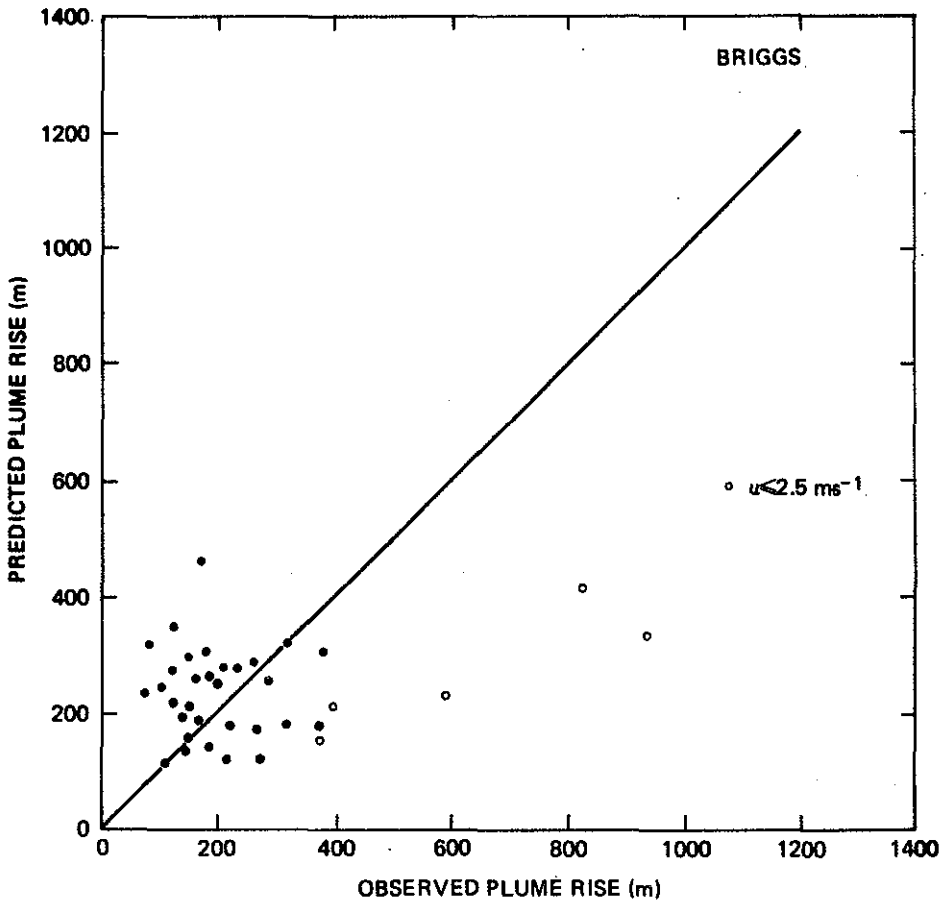

Figure 18. Comparison of predicted versus observed plume rise using Briggs' model. Solid line represents perfect agreement.

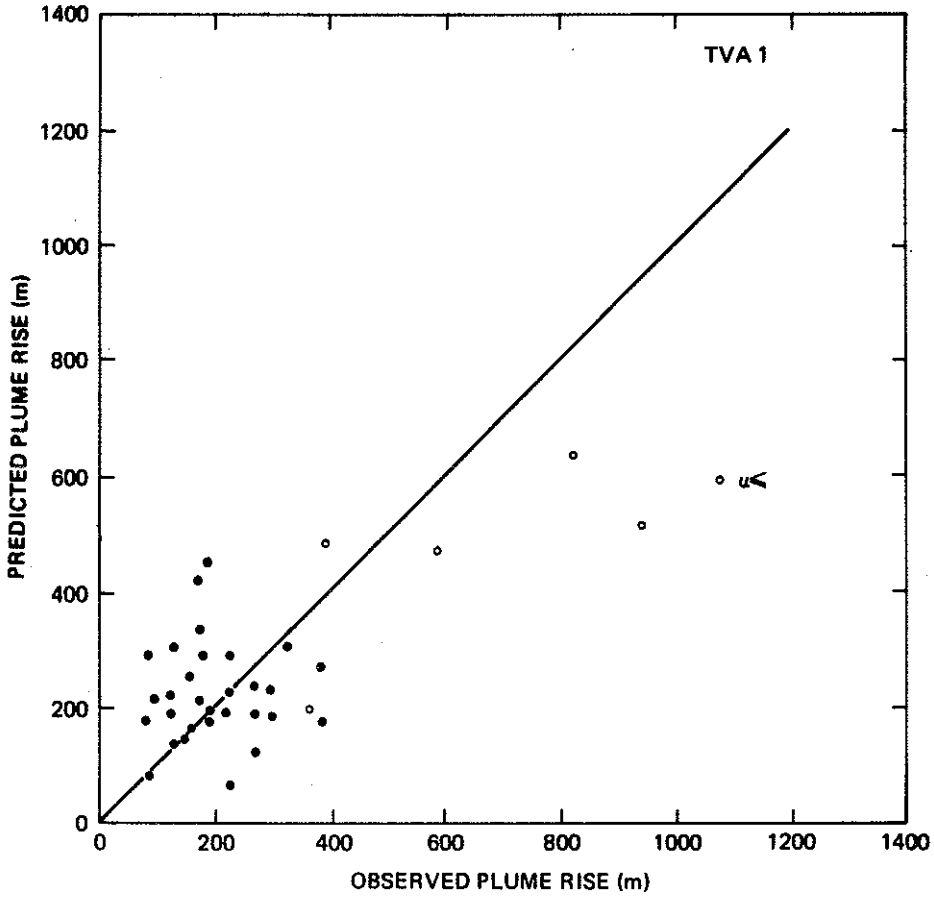

Figure 19. Comparison of predicted versus observed plume rise using TVA 1971 model. Solid line represents perfect agreement.

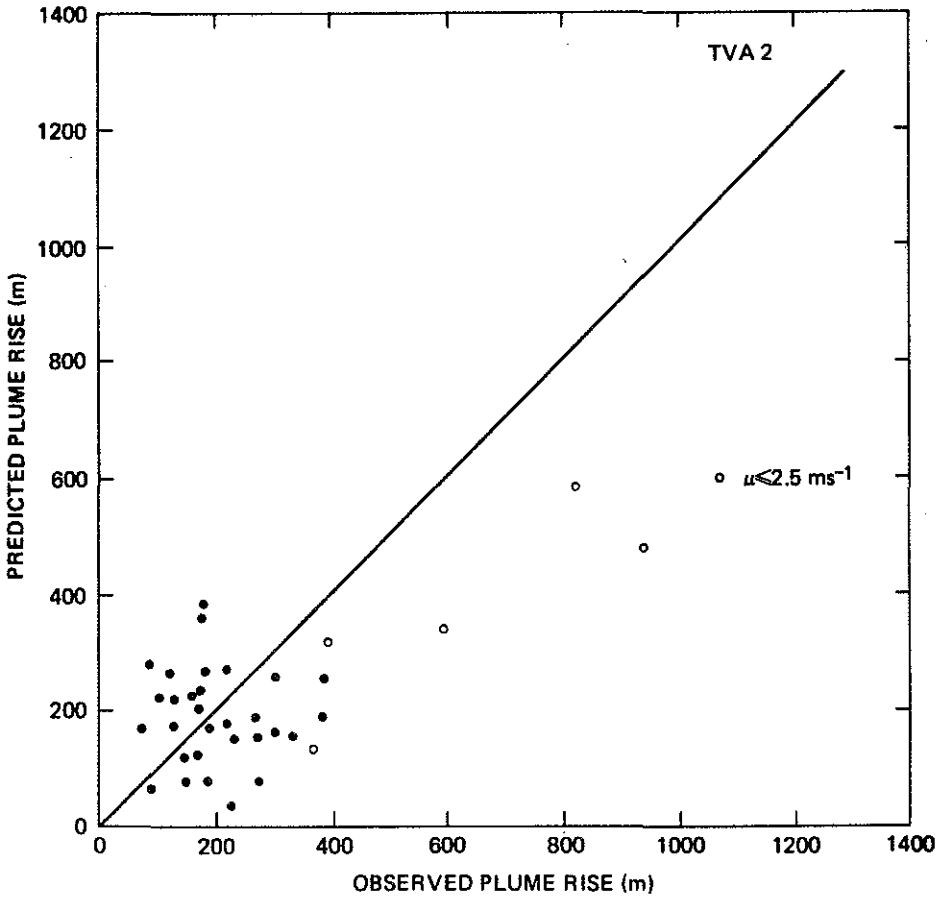

Figure 20. Comparison of predicted versus observed plume rising using TVA 1972 model. Solid line represents perfect agreement.

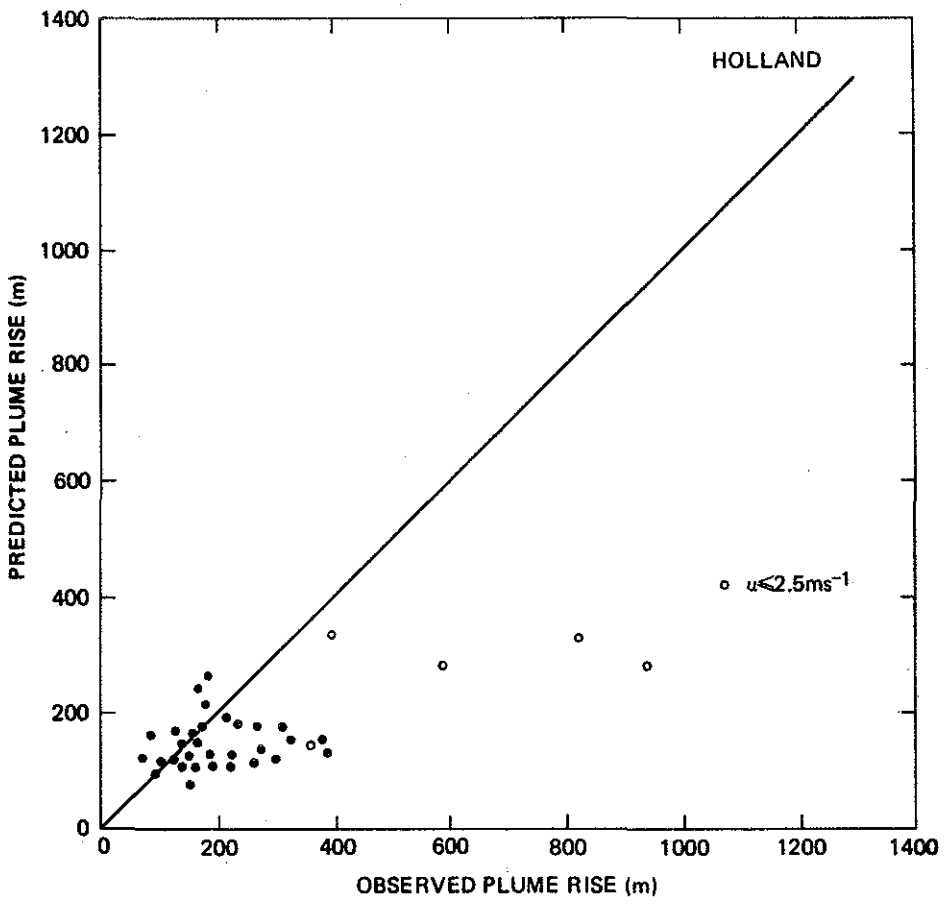

Figure 21. Comparison of predicted versus observed plume rising using Holland's model. Solid line represents perfect agreement.

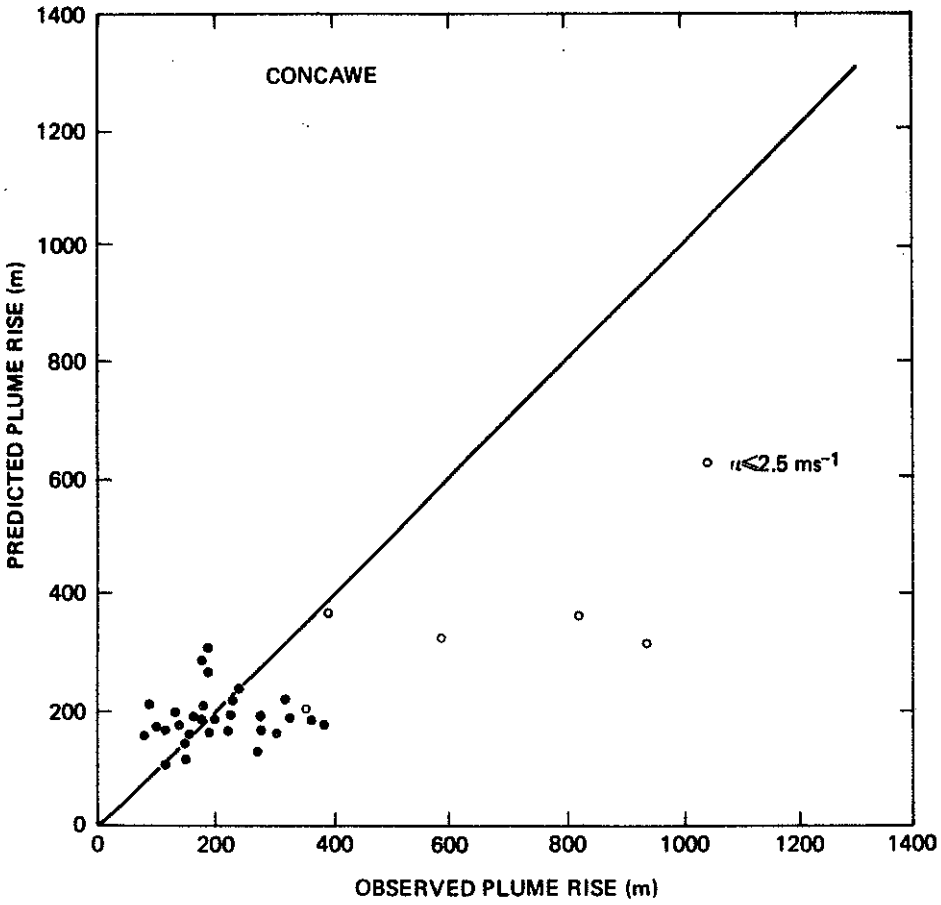

Figure 22. Comparison of predicted versus observed plume rise using Concawe model. Solid line represents perfect agreement.

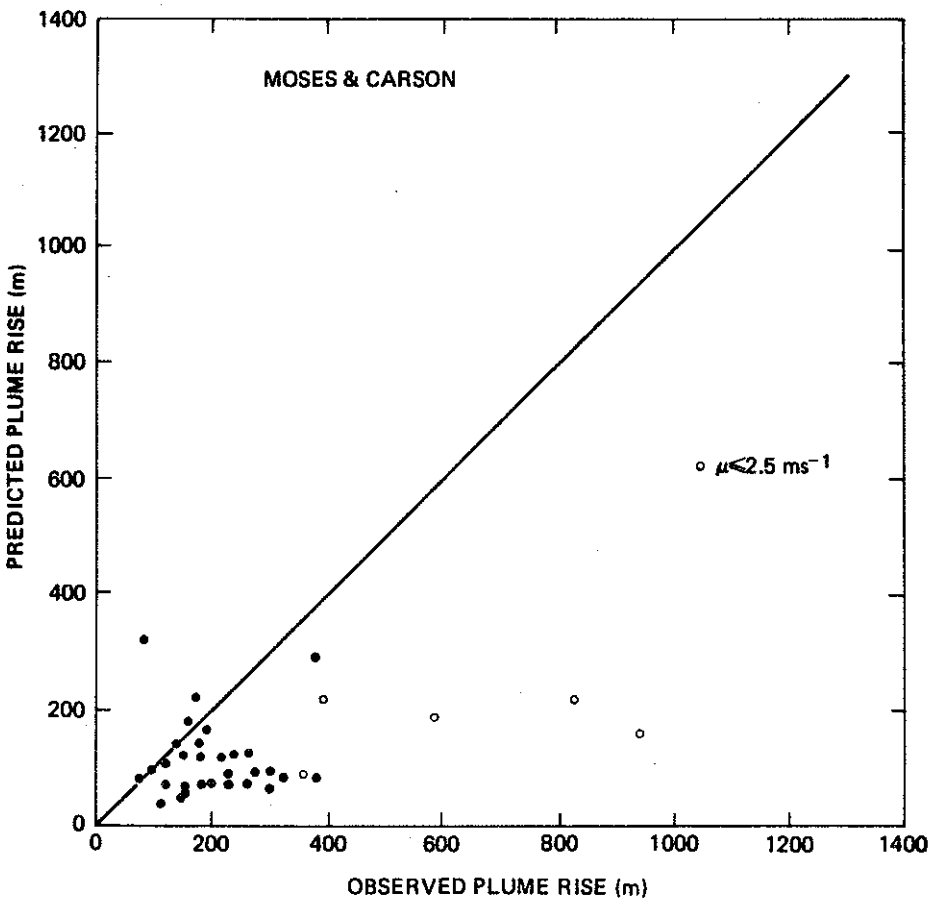

Figure 23. Comparison of predicted versus observed plume rise using Moses and Carson's model. Solid line represents perfect agreement.

It is apparent from the scatter of the data points (Figures 18 to 23) that the tested plume rise formulae are not good predictors. One reason for this discrepancy may be due to the incapability of the formulae to predict Δh well for different ranges of wind speed. In order to examine this relationship the ratio of the observed plume rise to the predicted value for different ranges of wind speed was tabulated in Table 3. All the formulae underestimate Δh for low wind speed ($u < 2.5$ m·s^{-1}). For average wind speed ($2.5 < u < 5$ m·s^{-1}) all the formulae except Moses and Carson's formula give realistic predictions. With all the formulae the fit becomes steadily worse with increase in the wind speed. By comparison, Moses and Carson's formula performs worse while Briggs' appears to perform best. However, for high wind speed $\mu > 7.5$ m·s^{-1} Briggs[1] overestimates by 20%.

Some intersting observations made on two types of GCOS plume behaviour may explain the disagreement between the observed and predicted values discussed earlier. Plume looping occurred quite frequently with the GCOS plume during the summer season at noon when solar insolation was greatest. The plume under these conditions is caught in the turbulent motion (convection) of the boundary layer and brought down to the underlying surface. Figure 24 shows a photograph of the GCOS power plant and the flare plumes under looping conditions. The point of impingement of the plume ranges from a few hundred metres to 1 km downwind from the source. In this case the plume produced high concentrations of SO_2 (<1 ppm) at the point of impingement over the few minutes of sampling duration. Vertical temperature and wind profiles under daytime convective conditions for a typical plume looping day are shown in Figure 25. It was calculated from this figure that the convective heat flux at 1430 amounted to about 226 J·m^{-2}·s^{-1}. The mixing layer extends to 900 m. The atmosphere is unstable at the plume level, and up to 900 m. At a higher level the atmosphere is relatively stable. Wind speed during plume looping ranged between 3 and 4 m·s^{-1} through the lowest 1 km

Table 3. Ratios of observed to predicted plume rise for different wind speed ranges for month of June 1977.

Wind Speed Range	Number of Observations	Briggs	TVA1	TVA2	Holland	Concawe	Moses & Carson
$U \leq 2.5$	4	2.2	1.3	1.6	2.2	2.0	3.7
$2.5 < U \leq 5$	6	1.0	.7	1.0	1.0	.9	1.7
$5 < U \leq 7.5$	15	1	1.1	1.4	1.6	1.2	2.3
$7.5 < U$	9	.8	1.2	1.6	1.7	1.2	3.1

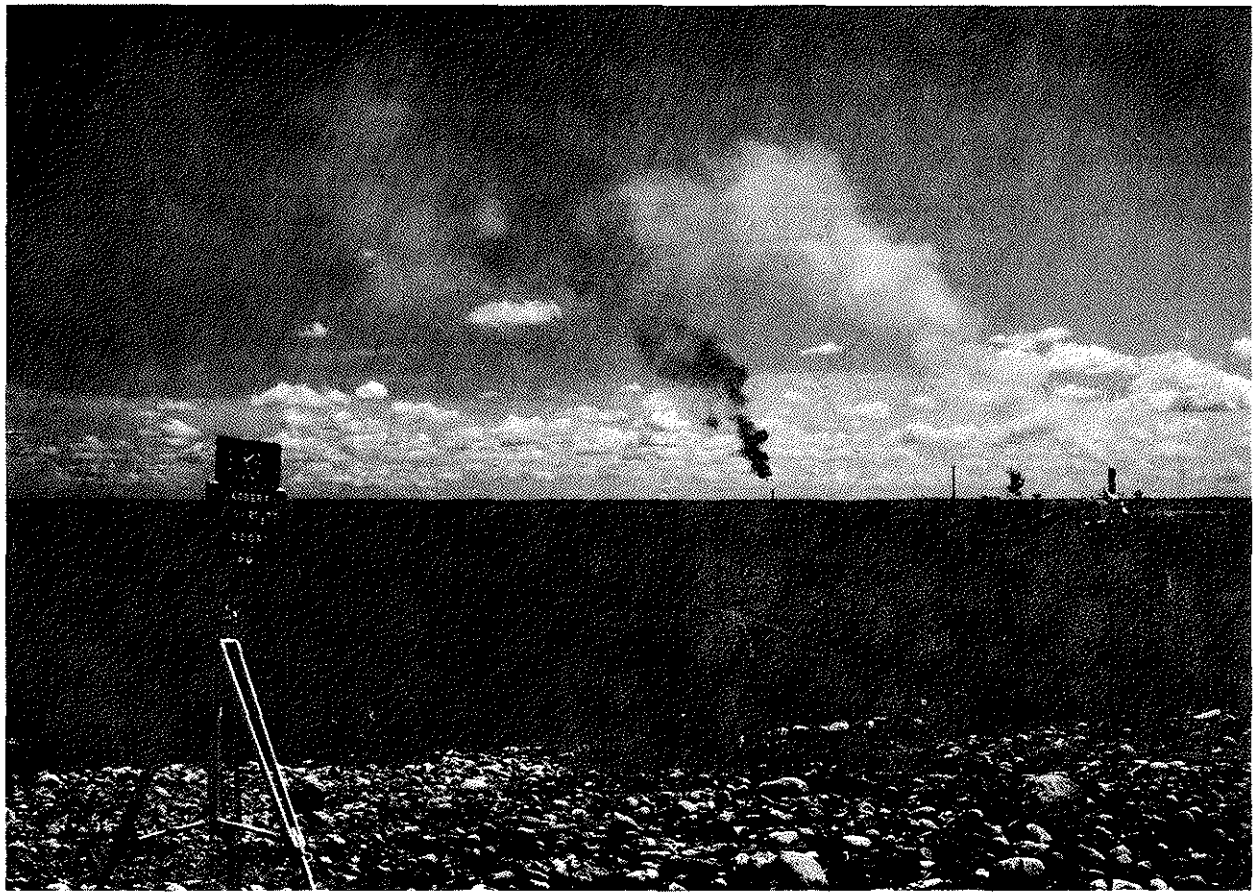

Figure 24. Photograph of looping GCOS plumes. The white plume is from the power plant stack; the dark plume is from the flare.

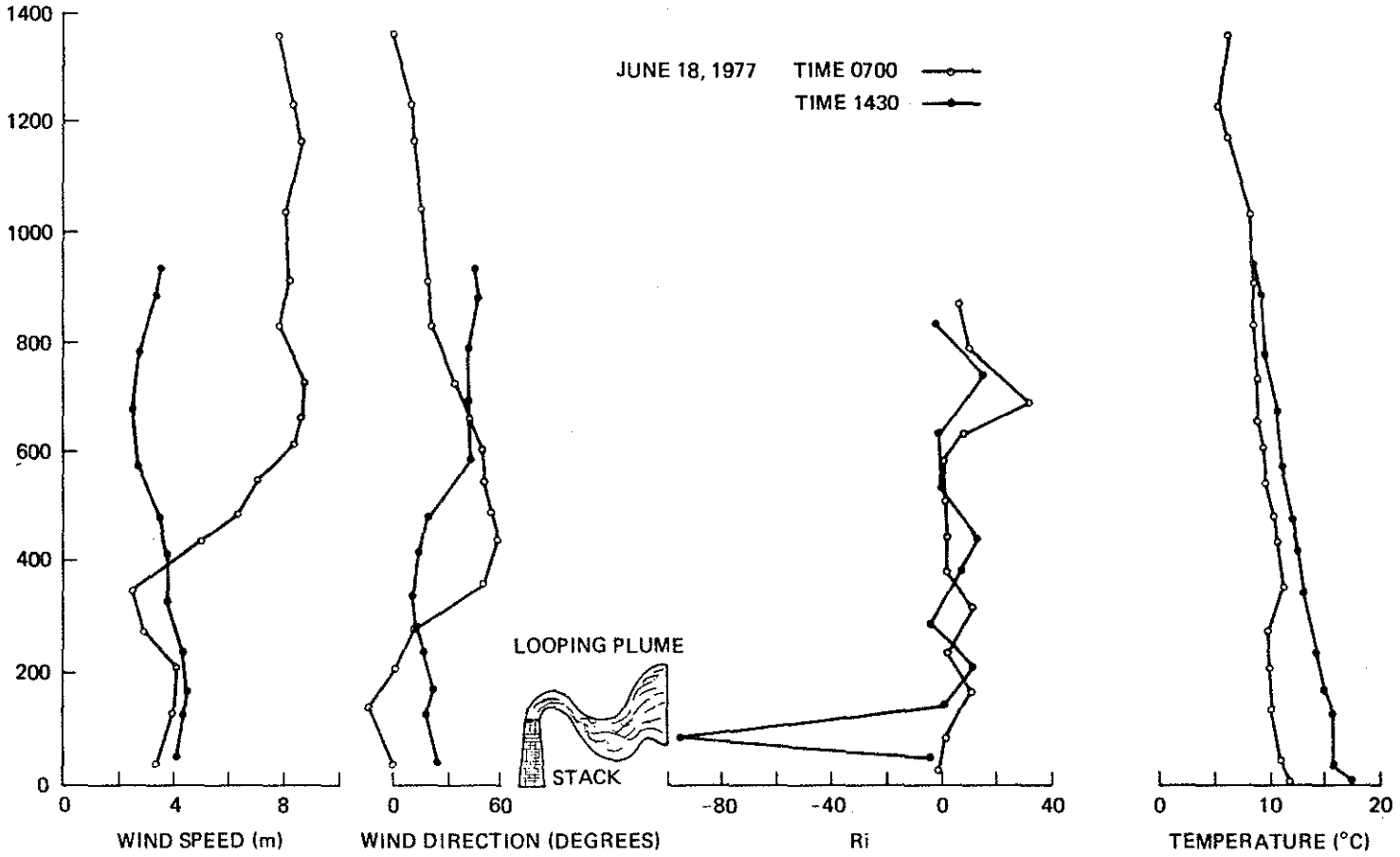

Figure 25. Profiles of wind, temperature, and Ri before and during looping conditions.

of the atmosphere. Wind direction remained relatively constant with height.

A gradient Richardson number defined as:

$$Ri = \frac{g}{\bar{\theta}} \quad \frac{(\theta_2-\theta_1)\ (z_2-z_1)}{(u_2-u_1)^2} \qquad (2)$$

was used to determine the stability conditions at the plume level. g is the gravitational acceleration 9.8 $(m \cdot s^{-1})$. θ_1 and θ_2 are the potential temperature at the two heights z_1 and z_2 respectively. $\bar{\theta}$ is the mean potential temperature in the layer z_1 and z_2 (^oK), and u_1 and u_2 are the wind speeds at height z_1 and z_2. Ri was calculated for two different times before and during the looping of the plume (at 1430). It will be noted that at the early hour of the day Ri is (+)ve, indicating relatively stable conditions. During that period the plume remains cohesive with little fluctuation along the vertical. During the afternoon hour Ri has a large (-)ve value through the level of the plume. This indicates a highly thermally turbulent region; the air is undergoing a highly convective motion of looping conditions. The layer above the plume is relatively stable.

The second case of interest describes the plume under wind shear conditions. Magnitude and direction of the wind in the atmospheric boundary layer change with height and produce a skewed Ekman layer. This type of skewed shear flow changes the plume's velocity with downwind distance. Under these conditions the diffusion of the plume is enhanced by shear along and across the plume.

A sample of contours of light scattering obtained by the LIDAR across the GCOS plume (Sec. 4) is shown in Figure 26. The results reflect the increase in horizontal growth due to the directional wind shear. In order to relate the horizontal spreading of the plume (σ_y) to the directional shear, the dispersion parameters of the plume, σ_y and σ_z, were calculated for all sampling days. Wind shear per unit height $\Delta\alpha/\Delta z$ was calculated between the top and bottom of the plume. The plume cross-section inclination $\frac{\Delta y}{\Delta z} = X \frac{\Delta\alpha}{\Delta z}$

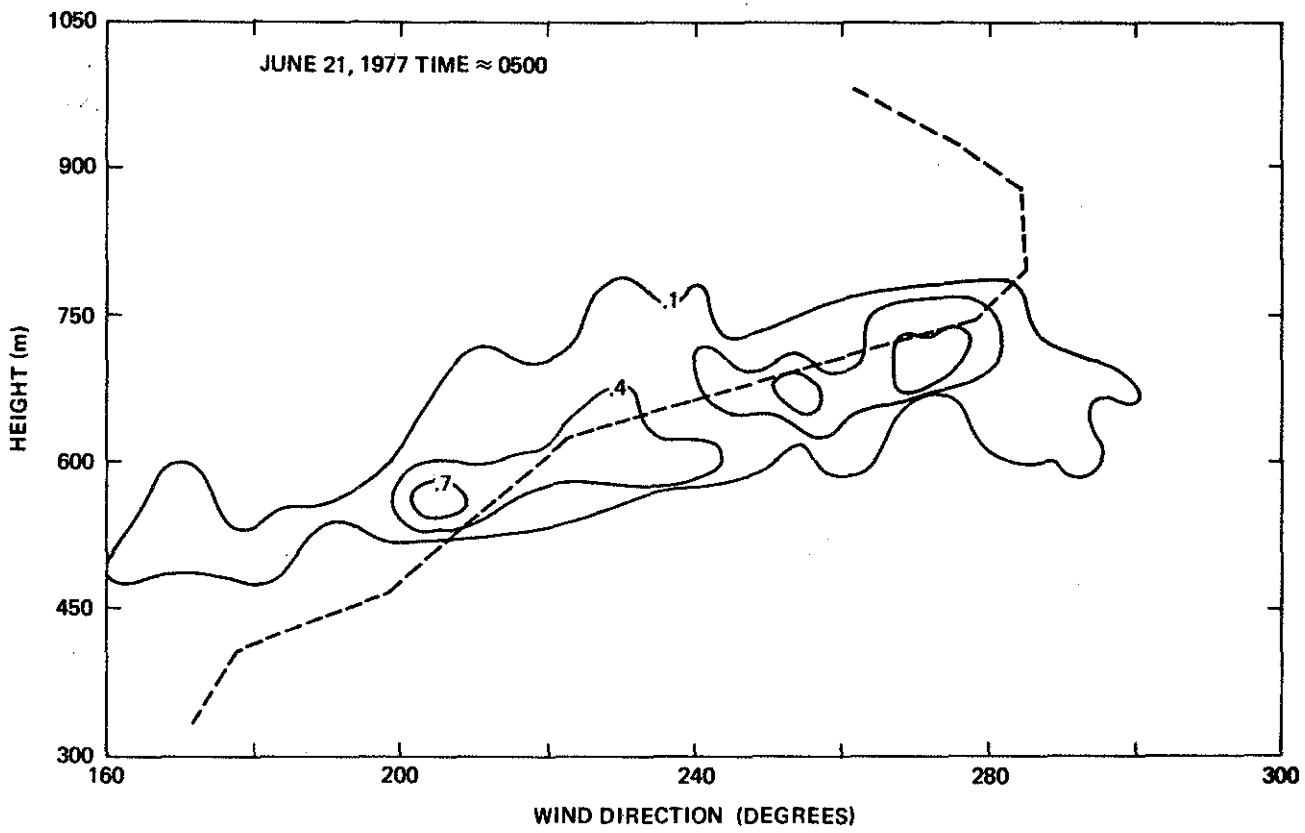

Figure 26. Example of measured isopleths of particulate across the plume under the influence of directional wind shear as shown by the wind direction profile.

was determined. The ratio σ_y/σ_z is plotted against X $\frac{\Delta\alpha}{\Delta z}$ in Figure 27 using a log scale for convenience. Due to the small number of observations the figure indicates an almost linear relationship between the $\frac{\sigma_y}{\sigma_z}$ ratio and the plume inclination. There is also a trend indicating that the ratio of the spread of the plume along the horizontal to the vertical increases with increasing wind shear.

3.2 PLUME DISPERSION COEFFICIENT MEASUREMENTS

Following the procedure outlined in previous field study reports (Fanaki 1978; Fanaki et al. 1979), we determined dispersion coefficients of the plume along the vertical. These coefficients are discussed in relation to the predictions of the classical Gaussian plume model. The observations are classified into different stability categories as described by Turner (1964). Meteorological observations from Fort McMurray Airport (45 km south of the oil sands study area) were used to determine stability categories of each day.

Observations of σ_z (Table 4) were compared with calculations based on Pasquill-Gifford dispersion parameters (Turner 1967). This was done not because of any preconceived notion that the theory ought to apply, but to provide a reference framework for discussion. Figures 28 to 31 show σ_z compared to Pasquill-Gifford values for different stability categories. Sec. 4 examines the predictive capability of the ASME curves of σ_y and σ_z using the LIDAR observations. According to the meteorological observations from the Fort McMurray Airport, stability categories ranged from A to D, i.e., from extremely unstable to neutral. Local meteorological observations, however, indicate that many stable conditions prevailed during the study period.

The scatter of the points is large and there is no apparent relationship between the measured σ_z classes. On the average all the data points compare with Pasquill-Gifford values for plume growth under stabilities B and C. Only one case compares with stability A.

It is not surprising that the observed σ_z does not agree with the Pasquill-Gifford curves. Pasquill-Gifford curves were constructed from measurements generally made in open level terrain using

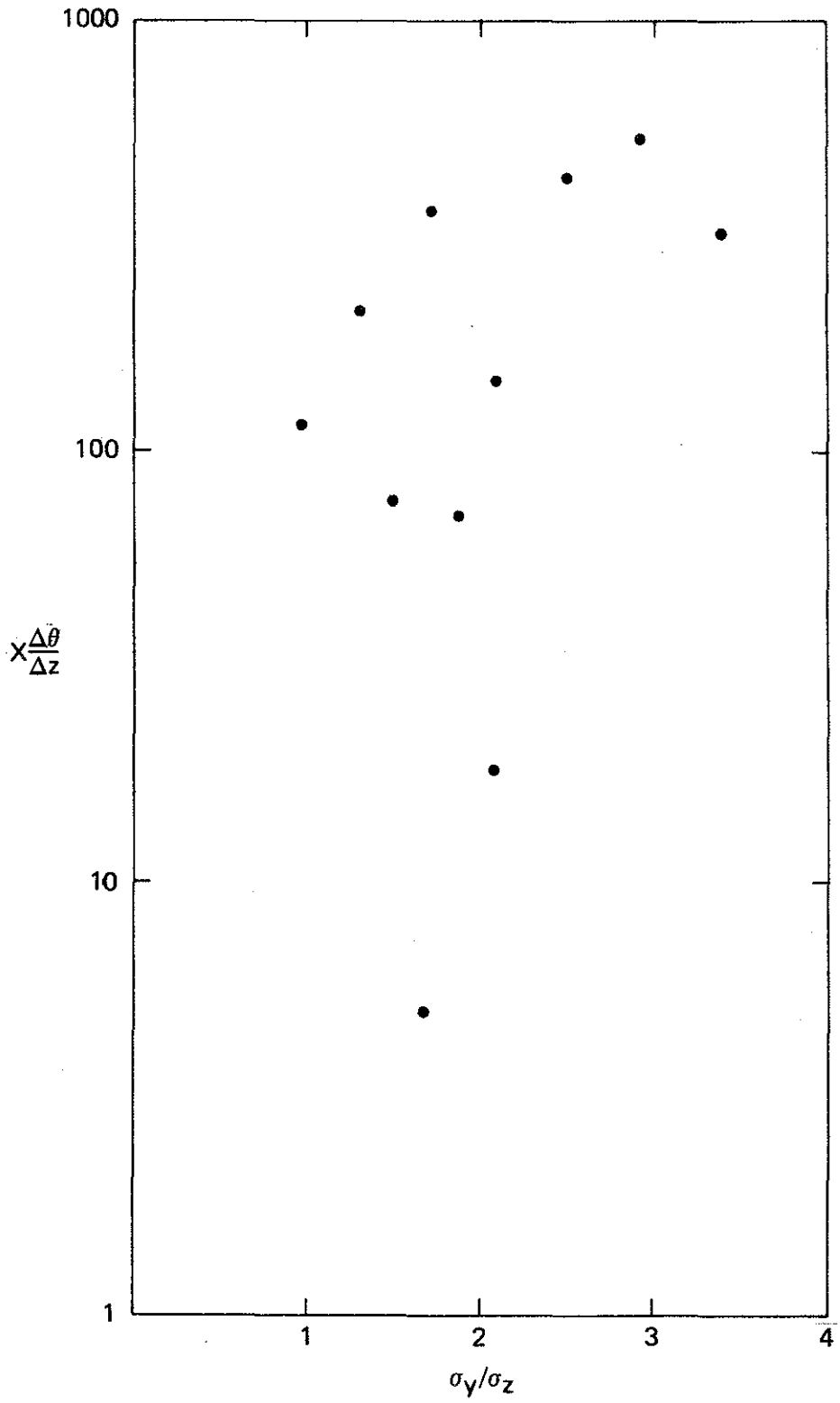

Figure 27. Normalized vertical direction wind shear versus ratio of horizontal to vertical plume dispersion coefficient.

Table 4. σ_z as a function of downwind distance for June 1977.

Date	Time	Downwind Distance (m) 0	200	400	600	800	1000	1200	1400	1600
June 16	1120	89	109	91	62					
	1500	0	23	51	60	69	69	67	67	69
June 17	0530		49	44	42	49	49	47	49	55
	0930	30	55	57	58	60	60	57	53	
	1015		49	60	64	71	73	71	69	69
	1100		33	46	46	42	40	40		
	1300		37	62	78	87	93	97	95	100
	1440		22	27	27	31	31	33		
June 12	0500		37	55	57	60	75	78	78	
	0600		33	60	73	73	84	87	86	
	0655		51	77	89	97	91	97	98	104
	0930		15	46	53	66	86	95	91	91
	1030		47	78	109	142	179	200	219	221
	1130		20	64	86	109	124	135	146	135
June 19	0500		18	27	33	40	46	47	53	
	0930		17	31	39	49	51	55	51	53
	1030		22	31	35	37	37	42	40	37
	1115		18	31	38	37	38	42	42	40
	1345		9	27	38	55	71	87	84	75
	1430		17	22	22	24	29	31		
June 20	0500		9	15	27	37	42	46	42	38
	0600		15	27	31	37	38	40	44	49
	0900		17	33	37	44	47	44	40	44
	1000		15	15	20	22	26	31	31	26

Table 4. Concluded.

Date	Time	Downwind Distance (m) 0	200	400	600	800	1000	1200	1400	1600
20	1100		20	26	27	37	42	40	40	42
	1340		11	22	44	57	62	60	66	66
	1430		11	20	22	27	37	38	40	40
June 21	0545		24	38	51	58	62	64	64	64
	1400		37	55	73	78	93			
	1510									
	1600									
June 22	1430		22	44	51	60	66	66		
	1515		40	60	89	104	119	140	133	
	1630		42	73	75	84	100	122	131	133
	1730		24	49	62	64	64	64	60	64
	2030		18	37	46	44	58	62	64	
	2130		9	20	29	35	31	33	33	33
June 23	0500		15	26	31	31	31	29	37	42
	0600		33	37	40	42	40	44	44	44
	0900		29	57	75	89	100	108	111	
	1330		18	58	98	115	119	120	124	126
	1430		13	18	15					
June 24	0430		24	40	49	53	51	51	53	
	0600		18	31	38	47	51	55	53	
	1000		22	31	40	40	42	46	46	44
	1100		18	35	42	44		42	44	44
June 25	2030		26	44	69	73	77	77	69	67
	2130		15	18	26	29	35	35	35	37
June 26	1000		22	31	40	46	49			
	1100		13	20	31	35	31	35	35	35

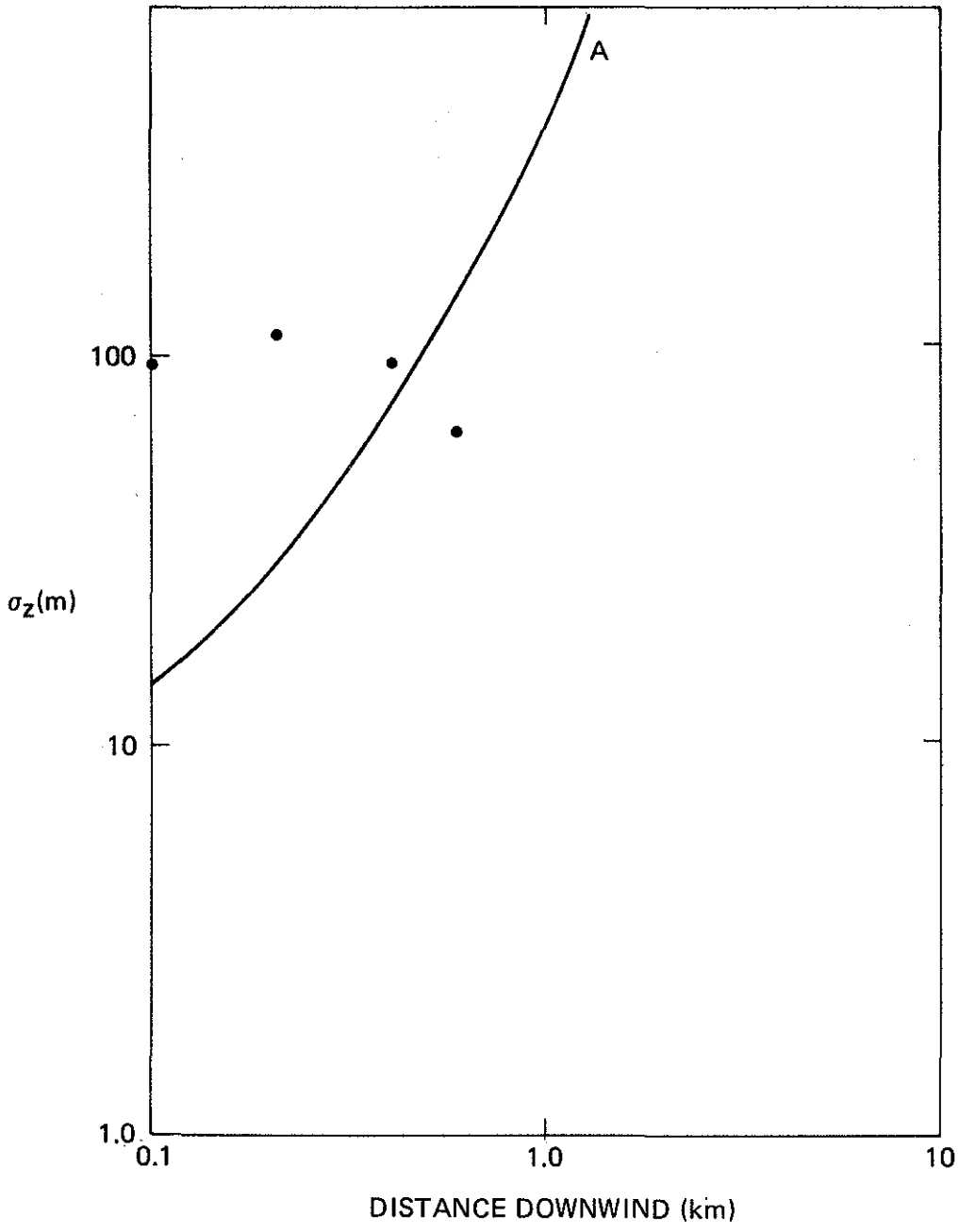

Figure 28. Comparison of observed vertical dispersion coefficient with Pasquill-Gifford prediction for A stability.

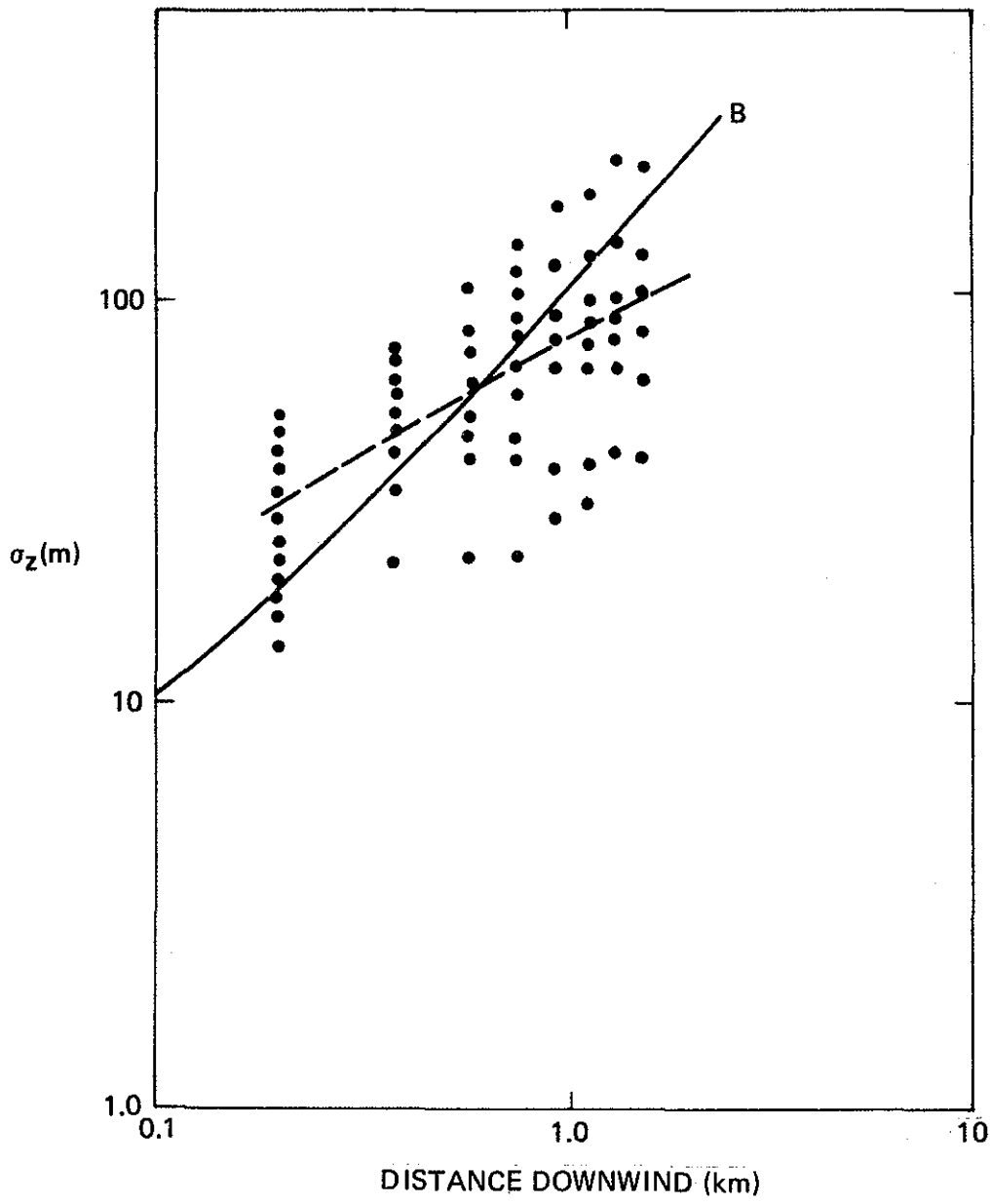

Figure 29. Comparison of observed vertical dispersion coefficient with Pasquill-Gifford prediction for B stability.

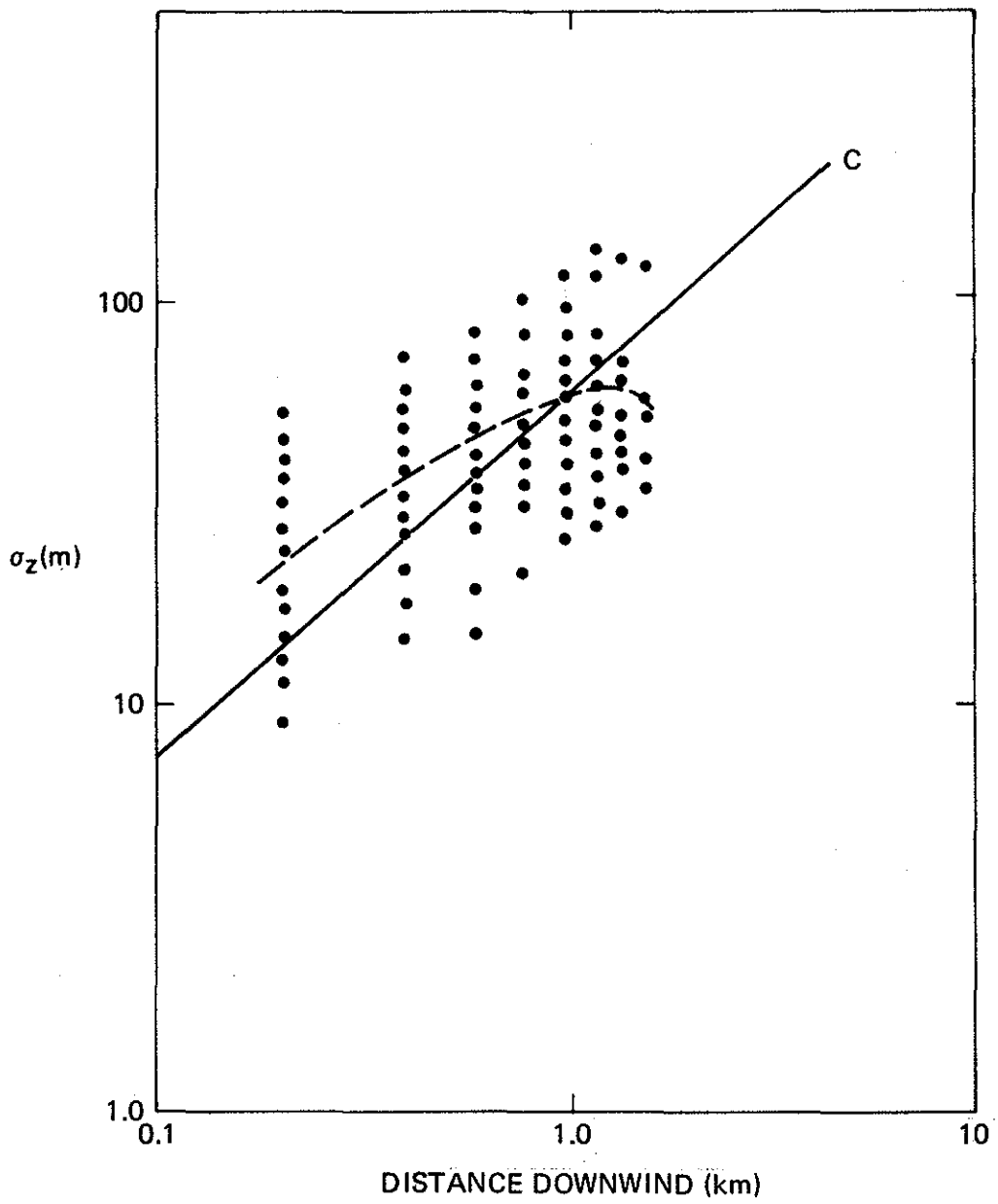

Figure 30. Comparison of observed vertical dispersion coefficient with Pasquill-Gifford prediction for C stability.

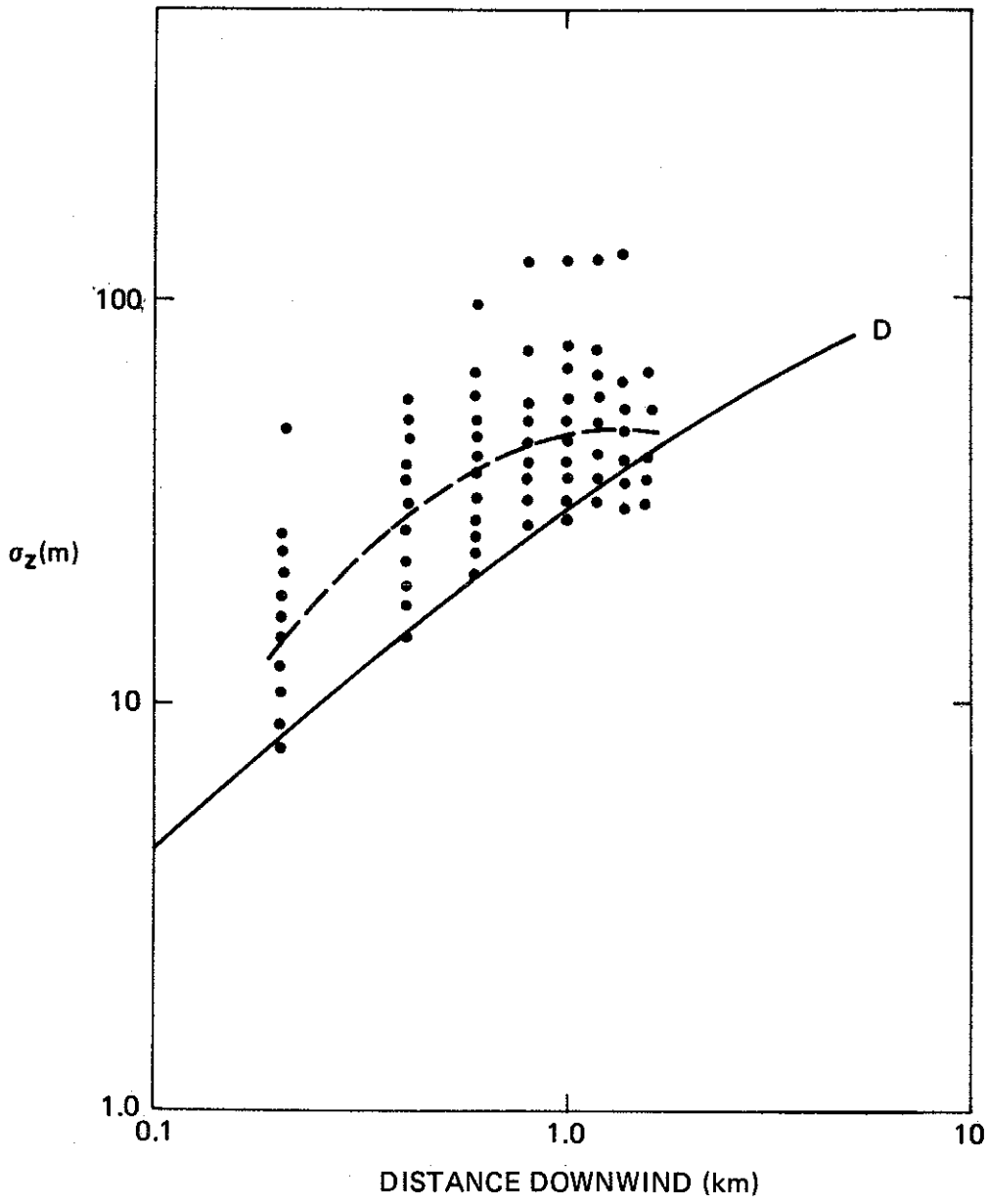

Figure 31. Comparison of observed vertical dispersion coefficient with Pasquill-Gifford prediction for D stability.

a ground source (Pasquill 1961). Also, Pasquill indicated that the results are valid to a downwind distance of 800 m. Beyond that distance the proposed σ_z were speculative.

It will be noted from the figures that the rate of increase of the average σ_z (broken line Figures 28 to 31) is not as rapid as Pasquill-Gifford curves indicate.

In his study of plume behaviour under lake breeze conditions, Koczkur (1968) attributed the slow vertical spreading of the plume partly to the absence of large-scale atmospheric turbulence and to the low wind speed.

3.3 COMPARISON BETWEEN PHOTOGRAPHIC AND LIDAR MEASUREMENTS

In order to assess the accuracy of the photographic technique applied in this study, a comparison between photographic and LIDAR measurements was made. Figure 32 shows a comparison of the plume rise Δh determined by the camera and by the LIDAR.

In determining σ_z from photography it is assumed that the plume is normally distributed. Calculation of σ_z by the LIDAR, however, was made using actual measurements of plume light backscattering. Figure 33 compares the two sets of measurements of σ_z. The agreement is good close to the source; at a larger downwind distance the LIDAR tends to see more of the plume than the camera does.

3.4 CONCLUDING REMARKS

The main objective of this study was to obtain data on the rise and dispersion of the GCOS plume under summer conditions. The data are of good quality and will contribute to the AOSERP data bank.

Brigg's formula appears to predict the rise of the plume in the oil sands area better than the others reported in this study. As in the previous winter studies, the correlation between the observed and predicted is low, in particular under low wind conditions.

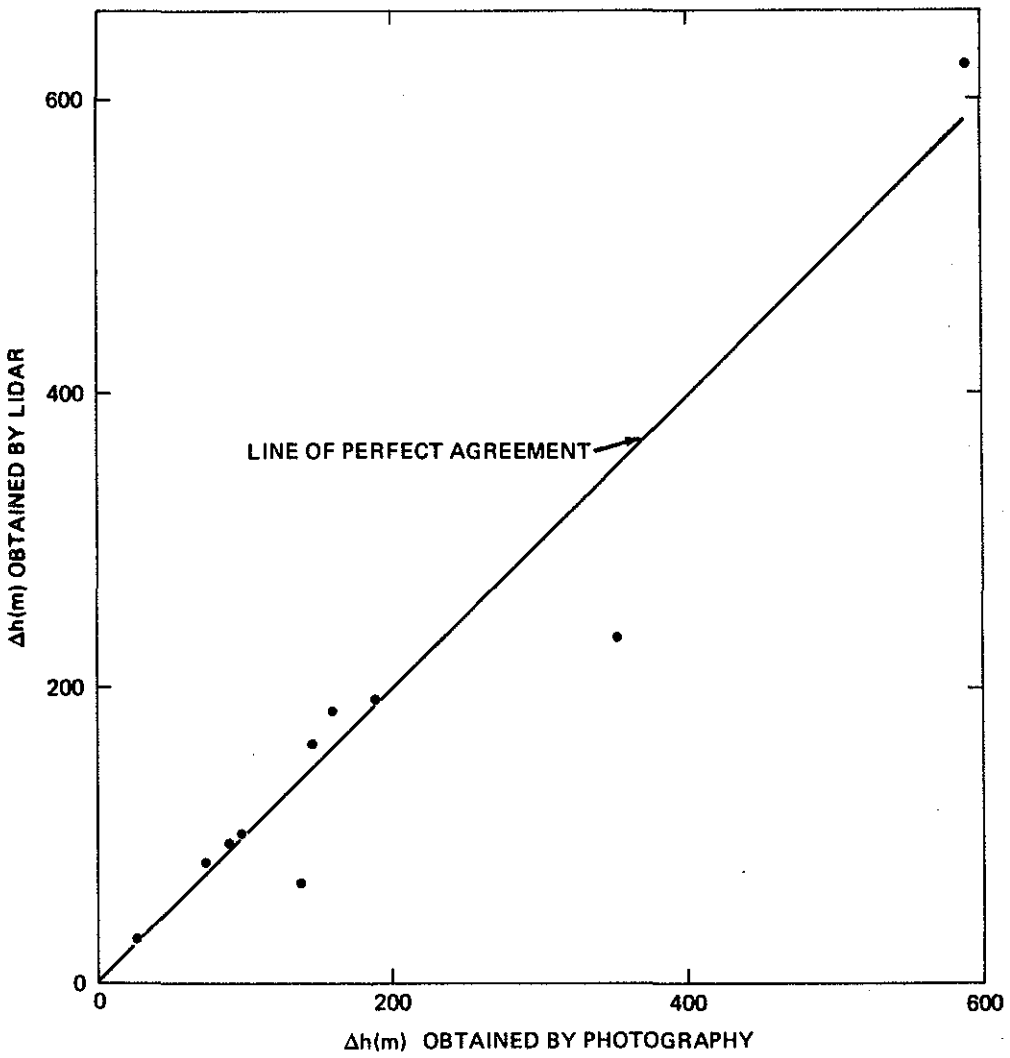

Figure 32. Comparison of photographic plume rise with LIDAR plume rise.

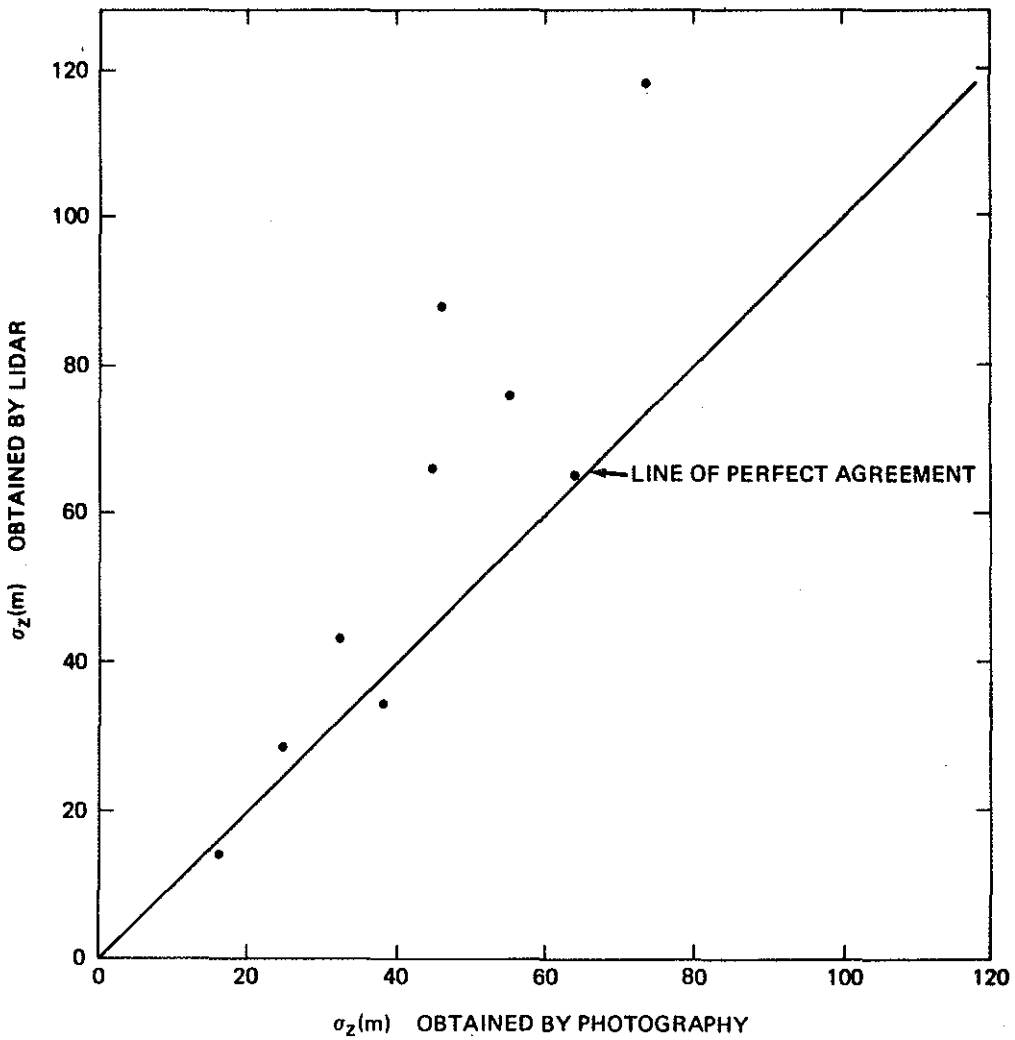

Figure 33. Comparison of photograph σ_z with LIDAR σ_z.

A new model for handling the rise of the plume in the oil sands area under different meteorological conditions must be developed. The model should include the effects of wind shear and looping.

The rate of vertical dispersion of the GCOS plume, as indicated by the standard deviation of the plume depth, is larger than that predicted by the Pasquill-Gifford curves. The discrepancy may be due to the fact that the Pasquill-Gifford curves were designed for a flat terrain and for a ground source. The source in this study is 106 m above ground in a valley. This area is characterized by differing wind speed at the surface and aloft, frequent occurrence of inversion layers, and changing topography around the source due to the continuous mining.

In this study each of the measured σ_z is the result of 10-min average of plume widths. Atmospheric eddies of that time scale will affect the observed σ_z. For a significant plume meandering (e.g., looping), the observed σ_z will be larger than the instantaneous values. The Pasquill-Gifford curves do not allow for such effects.

Plume rises, as measured by photography agree well with those obtained using the LIDAR. σ_z measurements obtained by the LIDAR are slightly larger than those obtained by photography. The LIDAR appears to sense more of the plume than the camera does.

4. LIDAR PLUME DISPERSION MEASUREMENTS

The use of the optical radar, or LIDAR (Light Detection and Ranging), to detect particulates in stack plumes has become increasingly common. The ranging property of the LIDAR provides information on the spatial dispersion of plumes, and the intensity of the returned light signal is related to the concentration of particulates in the plume. The use of the AES mobile research LIDAR was proposed for the AOSERP June 1977 field project as a means of obtaining the horizontal and vertical dispersion of the GCOS plumes and the associated plume rise.

Since the LIDAR technique may be unfamiliar to the reader, a brief introduction to the theory and limitations of the measurement process is appropriate. A LIDAR pulse consists of an intense, collimated, and highly monochromatic burst of light from a laser source. In the AES LIDAR this source is a ruby laser giving an intense red light pulse approximately 10-20 ns at 694.3 nm wavelength. By monitoring the time delay and intensity of the signal returned from an aerosol, one may determine both the range (R) of the aerosol from the LIDAR and characteristics of the aerosol density. The range can be unambiguously and accurately determined from time delay (t) and speed of light (c) by

$$R = ct/2 \qquad (3)$$

There is a factor of two because the light being observed by the receiver will have travelled out to range R and returned, giving a path of 2R.

The intensity of the returned signal contains information about the number density or concentration of particulate. For reasons shown below, this information is not unambiguous, and it is important that the reader understand the nature of the light scattering process involved.

At visible wavelengths, light is scattered by the atmospheric gas molecules (Rayleight scattering, which give rise to Alberta's blue skies) and by particulates (Mie scattering).

Scattering from a molecular atmosphere is easily quantifiable because the average density of molecules and their sizes are well defined and relatively homogeneous. For Mie scattering the amount of light scattered is dependent on a number of factors, including particle concentration, size distribution, index of refraction (both real and imaginary parts), and the optical length of the laser pulse. These dependencies can be quite dramatic, varying by orders of magnitude, and care must be employed in inferring the absolute concentration of an aerosol from a measurement of scattered light energy.

Figure 34 shows a schematic of the LIDAR measurement process. A pulse of light is sent out from the transmitter. This pulse probes a volume at range R of Length $L_L = ct/2$ where t is the laser pulse length of 10 to 20 ns (this length is typically 2 m). The telescope receiver examines a time interval $t' = 2L_D/c$ (which can be varied electronically) around the time $t = 2R/c$. The length $\ell = (L_L + L_D)/2$ represents the instrumental resolution.

The returned light power (P_r) is related to the output power (P_o) by:

$$P_r(R) = \exp(-2\int_o^R \alpha(R)\, dR) \cdot (P_o A_r\, {}^{e}\beta_\pi(R)\ell/R^2) + kN\lambda \qquad (4)$$

where ${}^{e}A_r$ = effective receiver area (includes solid angles)
$\alpha(R)$ = atmospheric extinction coefficient at range R
$\beta_\pi(r)$ = aerosol backscatter coefficient at range R
$kN\lambda$ = background light power.

The first exponential integral in Equation (4) is due to the absorption and scattering of the laser beam on its path to the plume. The term in brackets is the fraction of light scattered back to the receiver. The stray light term (kN_λ) is included because at low returned powers, sky radiance and photomultiplier dark current may become comparable to the signal.

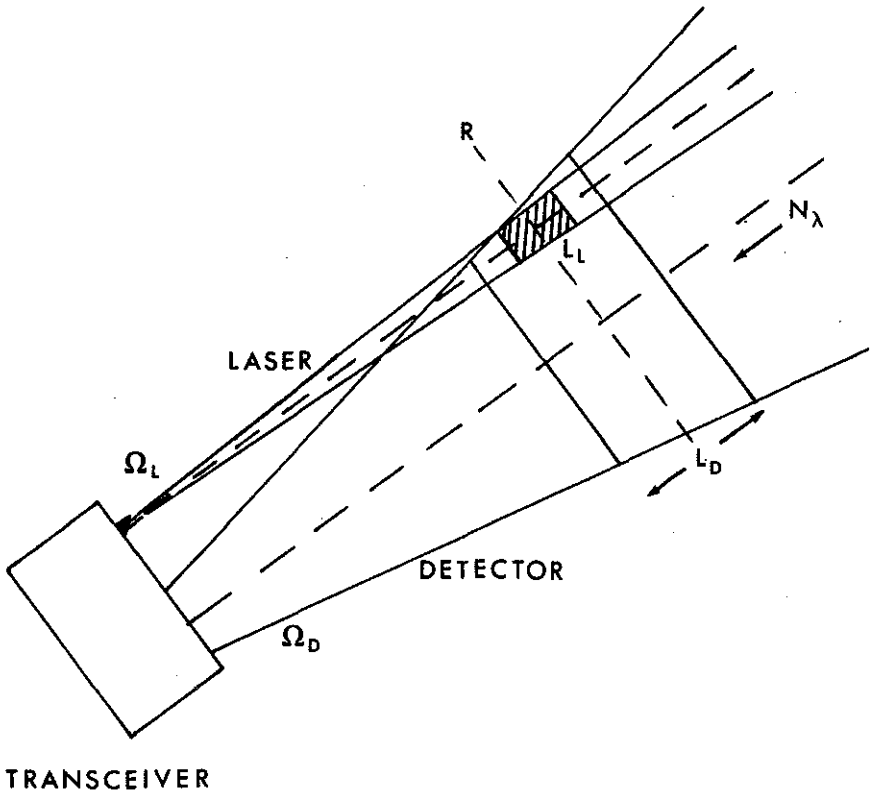

Figure 34. LIDAR measurement scheme. R represents range from LIDAR, L_L is the pulse length, L_D is the detector sampling length, Ω_L and Ω_D are the lasar and detector solid angles, and N_λ is the background sky radiance.

In a LIDAR technique, it is minimally necessary to measure R and P_r (and P_r only relatively). It is advantageous to monitor P_o for shot to shot variation; however, this facility is not available on the AES LIDAR. The authors therefore had to rely on the laser manufacturer's quoted specificiations of 10% pulse to pulse variation. For an optically thin aerosol, i.e., not of a density comparable to clouds, it is possible to assume that $\beta_\pi(R) < \alpha(R) << 1$ and the first exponential in Equation (4) goes to unity. Making this approximation, Equation (4) becomes:

$$S = \left(\frac{Pr(R) - kN\lambda}{Po\ Ar^e}\right) R^2 = \beta_\pi(R)\,\ell \qquad (5)$$

Since the left-hand side of Equation (5) is known, $\beta_\pi(R)$ can be determined, at least relatively. The authors have chosen to call the quantity P_r-kN a "baseline shifted power" and the quantity of the left-hand side of Equation (5) as the "range scaled power".

From a plume dispersion point of view, one would like to have some confidence in relating the measureable $\beta_\pi(R)$ to the number concentration of particulates at range R. It is implicit in the rest of this report that the number concentration is directly proportional to $\beta_\pi(R)$. What that assumption entails is that all other aerosol parameters are fixed, with only the concentration as a variable. One would hesitate to make such an assumption when the processes involved in aerosol formation were heterogeneous or multi-component. In a stack plume, however, if the incineration process is relatively constant, the size distribution of the aerosol and indices of refraction should change only minimally over the averaging time of the measurement, and the assumption of proportionality is probably valid. With these assumptions, geometric measurements on the plume profile can be made with confidence.

The authors will not attempt to derive actual plume concentrations because that would require a degree of calibration not warranted in the present system.

4.1 LIDAR SYSTEM AND SPECIFICATIONS

The AES Research LIDAR consists of a 1.0 J ruby laser mounted in a Dodge Tradesman van. The laser beam is steered through the roof assembly by means of five right-angle prisms. The receiver consists of a 20-cm Fresnel plastic lens that couples the returned light signal to a fibre-optic image guide connected to the photomultiplier on the laser rail.

On the photomultiplier output, a Biomation Model 8100 Transient Digitizer (essentially a digital oscilloscope) converts the analog returned pulse to a digital format of 500 data points, each of a preselected width in time. These points are immediately transferred to a Digital Equipment Corporation PDP 11/04 minicomputer for file structuring and insertion of housekeeping data. The shots are stored on magnetic floppy disk for later processing. Figures 35, 36, and 37 show the external assembly, laser rack, and electronics rack, respectively. The LIDAR specifications are given in Table 5.

4.2 DATA COLLECTION AND PROCESSING TECHNIQUES

The data collection used in the AOSERP June 1977 field study is shown schematically in Figure 38. The LIDAR vehicle was stationed some distance to the side of the GCOS plume (see Figure 41 for stations used), and the elevation assembly scanned to obtain vertical slices of the plume. Several of these scans at one azimuthal setting were performed to obtain one-half hour or one-hour average plume cross sections. The LIDAR was then reset in azimuth to perform scans at different downwind ranges.

Although data collection is primarily automatic, eye safety procedures in LIDAR operation allow manual triggering of the laser only after the operator has ascertained a clear field of view. In practice, this limited the operation to a shot roughly every 30 s, making a 10-shot scan about 5 min long. In general, then, a one-half hour average was calculated from three to six "instantaneous" scans.

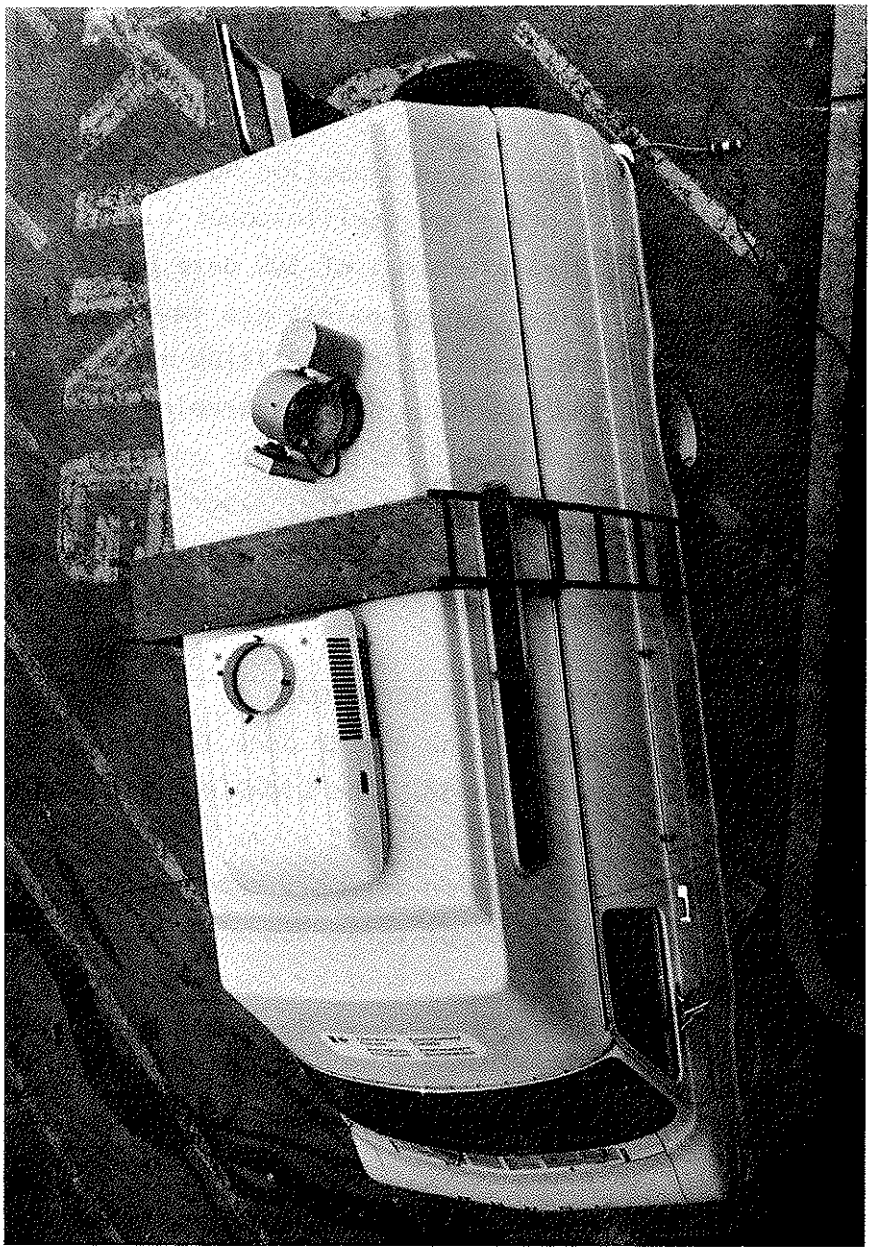

Figure 35. LIDAR external assembly and Dodge Tradesman van.

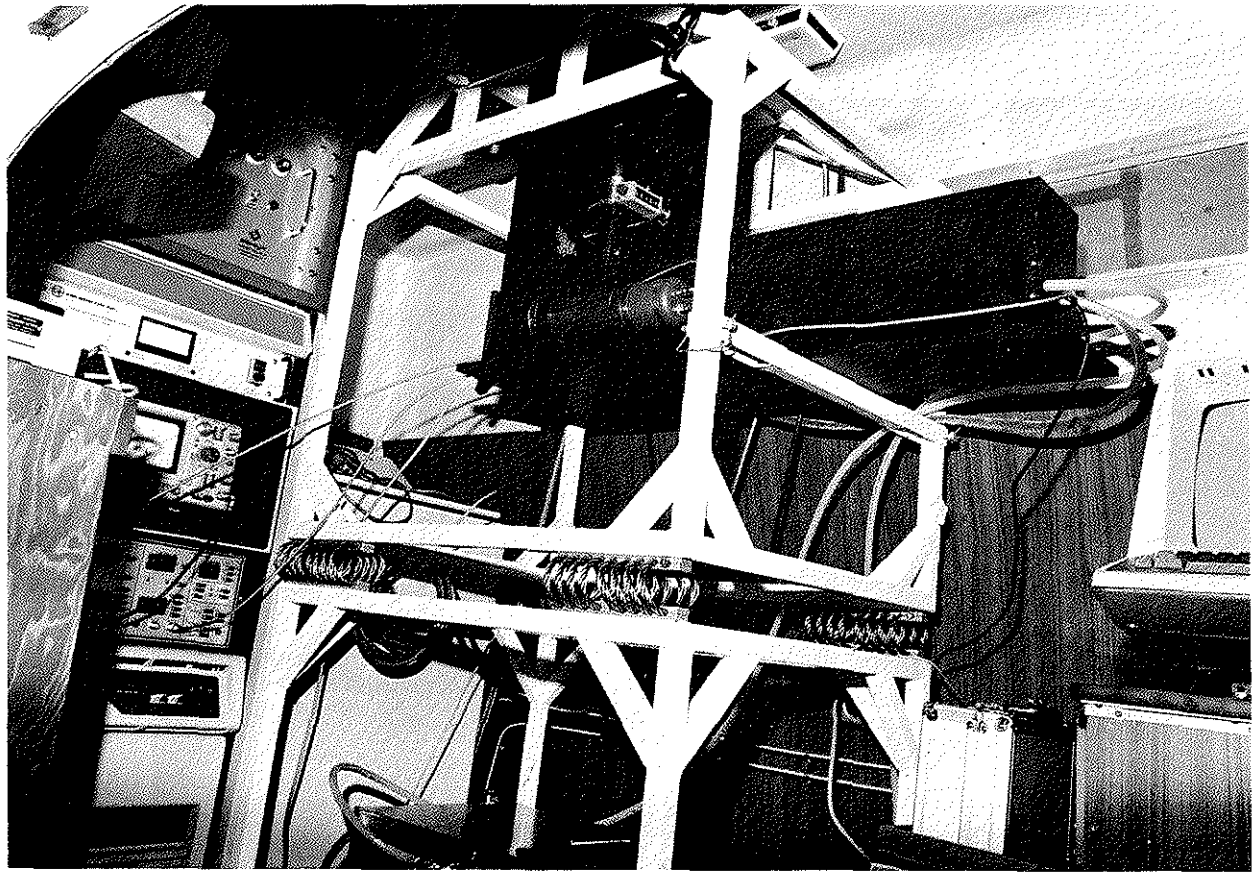

Figure 36. LIDAR lasar rack. Horizontal rail contains lasar, launching optics and photomultiplier (left centre) for detecting signal.

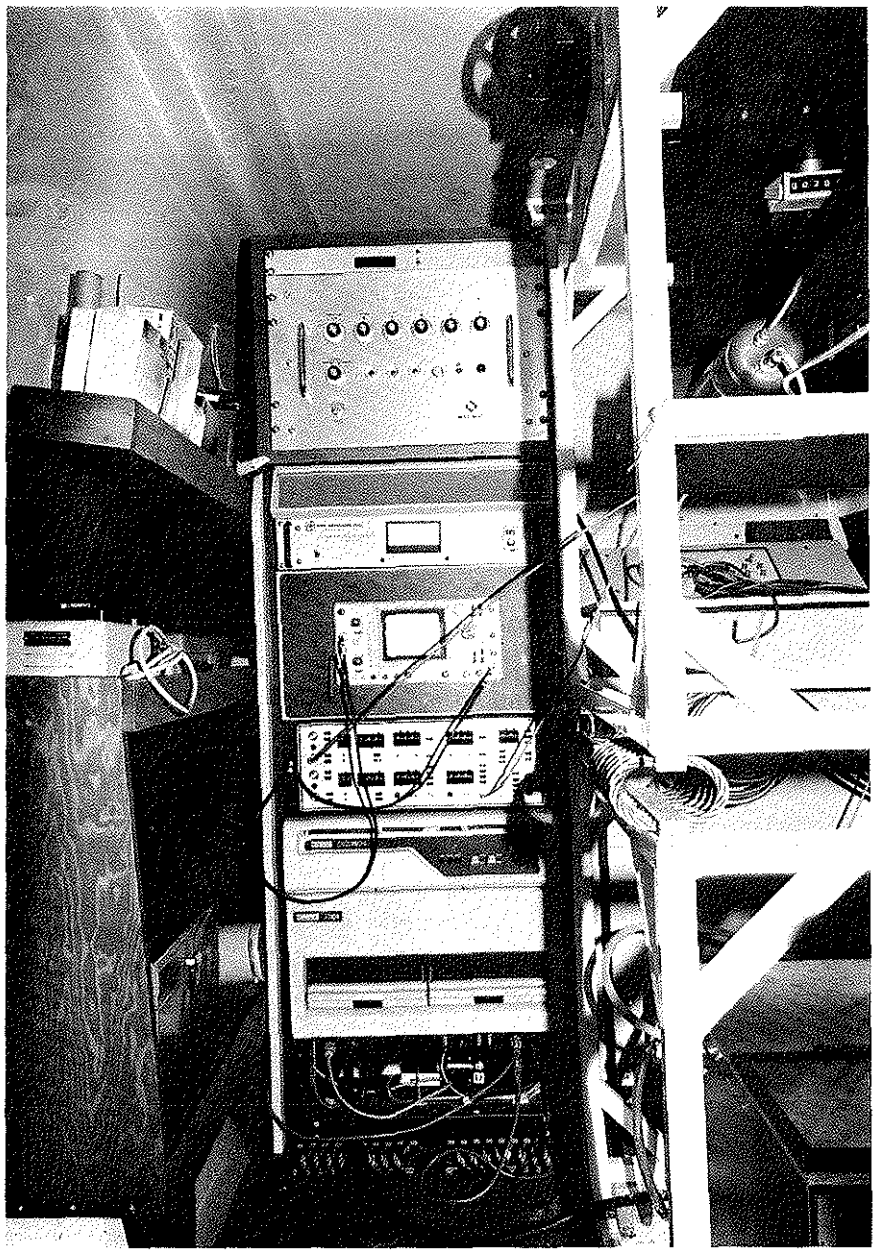

Figure 37. LIDAR electronics rack. Components from top to bottom: elevation encoder readout, elevation drive, photomultiplier power supply, oscilloscope, Biomation 8100 transient digitizer, PDP 11/04 computer, and floppy disk units.

Table 5. LIDAR specifications.

TRANSMITTER	RECEIVER
Laser: Ruby 694.3 nm	Diam.: 20 cm Fresnel f/1.0
Energy 0.5 - 1.0 J	F.O.V.: 10 - 25 mrad
Div.: 1 mrad (typical)	$\Delta\lambda$: 0.9 nm FWHM
Pulse Width: 10 - 20 ns	Dectector: RCA C31000A
Power: 50 MW (typical)	Ang. Res.: 0.1^{o} (hor., vert.)

DATA ACQUISITION

Biomation 8100 Transient Digitizer - PDP 11/04 Computer

$\rightarrow \Delta R_{min} = 1.5$ m

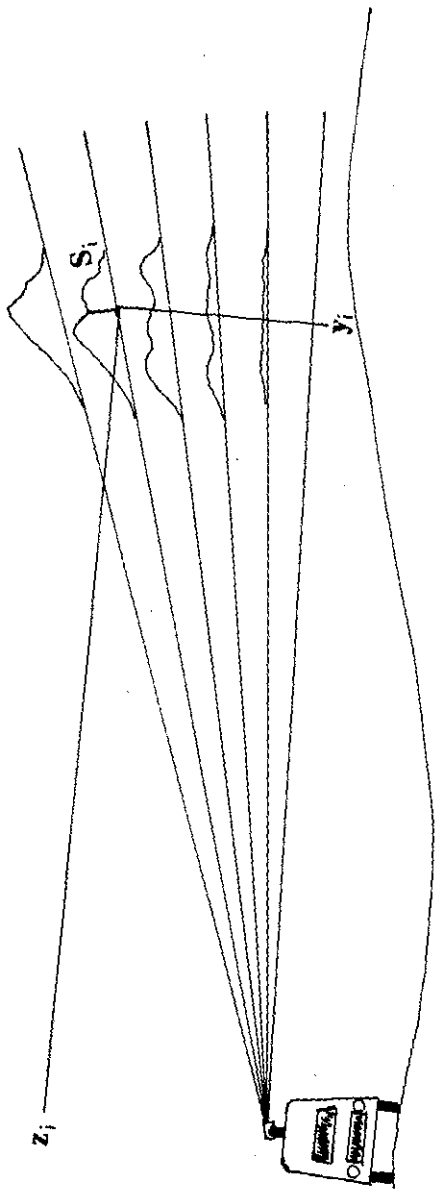

Figure 38. LIDAR scanning procedure.

The data processing procedure involves range scaling each shot within a scan to obtain a signal level $S_{i,j}$ at each digitigation increment i within the 500 data point array for each shot, j, and calculating the y and z moments of the scan distribution:

$$\nu_{y,n} = \sum_{j=1}^{N} \sum_{i=1}^{500} S_{i,j} Y_i^n R_i^2 \Big/ \sum_i \sum_j S_{i,j} R_i^2 \qquad (6)$$

$$\nu_{z,n} = \sum_{j=1}^{N} \sum_{i=1}^{500} S_{i,j} Z_i^n R_i^2 \Big/ \sum_i \sum_j S_{i,j} R_i^2 \qquad (7)$$

where N=number of shots in the scan and n labels the moment of the distribution. From these the following dispersion statistics have been calculated:

$\nu_{y,1}=\bar{y}$ ≡ Ycog horizontal and vertical centres-of-gravity, plume rise (8)

$\nu_{z,1}=\bar{z}$ ≡ Zcog (9)

$\sigma_y=(\nu_{y,2} - \bar{y}^2)^{\frac{1}{2}}$ horizontal dispersion coefficient (10)

$\sigma_z=(\nu_{z,2} - \bar{z}^2)^{\frac{1}{2}}$ horizontal dispersion coefficient (11)

and in the following assume that ρ = y or z:

$$S_\rho = (\nu_{\rho,3} - 3\bar{\rho}\,\nu_{\rho,2} + 2\bar{\rho}^3)/\sigma_\rho^3 \qquad \text{Skewness} \qquad (12)$$

$$K_\rho = (\nu_{\rho,4} - 4\bar{\rho}\,\nu_{\rho,3} + 6\bar{\rho}^2\,\nu_{\rho,2} - 3\bar{\rho}^4)/\sigma_\rho^4 \qquad \text{Kurtosis} \qquad (13)$$

The last two of these statistics seem to be primarily of interest to the researcher and have not been tabulated in this report for the sake of brevity.

In addition to the foregoing statistics, the horizontal co-ordinates of the centre of gravity in relation to the stack as origin are calculated and from these the plume bearing and downwind range were computed.

It can be seen from this discussion that these statistics are calculated in the LIDAR scanning plane. Only under fortuitous circumstances would this plane be normal to the plume axis. The angle between a horizontal line in the scanning plane and the normal to the plume axis is called the "cut angle". A horizontal projection technique similar to that used in COSPEC data processing (Hoff et al. 1977) is used here; it involves multiplying all crosswind distances by the cosine of the cut angle. This projection technique has been previously tested for accuracy (Millan 1976) and for all atmospheric stability regimes; the maximum error in σ_y is 10% as the cut angle is less than 40°.

4.3 EXPERIMENTAL RESULTS

During the study over 750 individual laser returns were stored on the disk medium for processing. Fifty-eight cross sections of the plume were obtained from which 11 "half-hour" and two "hourly" averages were calculated. Because of the time taken to perform a scan, these periods may in some cases be shorter than one-half hour. The times quoted in this report are start times of a scan, and thus the exact end time is not stated for each average. Well over 90% of the data taken was of sufficient quality to warrant full processing. The newness of the LIDAR system manifested itself by a technological breakdown in the laser power supply on 23 June. Despite this system malfunction, the quality of the data and variety of atmospheric conditions studied were sufficient for the project to be successful.

Figure 39 shows an example of a single return from the GCOS plume (note that the units of the abscissa are in tens of metres downrange from the LIDAR). In the near field the $1/R^2$ drop-off of signal due to molecular and background aerosol scattering is evident, while the plume itself is seen at 2400 m range. Figure 40 shows the same shot after range correction and normalization to maximize the plume signal.

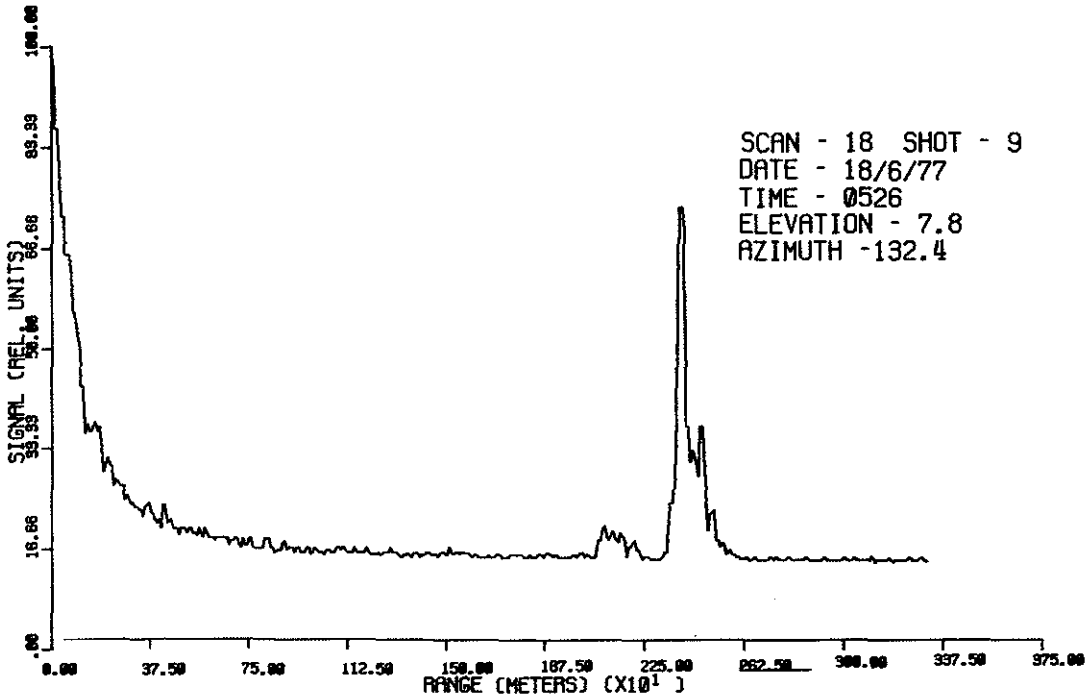

Figure 39. Uncorrected LIDAR returned signal. The plume is seen at 2400 m from the LIDAR.

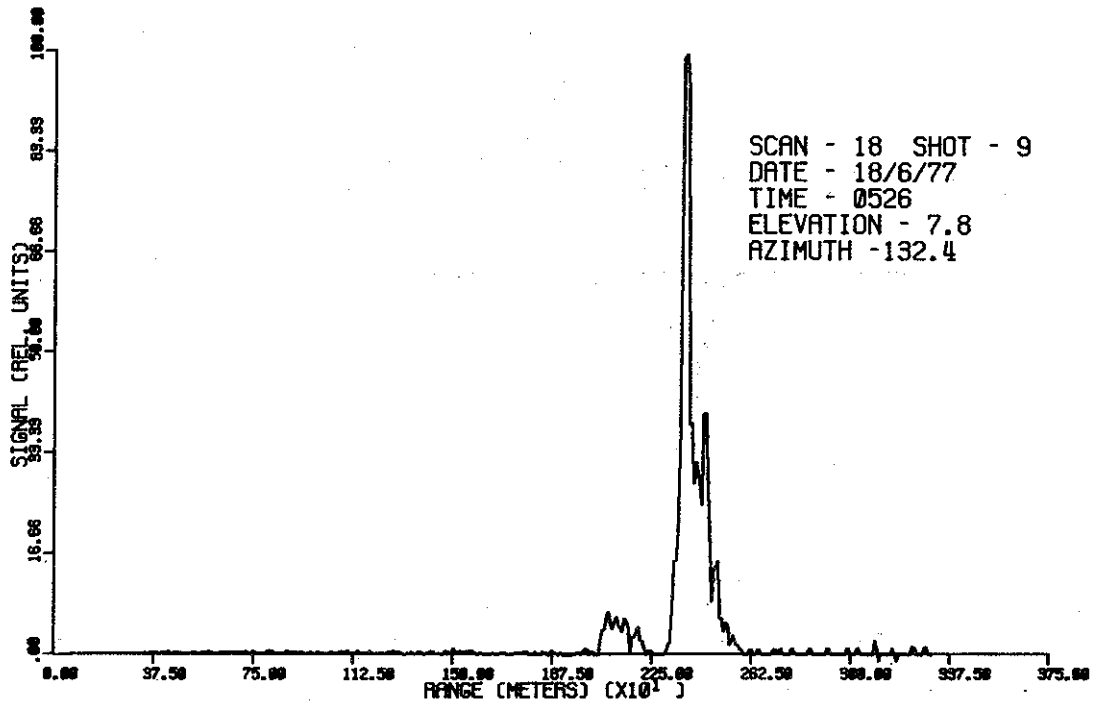

Figure 40. Ranged corrected return seen in Figure 39.

Table 6 gives the plume dispersion parameters measured during the 1977 summer study. Figure 41 is a diagram of the AOSERP study area showing the location of the four stations used. Stations C and D differ in that D was the top of the knoll at the Lower Syncrude site and C was at road level. Plume bearings for the 13 averages are also shown with the scanning direction.

4.4 ANALYSIS

In the following section each of the 13 plume averages will be discussed in relation to atmospheric stability, and contours of relative $\beta_\pi(R)$ will be presented. Since the form in which these contours are drawn and compared to the wind field is novel, some explanation is necessary. Figure 42 shows the position of the LIDAR vehicle, scanning plane, plume centreline, and wind direction. Contours will be drawn in the scanning plane rather than effective plane, and the uncorrected σ_y and σ_z values superimposed. The reader should recall that σ_y in Table 7 has been compressed by the cosine of the cut angle and will not, in general, be the same as that seen in the following figures. Each scan contour was constructed by normalization to the maximum of $\beta_\pi(R)$ in each scan. Thus, consecutive scans cannot be directly compared for absolute magnitude. The Eulerian average plumes seen at the end of each scan set were constructed from the unnormalized data and thus represent a true average over the period observed, although the average itself is again normalized for the contour plots.

Contours were drawn on a 0.1, 0.4, 0.7 grid, that is 10%, 40%, and 70% of peak value. The peak return in each scan is represented by a plus sign. Since the dispersion statistics are calculated from all signal levels, the reader is cautioned that there may be considerable amounts of plume that occur at less than 10% of peak signal yet still affect σ_y and σ_z. This explains why in a few of the contours, the cross-hatches for $2\sigma_y$ and $2\sigma_z$ extend beyond the "plume boundaries".

Table 6. Plume dispersion results. (all units are in metres except plume bearing, which is in degrees from true north. Distance is from the stack and Z cog is above sea level.)

SCAN	DIST.	Z COG	SIGMA Y	SIGMA Z	PBEAR	PLUME RISE
Scan Average 1 1048-1100 17/06/77						
1048	200	430	42	25	100	55
1052	204	424	34	39	98	49
1054	200	414	51	14	100	39
1100	273	442	35	34	81	67
AVER	230	429	72	29	90	54
Scan Average 2 0525-0615 18/06/77						
0525	240	563	102	79	239	188
0536	231	568	105	88	216	193
0546	267	548	91	70	192	173
0604	246	559	92	70	202	246
0615	285	564	80	62	186	189
AVER	235	558	145	77	210	183
Scan Average 3 0543-0627 21/06/77						
0543	1415	611	221	65	78	236
0602	2030	558	256	79	88	183
0627	1578	467	309	55	82	92
AVER	1536	566	294	86	81	191
Scan Average 4 0915-0934 21/06/77						
0915	1200	501	105	61	68	126
0918	1006	485	92	55	72	110
0924	842	512	146	67	77	137
0929	891	513	121	73	75	138
0934	806	491	132	57	78	116
AVER	854	503	99	47	76	128
Scan Average 5 1048-1105 21/06/77						
1048	700	532	102	65	83	157
1052	687	555	99	92	84	180
1058	672	596	127	137	85	221
1105	746	608	137	98	81	233
AVER	666	567	90	97	85	192
Scan Average 6 1350-1410 21/06/77						
1350	1153	1158	271	431	83	783
1400	347	999	63	362	113	624
1410	676	1044	194	220	55	669
AVER	814	1011	348	356	68	636

continued ...

Table 6. Continued.

SCAN	DIST.	Z COG	SIGMA Y	SIGMA Z	PBEAR	PLUME RISE
Scan Average 7 1631-1720 22/06/77						
1631	450	563	114	118	74	188
1641	463	558	96	81	77	183
1649	442	591	102	126	71	216
1657	433	593	72	35	41	218
1706	424	592	86	132	59	217
1715	425	494	81	59	47	119
1720	424	470	93	76	59	99
AVER	423	534	161	107	56	159
Scan Average 8 1922-1959 22/06/77						
1922	460	421	109	34	77	46
1933	472	447	67	43	80	72
1943	498	462	149	71	85	87
1959	528	461	105	84	90	86
AVER	488	445	103	58	83	70
Scan Average 9 2037-2101 22/06/77						
2037	82	404	32	16	78	29
2047	83	408	33	13	82	33
2050	85	416	30	8	84	41
2055	86	407	35	12.	85	32
2101	81	409	43	17	77	34
AVER	82	409	35	14	80	34
Scan Average 10 2123-2145 22/06/77						
2123	492	484	78	38	84	109
2127	466	462	105	44	79	87
2133	452	461	123	27	74	86
2137	481	465	105	48	82	90
2141	477	469	76	41	81	94
2145	484	458	76	33	83	83
AVER	467	472	75	35	79	97
Scan Average 11 0454-0506 23/06/77						
0454	504	467	86	50	75	92
0500	498	486	79	43	73	111
0506	486	537	126	76	69	162
AVER	456	492	70	53	73	117
Scan Average 12 0530-0553 23/06/77						
0530	989	562	137	58	77	187
0535	950	545	201	83	73	170
0538	940	540	154	76	72	165
0542	945	548	173	95	72	173
0545	938	561	162	77	71	186
0550	946	552	180	88	72	177
0553	927	542	184	90	70	167
AVER	940	548	137	80	72	173

continued ...

Table 6. Concluded.

SCAN	DIST	Z COG	SIGMA Y	SIGMA Z	PBEAR	PLUME RISE
Scan Average 13 0602-0610 23/06/77						
0602	1354	548	258	98	70	173
0610	1325	555	265	60	67	180
AVER	1331	553	265	60	67	180

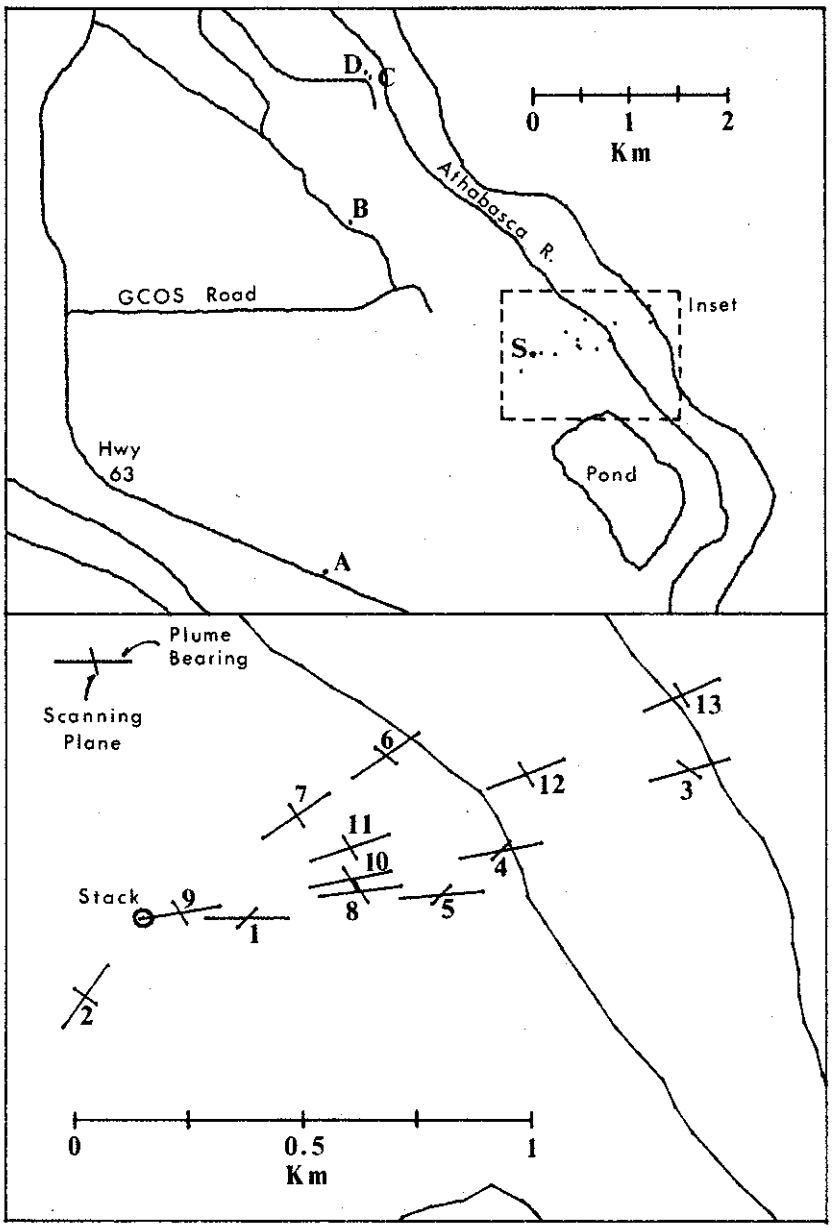

Figure 41. Map of AOSERP study area with inset showing locations of individual centres of gravity. The longer line indicates the plume bearing and the shorter line indicates the scanning plane.

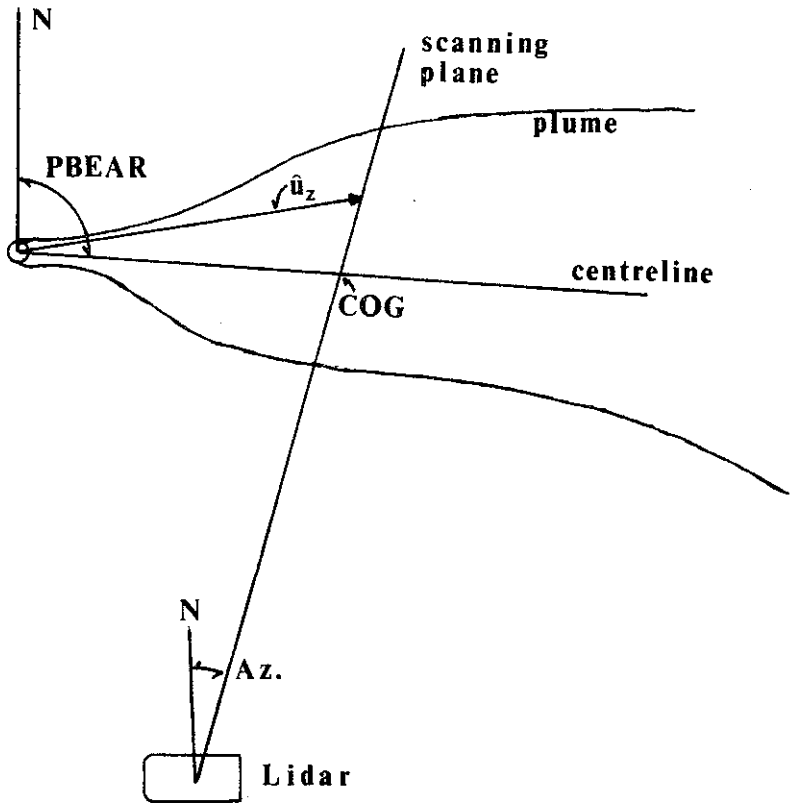

Figure 42. View of a LIDAR scan cross section. PBEAR is the plume bearing from the true north $\hat{U}_z$ is the horizontal component of the wind vector at the height z drawn from the stack to the scanning plane. The tip of this vector is shown in the contour plots in Figures 43, 44, 47-72.

Comparison with the wind field is done by plotting a directional wind vector $\hat{U}_z$, which represents the point at which a parcel emitted from the stack would strike the scanning plane if it linearly followed the horizontal wind field. Alternatively, it may be thought of as the locus of points in the scanning plane created by the horizontal component of the wind vector drawn from a vertical line at the stack position. However one chooses to view $\hat{U}_z$, it will aid the reader in visualizing horizontal or directional shears in the wind direction with height and make interpretation of some plume structures easier. The temperature (with first and third tic marks labelled) is plotted as well on those scans corresponding closest to minisonde or radiosonde releases from Lower Syncrude.

4.4.1 Scan 1--1048-1100, 17 June 1977 (Figures 43 and 44)

From analysis of the 1000 Lower Syncrude Radiosonde (LSR) the relative humidity was approximately 60%, and there was high pressure over the region with broken cumulus. The 1100 Lower Syncrude minisonde (LSM) release showed a lapse rate of $-7.8°\cdot km^{-1}$, which considering the ASME criteria (Smith 1968; USAEC 1972) would be classified as neutral. In spite of this lapse rate, there was a significant veer in wind direction backing 155° from 360 to 460 m above seal level (asl) (all further heights will be asl). The plume center of gravity was at a bearing of 90° at a height of 430 m (Figure 44). This puts the plume centerline at the interface between the shear layer and the layer from 460 to 800 m. Because the winds were relatively calm in the lower layer and 4 $m\cdot s^{-1}$ in the upper, this behaviour of the plume is reasonable because the plume appears to have risen to the upper flow and followed it. Dispersion parameters for this case are in relatively good agreement with those predicted from the parameterized form (Smith 1968) of the ASME Gaussian dispersion formulas (see Figures 45 and 46).

As will be seen, the discrepancy between the experimental data and Gaussian theories in general is larger than differences between the various forms of the theory such as the Pasquill-Gifford

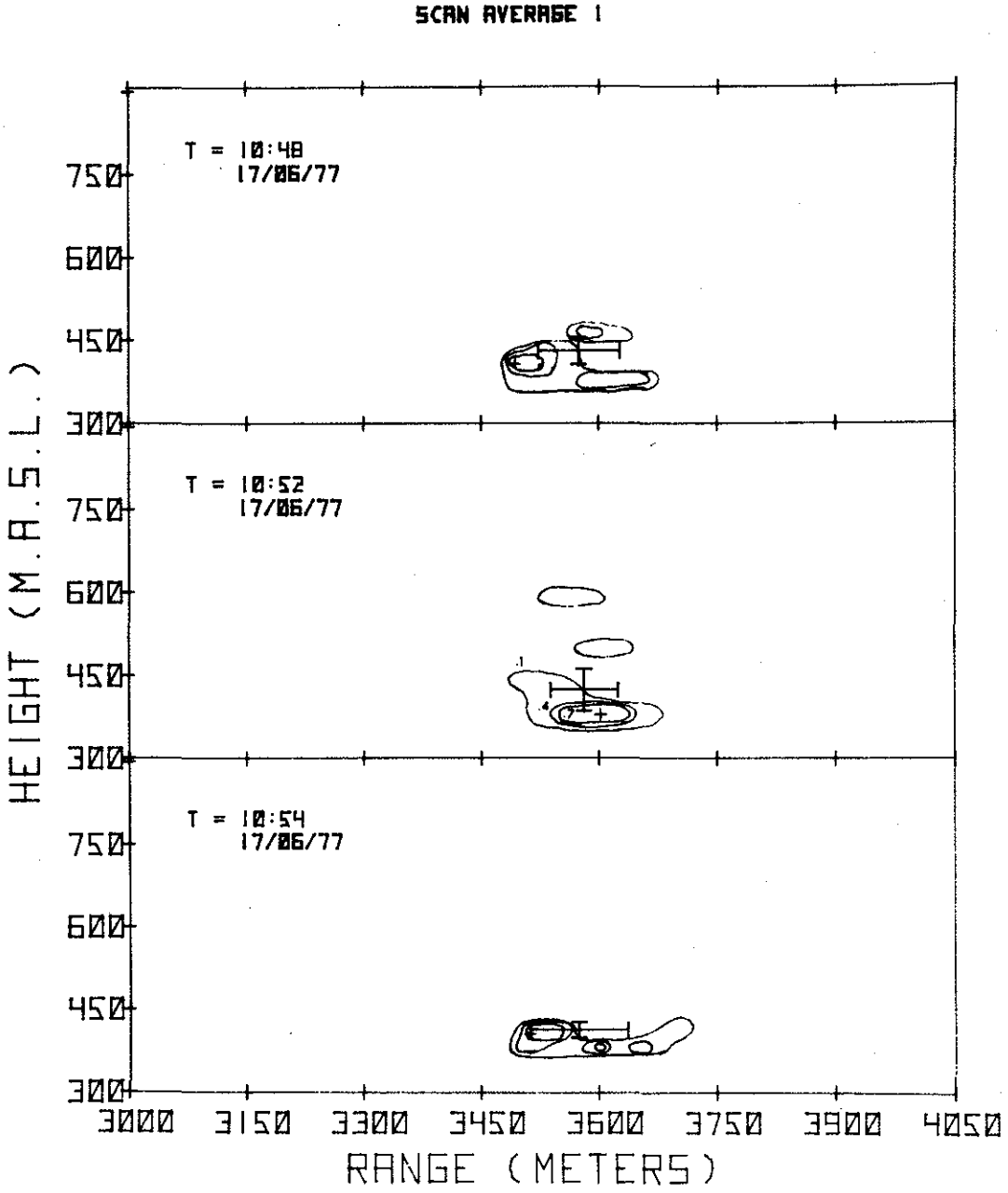

Figure 43. Plume cross-sections determined by LIDAR measurements. Time as indicated. Contours are drawn for 0.1, 0.4, and 0.7 of peak value of $\beta_{\pi}(R)$. (See text for description).

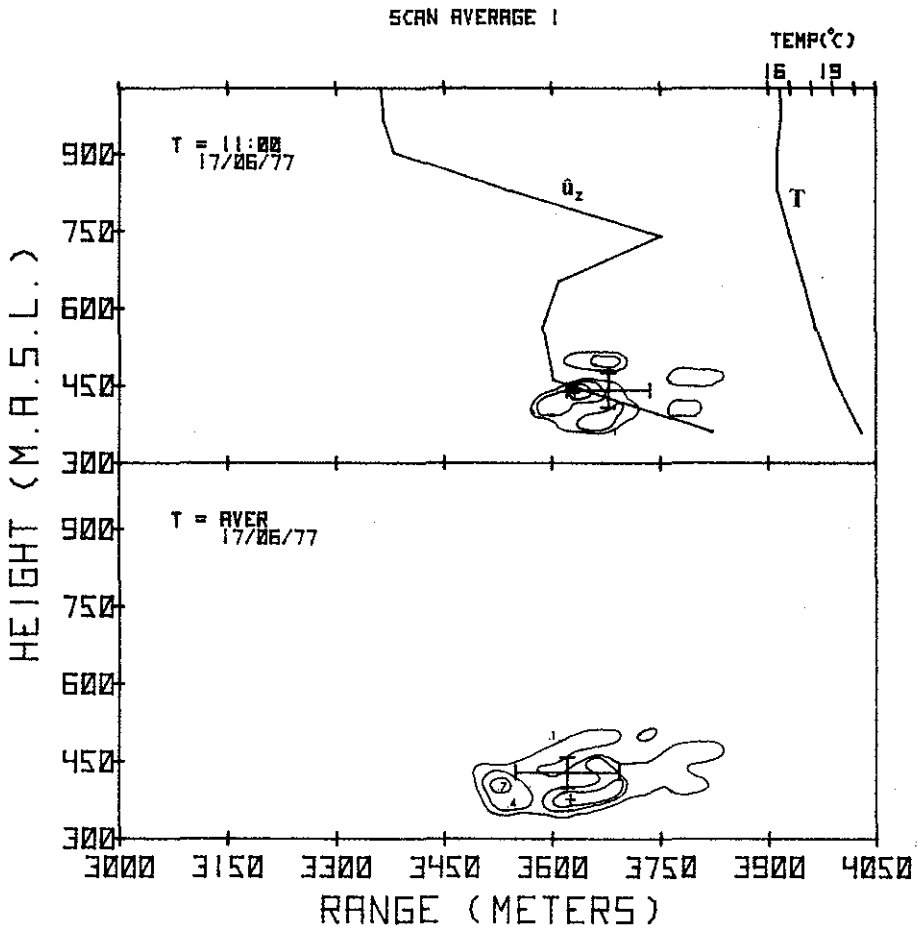

Figure 44. Plume cross-sections determined by LIDAR measurements. Time as indicated. Contours are drawn for 0.1, 0.4, and 0.7 of peak value of $\beta_{\pi}(R)$. (See text for description).

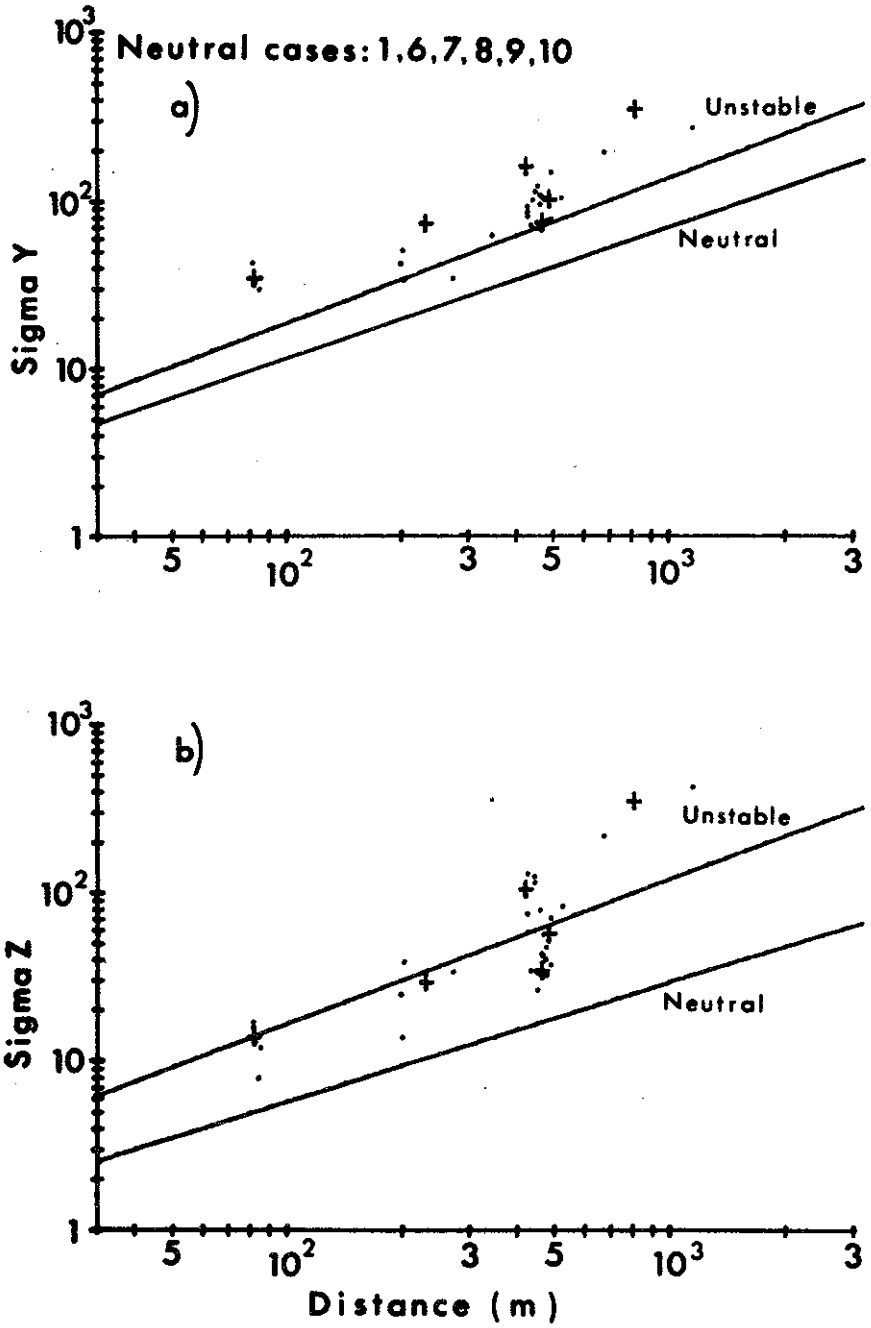

Figure 45. Comparison of ASME curves for the neutral cases with experimental results. Crosses represent Eulerian averages and points represent the individual scans.

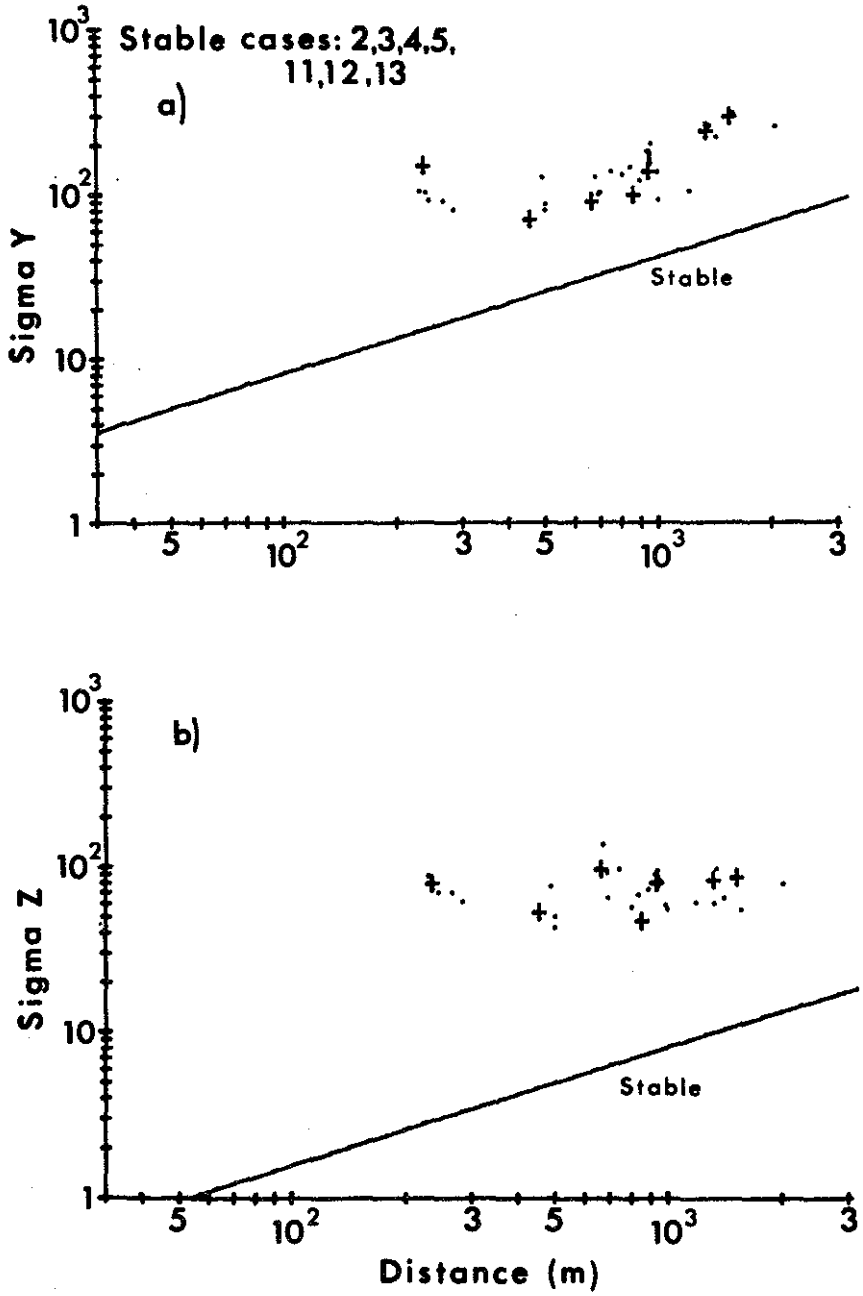

Figure 46. Comparison of ASME curves for the stable cases with the experimental results. Crosses represent Eulerian averages and points represent the individual scans.

and ASME formulations. For this reason, and since the ASME curves are parameterized, the ASME dispersion curves were chosen for comparison in this work.

4.4.2 Scan Average 2--0525-0615, 18 June 1977 (Figures 47 and 48)

This series of scans constitutes the first early morning case studied with the LIDAR. The morning was characterized by mostly clear skies and a slight inversion near the ground. Synoptic scale activity consisted of a slowly moving occluded front which passed through Fort McMurray from the northeast during the morning. Features of the front were evident at 1.5 to 2.0 km in the 0600; 18 June 1977 LSR flight. Humidity was quite high (90-96%) in the lowest 250 m, but above the valley it dropped off rapidly to about 75%. The Lower Syncrude temperature soundings showed the base of the lower inversion at 410 to 430 m, and the top at about 580 m for the 0500, 0600, and 0700 soundings. The Ruth Lake minisonde soundings, however, showed that the inversion top descended from 0500 to 0600 and rose again at 0700 (640 m to 497 m to 610 m). This was accompanied by a slight drop in temperature of the inversion (1 to 2°C)) from 0500 to 0600, suggesting some frontal as well as radiational influence. It also may serve to explain the slight discrepancy between the inversion height as seen by the LIDAR and the minisonde. In Figure 48, the contour plot of the plume profile in the 0604 scan can be seen to be well capped by the inversion. The height of this cap (630 m) is more closely related to that seen by the Ruth Lake minisonde than by the LSR. Because of the possibility that the inversion is frontal, gravity waves may appear in the inversion layer and may explain the height discrepancy.

The dynamic nature of the plume under stable meteorological conditions is apparent in the development of high concentration cells (puffs) as shown by Figures 47 and 48. The strong directional shear with height is seen in both these figures; the fact that the horizontal skewness for 0546, 0604, and 0615 varied between 0.54 and 0.73 indicates skewness in concentration to the left in the figures. The hourly average plume seen at the bottom of Figure 48 is quite remarkable.

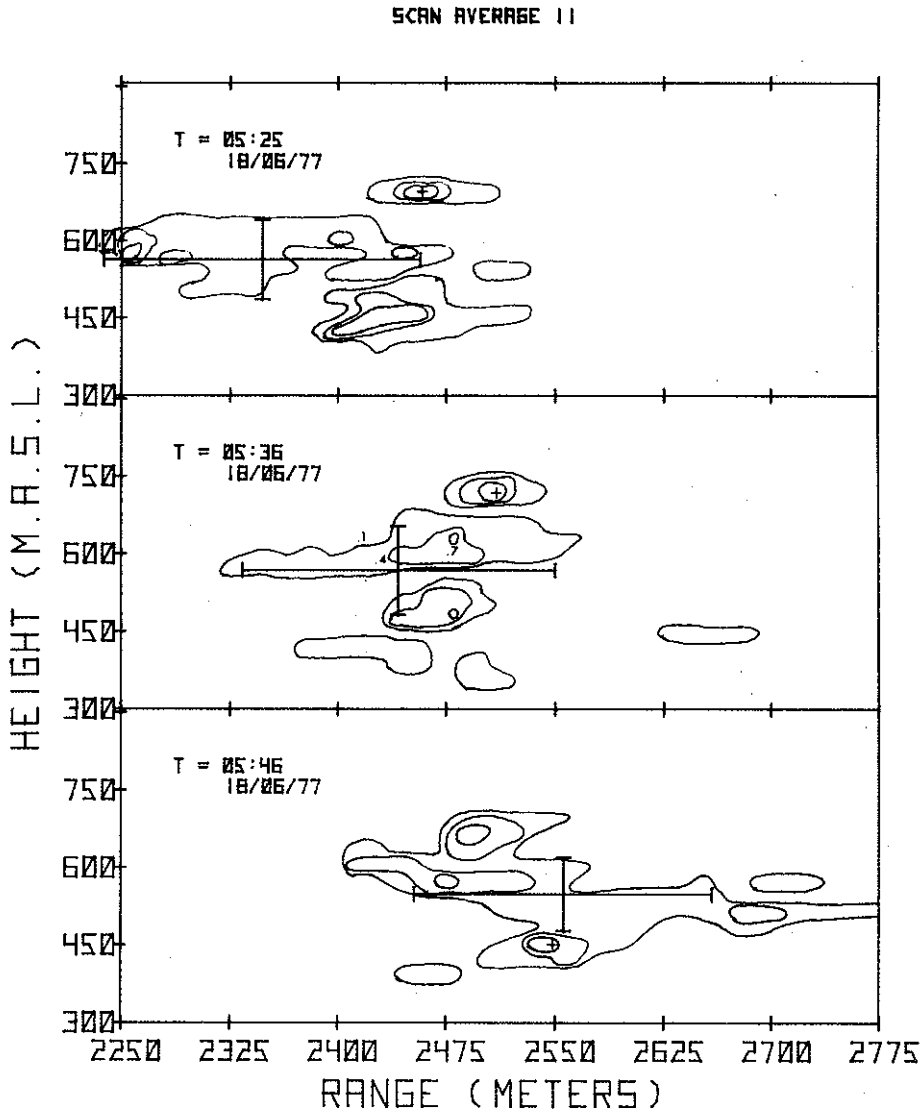

Figure 47. Plume cross-sections determined by LIDAR measurements. Time as indicated. Contours are drawn for 0.1, 0.4, and 0.7 of peak value of $\beta_{\pi}(R)$. (See text for description).

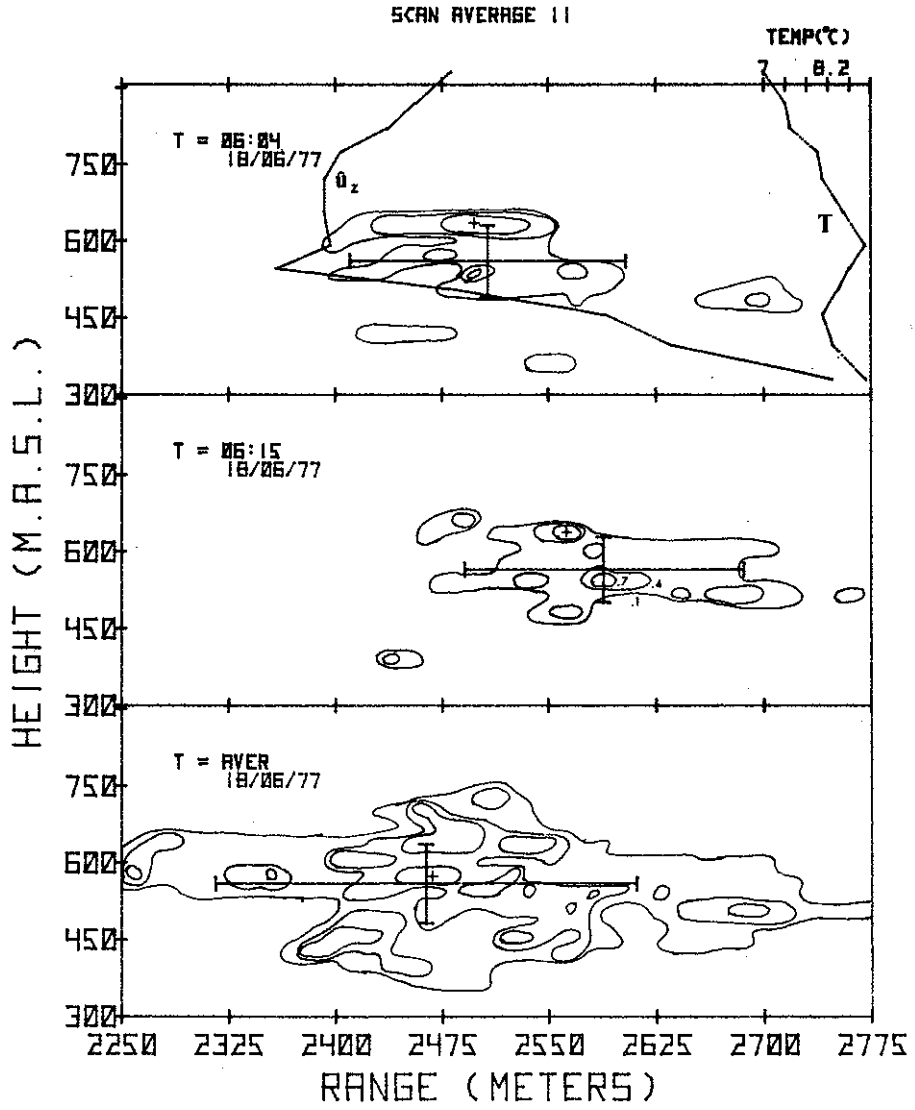

Figure 48. Plume cross-sections determined by LIDAR measurements. Time as indicated. Contours are drawn for 0.1, 0.4, and 0.7 of peak value of $\beta_{\pi}(R)$. (See text for description).

its centre of gravity almost coincides with its peak concentration, its skewness is relatively small, and its kurtosis in both the y and z directions is near 3.0, leading one to conclude that the concentration distribution has Gaussian statistics. However, its visual structure differs from an imagined Gaussian plume; this points out graphically how a real plume deviates from sylized mathematical representations. As will be shown later, the dispersion coefficients of this stable plume do not agree well at all with dispersion predicted from the ASME Gaussian dispersion curves. This proved to be a general result for all stable cases studied in this project.

4.4.3 Scan Averages 3, 4, and 5--0543-0627, 0915-0934, 1048-1105: 21 June 1977 (Figures 49 to 54)

The morning of 21 June was dominated by the passage of a rapidly moving weak cold front through the Fort McMurray area accompanied by rain showers at about 0830. The early morning scan was obtained at the tire dump site (Figure 41). From this site it appeared that the plume, with a bearing of 73°, was headed up the valley toward Fort McMurray. The LIDAR was moved to station A (at the GCOS pit) and two half-hour averages were obtained at this site. This was only a slightly better choice of sites because the plume was still going away from the LIDAR. This points up the need for real time processing of data in future studies to optimize site selection.

The 0600 LSR showed strong directional shear through a relatively isothermal layer to 860 m. The winds were moderate, and the plume followed this wind directional shear with height extremely well. The regions in Figures 49 and 50 labelled "diffuse" are regions where the normalized backscatter signal was greater than 10% in isolated spots, and thus the average concentration was not zero but rather less than 10%. This indicated that either the plume was so diffuse that background aerosol appeared in the scans at a 10% level or else fugitive emissions and parts of the plume separated by the

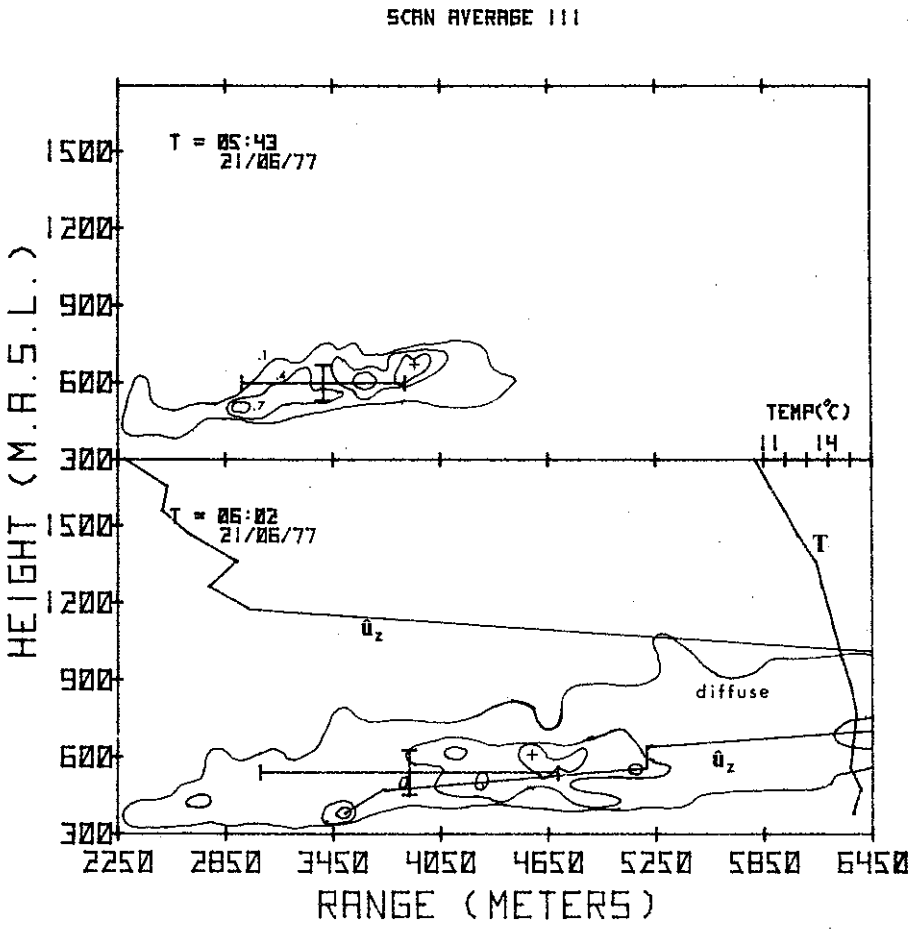

Figure 49. Plume cross-sections determined by LIDAR measurements. Time as indicated. Contours are drawn for 0.1, 0.4, and 0.7 of peak value of $\beta_\pi(R)$. (See text for description).

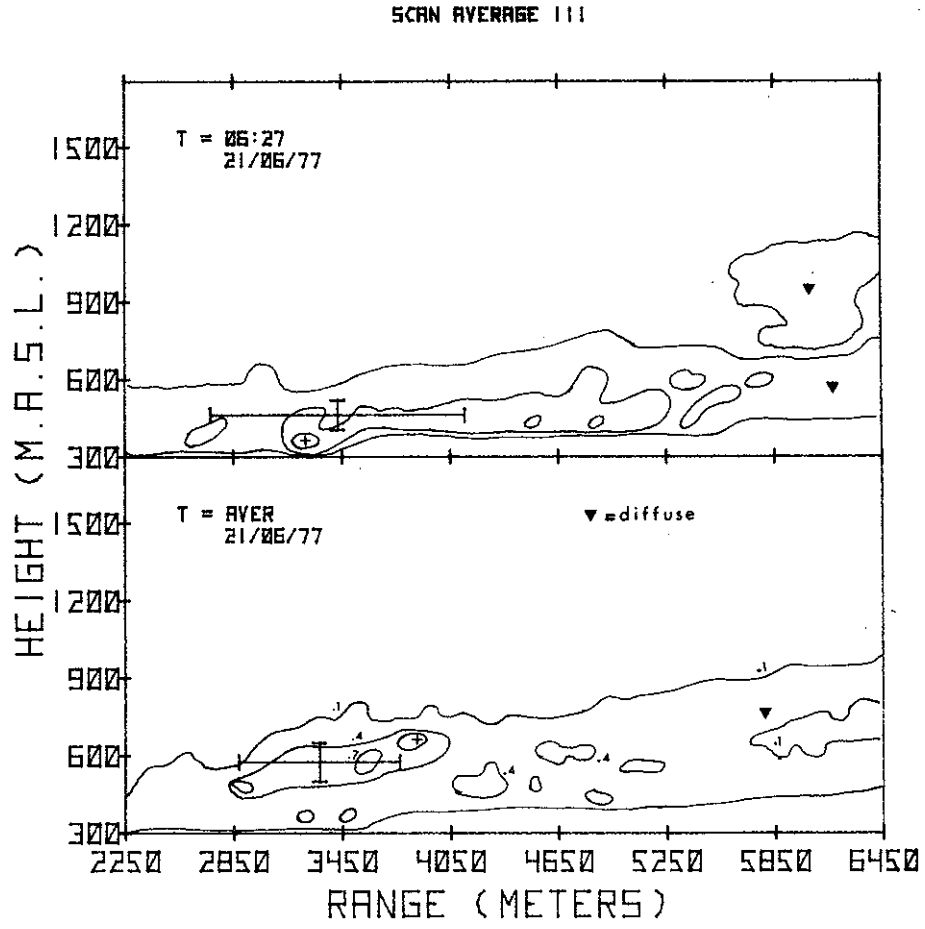

Figure 50. Plume cross-sections determined by LIDAR measurements. Time as indicated. Contours are drawn for 0.1, 0.4, and 0.7 of peak value of $\beta_{\pi}(R)$. (See text for description).

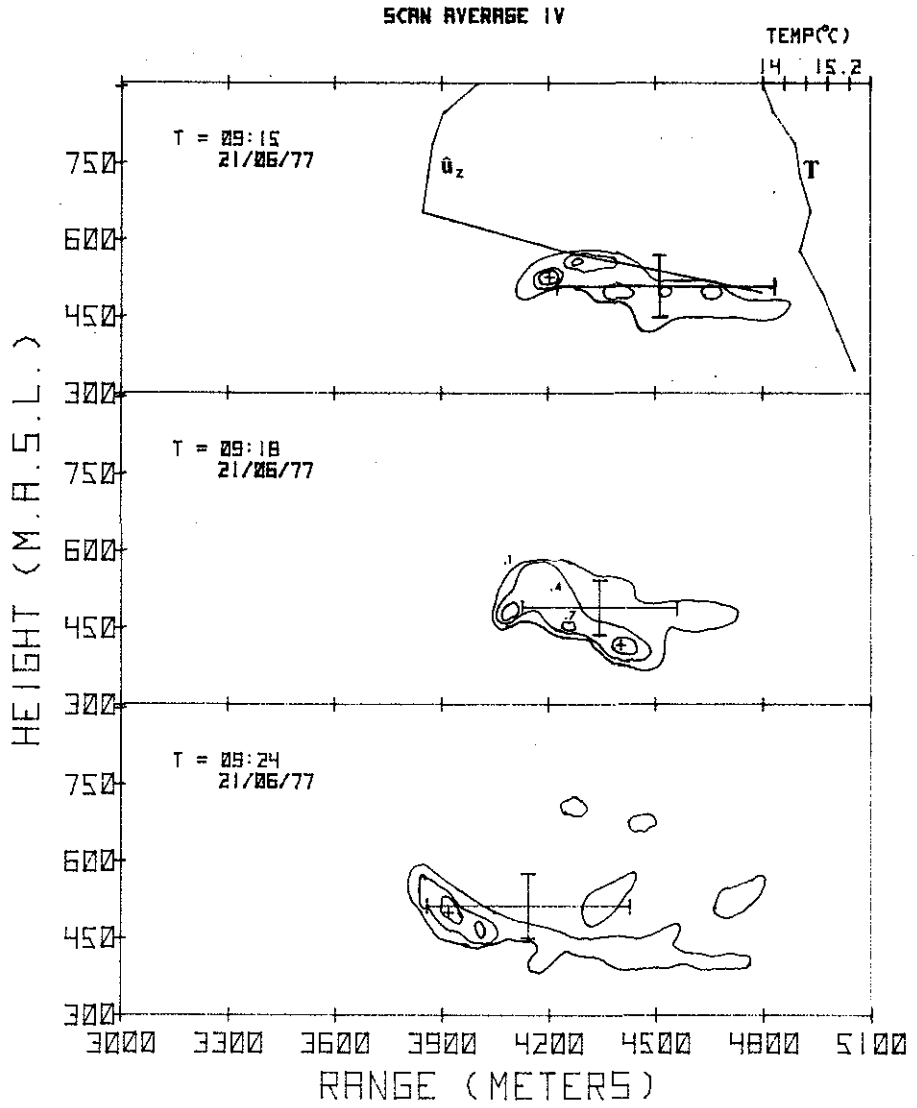

Figure 51. Plume cross-sections determined by LIDAR measurements. Time as indicated. Contours are drawn for 0.1, 0.4, and 0.7 of peak value of $\beta_{\pi}(R)$. (See text for description).

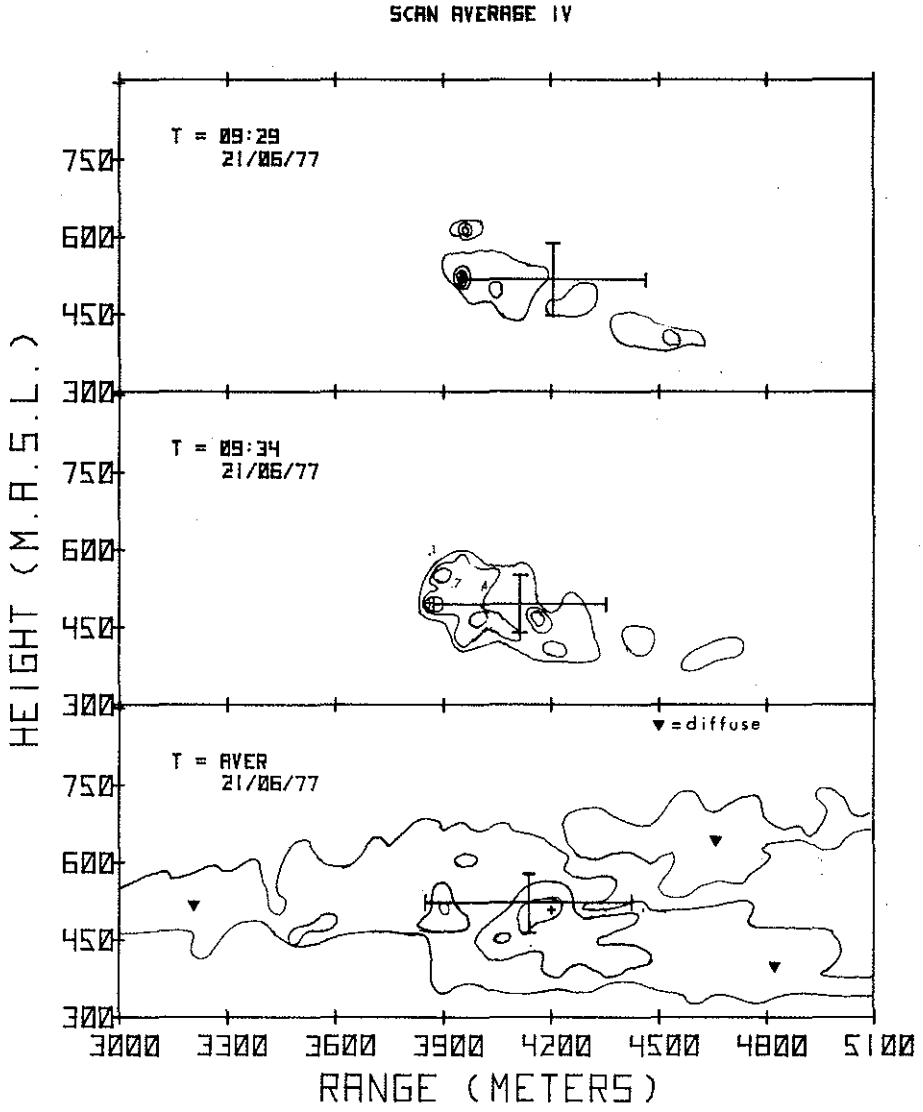

Figure 52. Plume cross-sections determined by LIDAR measurements. Time as indicated. Contours are drawn for 0.1, 0.4, and 0.7 of peak value of $\beta_{\pi}(R)$. (See text for description).

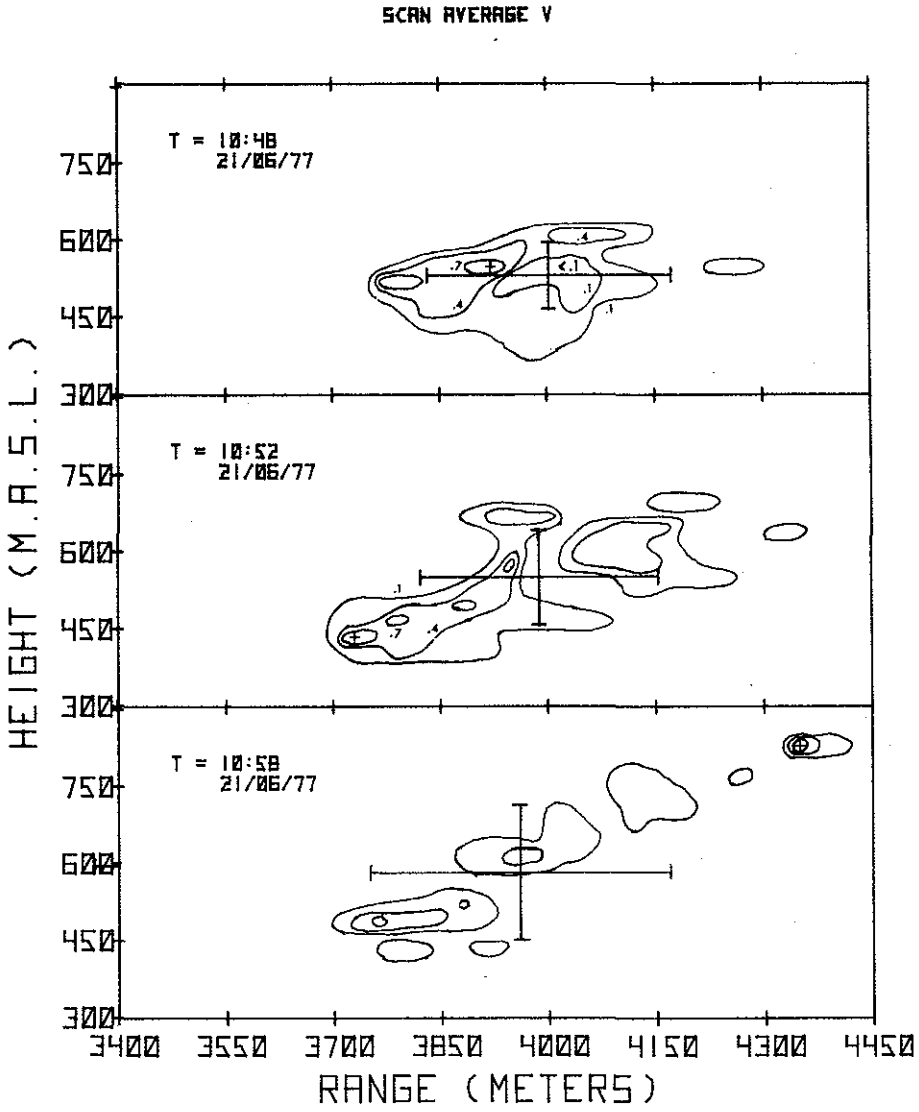

Figure 53. Plume cross-sections determined by LIDAR measurements. Time as indicated. Contours are drawn for 0.1, 0.4, and 0.7 of peak value of $\beta_{\pi}(R)$. (See text for description).

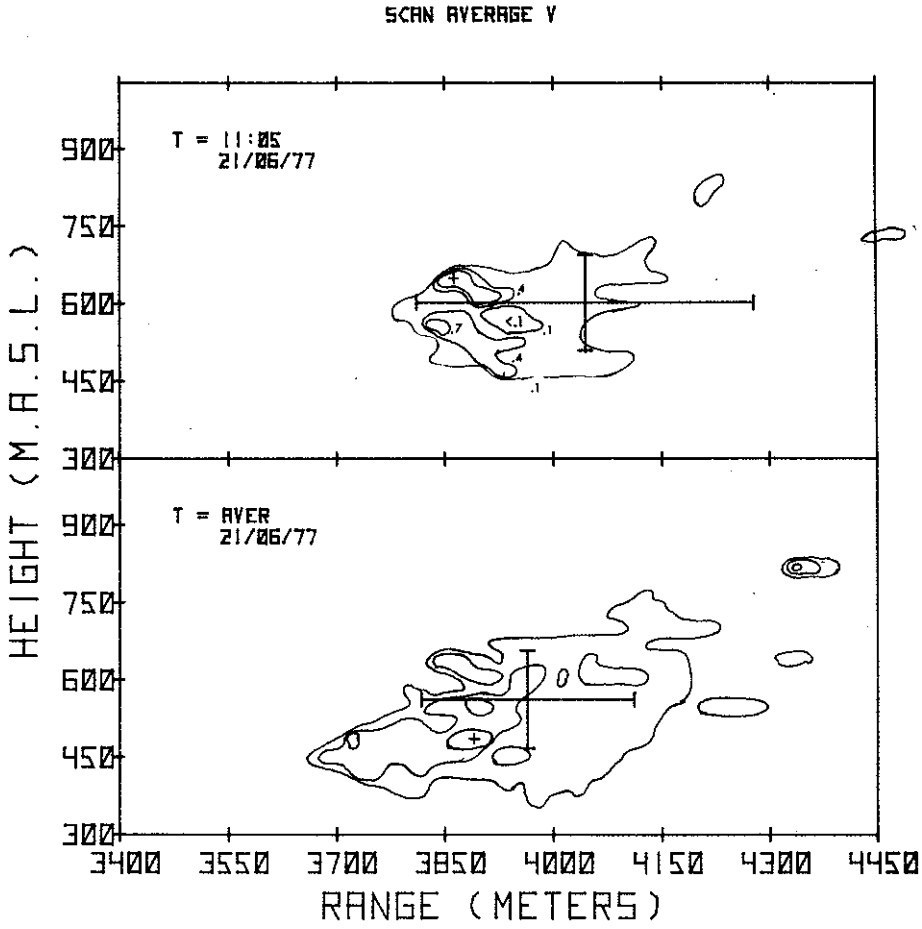

Figure 54. Plume cross-sections determined by LIDAR measurements. Time as indicated. Contours are drawn for 0.1, 0.4, and 0.7 of peak value of $\beta_{\pi}(R)$. (See text for description).

wind shear appeared at this range from the LIDAR. In any case, because of their magnitude, the regions labelled "diffuse" in this and the following figures contribute only slightly to the dispersion statistics.

By the time of the 0915 to 0934 average (4), it was raining moderately heavily. Despite the rain, plume profiles could still be obtained, and the plume bearing agrees quite well with that obtained in clear weather earlier. These averages are included for completeness; however, the previous caution about studying only "optically thin" plumes (i.e., where the absorption by the plume itself is small) might be violated in these cases. It has been found that in clouds, the laser pulse energy drops off by approximately 70% in the first 100 m. This is obviously not the case here; for example, see the 1052 scan, where a relatively high concentration cell is seen at 4100 m after the shot passed through about 50 m of plume. Yet it would be amiss not to point out that these two scan averages (4 and 5) may have inaccuracies due to condensation forming in the plume.

Averages 3, 4, and 5 comprise half of the stable cases studied. As in the others, the plume dispersions disagree with the ASME predicted values.

4.4.4 Scan Averages 6--1350-1410, 21 June 1977 (Figures 55 and 56)

In the afternoon the weather cleared with only fair weather cumulus aloft. Significant surface heating followed, and the afternoon provided the most unstable atmospheric case to be studied. The lapse rate was $-10.5° \cdot km^{-1}$ to 1 km, which is slightly unstable. The plume showed a great deal of rise, 530 m at a distance of 670 m from the stack. In addition, the incinerator stack was flaring over this period. The plume profiles in Figures 55 and 56 are complex, consisting of a well-defined main plume of 2700 m from the LIDAR and a very diffuse region of low concentration beyond 3 km. The vertical dispersion for this average reveals a larger vertical dispersion than horizontal. This proved to be the only unstable case that showed

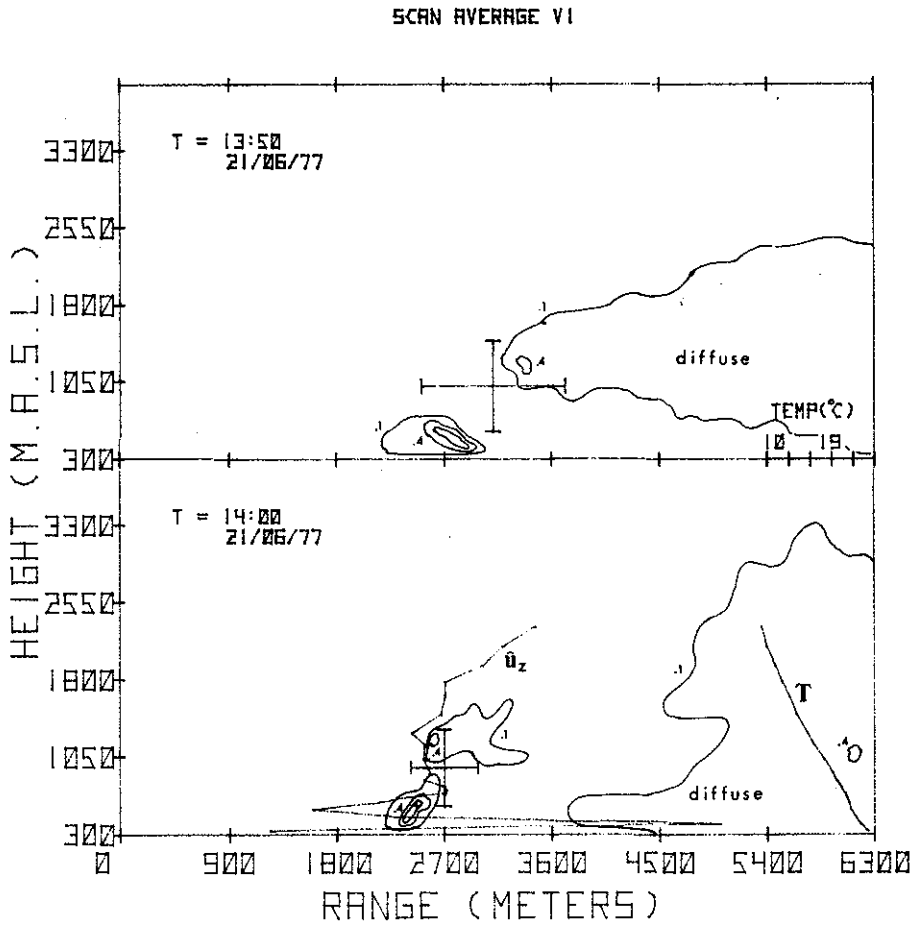

Figure 55. Plume cross-sections determined by LIDAR measurements. Time as indicated. Contours are drawn for 0.1, 0.4, and 0.7 of peak value of $\beta_{\pi}(R)$. (See text for description).

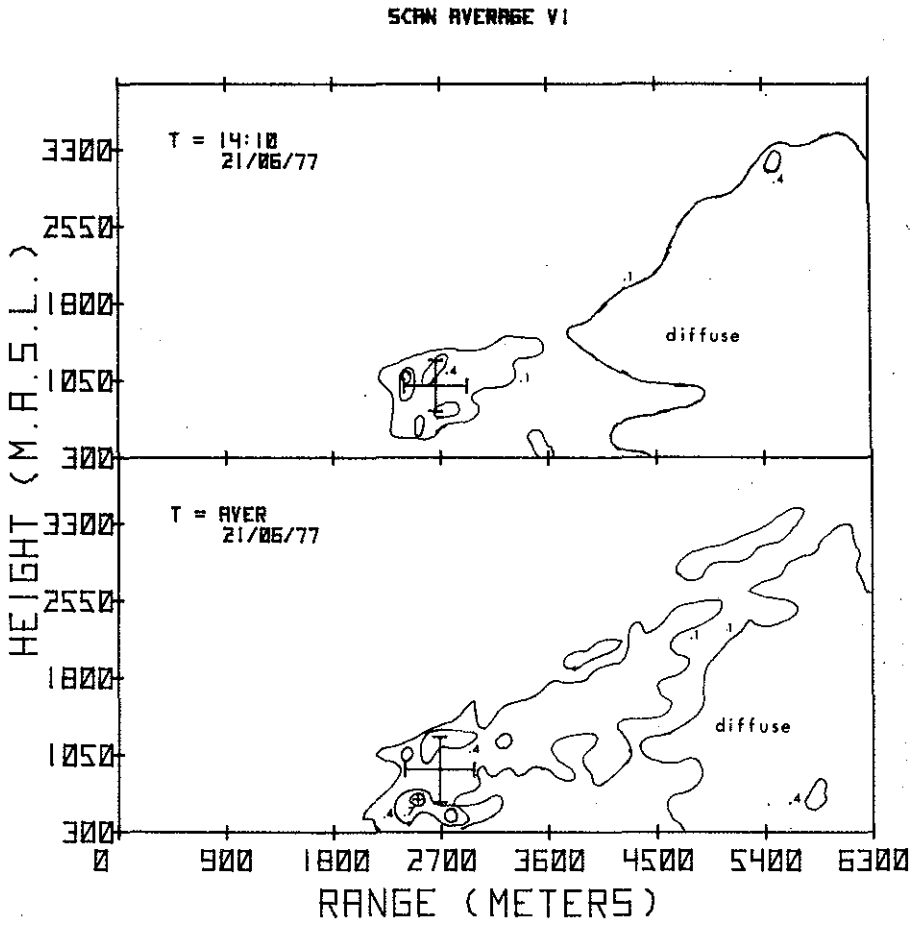

Figure 56. Plume cross-sections determined by LIDAR measurements. Time as indicated. Contours are drawn for 0.1, 0.4, and 0.7 of peak value of $\beta_{\pi}(R)$. (See text for description).

significant deviation from the ASME predictions of dispersion, but even so, its deviation was smaller than for all the stable cases.

4.4.5 Scan Averages 7, 8, 9, 10, 22 June 1977 (Figures 57 to 66)

The evening of 22 June was clear. The earlier frontal passage in the day was accompanied by rain ending at 1600 Mountain Standard Time (MST). The surface temperature was warm (around 20°C) and all LS soundings taken that evening showed lapse rates varying from $-10.1°\cdot km^{-1}$ at 1630 to $-8.3°\cdot km^{-1}$ at 2130. The stability with the relative humidity of 50 to 60% was conditionally unstable, or unstable then neutral, if the dry adiabatic lapse rate is considered. For purposes of consistency these cases are ranked neutral for comparison to the ASME formulae later.

Winds during the evening were moderate to strong, reaching 16 to 18 $m\cdot s^{-1}$ at 1 km, and were independent of directional shear after 1730 MST.

After this time, the plume was markedly coherent and rarely contained isolated puffs through the scanning plane. The Eulerian averages for scan averages 9 and 10 are correspondingly well behaved, with contours showing little of the structure seen in earlier averages with the more prevalent shear layers. The dispersion statistics for this set of averages agrees fairly well with ASME predictions.

4.4.6 Scan Averages 11, 12, 13; 22 June 1977 (Figures 67 to 72)

The morning of 23 June was characterized by fair weather with a high-pressure region moving into the Fort McMurray area from the west. Surface winds at Fort McMurray at 0500 MST were calm and the pressure was rising. Humidity from the LSR was 60 to 70% at 0600 and the winds aloft were moderately brisk ranging to 14 $m\cdot s^{-1}$. In the 0500 LSM trace there was a surface inversion in the lowest 40 m with an elevated inversion top at 650 m. By the 0600 LSR flight surface heating had caused a slight lapse to 590 m, with the inversion top moving to 730 m.

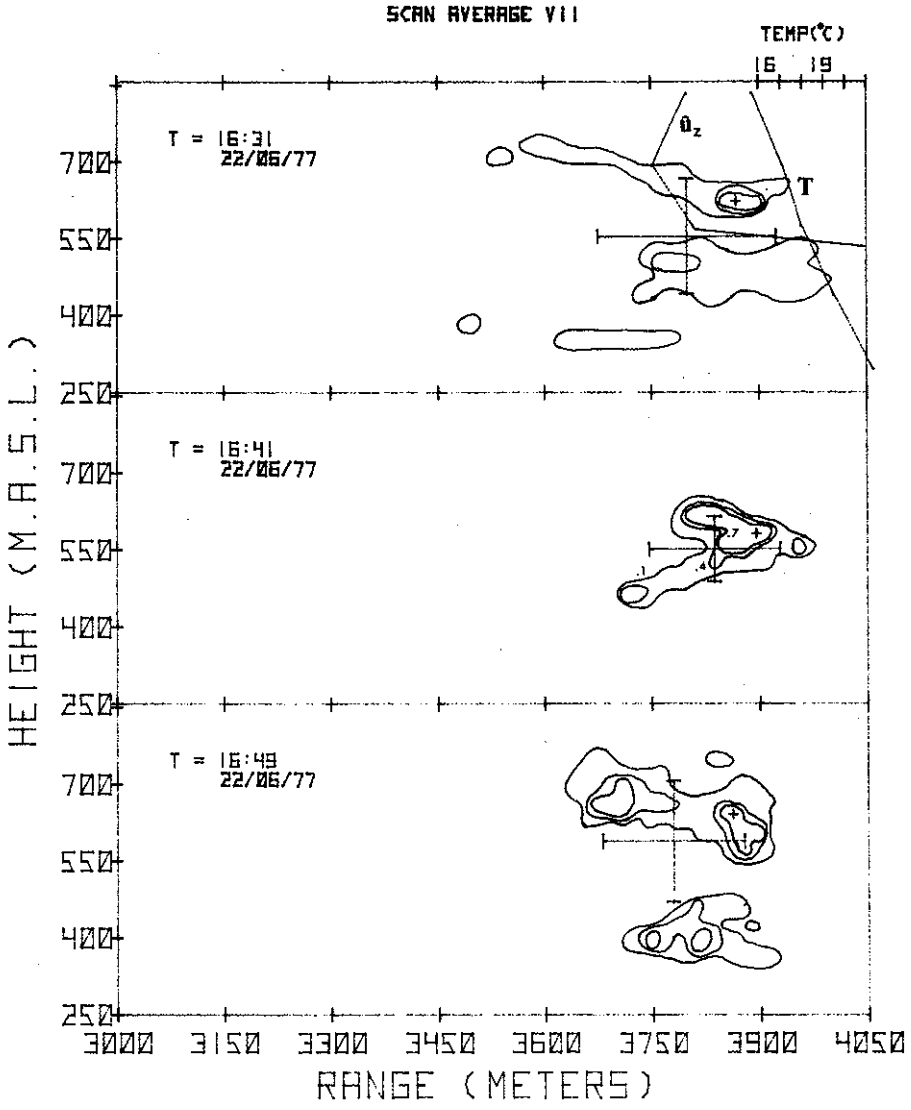

Figure 57. Plume cross-sections determined by LIDAR measurements. Time as indicated. Contours are drawn for 0.1, 0.4, and 0.7 of peak value of $\beta_{\pi}(R)$. (See text for description

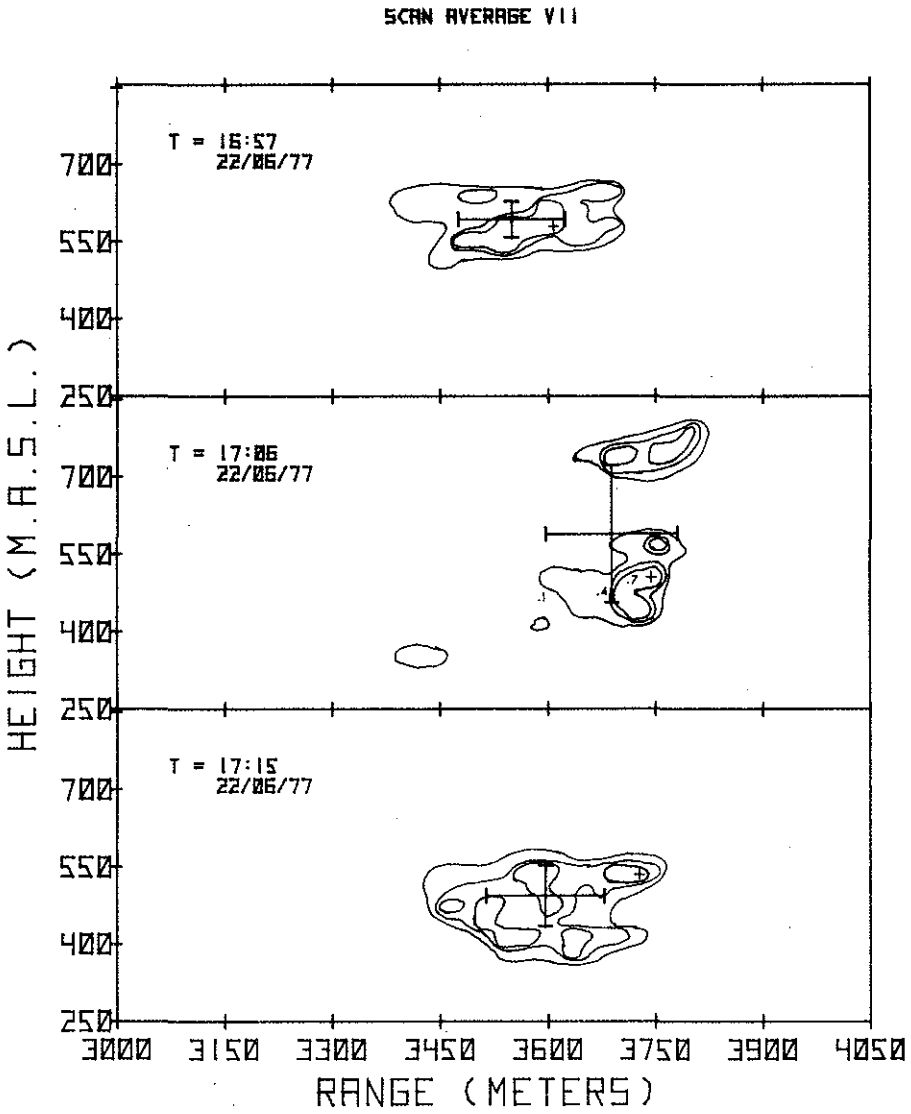

Figure 58. Plume cross-sections determined by LIDAR measurements. Time as indicated. Contours are drawn for 0.1, 0.4, and 0.7 of peak value of $\beta_{\pi}(R)$. (See text for description).

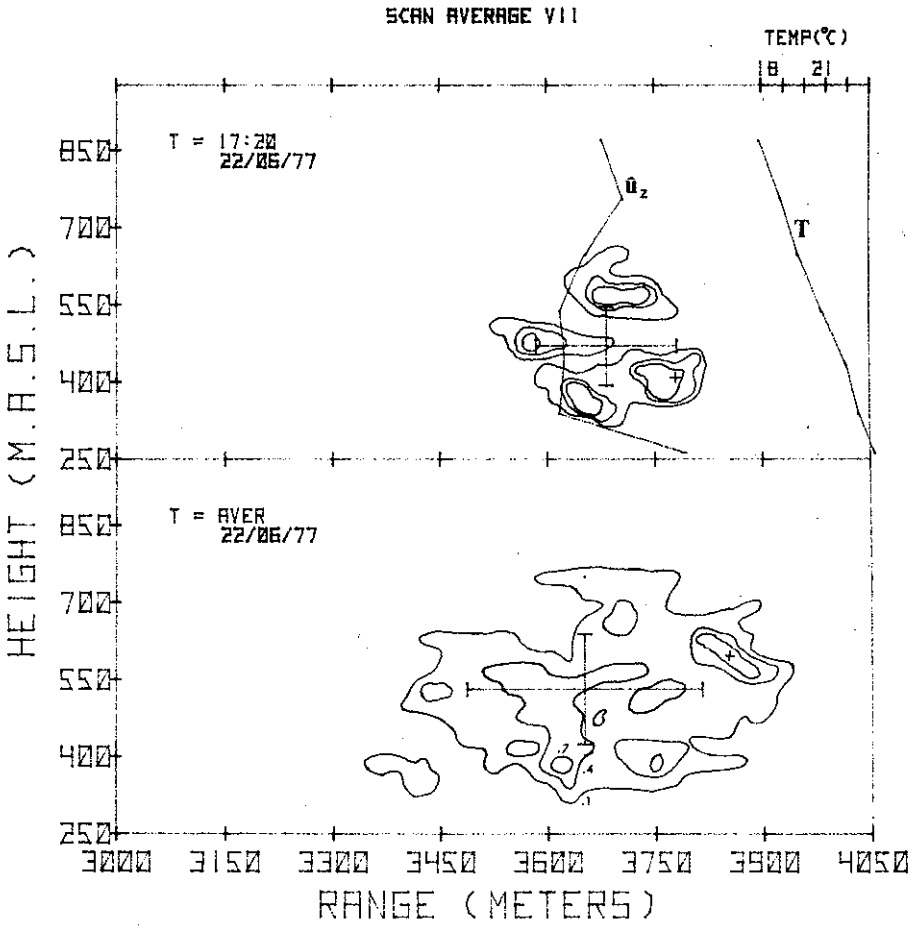

Figure 59. Plume cross-sections determined by LIDAR measurements. Time as indicated. Contours are drawn for 0.1, 0.4, and 0.7 of peak value of $\beta_{\pi}(R)$. (See text for description).

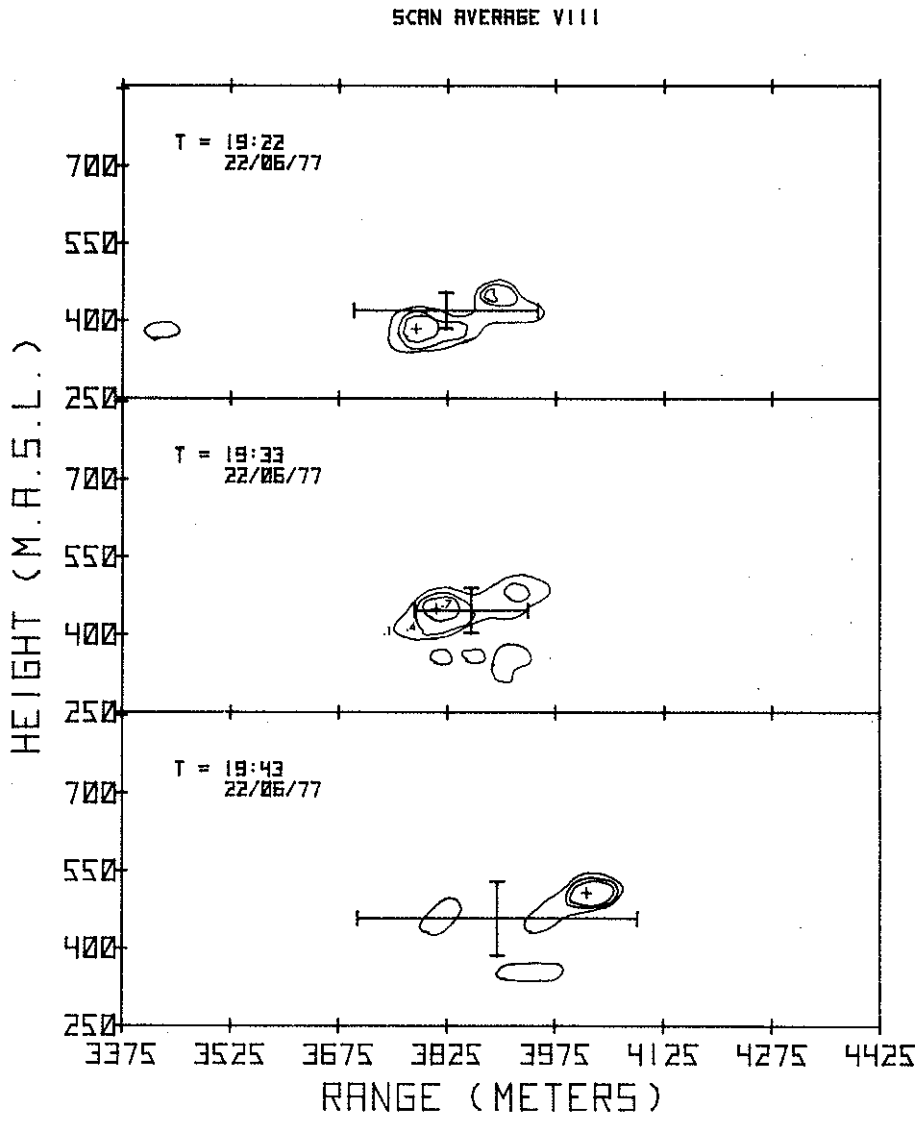

Figure 60. Plume cross-sections determined by LIDAR measurements. Time as indicated. Contours are drawn for 0.1, 0.4, and 0.7 of peak value of $\beta_{\pi}(R)$. (See text for description).

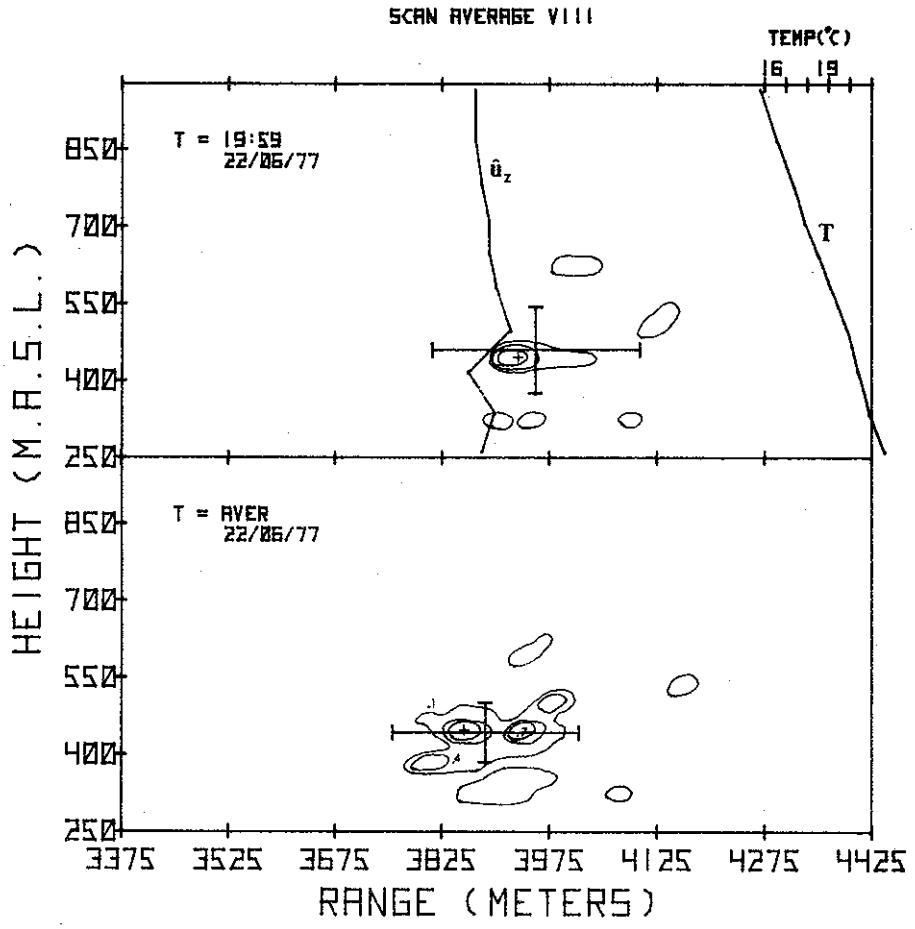

Figure 61. Plume cross-sections determined by LIDAR measurements. Time as indicated. Contours are drawn for 0.1, 0.4, and 0.7 of peak value of $\beta_{\pi}(R)$. (See text for description).

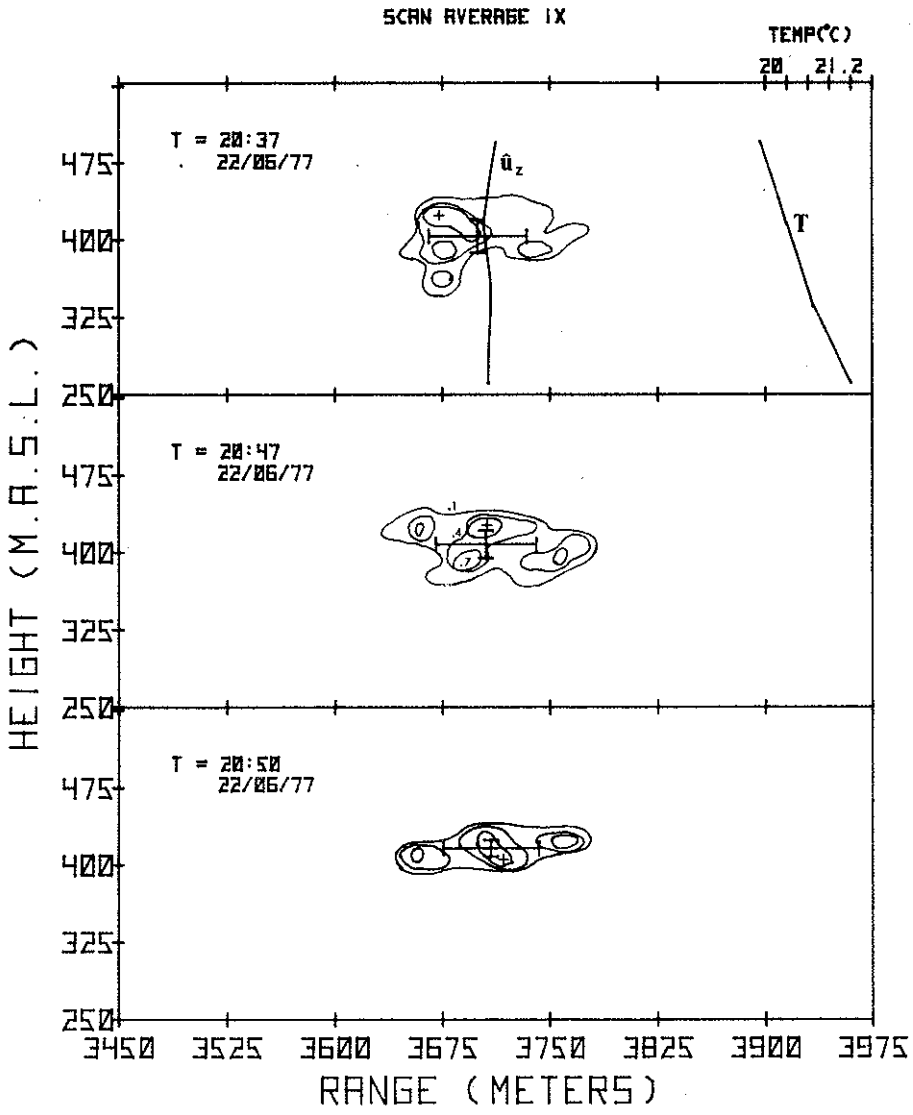

Figure 62. Plume cross-sections determined by LIDAR measurements. Time as indicated. Contours are drawn for 0.1, 0.4, and 0.7 of peak value of $\beta_{\pi}(R)$. (See text for description).

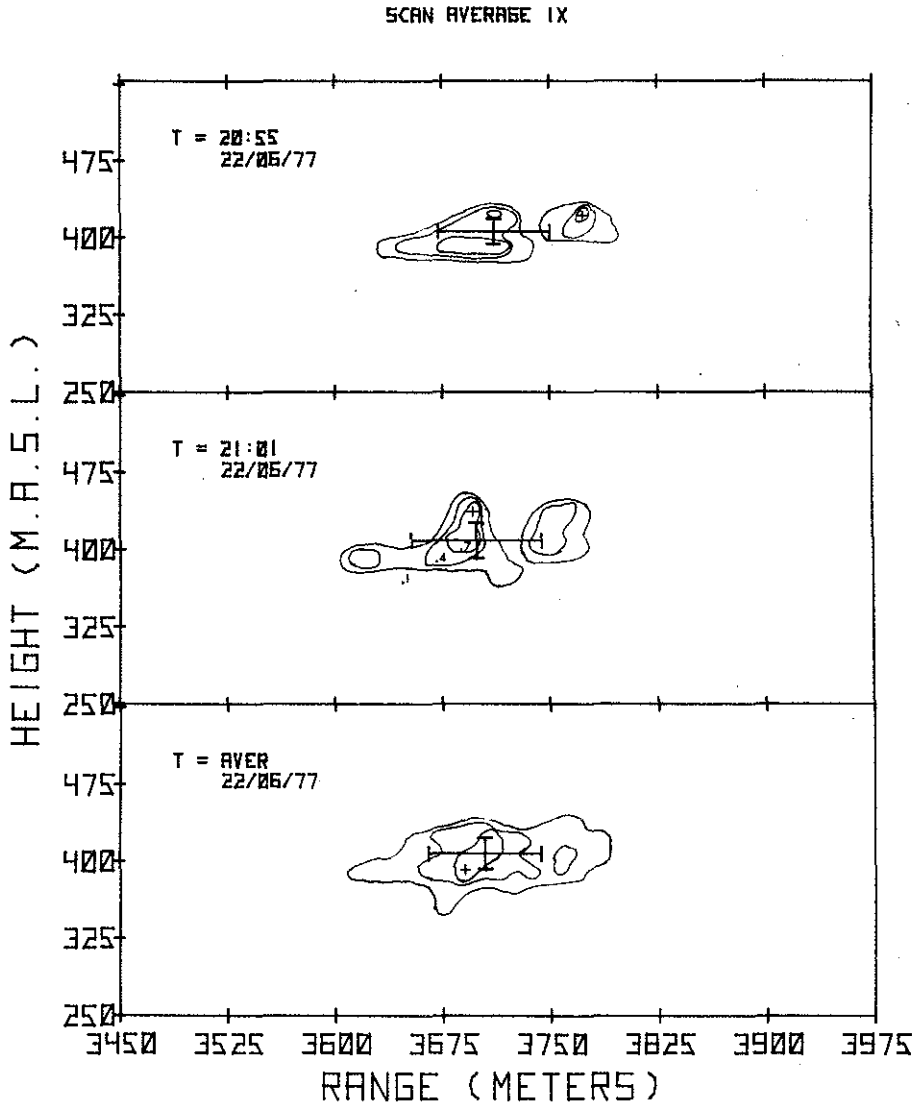

Figure 63. Plume cross-sections determined by LIDAR measurements. Time as indicated. Contours are drawn for 0.1, 0.4, and 0.7 of peak value of $\beta_{\pi}(R)$. (See text for description).

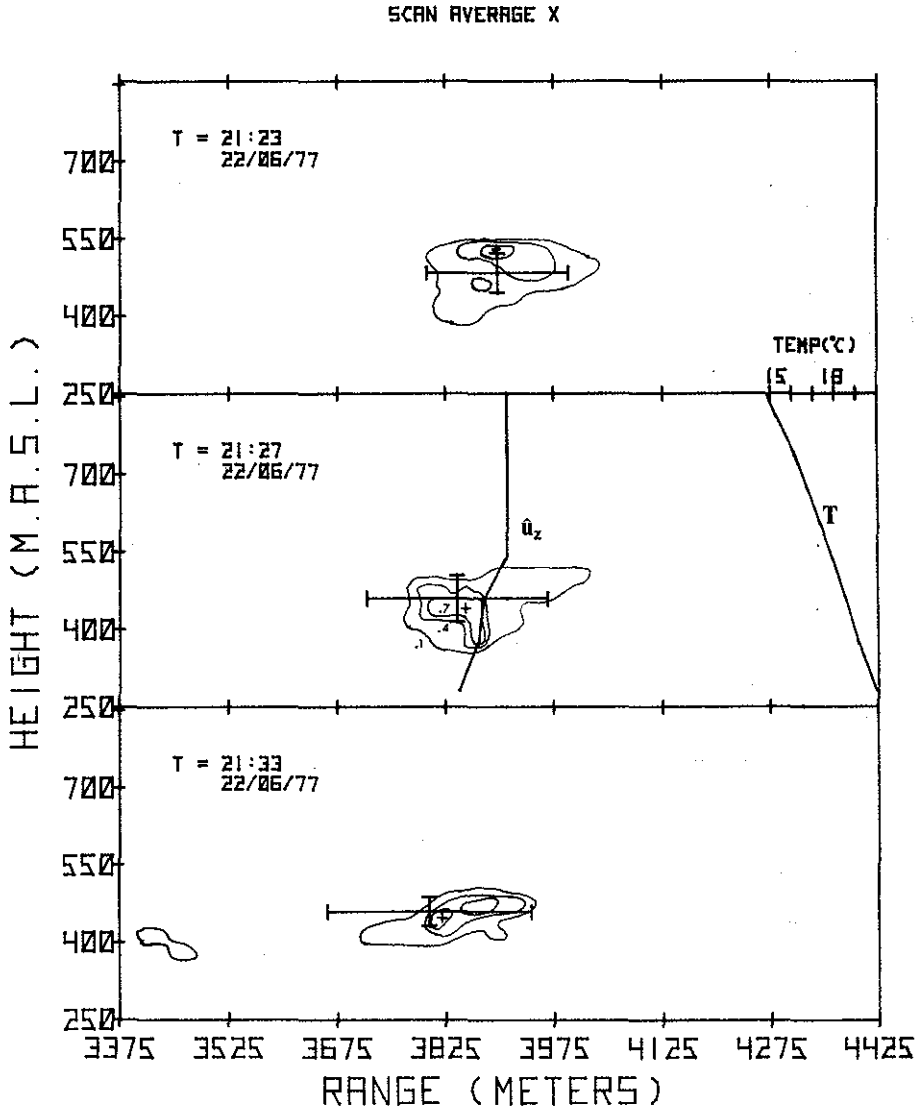

Figure 64. Plume cross-sections determined by LIDAR measurements. Time as indicated. Contours are drawn for 0.1, 0.4, and 0.7 of peak value of $\beta_{\pi}(R)$. (See text for description).

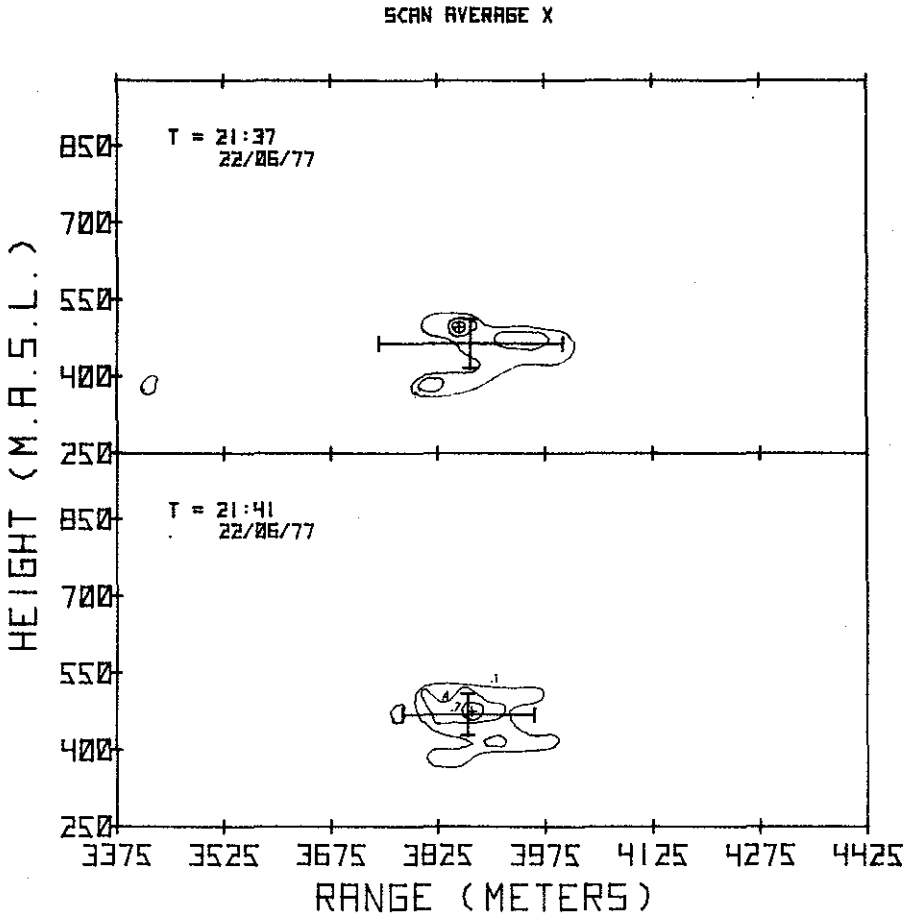

Figure 65. Plume cross-sections determined by LIDAR measurements. Time as indicated. Contours are drawn for 0.1, 0.4, and 0.7 of peak value of $\beta_{\pi}(R)$. (See text for description).

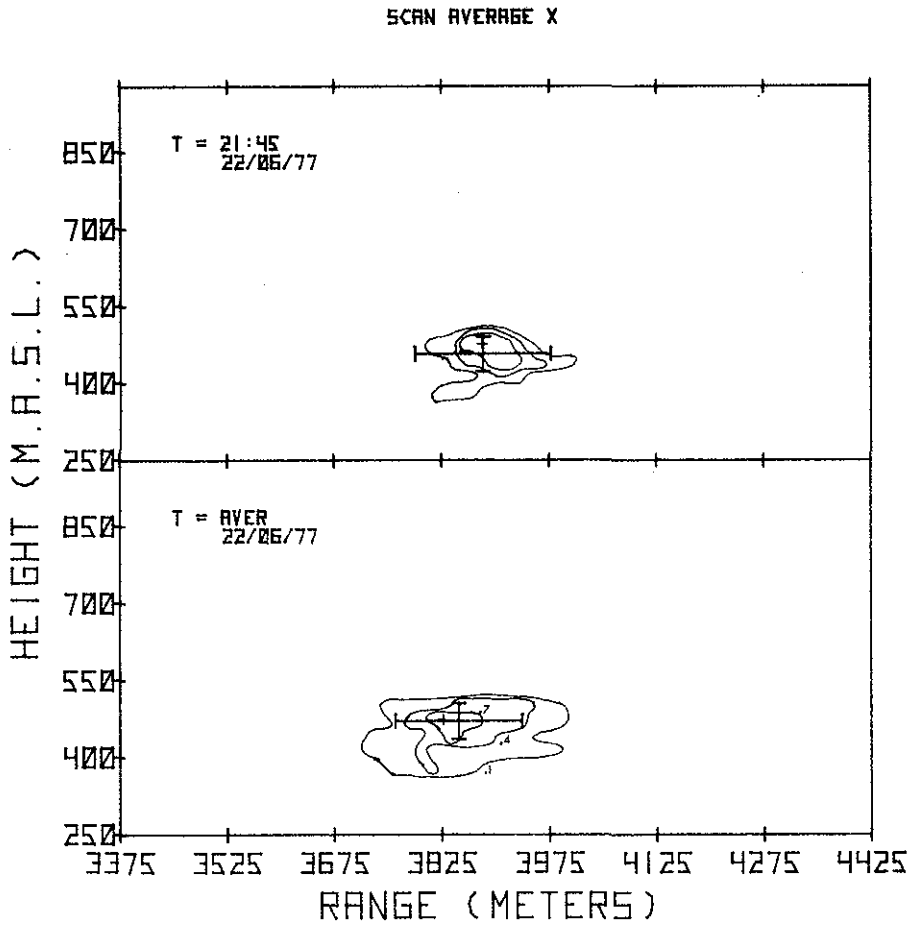

Figure 66. Plume cross-sections determined by LIDAR measurements. Time as indicated. Contours are drawn for 0.1, 0.4, and 0.7 of peak value of $\beta_{\pi}(R)$. (See text for description).

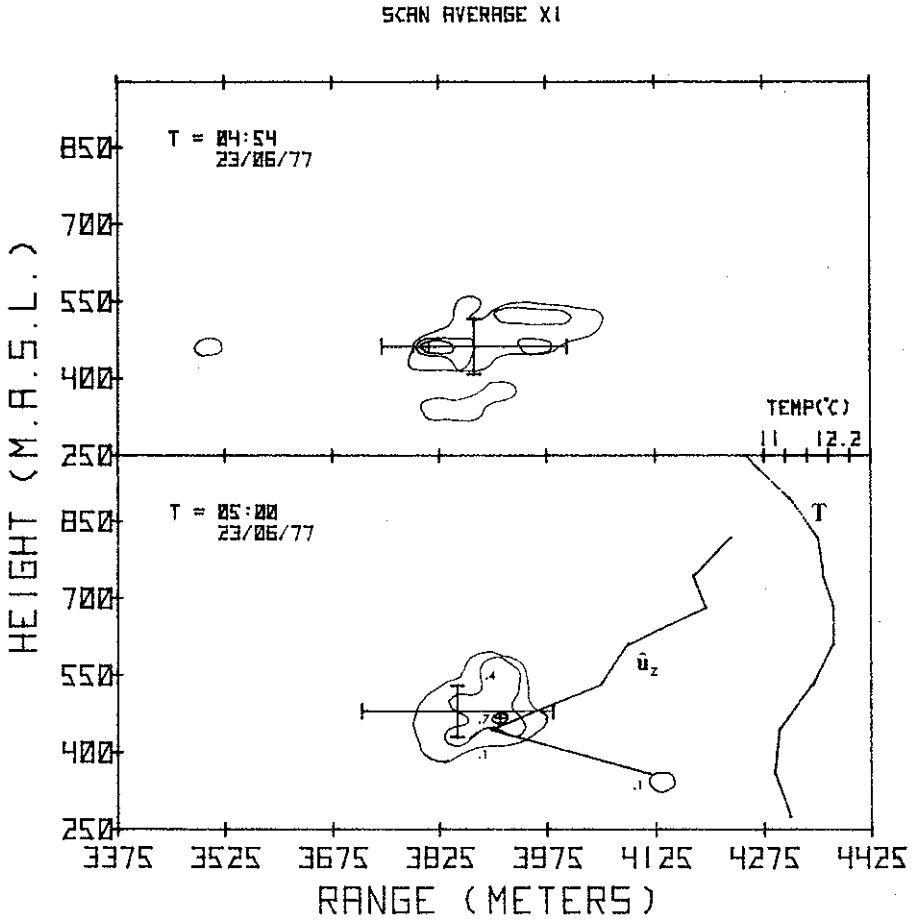

Figure 67. Plume cross-sections determined by LIDAR measurements. Time as indicated. Contours are drawn for 0.1, 0.4, and 0.7 of peak value of $\beta_{\pi}(R)$. (See text for description).

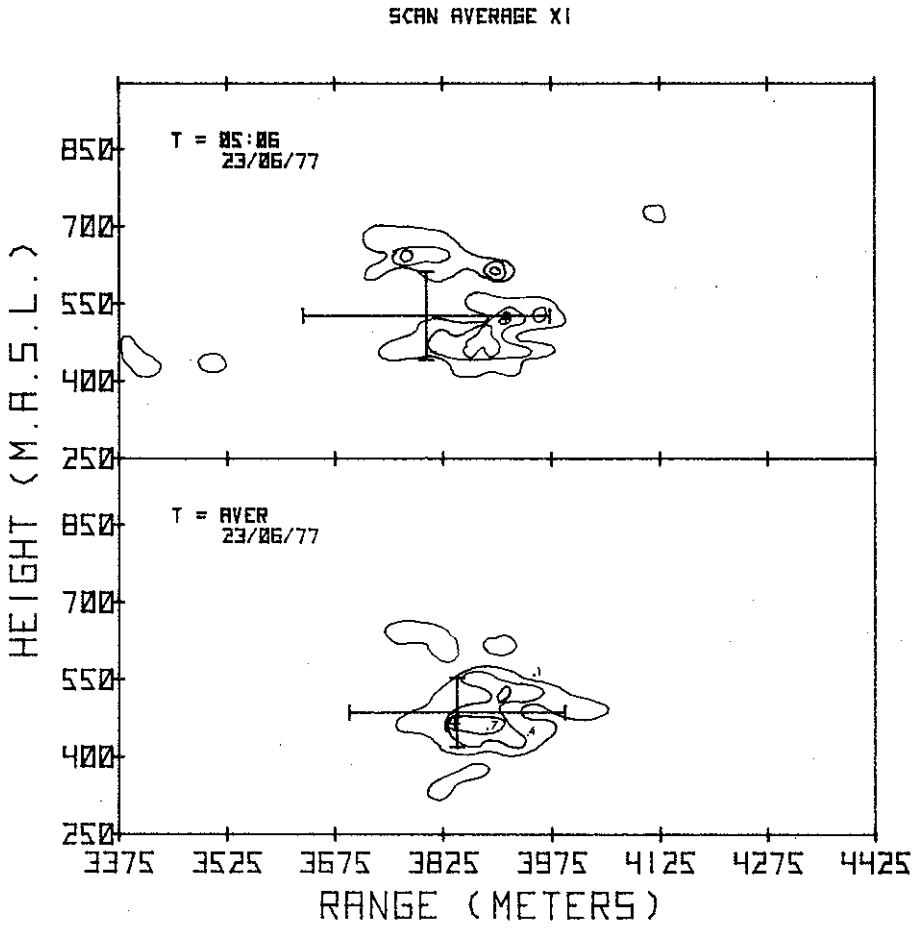

Figure 68. Plume cross-sections determined by LIDAR measurements. Time as indicated. Contours are drawn for 0.1, 0.4, and 0.7 of peak value of $\beta_{\pi}(R)$. (See text for description).

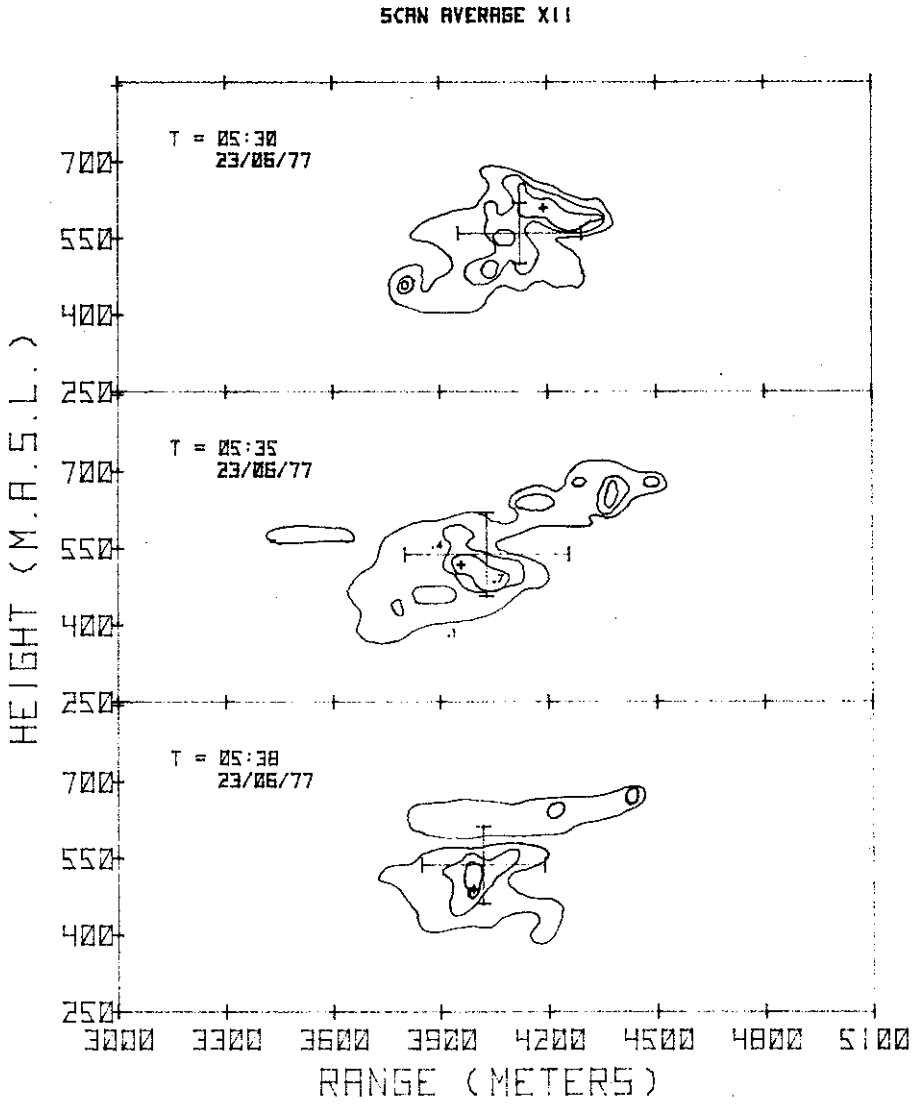

Figure 69. Plume cross-sections determined by LIDAR measurements. Time as indicated. Contours are drawn for 0.1, 0.4, and 0.7 of peak value of $\beta_{\pi}(R)$. (See text for description).

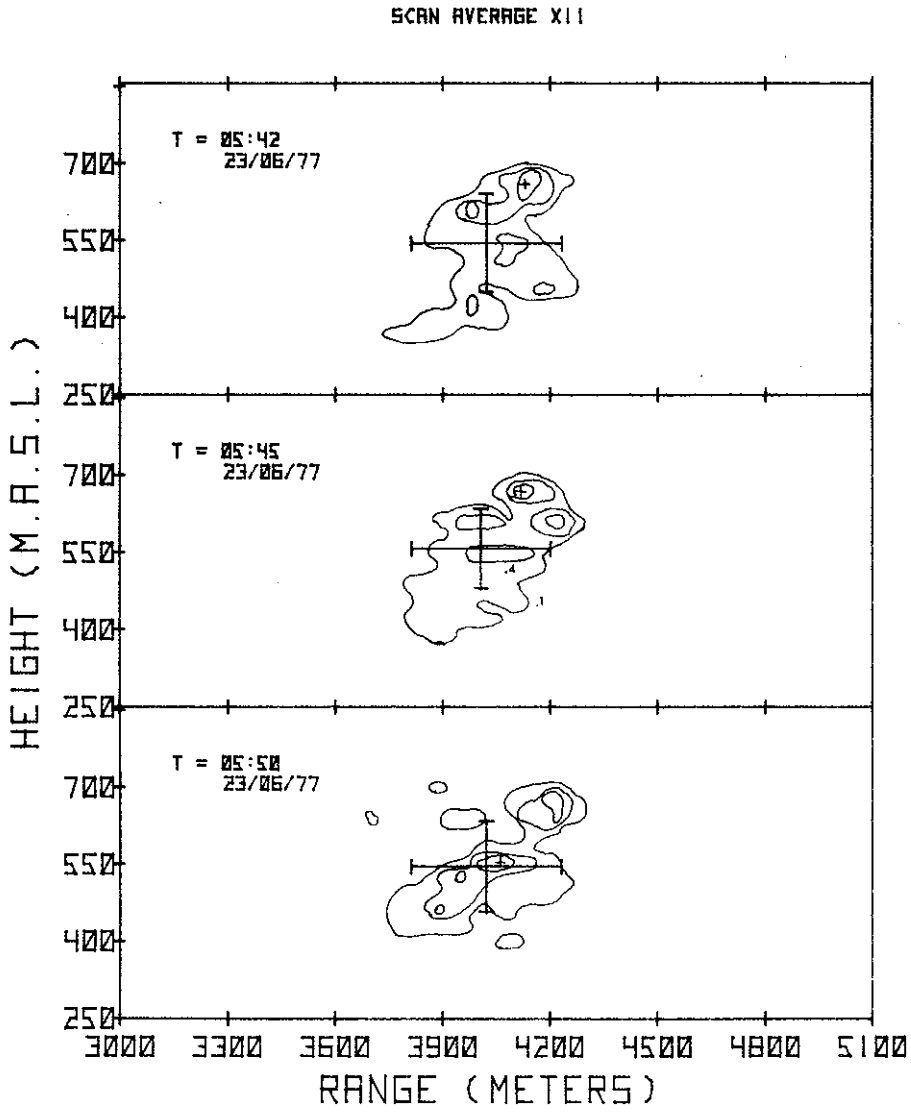

Figure 70. Plume cross-sections determined by LIDAR measurements. Time as indicated. Contours are drawn for 0.1, 0.4, and 0.7 of peak value of $\beta_{\pi}(R)$. (See text for description).

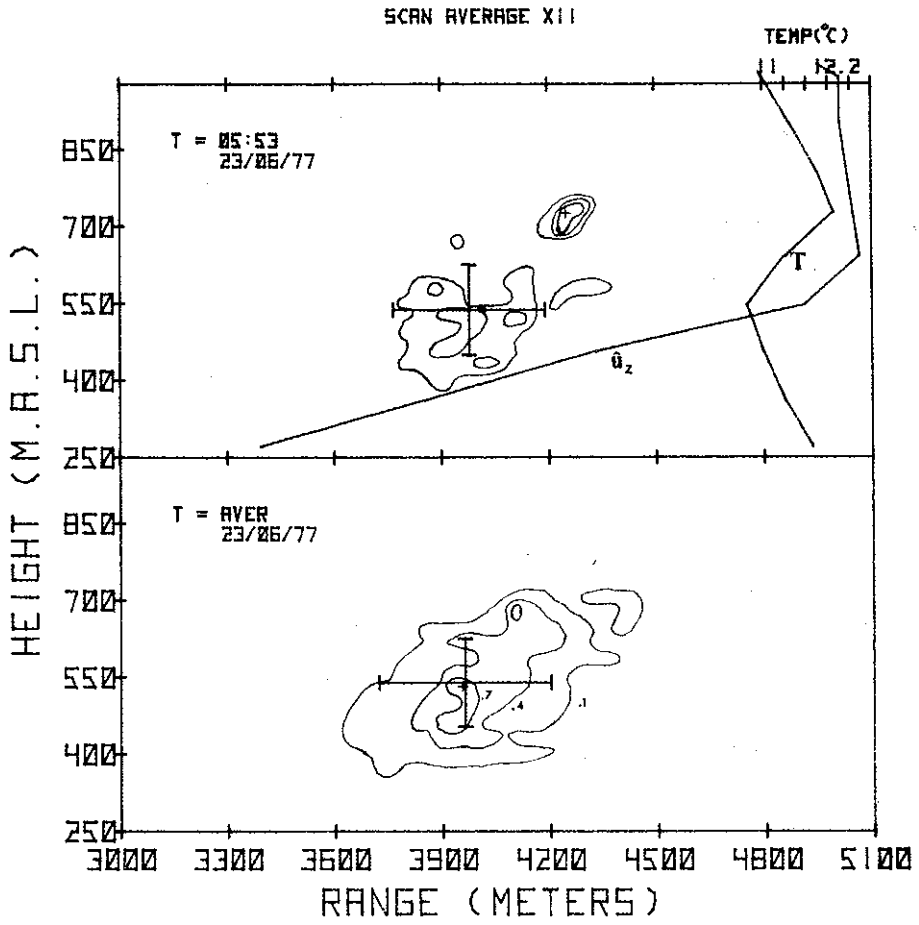

Figure 71. Plume cross-sections determined by LIDAR measurements. Time as indicated. Contours are drawn for 0.1, 0.4, and 0.7 of peak value of $\beta_{\pi}(R)$. (See text for description).

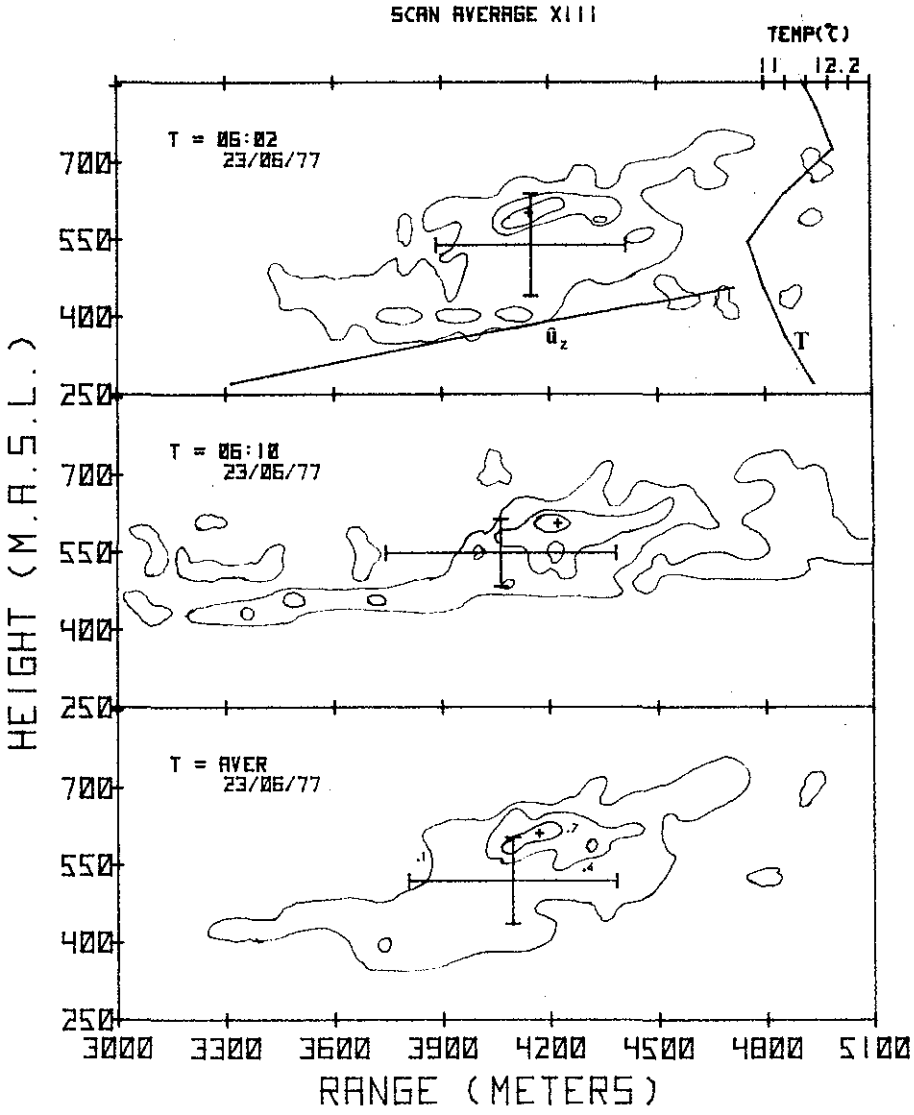

Figure 72. Plume cross-sections determined by LIDAR measurements. Time as indicated. Contours are drawn for 0.1, 0.4, and 0.7 of peak value of $\beta_{\pi}(R)$. (See text for description).

From Figures 67 to 72, the plume can be seen trapped completely under the inversion and appeared tied to the inversion base. This is consistent with the observation of a maximum wind jet at this height that the plume seemed to follow. Figure 67 shows that the 0500 LSM wind direction and shear were also coupled to the inversion base. At the 0600 LSR release the wind was quite strongly sheared in the horizontal, 70° over the lowest 500 m to the inversion base. The plume contour does not correspond to the wind direction particularly well (Figure 71). This discrepancy occurs because at the distance of averages 12 and 13 (912, 1340 m) the plume was curving in the shear flow (towards the north), and the straight vectors drawing the curve $\hat{U}_z$ are not valid indicators of the plume trajectory. As before, these stable cases do not agree with the ASME curves.

4.5 PREDICTIONS FROM A SINGLE SOURCE GAUSSIAN PLUME MODEL

Throughout the previous section reference was made to the dispersion coefficient predictions from the ASME parameterized form of the Pasquill-Gifford equation. Those parameters are (Smith 1968):

Stable:

$$\sigma_y = 0.31 \; x^{0.71}$$

$$\sigma_z = 0.06 \; x^{0.71}$$

Unstable:

$$\sigma_y = 0.36 \; x^{0.86}$$

$$\sigma_z = 0.33 \; x^{0.86}$$

Neutral:

$$\sigma_y = 0.32 \; x^{0.78}$$

$$\sigma_z = 0.22 \; x^{0.78}$$

Curves for these equations are plotted in Figures 45 and 46 for σ_y and σ_z in the stable and neutral-unstable cases. The relative agreement for the neutral cases and the striking disagreement for the

stable cases is obvious. In fact, a least squares fit to the stable σ_z data gives nearly a horizontal line, indicating no dispersion with distance.

These results for the stable cases are in agreement with those previously seen by Fanaki (1978) and Hoff (1977) in the first AOSERP field study.

Turbulent motion of the buoyant plume in the region of active rise has been noted to account for a larger portion of plume dispersion near the stack (Pasquill 1976; Hamilton, personal communication). Pasquill (1976) has suggested modifying the Gaussian predictions for a passive or cold plume by

$$\sigma_z^2 = \sigma_z^2 \text{ (passive)} + \Delta h^2/10$$

where Δh is the plume centreline height above the stack exit. Figure 73 shows the correspondence between σ_z and Δh measured in this study. The results reveal that these buoyant effects have larger influence on initial plume dispersion than Pasquill predicted and cannot be neglected in modelling plume dispersion from this source.

The larger values of σ_y under stable flows can also be attributed to shear effects within the valley. Unless provision is made in modelling for a dynamic wind field, under these regimes predicton of ground level concentrations and impingement distances may be orders of magnitude in error.

4.6 CONCLUSIONS

The LIDAR project accomplished its objectives of obtaining plume dispersion statistics, plume bearing, and plume rise from the GCOS emissions. An interesting cross-section of atmospheric conditions revealed that plume dispersion was more marked for unstable and neutral atmospheric situations and that the agreement with ASME predications for these cases was generally acceptable. In stable cases, however, the most dynamic portion of plume dispersion occurred within 100 or 200 m of the stack, and predictions from Gaussian models were inadequate. This indicates the need for dispersion models that

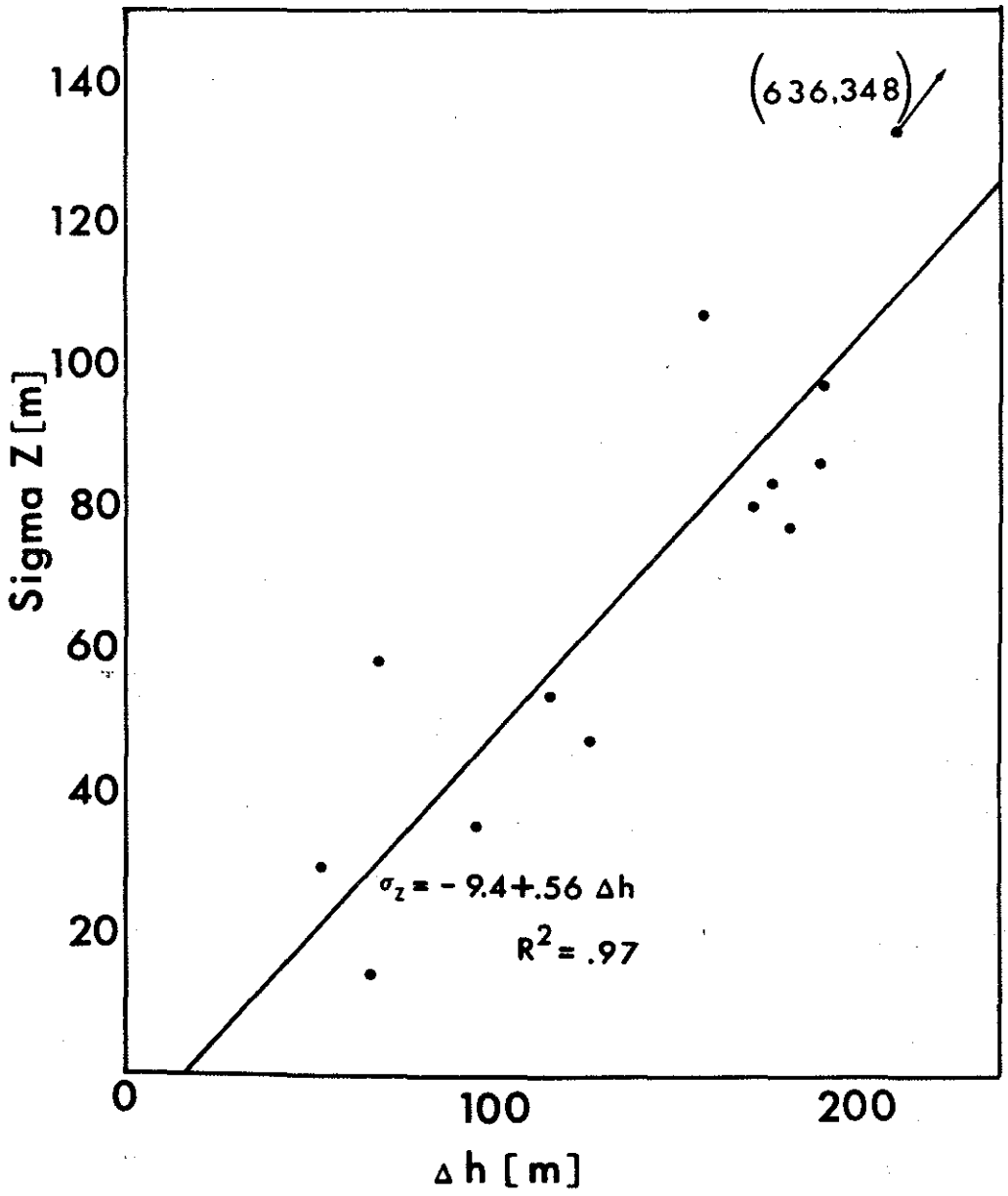

Figure 73. Linear regression of measured σ_z versus Δh (height above stack).

properly consider the dynamic effects at the stack exit and couple plume rise to the vertical and horizontal dispersion. The model should be able to treat shear effects and consider site topography.

5. SURVEY OF GCOS PLUME USING CORRELATION SPECTROMETER

The objectives of the June 1977 study were as follows:

1. To investigate the behaviour of unstable plumes in the AOSERP study area.
2. To investigate the logistics of plume traverses under summer conditions.

It is recommended that reference be made to the AOSERP field study report by Fanaki (1978) for a discussion of instrumental technique, data handling, and analysis.

The Barringer Correlation Spectrometer (COSPEC) is a passive remote sensor that uses ultraviolet radiation from the zenith sky to produce a vertically integrated profile of atmospheric SO_2. As used in the June 1977 AOSERP study, the COSPEC was operated viewing vertically upward by means of a 45° mirror mounted ahead of the telescope. To cover the area west of the GCOS plant, an Alberta Department of Environment/AOSERP GMC truck was used to make traverses on existing roadways (mainly Highway 63 and the Alberta Forestry Service gravel pit road, see Figure 74). During the winter study when unsafe ice made travel on the Athabasca River hazardous, the ice-free waters of the river in June invited the use of this route for traverses to the east of the plant. A boat was supplied by AOSERP, and the COSPEC (and later a Sign-X point monitor) was mounted on it. In both the boat and the truck, power was supplied by the vehicle battery and converted to 120 AC by an inverter that drove the instruments and a chart recorder on which the data were recorded. Difficulties were experienced in finding a battery capable of driving both the COSPEC and the Sign-X mounted in the boat, and the Sign-X was later assigned to a stationary monitoring role because of this. Figure 74 shows the location of the stationary monitoring site plus the road and water traverses used during this study.

All together, 132 runs were made during the course of the study; 112 were digitized and made available on magnetic tape. The remaining 20 runs were not digitized because zero ppm-m readings were not present. Two days were chosen for case studies. The first

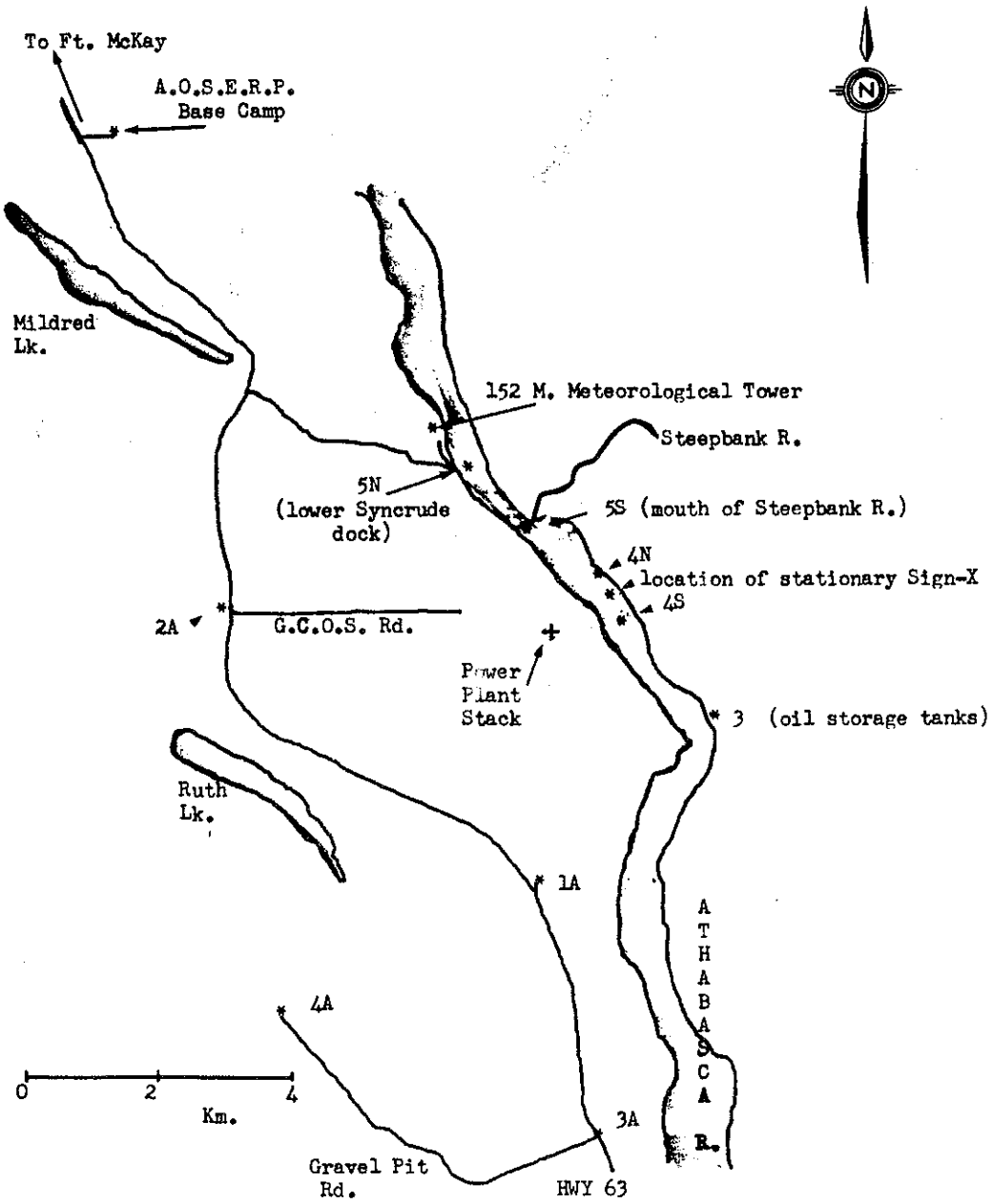

Figure 74. Map of the AOSERP study area and COSPEC traverses.

day, 18 June, shows traverses made on the road network at two successive downwind distances from the stack. The second day, 22 June, shows traverses made on the Athabasca River with the Sign-X in the mobile mode.

A daily log of activities covering the period of the study (15 to 26 June) and a listing of the data stored on magnetic tape is available through the AOSERP managment office of Alberta Environment.

5.1 CASE STUDY 18 June 1977

The day dawned clear and bright with a temperature of 10°C; by afternoon a few cumulus clouds had developed and the temperature reached 19°C. A north easterly wind prevailed throughout the day.

As the plume was crossing the highway south of the plant, runs were made with the truck along Highway 63 and on the gravel pit road, which runs off Highway 63 south of the plant and turns to run parallel to and approximately 4 km to the south of Highway 63. On this particular day the plume took about 10 min to cover the distance between the two roads. The plotted runs for this day are available through the AOSERP management office of Alberta Environment.

Figure 75 is a plot of successive Eulerian averages on this day and shows the increase in σ_y as solar heating progressed and began to affect the dispersion of the plume. Table 7 is a listing of σ_y, bearing of the centres of gravity and area for the profiles plotted in Figure 75. Also of interest is a comparison of the runs made on Highway 63 with those made on the gravel pit road. These runs, made at different downwind distances from the source, show the increase in σ_y as the plume ages and also describe the meander in the plume (Figure 76, Table 8).

5.2 CASE STUDY 22 June 1977

The prevailing wind was south westerly. The temperature regime was similar to that of 18 June, with an afternoon maximum of 22°C.

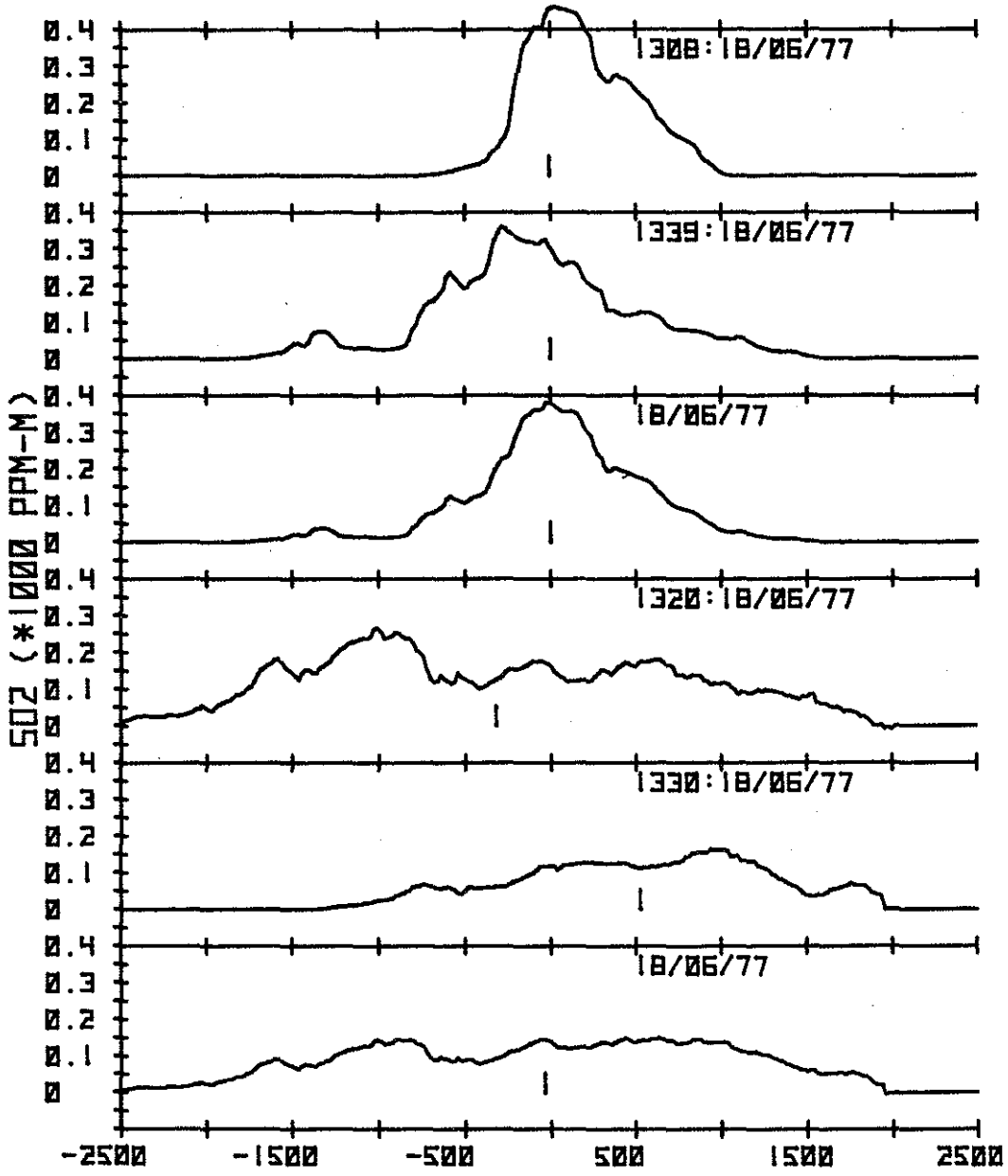

Figure 75. Plots of Eulerian averages for 18 June 1977 1308-1330 MST.

Table 7. List of relevant COSPEC parameters.

TIME	COG	BRG	SIGMA Y	AREA
0615	-8	233	449	221
0708	-11	232	327	202
0830	-3	211	512	292
0900	-7	213	649	278
0930	71	196	614	307
0942	111	195	623	275
1325	42	205	478	360
1400	44	203	620	452
1436	19	209	826	379

TIME IS MST
COG = CENTRE OF GRAVITY
BRG = BEARING OF COG FROM TRUE NORTH
AREA IS IN PARTS PER MILLION PER METRE X 1000

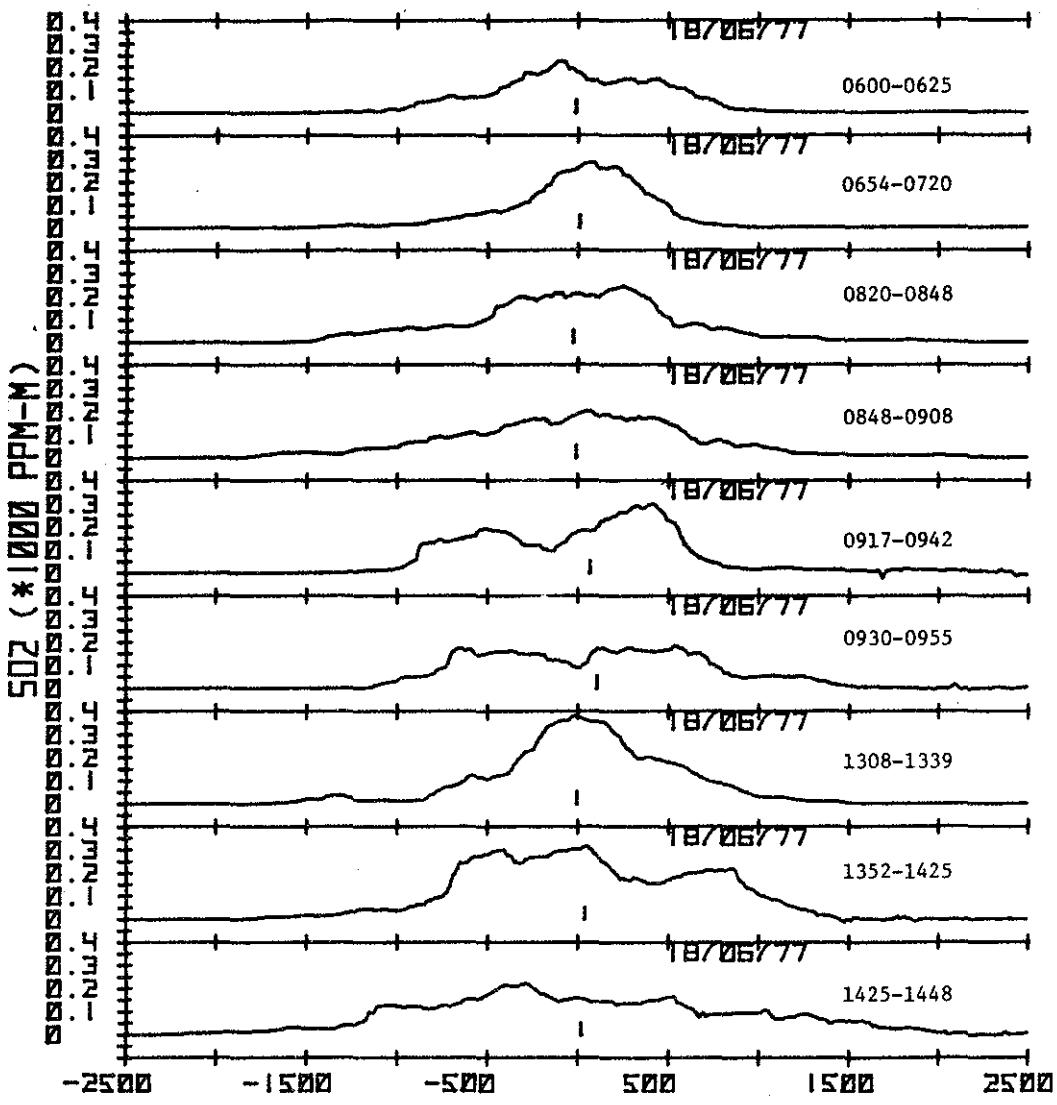

Figure 76. Eulerian averages for 18 June 1977, 0600-1425 MST.

Table 8. List of relevant COSPEC parameters for two different locations.

TIME	COG	BRG	SIGMA Y	AREA
Hwy 63				
1007	546	198	340	176
1020	340	195	557	272
1037	-134	188	907	280
9999	205	193	729	244
1308	193	207	301	334
1339	-82	202	575	390
9999	42	205	478	360
AFS Gravel Pit Rd				
1106	-83	261	832	346
1111	703	271	1110	297
1131	-243	259	906	221
9999	150	288	1040	
1320	-318	190	1016	539
1330	525	200	716	273
9999	-31	194	1003	406

TIME IS MST
COG = CENTRE OF GRAVITY
BRG = BEARING OF COG FROM TRUE NORTH
AREA IS IN PARTS PER MILLION PER METER X 1000
9999 = EULERIAN AVERAGE FOR ABOVE

A Sign-X point monitor of SO_2 was carried in the boat with the COSPEC to give a measure of surface level concentrations. Figures 77 and 78 show a sample of a traverse of SO_2 concentration and the corresponding COSPEC traverse for 22 June at 1619 to 1645 MST. On certain occasions the SO_2 concentration peaked at over 1 ppm on the Athabasca River. At a later time the concentration varied from 0.1 to 0.5 ppm.

A displacement in the centres of gravity of the Sign-X versus the COSPEC profiles can be taken as a measure of wind directional shear of the plume. Table 9 compares the bearing of centres of gravity from true north between the COSPEC and the Sign-X measurements.

The wide variations in the bearings of COSPEC versus Sign-X centres of gravity do not seem to be entirely due to horizontal wind shear (a shear of at most 15^{o} was present this day). It would seem that low-level sources are contributing SO_2 or that the plume has a tendency to spread laterally near the surface of the water when impingement conditions exist.

It should be remembered when comparing Sign-X and COSPEC σ_y that although the data were treated using the same procedures, the COSPEC data with concentrations less than 10 ppm-m were disregarded in order to eliminate any noise which may have been present, whereas no such constraints were placed on the Sign-X data. This explains the apparent contradiction in cases that show a wider σ_y for the Sign-X data than for the COSPEC. Also, it should be kept in mind that the Sign-X is a point monitor, while the COSPEC senses all the SO_2 above it.

In the runs made on the river (1.5 to 1 km from the source) it will be noted that the profiles show a number of clearly defined peaks (see 22 to 24 June data available through the AOSERP management office of Alberta Environment). This does not indicate break-up of the plume, but rather shows that usually three and occasionally four discrete SO_2 sources are in operation at any one time. The largest of these is of course the power plant, whose plume often show bifurcation; the others are flare stacks, which usually combine plumes to

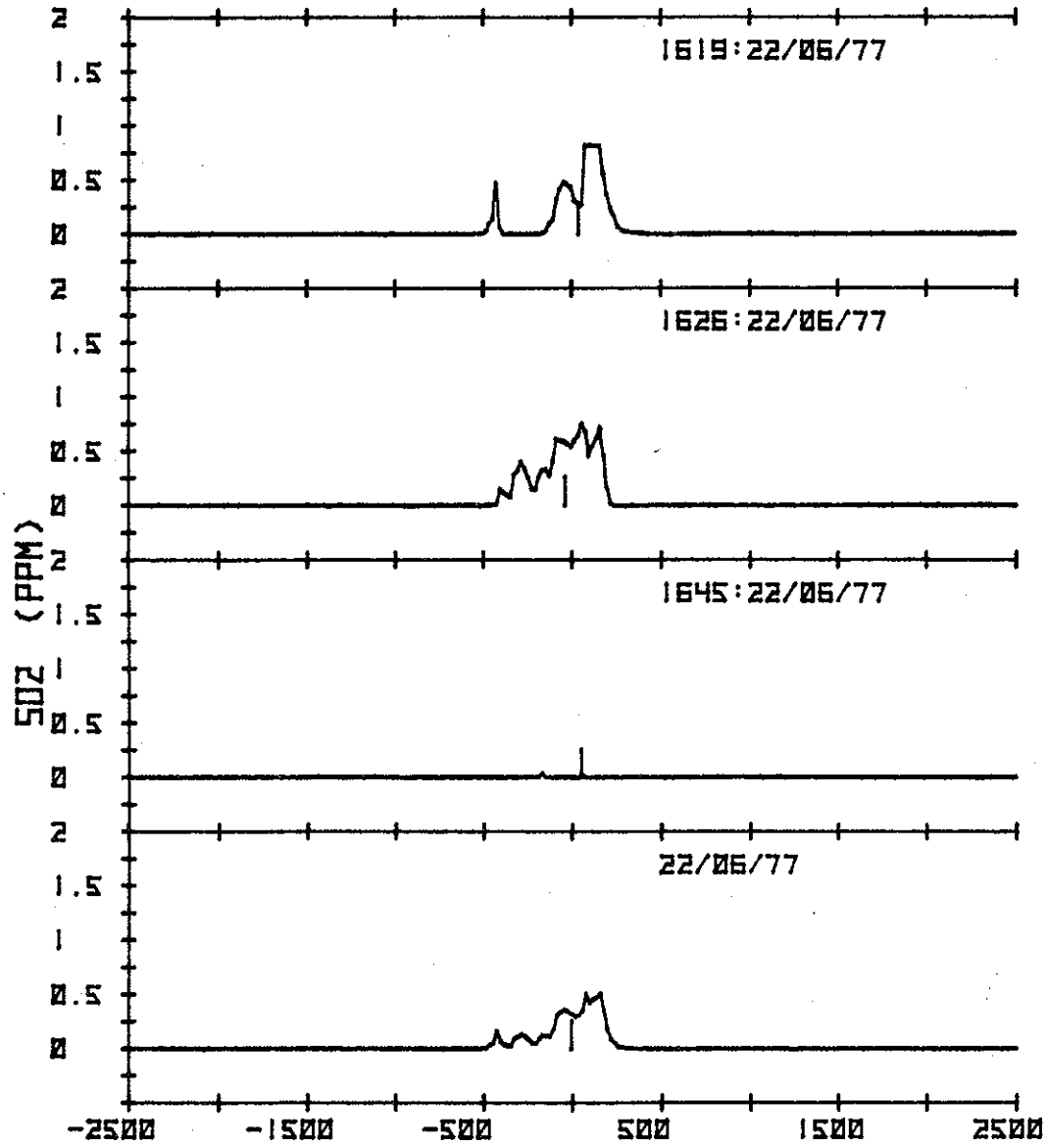

Figure 77. SO_2 surface concentration as a function of horizontal distance, 1619 to 1645, 22 June 1977.

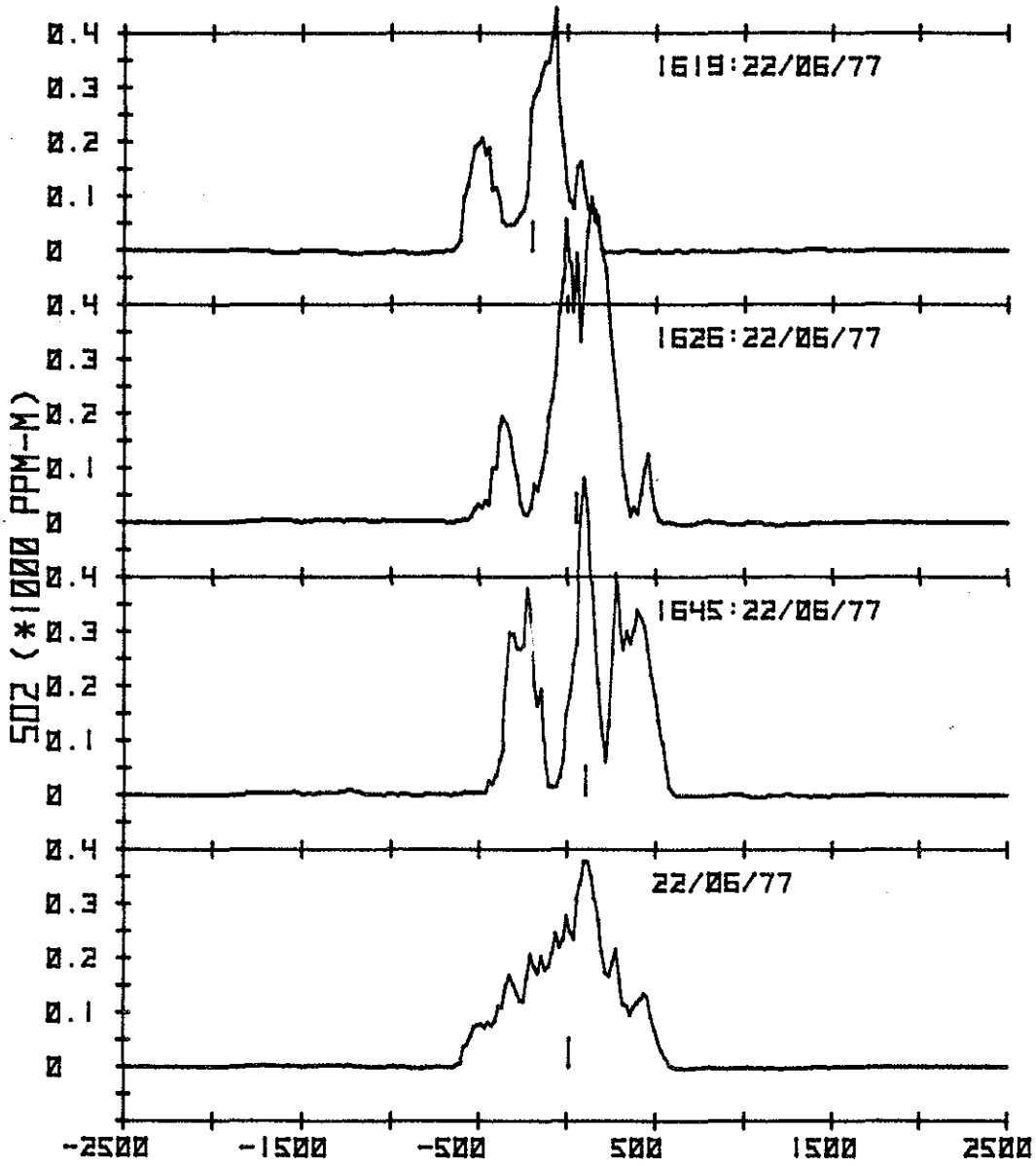

Figure 78. Eulerian averages for 22 June 1977, 1619 to 1645.

Table 9. COSPEC and sign-X centres of gravity for 22 June, 1977 at different times.

TIME	BRG COSPEC	BRG SIGN-X
1619	66	77
1626	81	73
1645	84	78
1730	61	98
1739	65	54
1747	79	77
1753	63	54
1802	69	75
1808	76	18
1817	80	41
1827	73	46
1833	77	18
1841	76	85
1847	92	85
1855	76	92

TIME IS MST
BRG = BEARING OF CENTRE OF GRAVITY FROM TRUE NORTH (IN DEGREES)

to make one or more larger plumes. The runs on the highway do not show this because the plumes were almost always well mixed by the time they had travelled that far downwind.

In cases which show high values for the Sign-X measurements, the plume was almost always looping directly overhead the boat track. Plume looping directly overhead leads to excessively high values of SO_2 seen by the COSPEC, because it looks along the centerline of a section of plume stacked vertically above it.

5.3 CONCLUSIONS

1. Operation of the COSPEC on the Athabasca River is a viable and useful procedure.
2. Operation of a Sign-X monitor with the COSPEC sensor is a useful method to obtain plume shear and ground concentration data.
3. Summer convective activity causes the power plant plume to impinge within 1 km of the stack, with ground concentrations of SO_2 exceeding 1 ppm.

5.4 RECOMMENDATIONS

1. Some attempt should be made to determine whether the period studied (16 to 25 June 1977) is a representative example of "typical" or "average" summer conditions in the AOSERP study area.
2. Future field studies should consider aircraft or helicopter mounting of the COSPEC in order to surmount the difficulties associated with the limited road/river network in the area.
3. Correlation of AES COSPEC data with any obtained by the Intera aircraft-mounted COSPEC for the same period would definitely be of interest.

4. All future studies should include mobile Sign-X or similar fast-response SO_2 monitors operated in tandem with the COSPEC to obtain ground truth data.
5. Operation of two or three COSPECs at different downwind distances to obtain plume dispersion data should be considered.

6. AERIAL SURVEY OF GCOS PLUME

6.1 EXPERIMENTAL PROCEDURE

The plume from the GCOS power plant chimney was surveyed during the period 16 to 26 June with a Bell Jet Ranger helicopter as the instrument platform. The instrument package and the experimental and chemical analysis procedures were in many respects the same as those used during the February 1977 field study, and the reader is referred to the AOSERP Report (Fanaki 1978) for a detailed discussion. However, the June field study differed from the February one in the following respects:

1. A Columbia Scientific Instruments Model 2000 ozone analyser was added to the instrument package. This analyser operates on the chemiluminescence principle using the reaction between ozone and ethylene and has a 95% response time of 15 s. It was connected to the same sample line as the Sign-X SO_2 analyser.
2. Delbag filters only were used as particulate filters in packs meant for sulphuric acid analysis. The use of Mitex filters Fanaki (1978) was abandoned because of difficulties experienced during the extraction of particulate matter from them.
3. No flights were carried out to obtain detailed plume concentration profiles, as had been done during the February study. The emphasis was on filter pack sampling for SO_2 oxidation studies and on examination of ozone concentrations within the plume
4. Weather permitting, an attempt was made to carry out one flight during the first two hours after sunrise, and one or more flights later in the day. Although the plume was generally coherent during the early morning hours, fumigations had occurred by 0900 MST, and the plume was rather diffuse. Therefore, to ensure

the collection of an adequately large sample and to make proper correction for "background" contributions of SO_2 and sulphates to the sample, the following flight plan was observed: the first sample was collected over the period of about 1 h at the farthest point downwind of the stack where the plume could definitely be distinguished from the background air. The helicopter then proceeded to a location about 5 km upwind of the stack, where a sample was collected for about the same period and at about the same altitudes, as the downwind sample. Finally, a sample was collected just downwind of the chimney.

5. Several special flights were carried out within about 1 km of the chimney to investigate the concentration and particle size distribution of sulphates and various metals in the GCOS power plant plume. As was the case during the February field study, samples were collected on fluoropore filters and analysed by neutron activation, but sample collection times were considerably longer. Particle sizing was done by connecting an Anderson ambient cascade impactor into one of the filter pack sampling lines. At a flow rate of about 0.5 $L \cdot s^{-1}$ this sampler collects particulate matter on eight stages in the 0.4 to 11 μm range. Whatman 541 filters were used as the collection medium of the stages, with a Whatman 40 filter in the backup position. These Andersen impactor filters were first analysed by neutron activation for metals, and then by isotope dilution for sulphates.

6.2 RESULTS

A total of 19 flights was carried out during the June 1977 field study, 7 of these within the first two hours after sunrise. Table 10 shows the concentration of sulphur (as total sulphate, sulphuric acid, and SO_2) collected in the plume and background air on those flights that were designed to study SO_2 oxidation rates. It should be pointed out that the results in Table 10 are expressed in terms of concentration so that the reader can assess the importance of contributions to plume S from the background air, and also get some idea of the reproducibility of data obtained with the filter pack method. (At each location, the $SO_4^=$ and H_2SO_4 packs should give the same SO_2 concentration, since the same air parcel is being sampled.) As can be seen from Table 10, the agreement is usually fairly good (see also Lusis et al. 1977a). The concentrations shown in Table 10 should not be used to calculate plume dilution rates or sulphur budget balances. The reason for this is that the sampling pumps were not turned off as the helicopter left the plume to turn around, and the percentage of time spent outside the plume varied with distance from the stack where the sample was collected.

During the chemical analysis of the samples, the filter blank was found to be quite large for the sulphuric acid samples--in some cases, greater than the collected sample itself--and generally too large to determine the small background air contributions with any confidence (hence the absence of S as H_2SO_4 background concentrations in Table 10). As can also be seen in Table 10, in four cases the S as H_2SO_4 even exceeded the S as total $SO_4^=$ concentration, which is of course impossible. The reason for this is unknown. Generally, the H_2SO_4 data are thought to be considerably less accurate than those for SO_2 or total $SO_4^=$.

The rate of conversion of plume S from the gaseous (SO_2) to the particulate ($SO_4^=$) form, for various times after emission, is shown in Table 11. In the calculation of SO_2 conversion rates, contributions to plume SO_2 and total sulphate from entrainment of ambient air were substracted only for those flights where background measurements were actually made. Background SO_2 concentrations were

Table 10. Total sulphates, sulphuric acid, and sulphur dioxide collected in the GCOS plume, June 1977.

Date June	Time of Sampling (LST)	Distance from Stack (km)	($\mu g\ Sm^{-3}$ as^{+}) $SO_4^{=}$	H_2SO_4	SO_2^{*}
17	0640-0711	0.5	13.2		616
				7.2	556
	0450-0537	16.0	4.49		211
				2.4	228
	0540-0620	44.7	3.00		160
				1.5	147
18	0615-0640	1.1	9.96		510
				4.3	496
	0540-0610	7.6	8.66		443
				4.9	352
	0450-0535	17.3	7.14		357
				3.0	297
18	1155-1205	0.5	8.05		314
				2.3	333
	1024-1115	18.9	1.60		36
				0.2	36
	1120-1150	Background	0.07		7
				-	3
19	0617-0635	2.5	11.0		652
	0540-0610	16.5	8.31		438
				4.2	442
	0448-0528	44.6	4.47		222
				0.2	204
	0955-1040	18.7	2.60		87
				0.6	104
	1045-1115	Background	0.12		8
					8
19	1446-1510	2.3	3.53		197

Continued . . .

Table 10. Continued.

Date June	Time of Sampling (MST)	Distance from Stack (km)	($\mu g\ S.m^{-3}$ as $^{+}$) $SO_4^{=}$	H_2SO_4	SO_2^{*}
				0.6	200
	1305-1405	23.9	1.04		37
				0.1	34
	1410-1442	Background	0.09		4
				-	1
20	0545-0610	15.9	4.24		246
				0	231
	0455-0535	25.4	2.52		109
				2.0	97
20	1200-1222	2.1	3.07		182
				2.2	193
	1007-1123	31.6	0.99		23
				0.1	23
	1130-1145	Background	0.15		0.2
				-	0.2
20	1600-1622	2.3	4.64		409
				4.2	-
	1415-1517	28.2	1.01		21
				2.0	22
	1527-1555	Background	0.36		6
				-	6
21	0605-0627	0.6	8.59		513
				5.7	551
	0542-0600	15.2	2.11		115
				0	85
	0445-0525	50.5	1.60		86
				0.6	68
22	1905-1920	0.5	9.69		664
				6.0	533
	1930-2025	24.6	0.26		13
				0	14

Continued . . .

Table 10. Concluded.

Date June	Time of Sampling (LST)	Distance from Stack (km)	($\mu g\ S.m^{-3}$ as^{+}) $SO_4^{=}$	H_2SO_4	SO_2^a
	2030-2057	Background	0		4
				-	2
23	0625-0644	1.1	6.29		358
				2.9	361
	0535-0615	13.3	2.12		101
				0.1	97
	0449-0525	55.1	1.71		88
				0	104
23	1535-1552	0.9	10.8		571
				9.0	671
	1354-1457	20.2	0.30		8
				0.5	8
	1505-1530	Background	0.80		2
				-	3
24	0535-0552	1.0	20.6		1264
				16	1471
	0450-0523	26.5	6.18		355
				4.2	350
26	1217-1248	3.2	5.97		323
				3.7	332
	1057-1202	32.5	0.58		15
				1.3	15

+ at 1 atmosphere, 21°C

[a] The first value for a given distance from the stack is the SO_2 concentration determined from the total suphate filter pack; the second, that determined from the H_2SO_4 pack.

Table 11. Conversation of plume sulphur from SO_2 to $SO_4^=$ and meteorological conditions, GCOS plume Study, June 1977.

Date June	Time (MST)	Av. Met. parameters at plume height[*a] Wind (km min^{-1})	Temp (^{o}C)	r.h.(%)	Plume age interval (min)	Av. conversion
17	0440-0715	0.51	16	65	1-31	-0.06
					31-88	-0.2
18	0440-0640	0.33	10	80	3-23	0
					23-52	0.1
18	1000-1215	0.27	14	55	2-70	2.0
19	0430-0630	0.44	10	80	6-38	0.4
					38-101	0.1
19	1300-1515	0.35	18	55	7-68	0.9
20	0440-0620	0.63	16	65	25-40	2.2
20	1000-1230	0.41	18	40	5-77	1.6
20	1400-1630	0.47	23	50	5-60	3.3
21	0430-0630	0.39	16	65	2-39	0.3
					79-129	0.02
22	1900-2100	0.42	21	55	1-59	1.2
23	0430-0650	0.64	12	65	2-21	1.0
					21-86	-0.1

Continued . . .

TABLE 11. Concluded

Date June	Time (MST)	Av. Met. parameters at plume height Wind (km min^{-1})	Temp (^{o}C)	r.h.(%)	Plume age interval (min)	Av. Conversion
23	1340-1600	0.45	17	55	2-45	3.0
24	0440-0600	0.48	16	55	2-55	0.1
26	1020-1300	0.68	11	70	5-48	2.7

*[a] Measured by radiosondes and/or minisondes at Lower Syncrude Site, about 4 km from power plant.

calculated by averaging the total sulphate and H_2SO_4 filter pack results. For the other flights (with the possible exception of that on 26 June), plume SO_2 and SO_4 concentrations were so high as to make corrections for entrainment of ambient air negligible.

The results of the neutron activation samples collected on fluoropore filters near the stack are shown in Table 12. (Iron was analysed by atomic absorption after extracting the particulate matter into 10 cm^3 of hot concentrated nitric acid. The analysis was carried out by F. Philbert of the Canada Centre for Inland Waters.) Also given is the weight of SO_2 trapped on the chemically impregnated filters in the same pack as each fluoropore filter. Table 13 shows the same data, expressed as milligrans of element in particulates per gram of SO_2 in the plume. Blank values have been subtracted from the data in Table 13.

As was noted above, plume samples collected on three flights using the Andersen impactor were first analysed for Mn, V, Al, and Ca by neutron activiation and then for sulphate isotope dilution. Manganese and vanadium are potential catalysts for SO_2 oxidation in particulates (Barrie and Georgii 1976; Newman et al. 1975), while calcium oxide can act as a neutralizing agent for the H_2SO_4 formed. Iron, another catalyst for heterogeneous SO_2 oxidation (Foster 1969; Freiberg 1974), was not examined, because sample irradiation times had to be kept short in order to allow further handling and analysis for sulphates. The results of these analyses are given in Tables 14 and 15. Filter blank values have already been subtracted from the data shown. The results for Ca were too near blank values to be signiciant and therefore are not shown. This was also true for Al on both flights of 21 June and Mn on the flight of 21 June, 1313-1425. Unexpectedly high blanks were obtained during the sulphate analysis, indicating that there may have been some contamination of the samples during the previous neutron activation analysis. Therefore, the accuracy of the sulphate results shown in Tables 14 and 15 may be rather poor.

TABLE 12. Results of neutron activation analysis of the particulate matter in the GCOS plume (all quantities in μg)

	Blank	Time of Sample Collection				June
	Filter	16/1547 - 1647 (LST)		21/1313-1425	21/1530-1645	26/1347-1507
SO_2	---	750	607	1200	706	5100
U	0.0015	0.001	0.004	0.004	0.006	0.011
Ba	0.16	0.30	0.50	<0.2	<0.2	0.95
Ti	<0.1	0.70	0.73	0.84	1.70	5.00
I	<0.003	<0.006	<0.007	<0.010	0.023	<0.013
Br	<0.006	<0.006	<0.006	<0.006	<0.008	<0.012
Mn	0.007	0.055	0.059	0.059	0.23	0.42
Na	1.0	1.4	0.8	0.5	1.1	1.6
V	0.035	0.957	0.924	1.52	5.19	11.00
Al	0.2	3.9	4.7	5.2	17.4	32.8
Cl	1.5	1.4	0.7	0.4	0.2	0.4
Ca	1	1	<1	<1	2	2
Sm	<0.0002	0.0008	0.0008	0.002	0.0045	0.010
Eu	<0.00004	0.0003	0.0002	0.0003	0.001	0.0022
La	<0.004	<0.004	<0.004	0.004	0.048	0.041
As	<0.003	<0.003	0.003	0.006	0.025	0.062
Sb	<0.006	<0.006	<0.006	<0.006	<0.006	<0.008
K	0.6	1.0	1.2	0.8	2.8	5.3

continued ...

TABLE 12. Concluded.

	Blank Filter	Time of Sample Collection			June
		16/1547 - 1647 (LST)	21/1313-1425	21/1530-1645	26/1347-1507
Cr	<0.1	<0.1	<0.1	<0.1	<0.1
Sc	<0.001	0.001	0.001	0.002	0.005	0.009
Fe*	2.6	4.7	4.6	5.2	9.7	15.4
Zn	<0.7	<0.7	<0.7	<0.7	0.7	1.1
Co	<0.03	<0.03	0.05	0.04	0.04	0.11

[a] Obtained by atomic absorption

Table 13. Milligrams of the elements in particulate matter per gram of SO_2 in the plume.

	Time of Sample Collection June				
	16/1545 - 1647 (MST)		21/1313-1425	21/1530-1645	26/1347-1507
U	∿0		0.004	0.006	0.002
Ba	0.2	0.6	<0.2	<0.3	0.2
Ti	∿0.8	∿1.0	∿0.6	2.3	1.0
I	<0.008	<0.01	<0.008	∿0.03	<0.003
Br	<0.008	<0.01	<0.005	<0.01	<0.002
Mn	0.064	0.086	0.043	0.32	0.081
Na	0.5	∿0	∿0	0.1	0.1
V	1.2	1.5	1.2	7.3	2.2
Al	4.9	7.4	4.2	24.4	6.4
Cl	∿0	∿0	∿0	∿0	∿0
Ca	∿0	∿0	∿0	1	0.2
Sm	∿0.0008	∿0.0008	∿0.002	0.006	0.002
Eu	∿0.0003	∿0.0003	∿0.0002	0.001	0.0004
La	<0.005	<0.007	<0.003	∿0.06	0.007
As	<0.004	<0.005	<0.005	0.03	0.01
Sb	<0.008	<0.01	<0.005	<0.008	<0.002
K	0.5	1.0	0.2	3.1	0.9

continued ...

Table 13. Concluded.

	Time of Sample Collection				June
	16/1545 -	1647 (LST)	21/1313-1425	21/1530-1645	26/1347-1507
Cr	<0.1	<0.2	<0.08	<0.1	<0.02
Sc	<0.001	<0.002	<0.002	<0.007	~0.002
Fe	2.8	3.3	2.2	10	2.5
Zn	<0.9	<1.2	<0.6	<1.0	<0.2
Co	<0.04	<0.08	<0.03	<0.06	0.02

Table 14. Mn, V, and $SO_4^=$ collected on the plates and backup filter of the Andersen impactor, GCOS power plant plume surveys of 21 June, 1977[a]

	1313 - 1425 flight		1530 - 1645 flight		
	V	SO_4	Mn	V	SO_4
Plate 0	0.017	∿0	∿0	0.091	1
1	0.013	∿0	∿0	0.054	1
2	0.070	∿0	0.016	0.240	∿0
3	0.380	∿0	0.060	1.27	1
4	0.470	∿0	0.060	1.58	1
5	0.400	∿0	0.047	1.37	2
6	0.140	∿0	0.008	0.410	∿0
7	0.088	3	0.050	0.240	4
Backup filter	0.086	5	0.028	0.240	2

[a] All values in micrograms. During both flights the sampling rate was 24 $L.min^{-1}$.

Table 15. Mn, V. Al and $SO_4^=$ collected on the plates and backup filter of the Andersen impactor, GCOS power plant plume survey of 26 June, 1347-1507.[a]

	Mn	V	Al	SO_4
Plate 0	0.032	0.160	1.6	2
1	0.006	0.170	0.9	1
2	0.055	0.740	3.9	1
3	0.130	3.03	10.9	1
4	0.190	3.65	11.0	3
5	0.130	3.08	8.1	2
6	0.048	0.780	2.4	2
7	0.025	0.450	1.9	4
Backup Filter	0.028	0.440	1.3	5

[a] All values in micrograms. The sampling rate was 24 $L.Min^{-1}$.

Table 16. Physical characteristics of plume particles containing Mn, V and Al, GCOS power plant, June 1977.

Element	Sampling Time	Mass Mean Daimeter, um	Geometric Standard Deviation um
V	21 June, 1313-1425	2.5	1.6
	21 June, 1530-1645	2.4	1.6
	26 June, 1347-1507	2.7	1.7
Mn	21 June, 1530-1645	3.3	1.6
	26 June, 1347-1507	3.1	1.7
Al	26 June, 1347-1507	3.3	1.7

The data in Tables 14 and 15 were analysed by J. Puttock of the Dispersion Division; details will be given in a forthcoming report. After particle bounce-off errors were corrected for, the mass mean diameters and geometric standard deviations shown in Table 16 were obtained for Mn, V, and Al. The sulphate data were not considered to be sufficiently accurate to permit a similar analysis.

One of the most interesting results obtained from the continuous SO_2 and O_3 analyser records was the detection of an O_3 "bulge" in the plume downwind of the chimney during several of the flights made in the late morning and the afternoon. These above-background-level O_3 concentrations occurred only at the far downwind sampling location. Near the chimney, there was always a depletion of O_3 in the plume, due to chemical scavenging by the emitted NO. Skies were relatively clear, and atmospheric turbulence was bringing the plume down to the ground well upwind of the sampling location, so that the plume was rather indistinct in the vertical direction, but its crosswind boundaries could usually be readily defined from the SO_2 analyser records. Figure 79 gives an example of excess O_3 formation far downwind of the chimney, and O_3 scavenging by NO just near the stack. It should be noted here that for all the flights before 0700 there was O_3 depletion in the plume for all the sampling locations.

Table 17 summarizes the O_3 observations made during passes through the plume at the far downwind sampling points. Only afternoon and late morning flights are included. As can be seen O_3 "bulges" were observed in the plume during most of the flights carried out between 1000 and 1500 MST.

6.2.1 Discussion of Results

Figure 80 shows a plot of the percentage of plume sulphate in the particulate form as a function of plume age. Contributions to plume sulpate from the ambient air have been subtracted. A distinction is made between runs carried out before 0700 MST (where solar radiation is still low), and runs carried out later in the day.

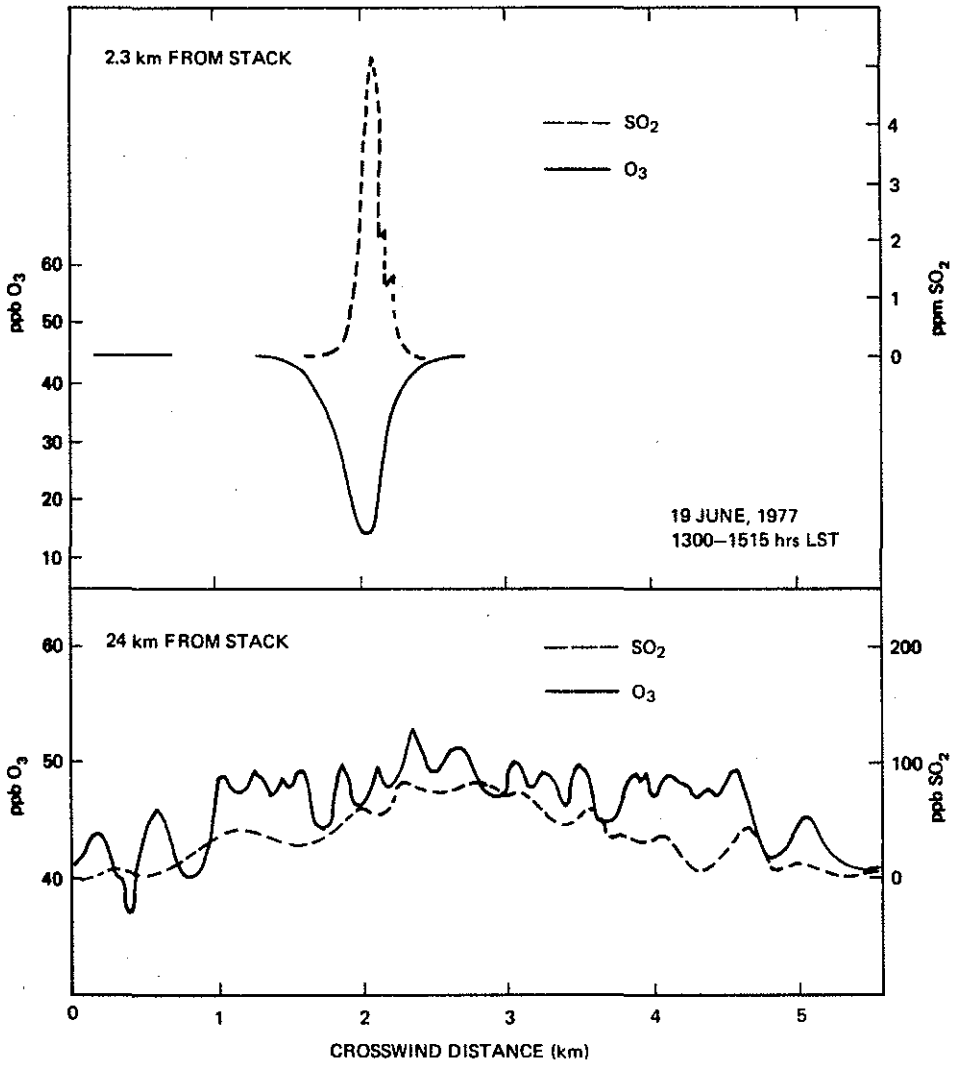

Figure 79. Crosswind O_3 and SO_2 profiles near the stack and 24 km downwind, 19 June 1977.

Table 17. Summary of plume O_3 and SO_2 obervations for flights after 0700 MST.

Date June	Time MST	Dist. from Stack, km	Background O_3, ppb (SO_2, ppb)+	Altitude m msl	Plume - background O_3, ppb [a]	Plume - background SO_2 ppb [a]
18	1024-1115	18.9	30-40 (4)	915	0	70
				880	5	40
				850	0	40
				820	-5	40
				790	<5	40
				760	0	50
				730	6	60
				700	0	70
				760	0	120
19	1000-1045	18.7	~45 (6)	520	8	200
				580	10	200
				580	6	160
				580	6	160

continued ...

Table 17, Continued.

Date June	Time MST	Dist. from Stack, km	Background O_3, ppb (SO_2, ppb)[+]	Altitude m msl	Plume - background O_3, ppb[a]	Plume - background SO_2 ppb[a]
				580	6	200
				580	14	200
19	1305-1405	23.9	40-45 (2)	945	0	70
				975	0	40
				945	0	40
				915	8	80
				880	6	60
				850	6	60
				820	< 5	40
				790	8	40
20	1007-1123	31.6	∿50 (0.1)	820	Plume boundaries vary indistinct	
				850		
				760	10	80
20	1415-1517	28.2	∿50 (4)	760	12	60
				820	< 5	40
				700	0	40
				760	0	40
				790	0	20

continued ...

Table 17. Concluded.

Date June	Time LST	Dist. from Stack, km	Background O_3, ppb (SO_2, ppb)+	Altitude m msl	Plume - back-* ground O_3, ppb	Plume - back-* ground SO_2. ppb
22	1930-2025	24.6	~40 (2)	1250	0	60
				1280	0	40
				1190	0	40
				1220	-4	60
23	1354-1454	20.2	O_3 analyser down during this flight			
26	1057 1202	32.5	Plume was very diffuse. The O_3 concentration did not seem to change during passes through the plume			

[a]Maximum departures from background

+Filter pack results

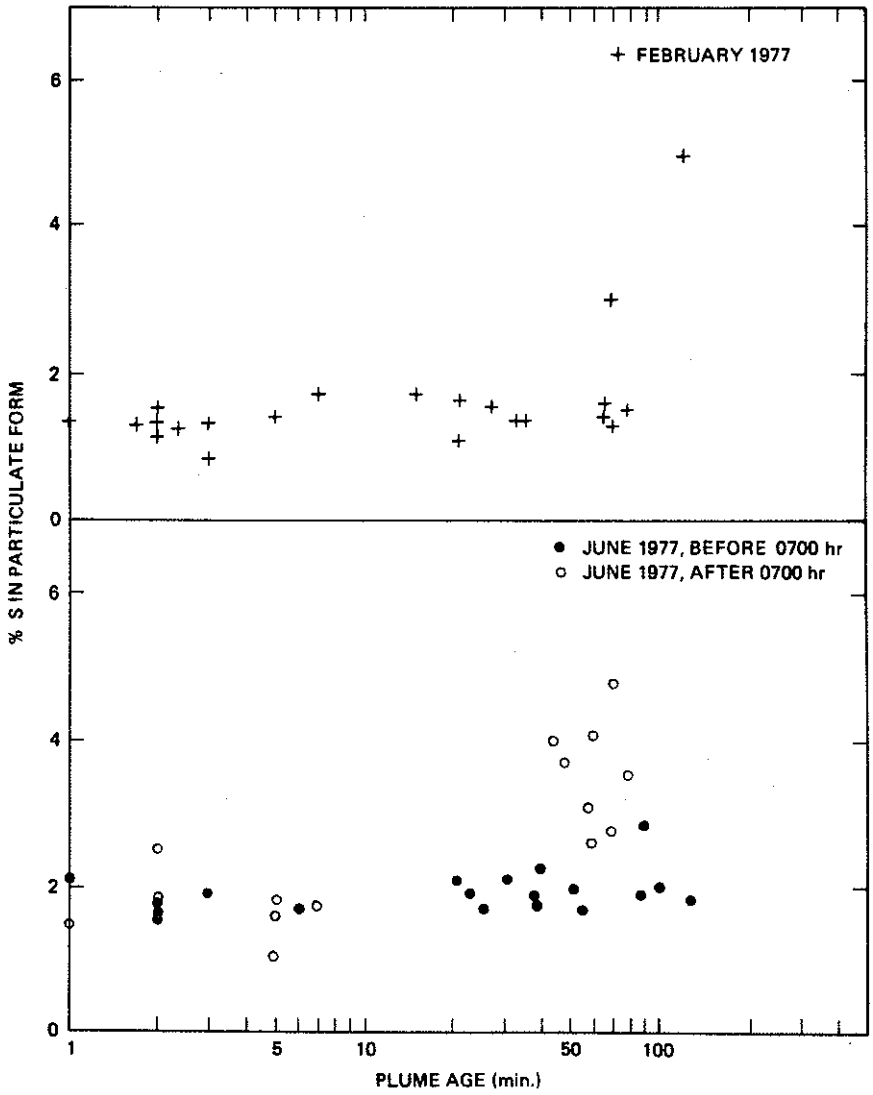

Figure 80. Percentage of S in particulate form as a function of plume age.

For comparison, data obtained during the February 1977 study are also shown. It can be seen that in June, the plume contained a slightly higher percentage of particulate sulphate than in February, about 2% more compared to 1.3%. Both in the February and the early morning June runs the fraction of total sulphate in particulate form remained fairly constant with downwind distance for at least the first two hours of plume age. However, after 0700 a definite increase was observed that reached values of about 3% or more within an hour of emission.

The percentage of particulate sulphate that was sulphuric acid is plotted as a function of plume age in Figure 81 (again, the February 1977 results are shown for comparison). It must be pointed out again that the June sulphuric acid data are thought to be of a rather low accuracy, but Figure 81 does suggest a significant difference between the February and June results. In February the percentage of sulphuric acid in the particulates remains approximately constant and fairly high, whereas in June there is neutralization of the acid downwind of the stack in many cases. This neutralization may be due to reactions with ambient NH_3, a project of biological processes.

It can be seen from Tables 13 and 14 that the concentration of the potential catalysts for SO_2 oxidation via heterogeneous processes--V, Mn, and Fe (Foster 1969; Freiberg 1974; Newman et al. 1975; Barrie and Georgii 1976) is appreciable. Expressed as milligrams of metal per gram of SO_2 in the plume, average values for V, Mn, and Fe are 1.5, 0.069, and 2.7. (To get these numbers, the results obtained on 21 June, 1530 to 1645 were disregarded, because the SO_2 concentration is thought to be in error.) It is interesting to note that, where a comparison of particulate matter compositions is possible, the results of this study seem to be in agreement with an analysis of some fly ash samples collected at the plant in November and December 1975 (SNC Tottrup Services Ltd. 1976). Thus, considering only those substances in Table 12 for which the concentration was significantly above the blank value and using Al as a reference, our

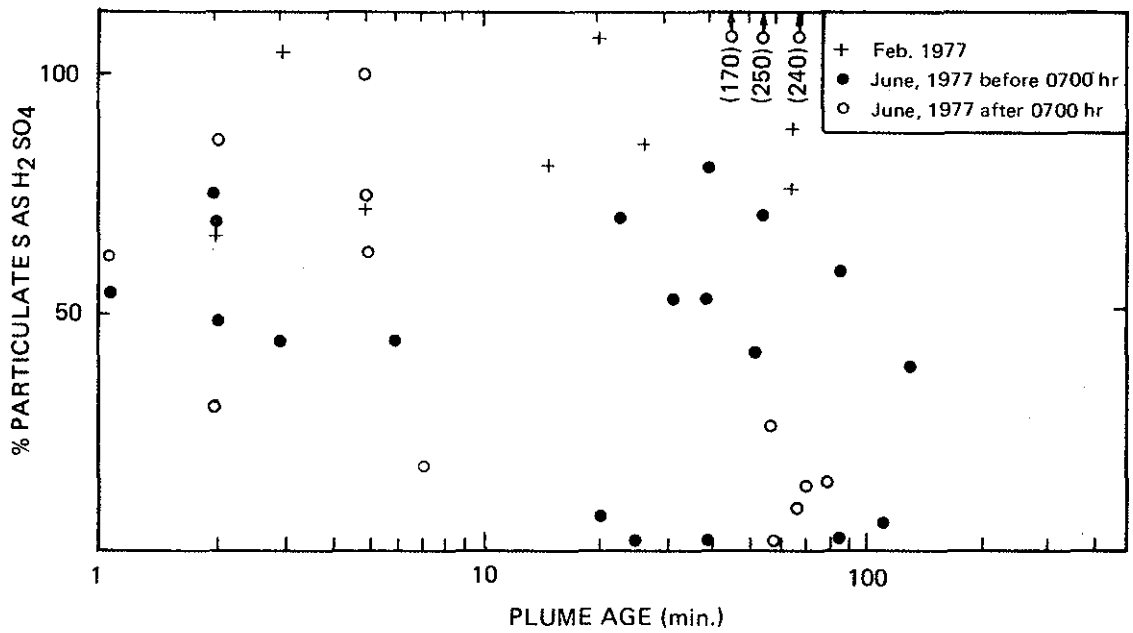

Figure 81. Percentage of particulate S as H_2SO_4 as a function of plume age.

study gives the following average values for the weight of metal in particulates divided by weight of Al: Ti, 0.14; Mn, 0.012, V, 0.28; Fe, 0.42; As, 0.0016 (two values only); Co, 0.002 (one value only). Using different methods of analysis, SNC Tottrup Services obtained the following values (average for three samples): Ti, 0.15; Mn, 0.0078; V, 0.22; Fe, 0.40; As, 7×10^{-5}; Co, 0.0016. With the exception of As the two sets of values are in reasonable agreement.

The Andersen impactor results of Tables 14 to 16 must be regarded with caution, because the sampling arrangement was not optimum for particle sizing work. The impactor did not project directly into the plume, but was connected to the exterior of the helicopter by a 2 m long line, on the walls of which some of the larger particles may have been removed by impaction. Also, the collection medium on the impactor stages was Whatman 541 filter paper rather than some of the sticky surfaces that have been recommended although some attempt was made to correct for particle bounce-off errors when calculating size distribution (J. Puttock, personal communication). However, the results do indicate that most of the potentially catalytic Mn and V occur in particles in a size range that will remain airborne for long times after emission (for example, a unit density sphere having a diameter of 3 μm has a sedimentation velocity of only 1 $m \cdot h^{-1}$), and hence should be available for reaction with the plume SO_2. This conclusion may not apply to Fe, however, because past work on particles emitted from coal- and oil-fired power plants has shown Fe to have a somewhat different size distribution than Mn and V (Davidson et al. 1974; Gladney et al. 1976; Shen et al. 1977). Some of the Fe may occur in particles large enough to settle out from the plume within relatively short periods after emission (Gladney et al. 1976), but the fraction of the emitted Fe in particles having appreciable Stokesian settling velocities is not known. The fact that the ratio of Fe to Al in fly ash samples collected within the plant is similar to that in plume particulate samples (see above) suggests that the Fe may be associated with the same particles as is the Al, and may therefore also be in a size range which can remain airborne for a long time. Although the size

distribution of sulphates is subject to uncertainty because of possible sample contamination (Sec. 6.2), the data in Tables 14 and 15 indicate that almost all of the S emitted in particulate form should stay airborne for long periods. For example, more than 60% of the S is found in particles having aerodynamic diameters of less than 1.5 μm, and more than 80% in particles less than 6 μm in diameter. This is consistent with the findings of other workers (Davidson et al. 1974; Shen et al. 1977), who have also found S to be concentrated in the smaller particles in coal- and oil-fired power plant emissions.

It can be seen from Table 11 that there is a difference between the early morning oxidation rates and those obtained later in the day. Thus, for the flights carried out prior to 0700 oxidation rates are very low, most of the observed values being well below $0.5\%\cdot h^{-1}$. The occasional negative value occurs, probably due to random sampling and analysis errors, or problems in locating the plume during sampling (i.e., different parts of the plume may have been sampled at different downwind distances). However, later in the day, the oxidation rate seems to increase to values greater than $1\%\cdot h^{-1}$, typically, about 2 to $3\%\cdot h^{-1}$.

The results obtained in the present work cast some light on the question of which mechanism is of importance for converting SO_2 to sulphates in power plant plumes. Some authors have proposed that heterogeneous SO_2 oxidation on particulate surfaces or in aerosols can explain the past experimental results (Foster 1969; Newman et al. 1975; Freiberg 1976; Forrest and Newman 1977). Others have suggested that conversion by gas-phase reactions involving photochemistry may be important (Davis et al. 1974; Husar et al. 1978; Gillani et al. 1978). Our results, though not conclusive, tend to favour the latter mechanism, for the following reasons.

1. Only heterogeneous conversion processes could have contributed to SO_2 oxidation during the February and early morning June experiments. Gas-phase conversions of SO_2 in the atmosphere involves photochemical

reaction rates (see Sec. 7 and also Bottenheim and Strausz 1977). Furthermore, the particulate loading of the plume is fairly high, and there should be several metals (such as V, Mn, and Fe) in the airborne particulates capable of acting as catalysts for SO_2 conversion (see discussion above of fluoropore filter and Andersen impactor results), so there was certainly a potential for heterogeneous oxidation reactions. Also, calculations based on Freiberg's model for the iron-catalysed oxidation of SO_2 in aerosols (Frieberg 1975; Lusis and Phillips 1977) indicated that oxidation rates by this mechanism should have been appreciable for some of the days in February (see Fanaki et al. 1979). In spite of these facts, the experimentally determined conversion rates during the February and early morning June runs were near zero.

2. There are some other pieces of evidence that argue against heterogeneous processes. If SO_2 were being catalytically oxidized in liquid films surrounding particles or droplets, then the oxidation rate would be expected to increase with increasing ambient relative humidity and solution pH and decreasing temperature (Junge and Ryan 1958; Foster 1969; Freiberg 1974). Although the ranges of temperature and relative humidity during the February and June studies were -13 to 23° and 40 to 93% respectively, no clear trends in oxidation rate are discernible in the data (Figures 82 and 83). Figure 84 shows a plot of average conversion rate versus average percent of S as H_2SO_4 in the plume particulate matter, for runs where acceptable H_2SO_4 data were available. If we assume that the percent of S as H_2SO_4 is an indication of the aerosol acidity, then again

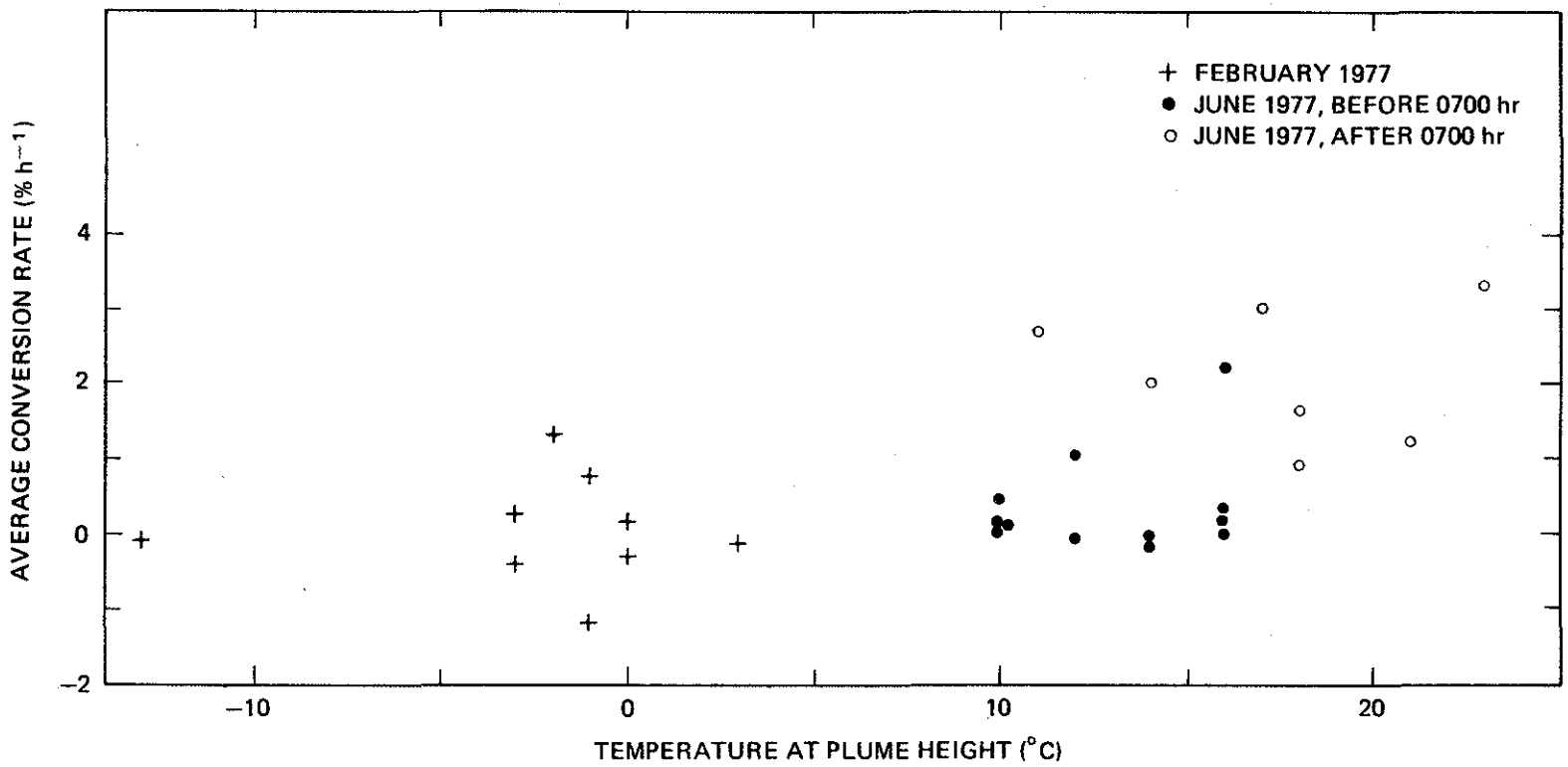

Figure 82. Conversion rate as a function of temperature at plume height.

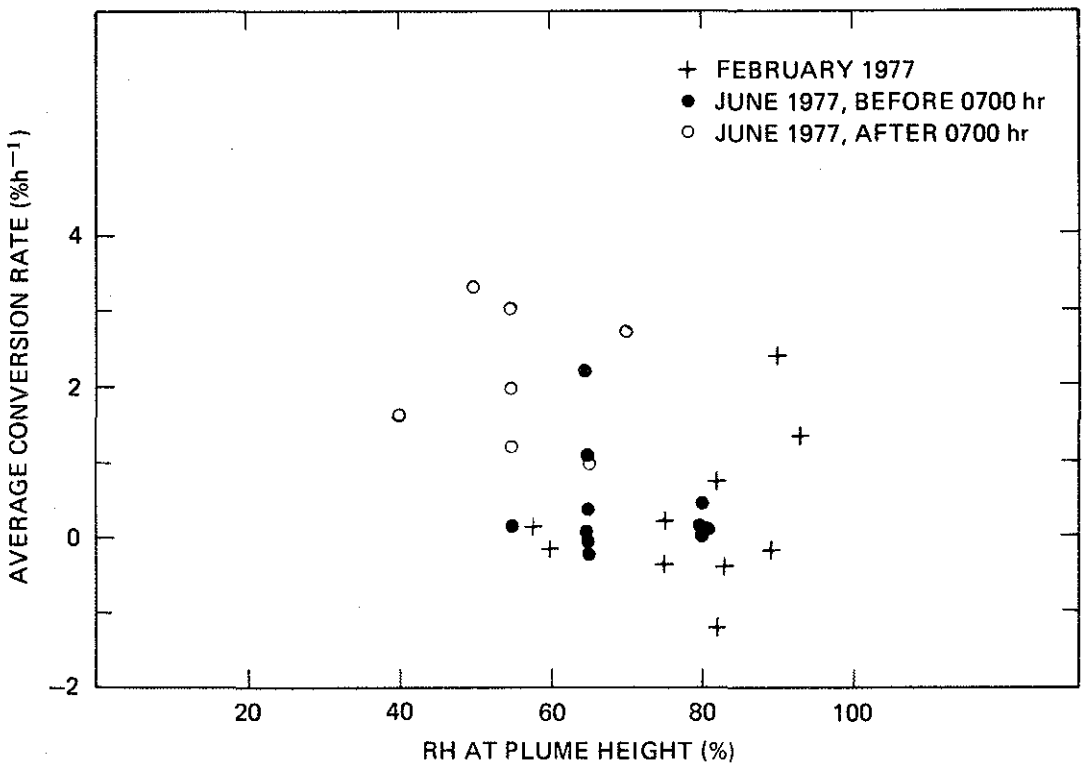

Figure 83. Conversion rate as a function of relative humidity at plume height.

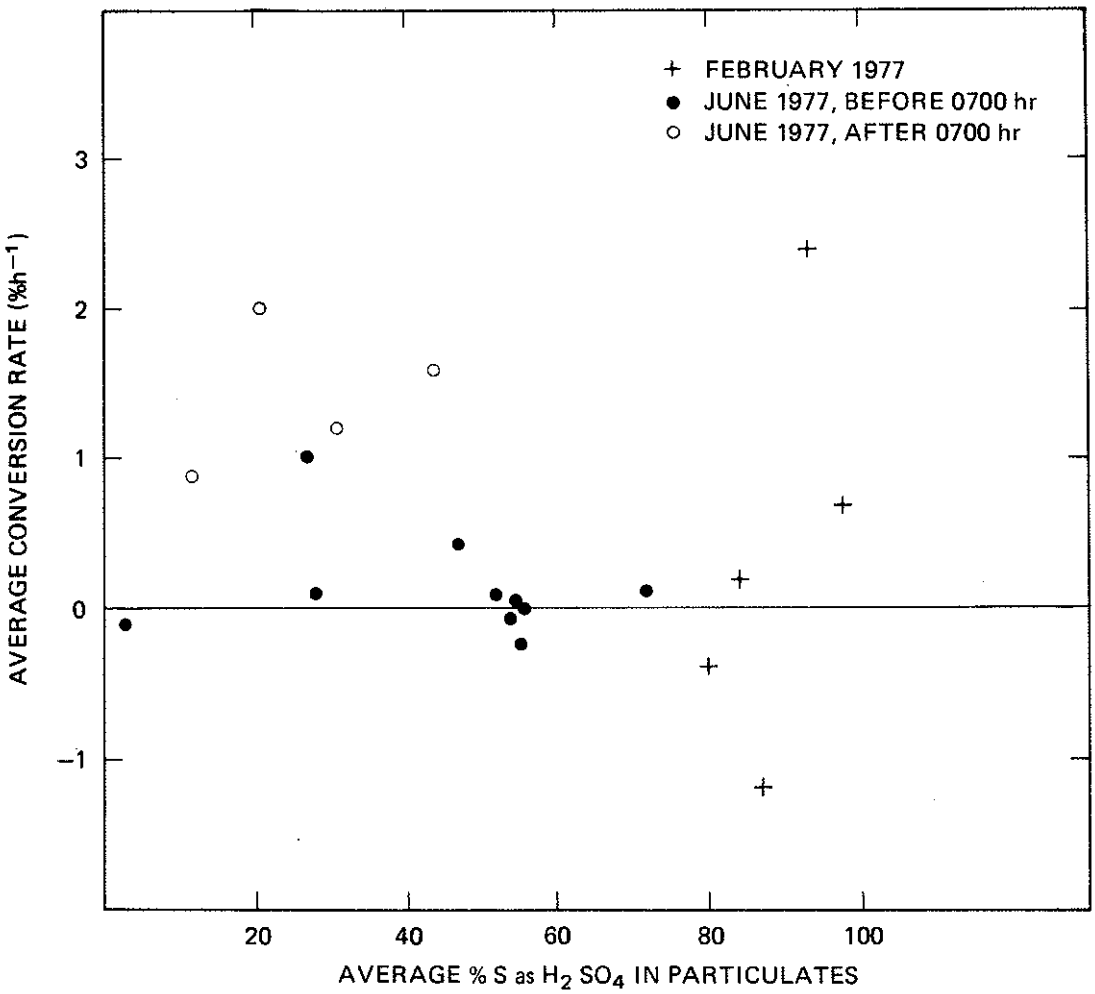

Figure 84. Conversion rate as a function of percent of S as H_2SO_4 in the particulate matter.

within the experiment scatter, there is no evidence for an increase of conversion rate with decrease in H_2SO_4 concentration (increase in aerosol pH) that might be expected from a heterogeneous mechanism.

3. On the other hand, SO_2 conversion rates later in the morning and during the afternoon in June were significantly greater than $1\%\cdot h^{-1}$. Simultaneous measurements of spectral radiance and irradiance (see Sec. 7) indicated that there is sufficient radiation available in the oil sands region to activate NO_2 and SO_2 photochemical processes. Indeed, the O_3 excess observed on several occasions in the plume is evidence of photochemical activity (c.f. Davis et al. 1974; Gillani et al 1978). A possible explanation for the increased SO_2 oxidaton rate as well as the O_3 excess is as follows: there are undoubtedly some low-level hydrocarbon emissions originating from various parts of the GCOS oil extraction and upgrading plant, while an appreciable concentration of nitrogen oxides (roughtly one tenth that of SO_2) is expected in the power plant plume. The intense atmospheric tubulence that occurs later in the day during June mixes these low-level hydrocarbon and plume nitrogen oxide emissions. In the presence of sufficient solar radiation, photochemical reactions occur in this mixture, leading to the formation of O_3 and free radicals capable of oxidizing SO_2 to sulphates (Bottenheim adn Strausz 1977).

This brings us to an important point, namely, that during all of the runs when appreciable SO_2 oxidation rates were observed, part of the plume was being diffused down to ground level within a few kilometres of the stack. This could introduce an error in the oxidation rates measured by the present method, which assumes that the ratio of particulate-to-gaseous sulphate within the plume is changing due to SO_2 oxidation only. However, particulate matter and SO_2 are expected to be removed by dry deposition at the ground

at different rates (Garland 1978), and thus the ratio of particulate-to-gaseous sulphur could change with downwind distance merely as the result of dry deposition. It is important to estimate the magnitude of this error.

During their studies of the Labadie power plant plume, Gillani et al. (1978) found the influence of dry deposition on the particulates S fraction in the plume to be at times comparable in magnitude to that of SO_2 oxidation. However, their observations were made after several hours of plume travel, whereas most of our late morning and afternoon sampling was done within 30 km of the chimney. This, and other differences between the two studies (e.g., the source strength and stack height, vegetation cover downwind of the chimney) makes it difficult to extrapolate their observations to our work. Therefore, an attempt was made to estimate the magnitude of the error introduced into the apparent oxidation rate by dry deposition using two mathematical models, together with field observations of plume rise and meteorological variables. One of these was a well-mixed Lagrangian box model, while the other was a Gaussian plume model, modified to account for multiple reflections in the mixed layer. Calculation details are given in Section 6.3. To accentuate the effects of dry deposition, rather extreme values of the deposition velocity were employed: that for SO_2 was assumed to be near the upper limit of the available experimental measurements (Garland 1978) at a value of 2 $cm \cdot s^{-1}$, while at the same time it was assumed that sulphate particles were not removed by dry deposition at all (deposition velocity = 0).

The results of these calculations showed that for the conditions of our field study, the rate of change of the particulate-to-total S ratio in the plume due to dry deposition should be small. The box model gave a value of 0.15%$\cdot h^{-1}$, while the Gaussian plume model gave values less than 0.25%$\cdot h^{-1}$. These values are small compared to the measured oxidation rates of 1 to 3.3%$\cdot h^{-1}$. It is interesting to note that the Gaussian model also predicted downwind SO_2 concentrations and plume widths in reasonable agreement with the observed values, which gives us some assurance that the

predicted dry deposition rates using this model are realistic. We therefore feel that the error introduced into our oxidation rate measurements by dry deposition during sampling flights when the plume was impinging on the ground was small, and would not change the conclusions of our field study in any substantial way. These conclusions may be summarized as follows.

1. During the winter months, as well as the early and late hours of summer days, SO_2 oxidation rates are low, less than $0.5\%\cdot h^{-1}$. Although there are several potentially catalytic metals present in the particulate matter emitted from the GCOS power plant, over the range of temperatures (-13 to 23°C) and relative humidities (40 to 93%) obtained during the February and June field studies there was no evidence for a heterogeneous SO_2 mechanism.
2. For most of the daylight hours during summer, representative SO_2 oxidation rate are in the range 2 to $3\%\cdot h^{-1}$ These elevated rates are probably due to homogeneous gas-phase reactions involving SO_2 and various free radical species. The free radicals are produced as a result of photochemical reactions between power plant NO_x emissions and hydrocarbons from the oil sands processing operations.
3. One of the objectives of the present work was to provide representative SO_2 oxidation rate values for mathematical models of the oil sands area. In view of the results obtained during the June study, it seems clear that any air quality model for the oil sands region should include a photochemistry sub-model capable of handling such phenomena as SO_2 oxidation and O_3 formation. Attention should also be directed towards a proper emissions inventory for the photochemical smog precursors nitrogen oxides and hydrocarbons.

In conclusion, it must be admitted that at present it is not known to what extent our results apply to chimneys other than that of the GCOS power plant. The SO_2 oxidation rate could depend on such parameters as the physical and chemical characteristics of the emitted particulates, the level of other gases (such as NO_x) present in the plume, and the height of the chimney (which would determine how efficiently low level hydrocarbon emissions are mixed with plume NO_x, for example). Further work with other stacks in the area is certainly warranted.

6.3 CALCULATION DETAILS FOR ESTIMATES OF THE CHANGE IN THE PARTICULATE-TO-GASEOUS SULPHUR RATIO IN THE PLUME DUE TO DRY DEPOSITION

In the calculations below,

Cp = concentration of particulate sulphur in the plume

Cg = concentration of gaseous sulphur in the plume

C_t = Cp + Cg

V = deposition velocity of SO_2

U = wind speed

h = height of the mixing layer

x.v= downwind, crosswind distance, resp.

To emphasize the effects due to dry deposition, changes in the particulate-to-total sulphur ratio in the plume due to chemical reactions will be ignored. It will also be assumed that only SO_2 is removed by dry deposition (i.e., the deposition velocity of particulate sulphates is zero).

The quantity of interest is the average rate of change of particulate-to-gaseous sulphur with plume age, due to dry deposition. A comparison of the calculated value with the measured one will then give some indication of the error introduced by dry deposition in our oxidation rate calculations. Two models will be used for the calculation:

1. The well-mixed, lagrangian box model.

In this model, it is assumed that the sulphate and SO_2 concentrations in a box of air having a volume ($\Delta x \cdot \Delta y \cdot h$) are uniform from the ground to the top of the mixing layer. The box moves downwind with the mean wind speed U.

At any distance downwind of the chimney, a mass balance for SO_2 in the box gives

$$h \frac{d\,Cg}{dt} = -V\,Cg \tag{14}$$

or $$Cg = Cg^{\circ} \exp\left(-\frac{Vt}{n}\right) \tag{15}$$

where superscript ° indicates conditions at t = 0 (i.e., at the chimney). Also, it follows from the assumption that particulates are not removed by dry deposition, or formed by chemical reaction, that

$$\frac{dCp}{dt} = 0 \tag{16}$$

$$Gp = Cp^{\circ} \tag{17}$$

Then $$\frac{d}{dt}\left(\frac{Cp}{Ct}\right) = -\frac{Cp^{\circ}}{C_t^{\,2}} \frac{dc_t}{dt} \tag{18}$$

$$= -\frac{Cp^{\circ}}{(Cp^{\circ} + Cg)^2} \frac{dCg}{dt} \tag{19}$$

Substituting from Equations (14) and (15), and noting that for the travel times of interest here Cp is only a few percent of Cg and can therefore be neglected in the sum of Equation (19), one obtains

$$\frac{d}{dt}\left(\frac{Cp}{C_t}\right) = \frac{Cp}{C_t^{\circ}} \frac{v}{h} \exp\left(\frac{vt}{h}\right) \tag{20}$$

The average rate of change of the particulate-to-total sulphur ratio over the first t hours after emission can be obtained by integration of Equation (20), to give

$$\frac{1}{t}\left[\left(\frac{Cp}{Ct}\right) - \frac{C_p^\circ}{C_t^\circ}\right] = \frac{1}{t}\left(\frac{C_p^\circ}{C_t^\circ}\right)\left[\exp\left(\frac{Vt}{h}\right) - 1\right] \qquad (21)$$

$$\frac{C_p^\circ}{C_t^\circ}\left(\frac{v}{h}\right) \qquad (22)$$

Equation (22) is a good approximation for the conditions of the present experiments.

Reference to the experimental data from the June afternoon helicopter flights, as well as the meteorological soundings, shows representative values for the variables on the right hand side of Equation (22) to be:

$$\frac{Cp^\circ}{C_t^\circ} = 0.02$$

$$h = 1000 \text{ m}$$

while $v = 2 \text{ cm } S^{-1}$.

Substituting these values into Equation (22) gives an estimated rate of change of (Cp/Ct) due to dry deposition of $0.15\% \ h^{-1}$.

2. Gaussian plume model

The approach taken here was to predict the ground-level SO_2 concentration field using measured plume rise and mixing height values, the multiple-reflection equation of Bierly and Hewson (1962), and dispersion coefficient data of Briggs (see Gifford 1976). The predicted ground-level concentrations were then combined with an assumed deposition velocity of 2 $cm \cdot S^{-1}$ to estimate the average ground removal rate from the stack to the farthest downwind point where plume sampling was carried out. The dispersion calculations were carried out by R.V. Portelli.

Two meteorological conditions were considered, depending on whether the direction of plume travel was mainly along the Athabasca River valley, or over the ridge and plateau to the east of the stack. The abrupt increase in ground level for the latter case was assumed to cause a decrease of 100 m in the effective stack height. In both cases, a Pasquill-Gifford stability class C was used to calculate dispersion coefficients. Four experimental runs in June fell into the first class, while three belonged to the second. Some of the relevant observations for these runs are summarized in Table 18.

Therefore calculations were carried out with the two sets of input variables shown as follows:

	Plume along river valley	Plume over ridge and plateau
SO_2 emission (g S^{-1})	2100	2100
plume height (m)	350	150
wind (m s^{-1})	6.3	8.6
mixing layer (m)	1000	1000
downwind distance considered	chimney to 25 km	

The ground-level concentration profiles generated by these models are shown in Figure 85. Then the total SO_2 removal rate at the ground, from the chimney to 25 km downwind, can be found from

$$dQ_s = -v\Sigma_i A_i C_i \qquad (23)$$

where Q_s is the flow of SO_2 across a plane perpendicular to the wind direction, and A_i is the total downwind area affected by average concentration C_i. If Qp is the flow rate of particulate sulphur,

Table 18. Observations made during late morning and afternoon runs of June 1977.

Date June	Time (LST)	Plume ht[a] (m)	Mixing layer[b] (m)	Wind[b] Speed (ms^{-1})	Dir[c]	Downwind Measurements		
						Dist. (km)	Max SO_2 ($\mu g\ m^{-3}$)	Plume width (km)
18	1000-1215	∿350	1030	4.5	S	19	∿125	∿4
19	1300-1515	∿350	1000	5.8	NE	19	∿125	∿4
20	1000-1230	∿350	730	6.8	NE	32	-[e]	-[e]
20	1400-1630	∿350	∿1000	7.8	NE	28	∿100	∿3
22	1900-2100	∿150[d]	>1500	7.0	E	25	∿100	∿3
23	1340-1600	∿90[d]	>1500	7.5	E	20	-[e]	-[e]
26	1020-1300	∿640[d]	730	11.3	E	33	-[e]	-[e]

[a] Measured by helicopter.

[b] Minisonde data.

[c] Direction of plume travel.

[d] 100 m have been subtracted from the measured height above the base of the stack, to account for the presence of a ridge and plateau for this plume direction.

[e] Plume too diffuse to get reasonable estimate.

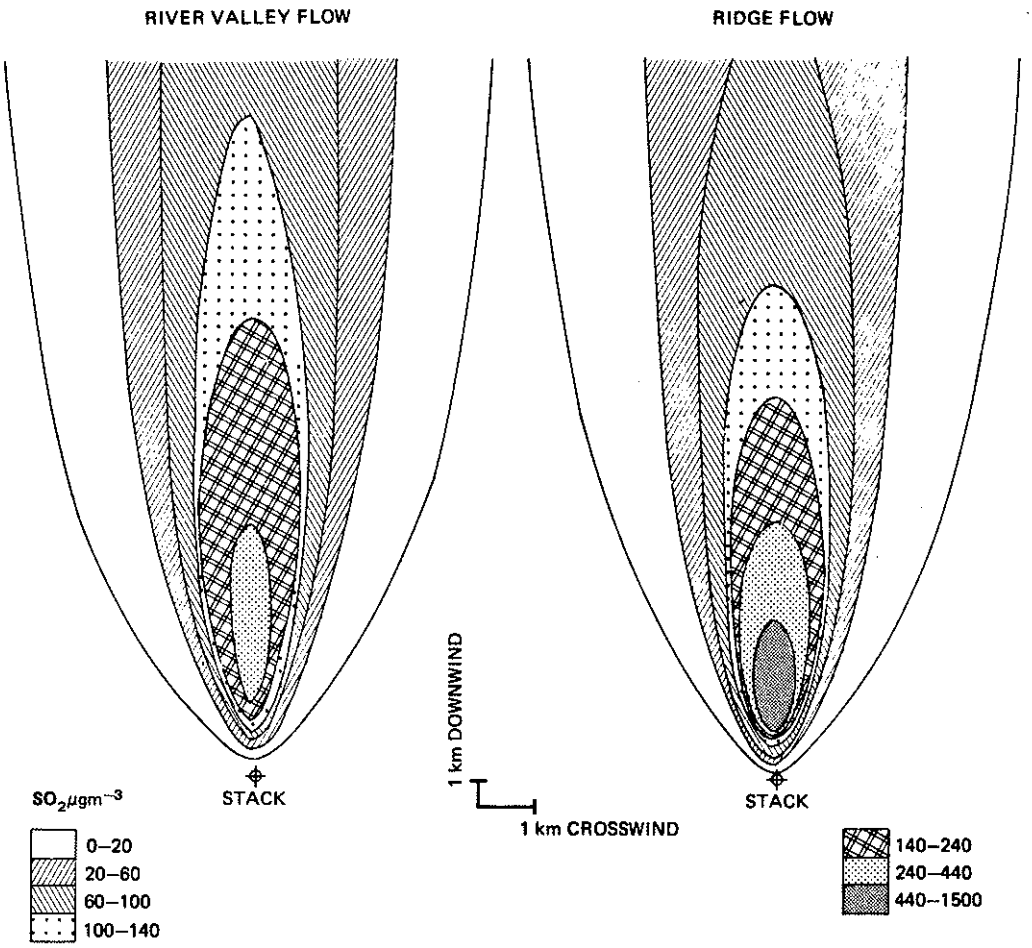

Figure 85. Ground-level concentration profiles generated by the Gaussian plume model for two meteorological conditions.

then the average rate of change of the particulate-to-total sulphur ratio due to dry deposition over the first 25 km of plume travel is

$$\left[\frac{d}{dt}\left(\frac{C_p}{C_t}\right)\right]_{Ave} = \left[\frac{d}{dt}\left(\frac{Q_p}{Q_t}\right)\right]_{Ave} \tag{24}$$

$$\sim \frac{Q_p^{\circ}}{(Q^{\circ}_s)^2} \frac{v\Sigma_i A_i C_i}{\Delta X/U} \tag{25}$$

with (Qp°/Qs°) of 0.02 and a deposition velocity of 2 cm s^{-1}, Equation (25) and the data on Figure 85 give the average rate of change of the particulate-to-total sulphur ratio due to dry deposition as 0.15 and 0.24% h^{-1} for the river valley and ridge flow cases respectively. It is interesting to note that the predicted downwind concentrations and plume widths agree rather well with the observed values of about 100 $\mu g \cdot m^{-3}$ and 3 to 4 km respectively.

7. MEASUREMENTS OF SOLAR SPECTRAL ZENITH RADIANCE AND SPECTRAL IRRADIANCE

The intensity of solar ultraviolet (UV) radiation (>290 nm) plays an important role in the formation of photochemical air pollution. In photochemical smogs, for example, UV radiation is necessary in order to initiate a series of chain reactions that ultimately leads to high ozone or other oxidant concentrations. The accumulation of these pollutants in conjunction with others initiates another chain of events leading to the formation of aerosols. This combination of gaseous pollutants and aerosols can cause appreciable absorption and scattering of incident short-wave (UV and visible) solar radiation. Photochemical smogs play perhaps a less important role in global long-term energy budgets than the well-known cases of increasing carbon dioxide and high-level aerosol concentrations. However, their local effects are no less detrimental. Their modification of the ground level radiative flux may have an effect on local meteorology (e.g., maximum surface temperature and stability of the atmosphere) or on biological systems (e.g., production of Vitamin D, which depends on UV solar radiation). Not only photochemical smogs, but also the oxidation of sulphur dioxide in urban, power plant, or industrial plumes is dependent to some degree on UV and visible solar radiation; however, the strength of this dependence has not yet been clarified.

In order to model correctly the photochemical air pollution, the solar intensity spectrum (solar radiance) in the UV and visible region is essential. Many calculations have been made on model atmospheres, but experimental measurements are few. Many detailed measurements of UV solar radiation have been made at Davos, Switzerland, generally under clear sky and unpolluted conditions (Bener 1970). In the United States, data are now available for some urban centres. For example, Peterson and Flowers (1974) have found that the average depletion of incident hemispheric UV solar radiation (diffuse and direct, 300 to 385 nm) by smog was 14% in Los Angeles and about 7% in St. Louis. During poor visibility days, the reduction in UV

intensity varied between 25 and 35% for Los Angeles. The effect on global radiation integrated from 300 to 3000 nm was substantially less. This is mainly because Rayleigh (molecular) and Mie (aerosol) scattering and ozone absorption of solar energy are more effective at UV than at longer wavelengths. Peterson also showed that cirrus (overcast) clouds can deplete the UV intensity by up to 10%, whereas stratus overcast can cause a decrease up to about 33%; this in turn would have an effect on photochemical air pollution. Recently, Peterson (1976) has published an extensive set of model calculations of actinic solar flux which may be compared with field measurements.

Photochemical model calculations by Peterson and Demerjian (1976) show that a UV variation as small as 10% has a noticeable effect on ambient ozone concentration. Their conclusion was that any attempt to accurately model or forecast the photochemical pollutant distribution should account for spatial variability of UV radiation. Recently, Nieboer et al. (1976) have made model calculations on the effect of latitude on the potential for formation of photochemical smog. They showed that for midsummer and for latitudes 34°N (Los Angeles) to 65°N (Fairbanks, Alaska) the light intensities integrated over the photoactive wavelengths are similar. As a consequence, the potential for photochemical oxidant formation would be similar as well. For the fall, winter, and spring seasons, their calculations show that this potential is greatly curtailed at the northern latitudes due to the decreased UV intensity.

In Canada, photochemical models (incorporating a calculated actinic flux) have been developed by Bottenheim and Strausz (1978). However, if these modelling calculations are to be developed further and used in Canada, then field measurements on the UV solar radiance and irradiance (direct and diffuse) must be made for comparison purposes. With this in mind, as part of AOSERP, measurements of spectral zenith radiance (300 to 510 nm) and spectral irradiance (global and diffuse sky, 300 to 500 nm) were made on 24 to 25 July 1977 north of Fort McMurray, Alberta (56°39' latitude and 111°13' longitude, 333 m asl).

A more detailed discussion of the definitions and interrelationships pertinent to solar radiation measurements has been included in Section 7.4.

7.1 EXPERIMENTAL PROCEDURE

The incoming solar radiation was measured by a spectroradiometer. Its central component was a 20 cm focal length (F 4.2) spectrometer (Jobin-Yvon, Model H20V, concave grating with a groove density of 1200 grooves/mm optimized for 450 nm). The 50 μm input and output slits offered a 0.2 nm bandpass. For all measurements, a depolarizing quartz wedge was inserted ahead of the entrance slit in order to eliminate detection variability due to polarization of the incident light. Also, calibrated ORIEL neutral density filters were inserted just ahead of this wedge in order to reduce light intensities.

For radiance measurements, the input optics consisted of a well-baffled Cassegrain telescope (20.8 cm focal length) that was optically matched to the entrance slit of the spectrometer to yield a rectangular field of view of 0.5 by 8 mrad.

For irradiance measurements, a quartz dome and sintered disk (part of a Fleming UV Sensor Type 524) were mounted on the front of the spectrometer. In this way, incident UV radiation was collected over the sky hemisphere and diffused by the translucent quartz disk. The cosine response of the dome-diffuser combination was within 2% at angles of incidence less than 40° and varied from 2 to 10% for angles of incidence greater than 40°. During diffuse sky irradiance measurements, the direct solar radiation was occluded by a 10 cm disk held at 100 cm from the quartz disk. Light was detected by a EMI-9781R side-window photomultiplier located within a magnetically shielded housing in order to eliminate the effects of the earth's magnetic field. The signal current from the photomultiplier was converted to voltage by means of a precision wirewound 1 MΩ resistor. This signal voltage was measured by a Moseley Model 7560A Logarithmic Converter, which in turn fed the logarithmic voltage output to a Hewlett-Packard Model 7132A strip chart recorder.

The spectrometer was mounted on a heavy-duty telescope mount set up in a horizontal, rather than celestial, orientation. Two gear drives scanned the spectrometer assembly theough the azimuth and elevation of the sky at a rate of 360° in 3.2 min. The wavelength scan was driven by a stepping motor and gear to produce a reversible linear scan of the spectrum from 270 to 510 nm in about 4.5 min.

For both radiance and irradiance calibrations, a 200-W GE quartz iodine lamp served as the standard lamp source. It had been calibrated for irradiance by the National Research Council (NRC) to within $\pm$4%. The irradiance calibration was carried out by directly measuring the light from the standard lamp at a distance of 100 cm from the front of the quartz diffuser disk. Spectral scans from 270 to 510 nm were made. To calibrate for radiance, the standard lamp source and diffuse surface were used. This combination had been also calibrated by NRC to an accuracy of $\pm$4%. The reflecting surface consisted of a 10 cm square piece of bakelite covered with Eastman High Reflectance ($BaSO_4$) white paint. It was placed with its normal at 10 to the incident light, and its surface was 100 cm from the standard lamp. The spectroradiometer then measured the spectral radiance of the central area of this surface. Again spectral scans from 270 to 510 nm were made.

For both cases, these spectral response calibrations were carried out a day before and after the field measurements. The corresponding chart records were electronically digitized and the average of the two calibrations was used to construct the instrument response curve, which was then stored on a cassette tape.

The AOSERP field research station was located in a small clearing of low pine trees. Hence, it was necessary to construct a wooden tower with an observation platform. This was placed on top of one of the residential trailers so that the spectrometer was about 8 m above ground level. With this arrangment, the field of view was obstructed only by trees at elevation angles below 5.7°. Hence for all irradiance measurements reported here, this restriction must be kept in mind.

The procedure for taking solar spectra was to attach an appropriate filter with either the telescope (for Zenith radiance) or the quartz dome (for irradiance) to the front of the spectrometer. Then a spectral scan was made from 270 to 510 nm. In turn, the corresponding chart records were electroncially digitized (1200 points per scan), converted to voltage, and recorded on cassette tapes. Individual experimental solar radiation spectra were then manipulated in matrix form by an electronic calculator and were corrected for instrument response, filter densities, and photomultiplier settings.

7.2 RESULTS AND DISCUSSION

An initial attempt at solar radiation measurements was made during the week of 23 to 27 June 1977. However, no clear sky conditions pervailed. Therefore, an arrangement was made with the Edmonton weather office to inform AES headquarters of future clear sky periods. The first opportunity came in the week of 22 to 26 July; the measurements reported here were made on 24 and 25 July. For both days the sky was almost clear of clouds, and spectral scans of solar radiance and irradiance from 270 to 510 nm were made throughout the day. The corresponding chart records were electronically digitized (1200 points per scan) and corrected, and the resultant spectra were plotted.

Figure 86 and 87 show a sample of plots of spectral solar zenith radiance; Figures 88 to 91 show the spectral solar irradiance. The remainder of the plots are available through the AOSERP management office of Alberta Environment. It should be noted that the ordinate has been multiplied by a factor of 100. The insert on the graphs gives the type of measurement, time of day, date, solar elevation (E), and azimuth (A). The term "G-Rad" refers to global irradiance (direct plus diffuse sky) and "D-Rad" to diffuse sky irradiance.

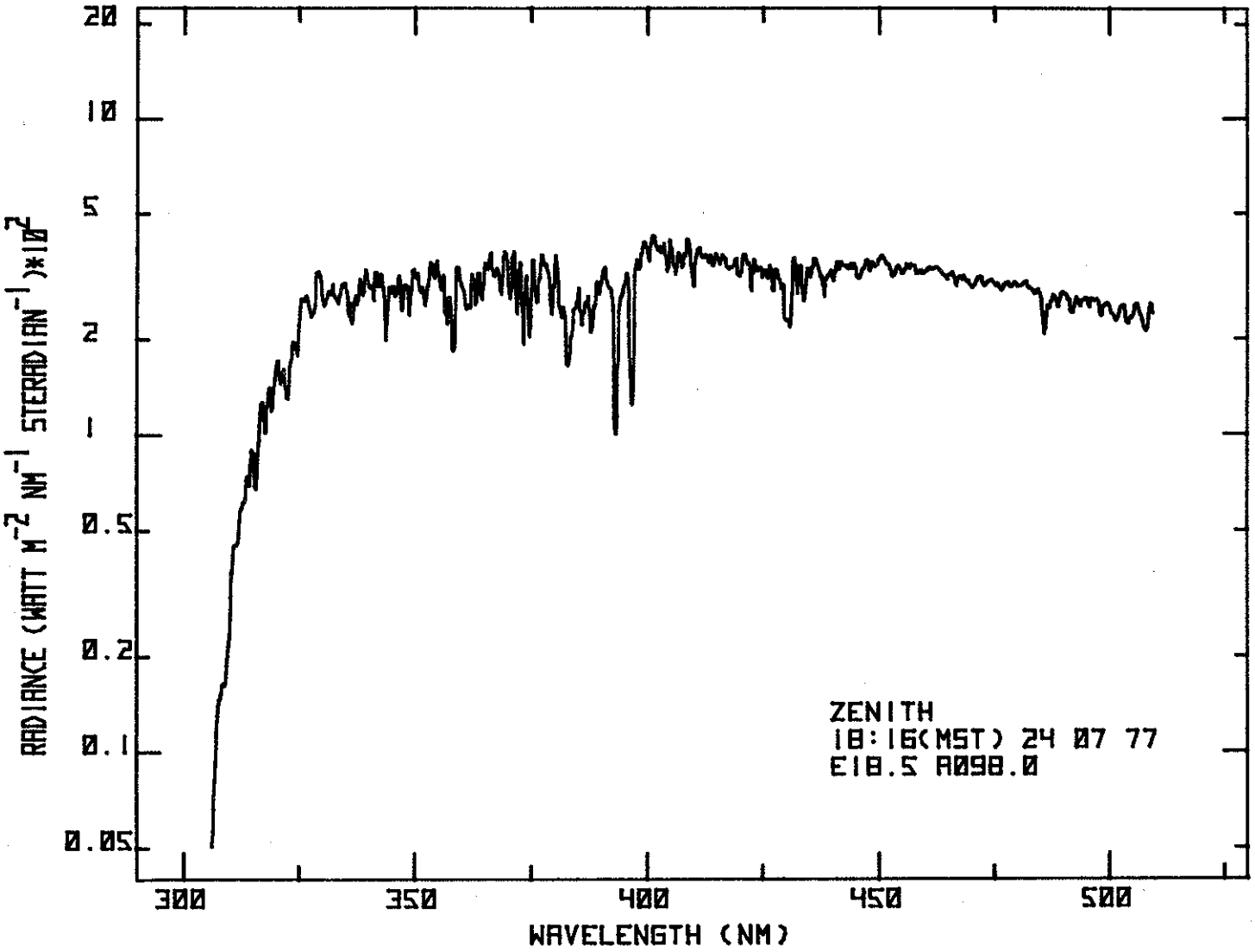

Figure 86. Spectral solar zenith radiance from 300 to 520 nm.

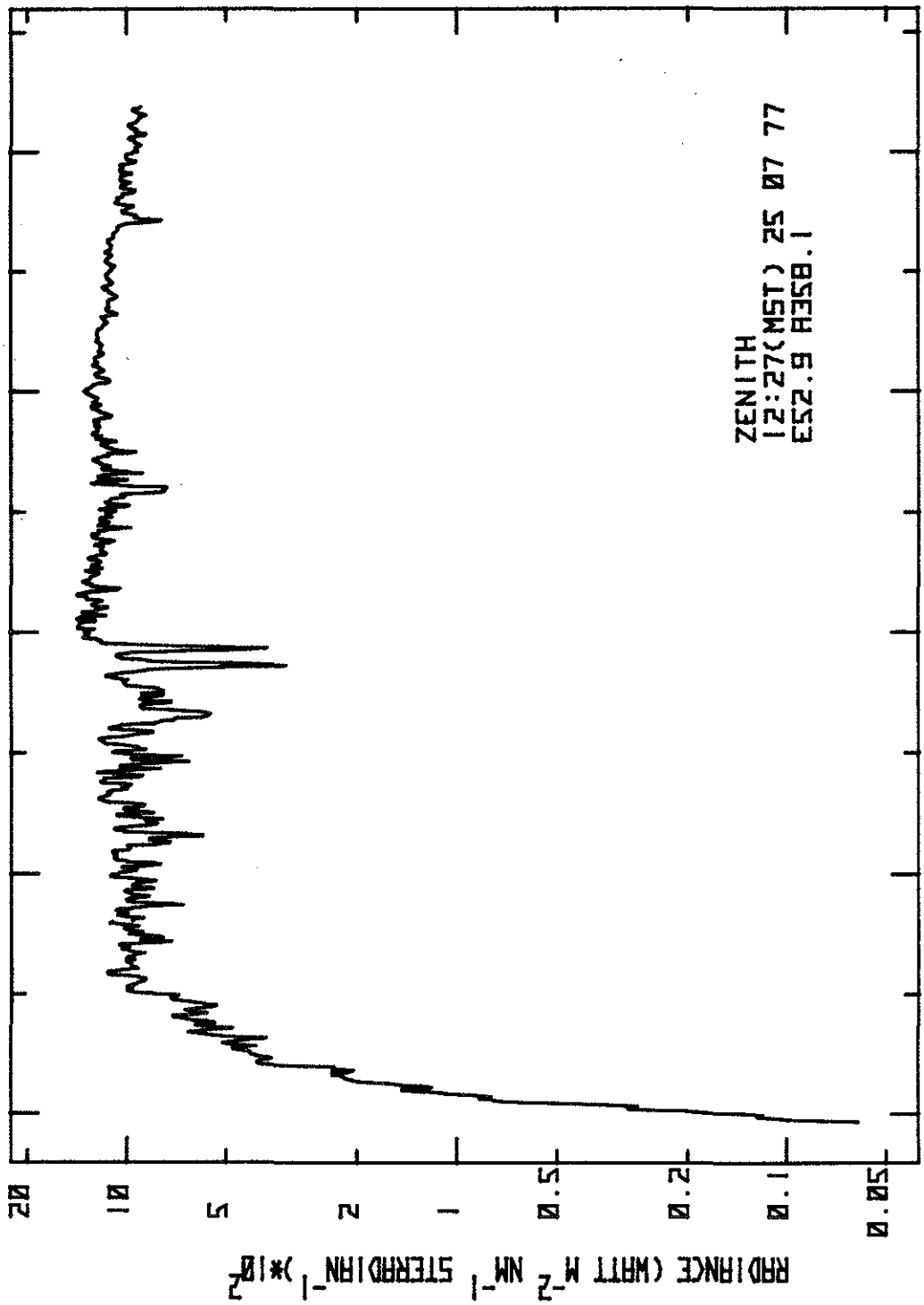

Figure 87. Spectral solar zenith radiance from 300 to 520 nm.

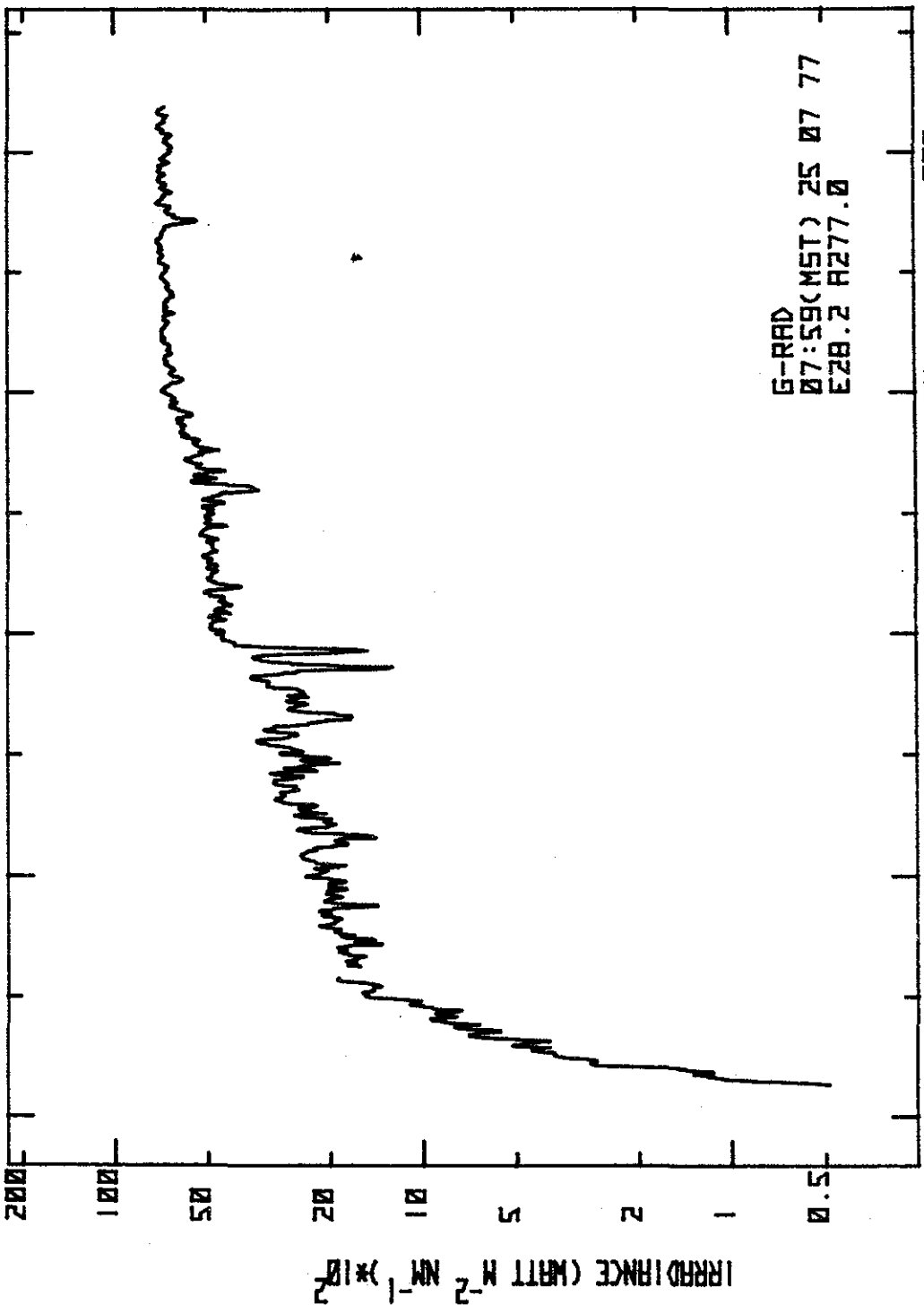

Figure 88. Spectral solar global irradiance from 300 to 520 nm,

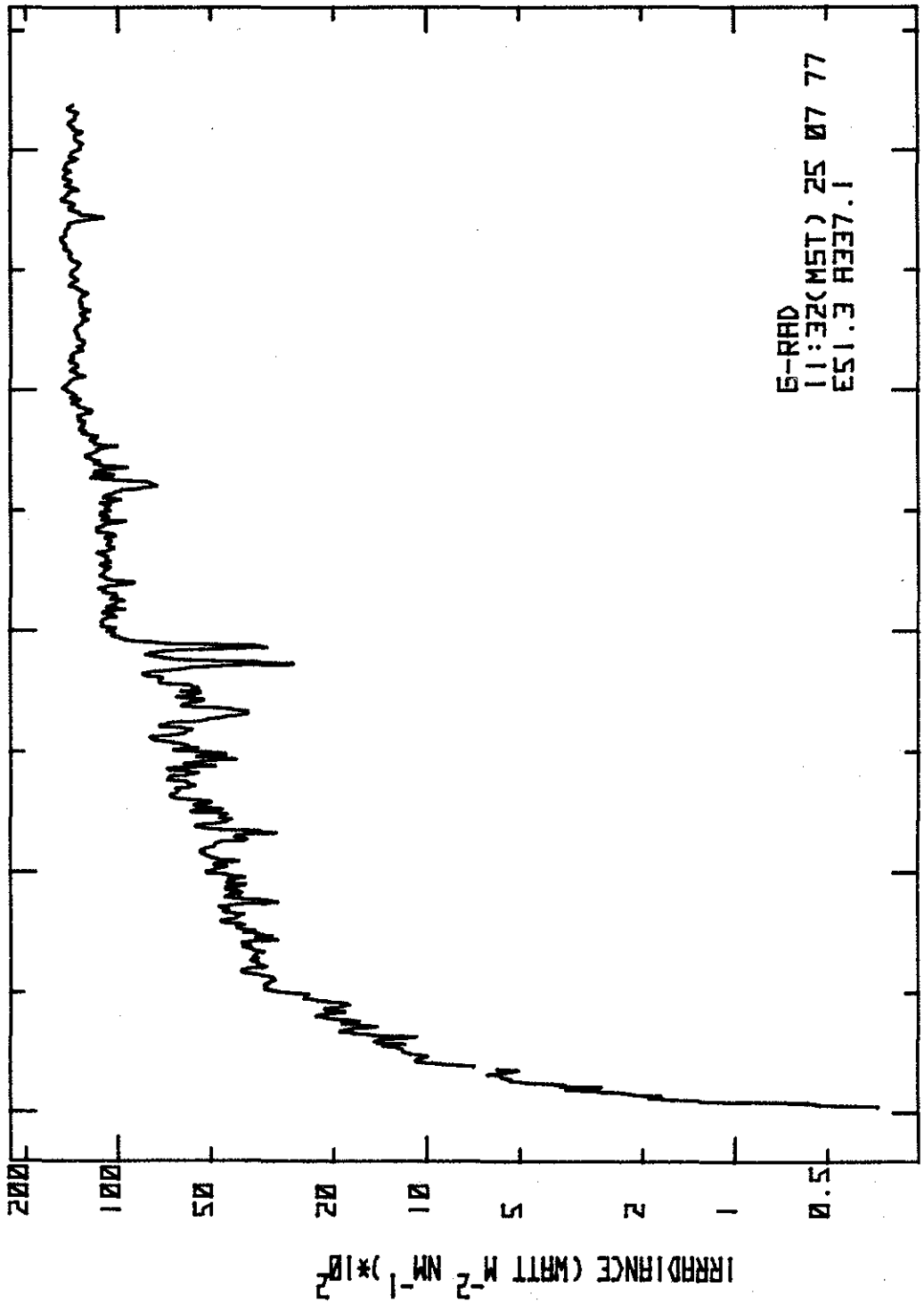

Figure 89. Spectral solar global irradiance from 300 to 520 nm.

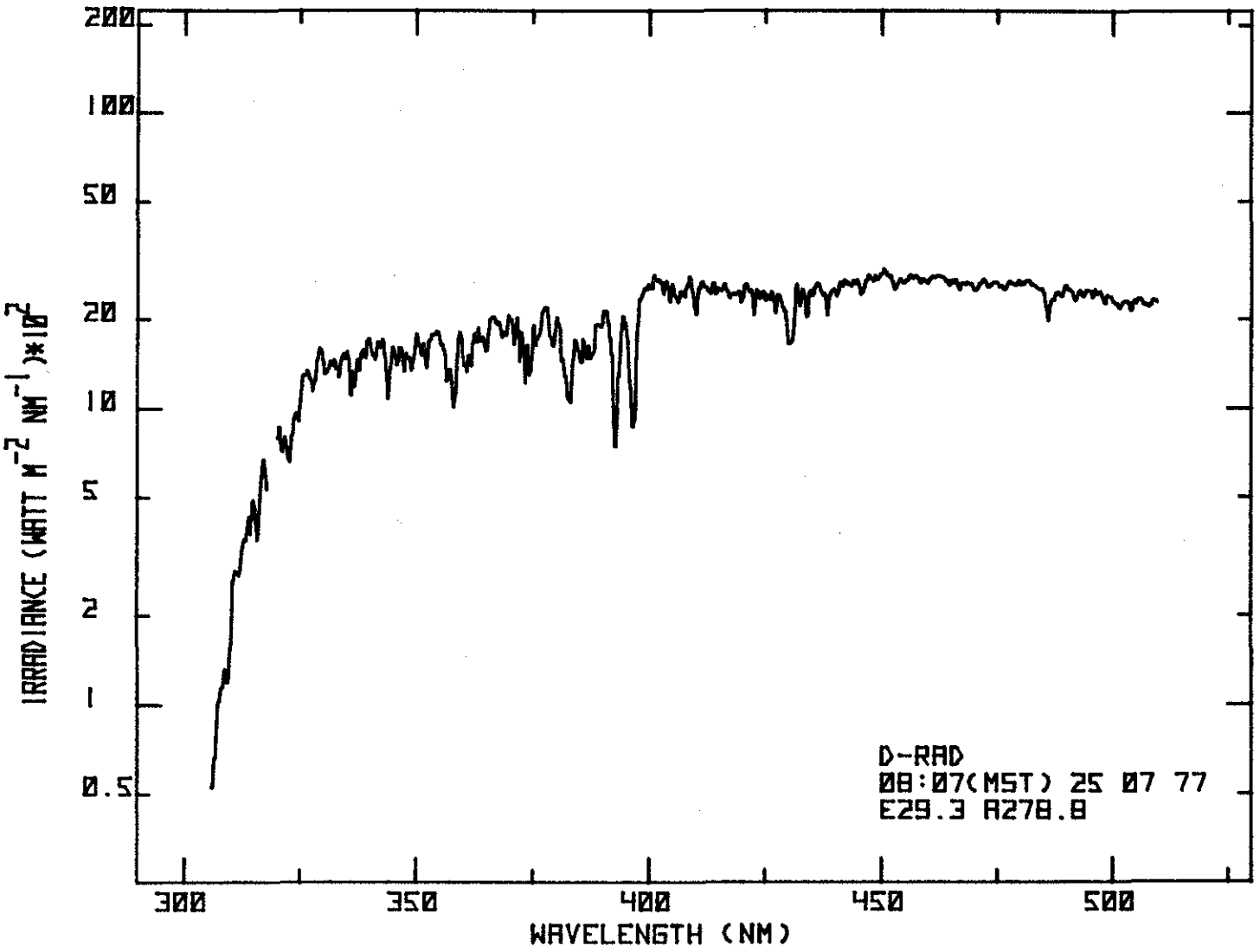

Figure 90. Spectral solar diffuse (sky) irradiance from 300 to 520 nm.

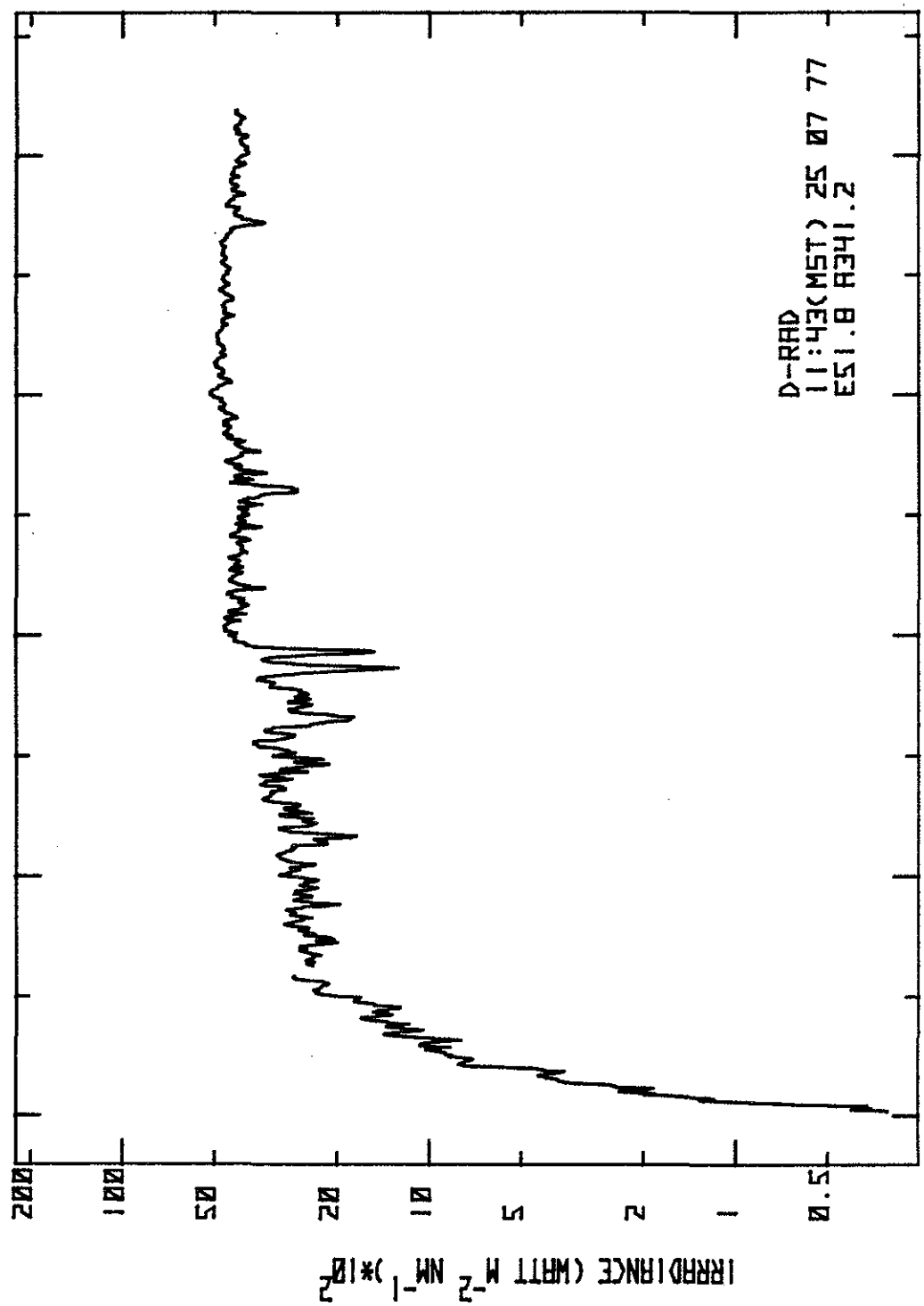

Figure 91. Spectral solar diffuse (sky) irradiance from 300 to 520 nm.

For the measurements, the lower limit of sensitivity appeared to depend on dark current and stray light rejection in the spectrometer itself. Since the spectrum changed by about three orders of magnitude in intensity, slight imperfections in stray light rejection became dominant only below about 300 nm. However, this was not viewed as a serious liability because the stray light was not significantly larger than the dark current itself. In fact, if the instrument had been limited only by dark current, the extension into the UV would have been no more than an additional 5 to 10 nm.

During this particular field study, a serious attempt had been made to keep the overall accuracy of the measurement within $\pm$10%. Unfortunately, an instability and non-linearity problem developed in the logarithmic converter. Even though the amplifier was recalibrated in the laboratory after the field study, this problem limited the overall accuracy of the measurements reported here to $\pm$15% in the region below 325 nm and to $\pm$10% above 325 nm.

The solar radiation spectra reported here may now be compared with model calculations. At present in Canada, only calculated values have been used in computer simulations of the polluted atmosphere (see for example, Bottenheim et al. 1977).

7.3 CONCLUSIONS

On the whole, the measurements of solar radiance and irradiance were successful. However, some improvements are suggested. The accuracy of the results was restricted by the unfortunate problem of the logarithmic amplifier. With some effort the overall accuracy could be kept within $\pm$ 10%. This limited accuracy, coupled with the fact that measurements were made only in late July, make it advisable to repeat and complete more measurements in the months of May to July. Additional measurements would yield more information on solar radiation in Canada.

The present results are experimental only. It would be desirable to complete radiation model calculations and compare these with the field measurements.

An improved location for radiation measurements is desirable. The present site had been restricted by trees near the horizon. A site on a slight elevation over adjacent land and well cleared of trees would probably be acceptable.

7.4 SOME DEFINITIONS AND INTER-RELATIONSHIPS PERTINENT TO SOLAR RADIATION MEASUREMENTS

There is a distinction to be made about the types of measurement of the incoming solar radiation and to a large extent this involves differences in terminology for various units of radiation measurement itself. Radiation reaching an observer on the ground can be expressed fundamentally as the number of photons reaching the observer per second from some direction of the sky. It will be shown that this is directly relatable to actinometric units of measurement. For reasons having to do with the conversion of the light quanta to electrical response of the measurement device, these fundamental quanta of light are expressed in terms of the energy delivered to the receiving system,

$$E = nh\nu \tag{26}$$

where n = number of photons

h = Planck's constant = 6.6×10^{-34} J Hz^{-1}

ν = frequency of the light quanta in Hertz

$= c/\nu$

c = speed of light

When one divides Equation (26) by the time interval of measurement in seconds, one obtains the power (P) in watts being delivered to the detector.

If one defines an area of the sky from which these photons arrive (the solid angle $d\Omega$ in Figure 92 and includes the effect of a detector of area A inclined to the incoming photons by the zenith angle (Θ) of the area of sky, one has the <u>spectral radiance</u>

$$N_\lambda(\lambda,\Omega,A) = \frac{\partial^3 P}{\cos\Theta\ \partial A\ \partial\lambda\ \partial\Omega} \left[\text{Watt m}^{-2}\ \text{sr}^{-1}\ \text{nm}^{-1}\right] \tag{27}$$

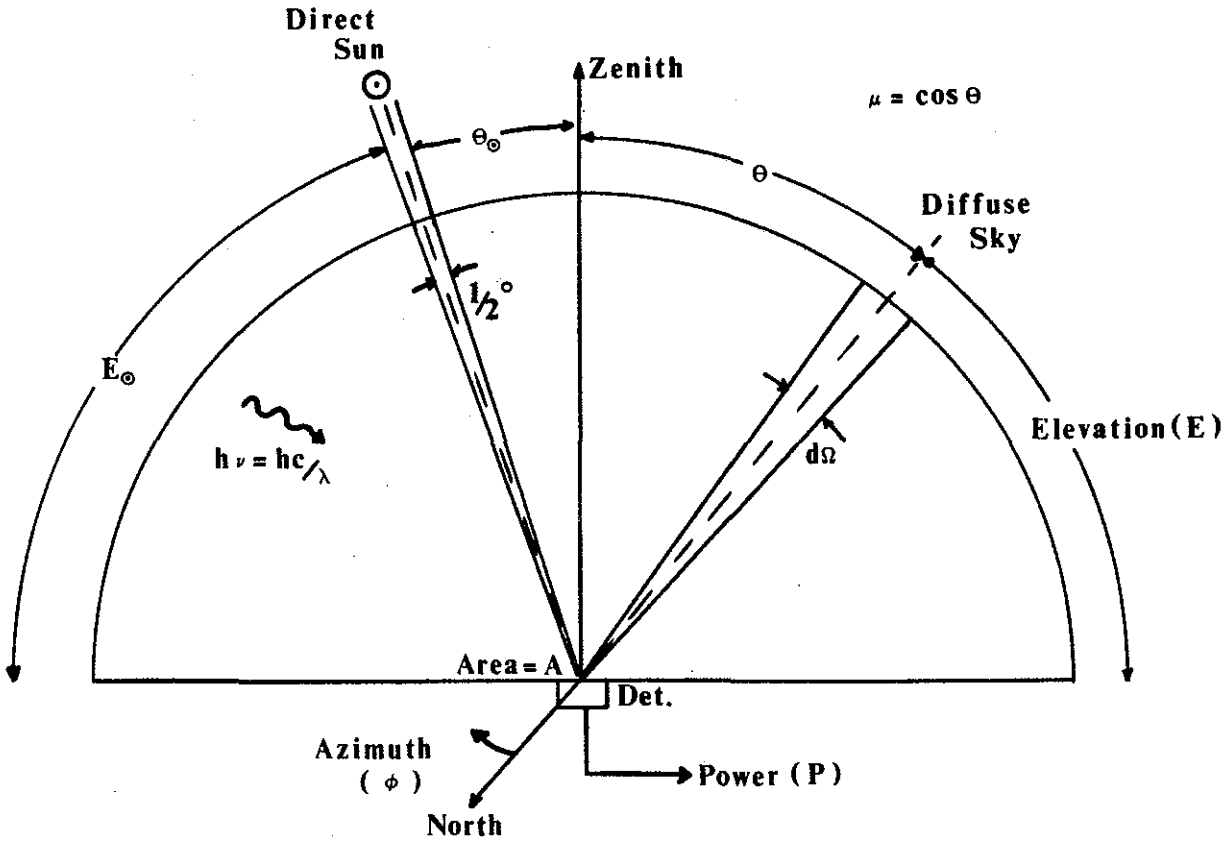

Figure 92. Parameters involved in direct and diffuse sky radiometric measurements.

Analogously, one can speak of the spectral irradiance (or spectral intensity) as that radiation received by a certain area on the ground from all direction of the sky:

$$H_\lambda = \int N_\lambda d\Omega' = \frac{\partial^2 P}{\partial A \, \partial A} \left[\text{Watt m}^{-2} \text{ nm}^{-1}\right] \qquad (28)$$

where now $d\Omega' = \cos \Theta d\Omega$ = 'projected' solid angle.

To measure spectral radiance one needs a spectrometer and a telescope to define the wavelength and area of sky. To measure spectral irradiance one needs a spectrometer and an integrating sphere or diffuser disk to accept all angles of the sky and thus perform the integral over Ω. In any case, the particular radiometric quantity desired will define the type of radiation measurement to be performed.

The list of terminology is still not complete since one has also actinometric units which are based on the number of quanta of light available for photochemical activity. For radiation subtended by a solid angle $d\Omega$ and incident at a zenith angle Θ on an atmospheric (polluted) layer of height h (m), the intensity absorbed per unit volume is given by

$$dI_{a\lambda} = h^{-1} \cos \Theta \{1 - \exp(-\alpha_\lambda n \, h \sec \Theta)\} \; N_\lambda \, d\Omega \qquad (29)$$

where N_λ is the spectral radiance of the radiation source, α_λ is the molecular absorption coefficient (m^2 molecule^{-1}) and n is the density of the absorbing molecular species (molecule m^{-3}).

For the case of direct solar radiation and weak absorption, the above equation reduces to

$$I^d_{a_\lambda} = d_\lambda n \, H^d_\lambda \qquad (30)$$

where H^d_λ is the spectral irradiance of the sun.

For sky or diffuse radiation, one must integrate equation (29) over the hemisphere of the sky and for the case of weak absorption this becomes

$$I^{s}_{a\lambda} = \alpha_{\lambda} n \int N_{\lambda} d\Omega \tag{31}$$

where N_{λ} is the spectral radiance of the sky.

It is evident that this actinometric (volumetric) intensity does not involve the projected solid angle as was the case for the radiometric irradiance discussed earlier (Equation 28). Basically, in actinometry one is dealing with absorbed radiation, whereas in radiometry it is incident radiation. The sum of $I^{s}_{a\lambda} + I^{d}_{a\lambda}$ would give the total absorption of radiation per unit volume within the atmospheric (polluted) layer in question. The units are watt $m^{-3} \cdot nm^{-1}$. This may be converted to fundamental units by dividing by $h\nu$, and one obtains the number of photons absorbed per $m^{3} \cdot s \cdot nm$ wavelength interval.

Let us consider a general photolysis reaction where a molecule A undergoes photodecomposition by the primary process

$$A + h\nu \rightarrow B + C \tag{32}$$

The primary quantum yield of this photodissociation reaction is defined as

$$\Phi = \frac{\text{no. of molecules of B(or C) formed/m}^3\text{/s}}{\text{no. of photons absorbed by A/m}^3\text{/s}}$$

$$= \frac{dB}{dt} \; (I_{abs})^{-1} \tag{33}$$

The rate of production of molecule B or C is defined by

$$\left(\frac{dB}{dt}\right) = \left(= \frac{dC}{dt}\right) = - \frac{dA}{dt}$$

$$= k_a \; [A] \tag{34}$$

where k_a is the photodissociation (photolysis) rate constant $(sec)^{-1}$ of the general reaction (32). From Equations (33) and (34), it is clear that

$$k_a [A] = \Phi \; I_{abs} \tag{35}$$

and if the photolysis proceeds within the atmosphere under solar radiation

$$k_e = \Phi \, (I^s_{a\lambda} + I^d_{a\lambda}) \, [A]^{-1}$$

This equation then links the solar radiation to the rate constant of the solar photolysis of the pollutant molecular species A. In order to account for solar radiation reflected by the earth's surface, Equation (36) must be modified to take into account the albedo. This added term is usually expressed as $aI_{t\lambda}$ where $I_{t\lambda}$ is the total irradiance incident on the reflecting surface and 'a' is its albedo.

8. THE CONCENTRATION AND DEPOSITION OF SULPHUR COMPOUNDS AND METALS AROUND THE GCOS OIL EXTRACTION PLANT

In order to understand the atmospheric budgets of substances emitted by oil extraction plants, ambient concentration and removal rates of pollutants must be known. Thus, two primary objectives of the AOSERP atmospheric monitoring program are:

1. To describe air quality conditions; and
2. To determine atmospheric input rates of pollutants to terrestrial and aquatic ecosystems.

A winter field study in March 1976 (Barrie and Whelpdale 1978) was conducted, and ongoing studies such as the air monitoring network of Alberta Environment and the regional precipitation chemistry network of AES are in operation to fulfill these objectives. To complement the winter field study, in which suspended particulates were collected and deposition was measured by sampling the snowpack, a 3-week summer field study in June 1977 was carried out in which the concentration of S compounds and dry deposition of particulates were measured. Suspended particulate matter was also collected for chemical analysis using neutron activation techniques. This report outlines the results of the field study.

8.1 ATMOSPHERIC SAMPLING

8.1.1 Introduction

Air monitoring took place at the Mildred Lake base camp (Ns in Figures 95 and 96), 10 km north of GCOS. The site was located in a jack pine forest. Three types of air sampling were done at the 13 m level of a meteorological tower (2 m above tree tops):

1. Separation and collection of particulate and gaseous S compounds;
2. Collection of suspended particulate for neutron activation analysis of elements, including heavy metals; and
3. particle size fractionation for S analysis.

Hourly wind speed and direction and air temperature measurements were available from instrumentation on the top of the tower.

8.1.2 Sampling Procedures

1. Techniques for sulphur and particulate sampling and analysis were essentially the same as those utilized in March 1976 and are described in detail elsewhere (Barrie and Whelpdale 1978). A brief description is given below.

   Particulate and gaseous S were sampled using a filter pack consisting of a prefilter for particulates (Whatman 40), an impregnated filter for gaseous S (Whatman 41), and a polypropylene filter holder. The performance of this filter pack has been thoroughly investigated (Lusis et al. 1977b). The filter pack was sheltered by an inverted polyethylene funnel. Air was sampled at about 40 $L \cdot min^{-1}$ (filter face velocity of 38 $cm \cdot s^{-1}$). Backup filters were impregnated with glycerol-potassium carbonate to trap SO_2. Particulate filters were extracted with 25 mL of deionized water at 80°C and impregnated filters with 25 mL of 3% H_2O_2 aqueous solution at room temperature. Extracts were analysed for S using an isotope dilution technique (Klockow and Denzinger 1976). Sampling was conducted from 13 to 26 June 1977, for 4-h periods during the day and for 12-h periods at night.

2. Particulates were collected for neutron activation analysis on Whatman 41 filter papers (47 mm) in open-faced polypropylene filter holders. These holders were mounted in the same way as the filter packs. Air was drawn through the filter at a face velocity of 25 $cm \cdot s^{-1}$. Exposed filters were transferred to polyethlene bags with teflon-coated forceps and transported to the lab. Unexposed and exposed filters were analysed by instrumental neutron activation techniques. Three 3-day samples were collected between 16 and 25 June 1977.

3. In addition to ambient S sampling, an Andersen cascade impactor (0.5 $L \cdot s^{-1}$ non-viable) was operated on the tower to determine particle size distributions. The impactor's inlet was located under an inverted funnel at the same height on the tower as the other aerosol samplers. Air was sampled at a rate of 28 $L \cdot min^{-1}$ for two 4-day periods between 13 and 25 June 1977. Then the cellulose back-up filters (Whatman 40), which collected all particles of diameter less than 0.4 µm, were extracted in 25 mL of deionized water at 80°C. The extract was subsequently analysed for S using the isotope dilution technique mentioned above.

8.1.3 Results and Discussion

8.1.3.1 Ambient sulphur. Gaseous and particulate S concentrations at Mildred Lake are shown in Figure 93 together with the prevailing wind speed and direction and air temperature. Four-hour average concentrations range from <0.1 to 2.3 µg $S \cdot m^{-3}$ and <1 to 14 µg $S \cdot m^{-3}$ for particulate and gaseous S, respectively. The peak 4-h average values for particulate and gaseous S found in March 1976 were 4.3 and 50 µg $S \cdot m^{-3}$ respectively (Barrie and Whelpdale 1978).

Episodes of high S concentrations occurred during periods of south-southeasterly winds when the site was downwind of the oil extraction plant. The mass-median-diameter of sulphur-bearing particles was 0.4 µm during two sampling periods, 13 to 17 June and 21 to 25 June. Thus, as is commonly observed elsewhere (Stevens et al. 1978), the bulk of atmospheric particulate S from oil extraction plant emissions occurs in respirable particles (those with diameter $< \sim 2$ µm). Consequently, S compounds are important substances to consider when dealing with the health effects of suspended particulate matter in the area.

In order to more quantitatively assess the problem of air quality in the vicinity of GCOS, ambient S concentrations measured at Mildred Lake during this field study and the March 1976 one were used to calculate 24-h average particulate and gaseous S concentrations for comparison with existing air quality criteria. Data for 8 full days in March 1976 and 11 in June 1977 were available.

Twenty-four hour average particulate S concentrations ranged from 0.11 to 1.9 μg $S \cdot m^{-3}$. The mean was slightly higher in March 1976 than in June 1977 (0.97 and 3.2 μg $S \cdot m^{-3}$, respectively). The mean concentration is about an order of magnitude lower than the particulate standards established by the states of California and Louisiana (8 and 4 μg $S \cdot m^{-3}$ respectively) As yet, no Canadian or U.S. particulate S standards exist. Even the maximum concentration observed, 1.9 μg $S \cdot m^{-3}$, falls well below these limits.

Federal and provincial air quality objectives do exist for gaseous S. The federal criteria (Department of Environment 1976) stipulate maximum acceptable and desirable 24-h averages of 150 and 76 μg $S \cdot m^{-3}$. During 19 days of sampling at no time were these objectives exceeded. The maximum observed in March 1976 and June 1977 was 49.3 and 5.1 μg $S \cdot m^{-3}$, respectively.

8.1.3.2 Particulate elemental composition. Three 3-day samples of suspended particulate were collected and analysed for their elemental content using neutron activation analysis. The sampling intervals (marked A, B, C) are shown in Figure 93 under the abscissa of the particulate S concentration diagram. As indicated by ambient S concentrations, samples A and B contain a larger proportion of anthropogenic particulates than sample C, which was collected when gaseous and particulate S levels were extremely low.

The atmospheric concentration of various elements in particulates at Mildred Lake in June 1977 and at Birch Mountain in March 1976 are compared in Table 19. The results of three samples taken in each study are listed for 21 elements. Only 12 elements were common to both data sets because fewer were detectable at Birch Mountain,

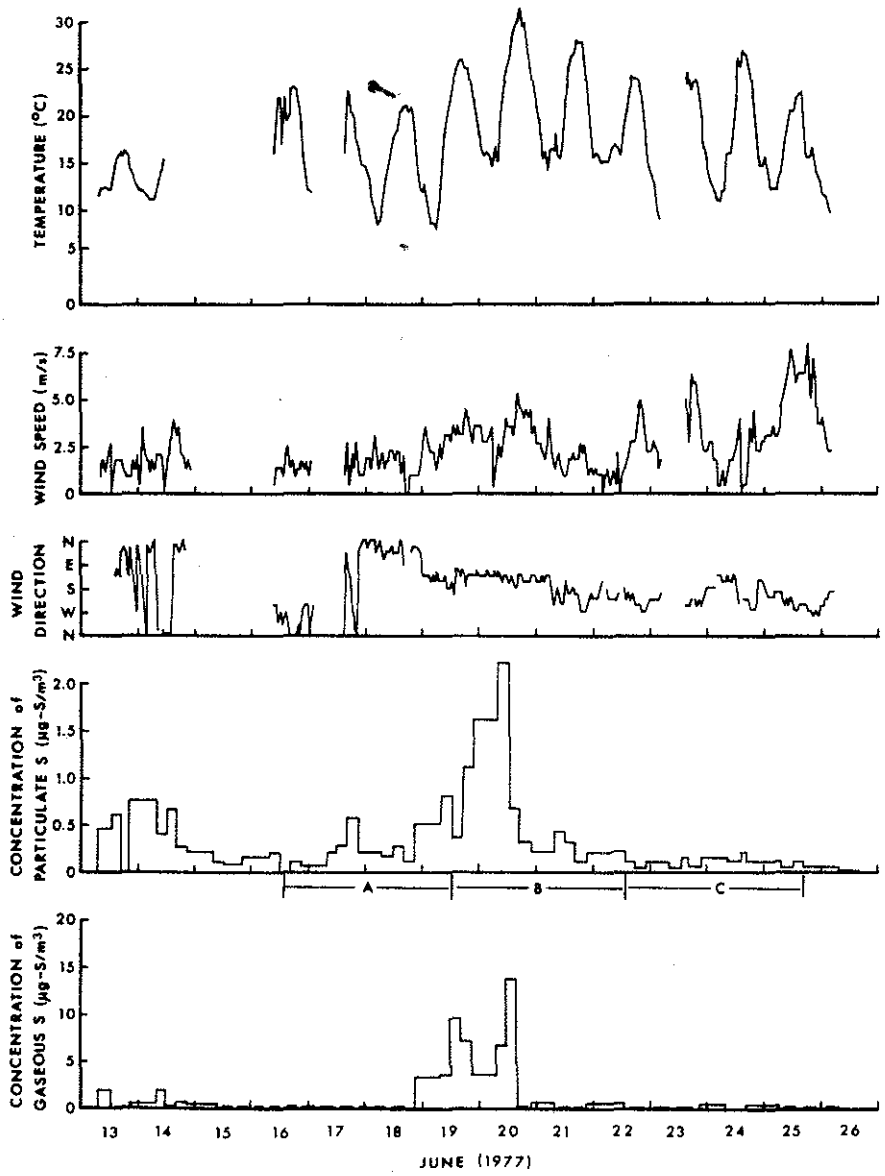

Figure 93. The temporal variation of wind speed and direction, temperature, and gaseous and particulate S concentration at Mildred Lake base camp durin the field study. Atmospheric particulate samples, A, B, and C were taken for the period indicated on the abscissa.

Table 19. Atmospheric concentration ($ng.m^{-3}$) of various elements in suspended particulates at Mildred lake, June 1977 and Birch Mountain, March 1976.

Element	June 77 Mildred Lake			March 76 Birch Mountain *		
	A 16 - 19	B 19 - 22	C 22 - 25	1 3 - 7	2 7 - 13	3 13 - 17
Al	1500.	2300.	1500.	41.	56.	70.
As	.68	.87	.37	.37	1.1	.44
Ba		37.9				
Br		4.66		4.7	2.1	1.8
Ca	2200.	2800.	2700.	19.	41.	40.
Cl				190.	54.	60.
Dy	.11	.24	.074			
Eu	.035	.066	.030			
Fe	3000.	2400.	890.			
K	350.	650.	430.	32.	25.	35.
La	1.0	1.8	0.89			
Mg	260.	870.	780.	31.	23.	26.
Mn	28.	49.	38.	0.66	0.93	7.0
Na				130.	76.	67.
Sb		1.3			0.17	
Sc	0.45	0.41	0.16		~0.014	~0.017

Continued . . .

Table 19. Concluded.

Element	June 77 Mildred Lake			March 76 Birch Mountain [a]		
	A 16 - 19	B 19 - 22	C 22 - 25	1 3 - 7	2 7 - 13	3 13 - 17
Sm	0.18	0.31	0.14			
Ti	110.	210	82.		6.7	7.9
U		0.21				
V	80.	110.	4.2	0.52	4.5	4.7
Zn		23.			~5.9	

[a] Barrie and Whelpdale 1977

where particulate concentrations are considerably lower. Of the elements common to both data sets, ten--Al, Ca, K, Mg, Mn, Sb, Sc, Ti, V, and Zn--were more abundant in June near the source than in March remote from the source, while As and Br levels were similar at both sites.

Atmospheric particulate matter sampled at the Mildred Lake site can be subdivided into three components:

1. D, a wind-blown dust component originating from particles raised from the earth's surface by natural or man-made processes;
2. E, an anthropogenic component originating from GCOS particulate emissions; and
3. X, a background component that prevails in the absence of D and E and owes its existence to a variety of complex processes that contribute to the residual particulate content of an air mass remote from large sources (Ludwick et al. 1977).

From the data in Table 20, is is possible to quantitatively estimate the relative magnitude of components D, E, and X in suspended particulate during a pollution episode that occurred at Mildred Lake in June 1977 (that is, for the period in which sample B was collected, Figure 93). X can be represented by the average concentration of samples 1, 2, and 3 collected on Birch Mountain in March 1976. At that time on Birch Mountain, 80 km north of GCOS, components D and E were zero because the land was snow covered (no wind-blown dust) and winds were persistently from the northern sector. D, the wind-blown dust component, is represented by sample C at Mildred Lake minus the background concentration X. As noted earlier, sample C was taken when GCOS emissions did not affect the air quality at Mildred Lake (as indicated by low ambient S concentrations, Figure 93). Finally, E is represented by B-C, the difference between concentrations at Mildred Lake during the pollution episode and in the absence of GCOS emissions at the site.

Table 20. The relative contribution of particulate sources to the ambient concentration of various elements in particulate matter at Mildred Lake during a pollution episode 19 to 22 June, 1977.

ELEMENT	WIND BLOWN BACKGROUND (D/X)	ANTHROPOGENIC BACKGROUND (E/X)
Al	28.	20.
As	0.	.6
Ca	80.	3.
K	13.	7.
Mg	28.	3.3
Mn	43.	13.
Sc	9.3	16.
Ti	10.	18.
V	1.30	32.
S*	1.0	5.9

[a] Used a background value of 0,1 µg $S.m^{-3}$

In Table 20 the contributions of wind-blown dust and anthropogenic emissions relative to background are shown for 10 elements. At Mildred Lake during a pollution episode, Ca, Mg, and Mn originate mainly from wind-blown dust sources. For instance, Ca concentrations are increased above background 80-fold by wind-blown dust but only threefold by anthropogenic emissions, while V and S levels are predominantly due to anthropogenic emissions from GCOS. Ambient concentrations of Al, K, Sc, and Ti are influenced almost equally by both sources during the most polluted episode at Mildred Lake. In winter, when wind-blown dust sources in the region are largely eliminated, Al, Mn, Sc, and Ti could also be added to S and V in a list of elements originating mainly from anthropogenic sources.

In a previous report (Barrie and Whelpdale 1978) the concept of enrichment factor E was introduced as an aid in interpreting particulate chemical composition data and as a means of determining the origin of that particulate. Recently, enrichment factors based on aluminum and average crustal rock (Mason 1966) and defined as

$$E = \frac{\{[Y / Al]\}_{air}}{\{[Y / Al]\}_{crustal\ rock}}$$

where Y is any element, have been widely adopted (Rahn et al. 1976) and extensively used (Rahn 1976; Dams and De Jonge 1976; Duce and Hoffman 1976; Ludwick et al. 1977).

Elemental enrichment factors for particulates at Mildred Lake in June 1977 are compared to those for Birch Mountain aerosols in March 1976 in Table 21. The influence of different particulate sources at the two sites results in very different enrichment factors, background, and polluted air for such elements as As, Sb, Br, and Zn.

Enrichment factors of several elements in plume particulates collected by helicopter (Lusis et al. 1978) and in flyash collected in the power house stack by electrostatic precipitation (SNC Tottrup 1978) are compared to those in particulates collected at Mildred Lake

Table 21. Enrichment factors with respect to aluminum in crustal rock for various elements in suspended particulates at Mildred Lake, June 1977 and Birch Mountain, March 1976. (See Table 19.)

Element	June 77	Mildred Lake		March 76	Birch Mountain	
	A 16 - 19	B 19 - 22	C 22 - 25	1 3 - 7	2 7 - 13	3 13 - 17
As	20.	17.	11.	410.	890.	290.
Ba		3.1				
Br		65.		3700.	1200.	840.
Ca	3.2	5.4	3.9	1.0	1.7	1.3
Cl				2800.	610.	540.
Dy	2.0	2.7	1.3			
Eu	1.6	1.9	1.3			
Fe	3.2	1.6	.94			
K	.72	.87	.88	2.5	1.4	1.6
La	1.8	2.1	1.6			
Mg	.66	1.5	2.0	2.9	1.6	1.4
Mn	1.6	1.8	2.1	1.4	1.4	1.2
Na				9.0	3.9	2.8
Sb		230.			1230.	
Sc	1.1	.65	.39		~0.9	~.8

Continued . . .

Table 21. Concluded.

Element	June 77 Mildred Lake			March 76 Birch Mountain		
	A 16 - 19	B 19 - 22	C 22 - 25	1 3 - 7	2 7 - 13	3 13 - 17
Sm	1.6	1.8	1.2			
Ti	1.4	1.6	1.0	2.2	2.2	2.1
U		4.0				
V	31.	29.	1.6	7.6	49.	40.
Zn		12.			~130.	

in Table 22. Two samples from Mildred Lake were used: the unpolluted sample C and the polluted sample B (see Figure 93). Furthermore, enrichment factors for the anthropogenic component of sample B were calculated using difference in concentration between samples B and C (column headed B-C). With the exception of Fe, enrichment factors of the anthropogenic component are very similiar to those of plume particulate or fly ash (the As enrichment factor in fly ash may be low because of volatilization of the element in the electrostatic precipitator). The good agreement clearly speaks for the consistency of the neutron activation analysis and good handling techniques.

8.2 DEPOSITION OF PARTICULATES

8.2.1 Measurement Technique

Dry deposition of particulates occurs by sedimentation, impaction, interception, and diffusion to objects at the earth's surface. Aerodynamics plays a strong role in the last three processes. Thus, in order to relate a dry deposition measurement from a collector (e.g., a bucket) to the actual removal, extensive wind tunnel comparisons and tests must be conducted. The only collector whose performance has been extensively examined and compared to that of natural surfaces is a device developed and widely used at Harwell, England (Cawse 1974).

The Harwell Collector is shown schematically in Figure 94. A filter pack (Whatman 541: 25 x 20 cm) enlcosed in a polyethylene filter holder is exposed face-up and horizontally 12 cm beneath an acrylic sheet (100 x 100 cm) and 150 cm above the ground. In order to avoid metal contamination, nylon rods were used to connect the filter holder to the plastic rain shield. The latter is supported by adjustable legs (tent poles, 200 cm maximum length) set into a square base assembled from 2.54 cm pipe and key clamp fittings. The whole unit, except for the acrylic sheet, could be easily dismantled and placed in a tent bag for transport to remote sites.

Table 22. Enrichment factors of elements in atmospheric particulate matter Mildred Lake, June 1977 compared to those of elements in plume particulate and fly ash. (B and C are calculated from samples in Table 19, B-C is calculated using the difference between samples B and C.)

Element	Unpolluted Sample (C)	Polluted Sample (B)	B-C	Plume Particulate June 77	Electrostatic Precipitator Fly Ash
As	11	17	20	72.[a]	3.3
Ca	3.8	2.7	2.6		0.45
Fe	.94	1.6	3.1		0.68
K	.88	.87	.85		0.54
Mg	2.0	1.5	.42		0.28
Mn	2.1	1.8	1.1	1.0	0.70
Ti	1.0	1.6	3.0	2.6	3.2
V	1.6	29	84.	168.	131.

[a] Based on one measurement

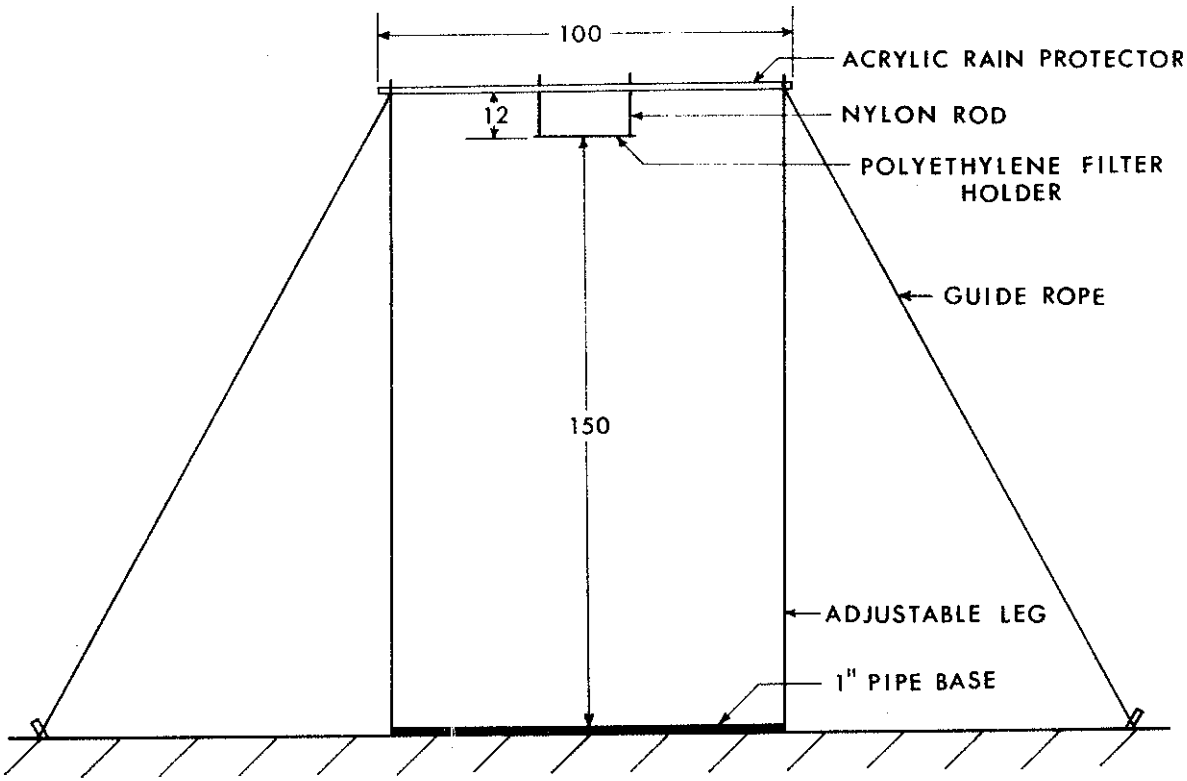

Figure 94. Harwell dry deposition collector.

Deposition of particles to the Harwell collector was measured in a wind tunnel by Clough (1973) and compared to deposition of particles to rye grass measured by Chamberlain (1966). Particle collection efficiency is a function of size. It was found that for diameters 2 to 10 μm, deposition to the Harwell collector is nearly the same as deposition to a grass surface beneath. Below 2 μm diameter, the Harwell collector underestimates deposition to grass. Since deposition rates to grass cannot at present be quantitatively related to uptake by forests, observations with the Harwell collector are strictly relative. They are, however, useful for comparing the behaviour of various elements, especially since the particle size distribution of these elements in GCOS particulates is known (Lusis et al. 1978). It is possible to relate the findings below to grass surfaces and sometime in the future, we hope, to forests.

At 15 sites (Figure 95), Harwell collectors were exposed for 14 days between 10 and 26 June 1977. All sites on the east side of the river, as well as SW2 and NW2, were reached by helicopter, the rest by automobile. Muskeg Mountain was farthest away, 40 km to the east of GCOS and approximately 320 m higher than the river. Each site was in a forest clearing. Care was taken to place the collector as far from the forest as possible. Three collectors were placed at site LS to determine reproducibility; two survived. On 16 June, the collector at site G1 had to be reset and moved about 0.5 km due to human interference. Another sampler was stolen from a site near Fort McMurray.

Filters were transported to and from the field in filter holders enclosed in clean polyethylene bags. After exposure, they were removed in a clean laboratory using teflon forceps and plastic gloves. Three unexposed filters handled in the same way were treated as blanks. Each filter was folded in half, and two pairs of 47-mm diameter discs were cut from the centre with a stainless steel punch. One pair was analysed by instrumental neutron activation analysis. The second pair was extracted in 50 mL of water at 80°C which was then analysed for S using the isotope dilution technique.

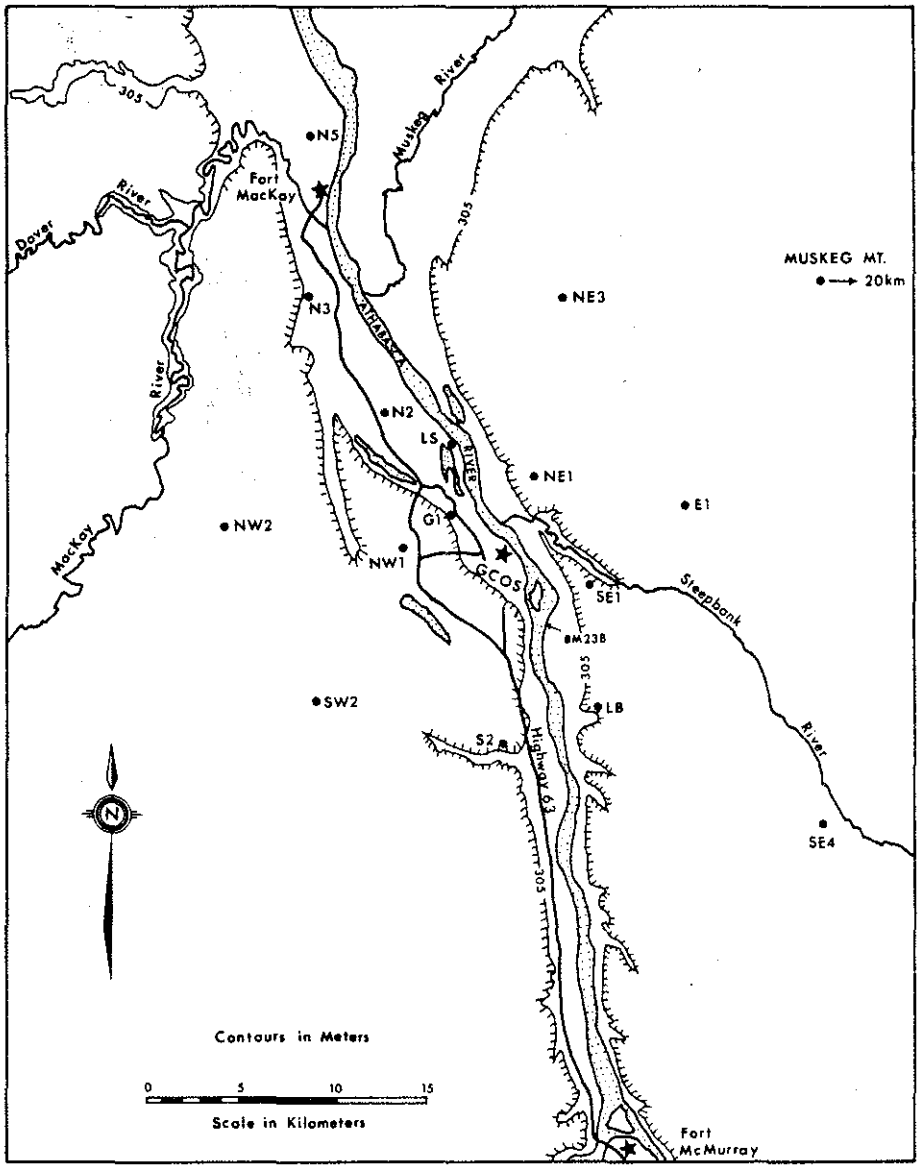

Figure 95. Location of sites at which Harwell dry deposition collectors were exposed.

8.2.2 Results and Discussion

After 2 weeks of exposure, seven elements were detected above the filter's background impurity--Al, Ca, Mg, Mn, particulate -S, Ti, and V. The rate of deposition of each of these elements at 15 sites is listed in Table 23. Deposition patterns around GCOS for each element are shown in Figures 96 and 97.

Independent studies of the reproducibility of the dry deposition rate measurement were carried out by Puttock and Barrie (1978). Two sets of four Harwell collectors were exposed for 2 weeks. It was found for both Al and V (representing large and small particle size ranges, respectively) that the most extreme deviation from the means was less than 50%. Similar conclusions are reached when one compares deposition rates to the two samples at LS (LS1 and LS2 in Table 23). This accuracy should be kept in mind when applying these results. As mentioned earlier, the Harwell collector estimates deposition rates to grass fairly well for an element whose main mass lies in the particle size range 2 to 10 μm. This is the case for particulates originating from wind-blown dust sources (Whitby 1978). It is also the case for Al, Mn, and V (Lusis et al. 1978) originating from the power plant plume. Their mass median diamter is 3 μm. As was noted earlier, particulate S is in submicron particles, and therefore its deposition is underestimated by the Harwell collector.

A comparison of particulate S deposition rates with total deposition rates measured in winter as well as with annual estimates for central Alberta is made in Table 24. Bearing in mind that particulate S deposition is underestimated by the Harwell collector, one can see that near the source it is quite comparable to annual averages for central Alberta and maximum deposition in winter. Away from the influence of the GCOS operation, particulate S deposition is very low compared to total deposition rates in central Alberta.

From the discussion in Section 2.3 concerning the relative contribution of wind-blown dust and anthropogenic particulates to the ambient concentration of various elements at Mildred Lake (see Table 20), one would expect the deposition patterns of V and particulate S (Figure 96), which originate mainly from anthropogenic sources, to be

Table 23. Deposition rates of elements in particulate matter at sites around GCOS (see also Figures 96 and 97).

	Exposure			Deposition Rate ($K_g H^{-1} Y^{-1}$) [a]						
	June 77 (Days)			Al	Ca	Mg	Mn	Part S	Ti	V
	from	to	total							
LS_1	11	25	14	0.98	0.98	0.24	0.019	1.2	0.11	0.036
LS_2	11	25	14	1.9	1.9	0.62	0.030	0.77	0.20	0.061
G1	16	25	9	3.2	2.3	0.49	0.047	0.35	0.26	0.050
N3	10	25	15	3.3	1.8	0.36	0.046	0.036	0.23	0.045
N5	10	25	15	1.4	0.63	0.15	0.018	0.47	0.15	0.048
NW1	10	25	15	3.7	5.0	0.78	0.059	0.58	0.23	0.019
NW2	11	26	15	2.2	6.4	0.78	0.050	0.16	0.13	0.037
SW2	10	25	15	0.49	0.21	0.15	0.0084	-	0.040	0.013
S2	10	25	15	0.40	0.07	0.15	0.0049	0.0	0.007	0.006
SE1	11	26	15	2.0	0.98	0.36	0.027	0.47	0.18	0.081
LB	11	26	15	0.77	0.91	0.084	0.014	0.13	0.063	0.025
SE4	11	26	15	0.35	0.07	0.084	0.011	0.13	0.035	0.011
NE1	11	26	15	0.98	0.49	0.084	0.017	0.47	0.077	0.050
E1	11	26	15	0.77	0.0	0.014	0.0098	0.35	0.077	0.060
NE3	11	26	15	0.49	0.0	0.084	0.0098	0.19	0.063	0.024
Muskeg	11	26	15	0.28	0.0	0.00	0.0091	0.26	0.000	0.023

[a] $1\ Kg\ H^{-1}\ Y^{-1} = 3.17 \times 10^{-9}\ g\ m^{-2} S^{-1}$

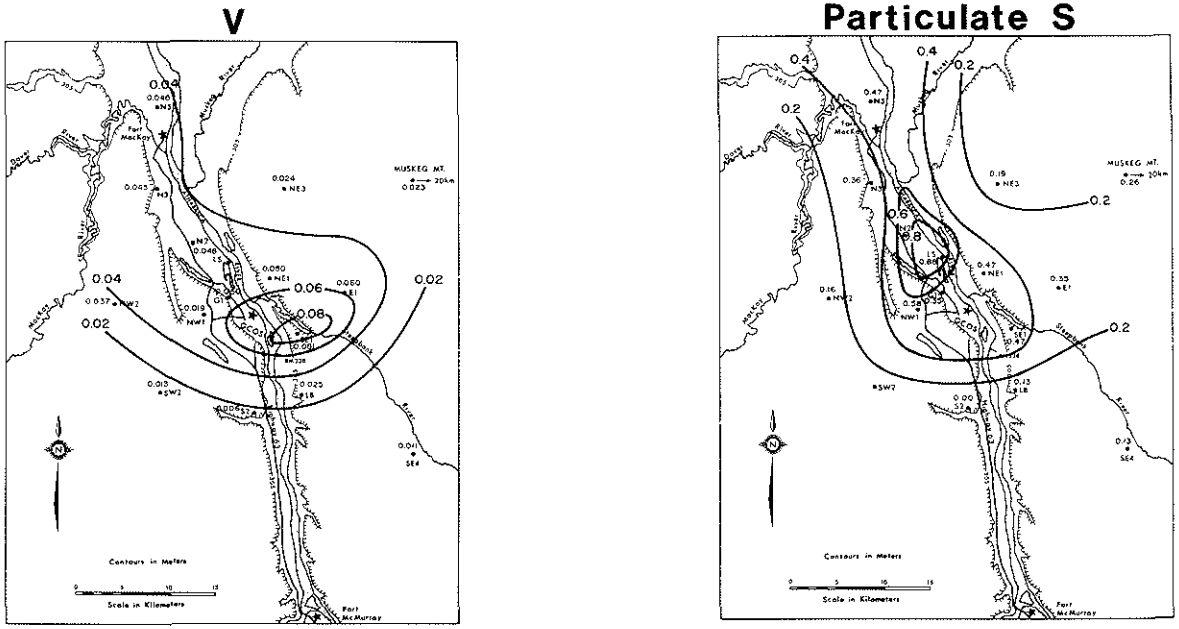

Figure 96. Deposition patterns of elements of predominantly anthropogenic origin. (Deposition isopleths are in $kg \cdot h^{-1} \cdot y^{-1}$).

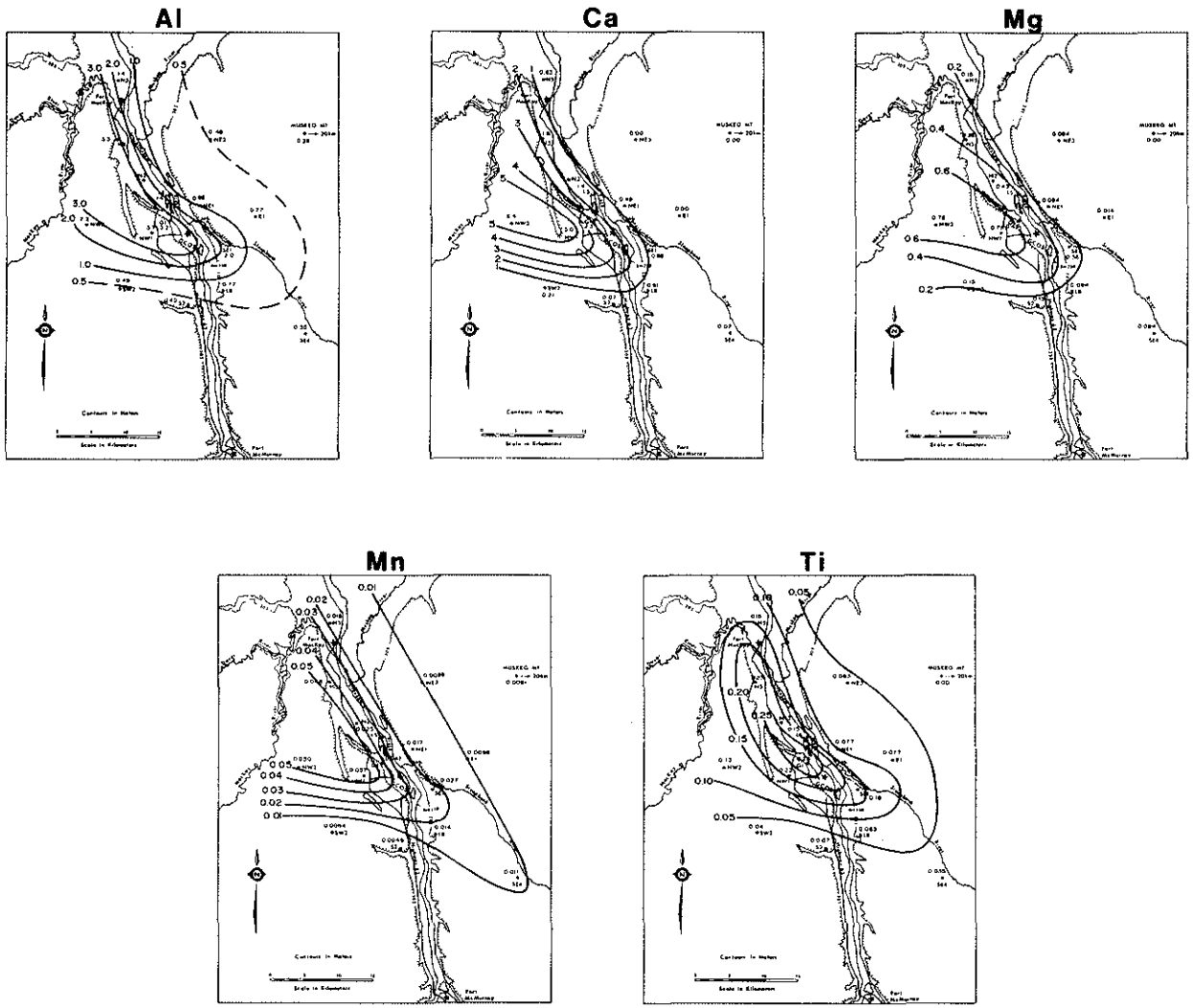

Figure 97. Deposition patterns of elements having a strong wind-blown dust component. (Deposition isopleths are in $kg \cdot H^{-1} \cdot y^{-1}$).

TABLE 24. A comparison of particulate sulphur deposition rates from this study with rates measured at other times and places in Alberta.

Location	Period	Deposition Rate ($Kg\text{-}S\ H^{-1}Y^{-1}$)	Reference
Athabasca oil sands			
maximum	June 77	0.99	This study* (part-S deposition)
background		0 - .04	
maximum	Feb 76	3.6	Barrie & Whelpdale 1978 (total deposition)
background		<.44	
Central Alberta			
average	annual	0.5 - 1.1	Walker, 1969 (total deposition)
average	annual	2.1	Klemm, 1977 (total deposition)

[a]These values are underestimates (see Section 3.1)

quite different from those of the other elements Al, Ca, Mg, Mn, and Ti (Figure 97), whose main source in ambient air is wind-blown dust. This is indeed the case. The wind-blown dust elements are deposited in a region running northwest of GCOS engulfing Syncrude's operations and the road where a great deal of dust is stirred up. Vanadium and S deposition no only occurs to the northwest and north but also to the east. For elements from wind-blown dust, the lowest deposition rates occur at Muskeg Mountain 40 km to the east. However, deposition of V and S is not lowest at Muskeg even if one reduces Muskeg by a factor of 50% (the uncertainty in the deposition measurement). This indicates that particulate S emitted by GCOS was influencing particulate deposition 40 km away.

A principal component analysis, conducted independently on the deposition data, also grouped the data in the same way as was done above from the deposition patterns. A wind-blown dust component together with a particulate S component and a V component were found to be the best combination to use in a linear regression analysis to explain the variance in the data set.

Measured deposition patterns correlate well with the frequency distribution of hourly wind direction at Mildred Lake (Figure 98) during the study period (13 to 26 June 1977). In order of decreasing frequency, winds were from the southwest quadrant, south-southeast sector, and north-northeast sector. Since S and V are predominantly of anthropogenic origin in ambient air around GCOS (Table 20), their deposition patterns about the source (Figure 96) will reflect the predominant wind directions. This is indeed the case; there is a region of high deposition east and northwest of the plant (one must bear in mind that sourthwesterly surface winds are likely associated with westerly upper level winds). Deposition patterns of elements that are predominantly or partially of wind-blown dust origin, Al, Ca, Mg, Mn, Ti (Table 20) Figure 96), are more difficult to correlate with the wind rose data because the source is an areal one. It does seem, however, that the absence of high deposition to the northeast or east of the GCOS-Syncrude region that one would expect from the predominant south-southwesterly wind, suggests that the wind-blown dust carrying these elements to the collector is of relatively local origin.

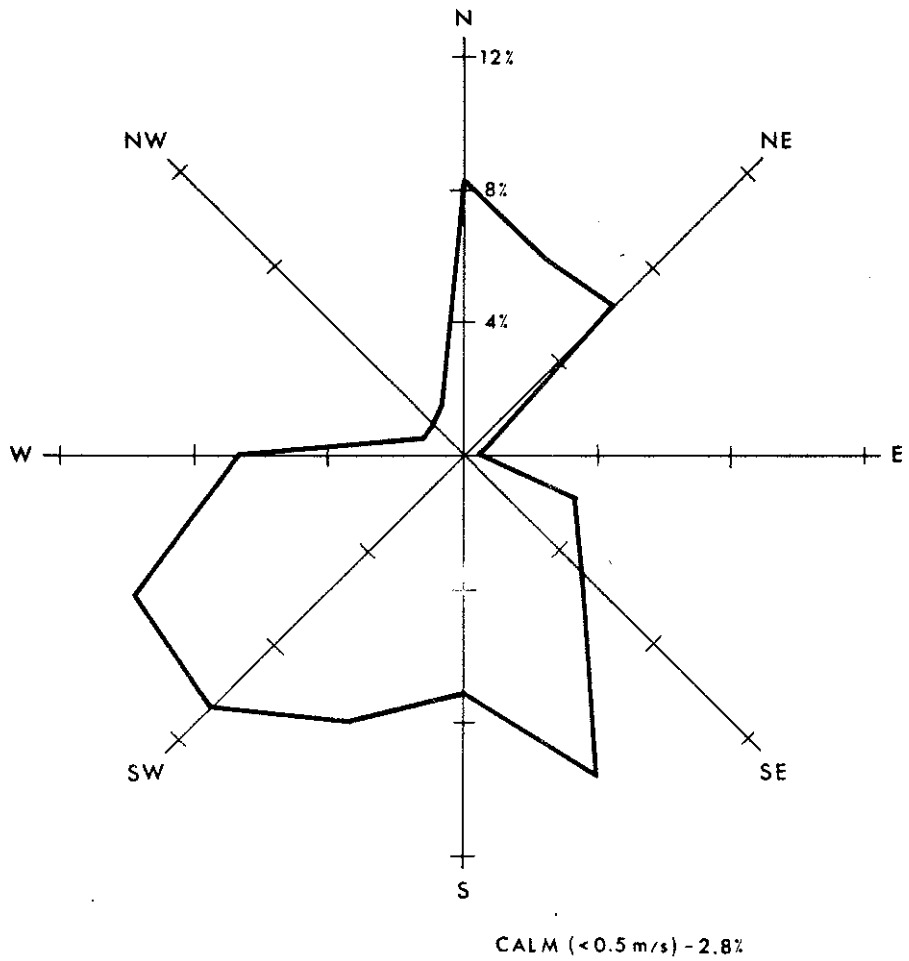

Figure 98. Surface wind rose at Mildred Lake base camp for the period 13 to 26 June 1977.

A useful parameter that can be derived from the data is the deposition velocity V_d of an element defined as:

$$V_d = \frac{\text{deposition rate}}{\text{ambient concentration}}$$

The average deposition velocities of elements in Table 23 were calculated (Table 25) using the average ambient concentration of each element at Mildred Lake (N2) and the deposition flux read-off Figures 96 and 97 at site N2. The calculated deposition velocities are only approximate ones (correct within a factor of 2) because the ambient concentrations were not available for the whole period of time that the Harwell collectors were exposed (see footnote to Table 25), and because of the uncertainty in the deposition rate measurements. They prove useful, however, in estimating deposition rates if an ambient concentration is available from model calculations or measurements. They are somewhat lower than the deposition velocities to the Harwell collector measured by Cawse (1974).

8.3 CONCLUSION

The ambient concentrations of S compounds and metals in suspended particulates have been measured near the only existing oil extraction plant in the Athabasca Oil Sands area. Twenty-four hour average ambient S concentrations, although higher near the mining operation, did not exceed or even approach commonly accepted ambient air criteria for 19 days of availabe data. Ambient particulate concentrations at Mildred Lake are sustained by sources of wind-blown dust and anthropogenic particulate emissions. The relative magnitude of these sources varies from element to element and season to season. High ambient V and S concentrations at Mildred Lake originate mainly from power plant stack emissions. This observation is reflected in the deposition pattern of these elements, which are quite different from deposition patterns of elements such as Al, Ca, Mg, Mn, and Ti, which have a strong wind-blown dust source. Transport and deposition of anthropogenic particulate S as far away as Muskeg Mountain 40 km to the east was observed.

Table 25. Deposition velocities of elements in suspended particulate to the Harwell collector.

Element	Al	Ca	Mg	Mn	Parts-S	Ti	V
Deposition Rate (Kg/H-yr)	2.8	1.8	0.5	.045	0.70	0.24	0.045
Average* Concentration (ng/m)	1800	2500	640	38	320	130	66
Deposition Velocity (cm/s)	.49	.23	.25	.38	.69	.59	.22

[a] Average concentrations are for 13 to 23 June for particulates and 16 to 25 June for other elemetns while deposition rates are for 11 to 26 June.

Summertime measurements of dry deposition of particulate matter as conducted in this study must in future be augmented by studies of wet deposition (a contracted study, As 3.6.2, in in progress). Wet removal measurements of anthropogenic emissions are difficult because of the localized nature of the plume during rain events. This requires a very dense network of rain samplers. In the meantime, baseline wet deposition rates in the region are being measured routinely during summer months at 19 sites within 150 km of GCOS (Barrie et al. 1978).

9. CONCLUDING REMARKS AND RECOMMENDATIONS

One of the main objectives of the AOSERP Air System is to predict the impact of air pollution on the oil sands area by means of modelling. The use of such models will require detailed information on the wind flow and temperature structure of the planetary boundary layer of that area, on the rise and dispersal of industrial plumes, on the chemical transformation and deposition of pollutants, and on the background and ambient air quality.

This report, which represents the outcome of the third field study in the oil sands area, supplied the foregoing required information for summer conditions. Measurements of the local meteorological parameters were carried out at different locations in the oil sands area. These data permitted the calculation of wind, temperature, and humidity profiles. To study the structure of the atmospheric boundary layer in more detail a tethersonde was used, and the variables measured were the three components of wind speed, wind direction, temperature and relative humidity.

From the tethersonde results it was noted that at the Lower Syncrude Site, valley effects are apparent in the wind field during stable conditions, i.e., a large percentage of the time during the winter season and early morning conditions during the summer. Under these conditions it is therefore apparent that the tower which now exists at this site is measuring flow that may in no way reflect winds aloft.

Under layered inversion conditions, there appears to be increased frequency of low level wind (jets) associated with these inversions. Measurements of these wind maxima with minisondes may tend to underestimate the associated wind speed.

The good agreement between the acoustic sounder data and the temperature profiles at the Lower Syncrude Site implies that the sounder will be useful in studying the depth of the mixing layer of that area. The sounder, however, will require a separate system for the measurements of temperature for support purposes.

It is apparent from the observations presented in the plume rise section that there is no one simple universal formula that will describe the plume rise in the oil sands area. It is believed that several aspects of the plume behaviour (e.g., looping and shear) should be taken into account before a satisfactory formula can be derived.

In analysing plume dispersion information, it is apparent that the dispersion along the vertical is not well represented by Pasquill-Gifford curves. However, information from the LIDAR project indicated that the dipsersion of the GCOS plume is reasonably well represented by the ASME model for unstable and neutral atmospheric conditions. However, as was seen in previous studies, dispersion in stable atmospheric conditions is larger than would be predicted by tabulated Gaussian dispersion coefficients. It is believed that this increased dispersion is predominantly due to the dynamic behaviour of the buoyant plume near the stack. Plume dispersion models to incorporate these dynamic effects as well as wind shear and looping in the prediction of dispersion in this region are definitely required.

The observed vertical dispersion coefficient did not correlate well with the bivane measurements through the use of the Hay-Pasquill theoretical model. There may be several explanations for this discrepancy. Atmospheric turbulence levels at the plume height are different than those at the bivane level. A better selection of the Lagrangian-Eulerian time scale β than the one commonly used is needed.

LIDAR and photography have been shown to be extremely useful tools for the measurement of plume rise and dispersion in the AOSERP study area, especially in light of the limited road network for other types of sampling (e.g., COSPEC). LIDAR, however, is a technique still in the research rather than operational stage. It requires a fair degree of sophistication in its operation and a high degree of interpretation of the data. While recognizing these restrictions in LIDAR usage, we recommend that the LIDAR be used in future experimental studies planned by AOSERP.

Operation of the COSPEC and Sign-X has rendered valuable and useful information on the concentrations of SO_2. Future field studies in the AOSERP study area should consider aircraft of helicopter mounting of the COSPEC in order to surmount the difficulties associated with the limited road/river network in the area.

Early morning SO_2 oxidation rate in the GCOS power plant plume is low; typically less than $0.5\% \cdot h^{-1}$. Later in the day, under the influence of intense atmospheric turbulence, the conversion rate can increase to values as great as $3\% \cdot h^{-1}$.

Significant amounts of potentially catalytic metals occur in the particulate matter emitted from the power plant chimney. These metals are found in particles having a mass-mean diameter of around 3 μm, and thus should remain airborne and available for reaction with SO_2 for long periods of time. However, there seems to be little evidence in our results that heterogeneous SO_2 conversion processes are important.

On the other hand, heterogeneous gas-phase reactions, involving emissions of SO_2, nitrogen oxides, and hydrocarbons, seem to result in significant SO_2 oxidation rates. These reactions are probably also responsible for the O_3 buildup in the plume that was observed on several occasions.

The applicability of these results to emissions of other plants in the oil sands should be checked.

It is recommended that future SO_2 oxidation experiments be carried out in the plume of the Syncrude power plant, once full-scale operation is attained, since the oxidation rate could depend on such parameters as the characteristics of the emitted particulate, the level of other gases in the plume, and the height of the chimney. Thus, the applicability of our GCOS power plant results to other oil sands processing plants should be verified.

The solar radiation measurements were successful, and it is recommended that these be compared with radiation model caclulations. In the future, a site less obstructed by trees would be desirable. More measurements in May to August would increase the solar radiation data base.

Twenty-four hour average ambient S concentrations, although higher near the oil extraction operation, did not exceed or even approach commonly accepted ambient air criteria for 19 days of available data.

High ambient V and S concentrations in ambient particulate matter at Mildred Lake orginate mainly from power plant stack emissions. This observation is reflected in the deposition patterns of these elements, which are quite different from deposition patterns of elements such as Al, Ca, Mg, Mn, and Ti that have a strong wind-blown dust source. Transport and deposition of anthropogenic particulate S as far away as Muskeg Mountain 40 km to the east was observed.

Summertime measurements of dry deposition of particulate matter as conducted in this study must in future be augmented by studies of wet deposition.

10. REFERENCES CITED

Barrie, L.A., and H.W. Georgii. 1976. An experimental investigation of the absorption of sulphur dioxide by water drops containing heavy metal ions. Atmos. Environ. 10:743-749.

Barrie, L.A., V. Nespliak, and J. Arnold. 1978. Chemistry of rain in the Athabasca Oil Sands region, summer 1977. AOSERP Report, Sub-project ME 1.4 (in press).

Barrie, L.A., and D.M. Whelpdale. 1978. Background air and precipitation chemistry. Pages 124-159 in F.H. Fanaki compiler. Meteorology and air quality winter field study in the AOSERP study area, March 1976. Prep. for the Alberta Oil Sands Environmental Research Program by Fisheries and Environment Canada, Atmospheric Environment Service. AOSERP Report 27. 249 pp.

Bener, P. 1970. Measured and theoretical values of the spectral intensity of unltraviolet zenith radiation and direct solar radiation at 316, 1580, and 2818 m a.s.l. AFCRL Report F 61052-67-C-0029, 1970.

Bierly, E.W., and E.W. Hewson. 1962. Some restrictive meteorological conditions to be considered in the design of stacks. J. Appl. Meteorol. 1:383-390.

Bottenheim, J.W., S.E. Braslavsky, and O.P. Strausz. 1977. Modeling study of seasonal effect on air pollution at 60° N latitude. Environ. Sci. Technol. 11:801-808.

Bottenheim, J.W., and O.P. Strauz. 1977. Review of pollutant transformation processes relevant to the Alberta Oil Sands area. Alberta Oil Sands Environmental Research Program Report, Project ME 3.5.0. AOSERP Report 25. 166 pp.

Bottenheim, J.W., and O.P. Strausz. 1978. Computer modelling on polluted atmospheres and the conversion of atmospheric sulphur dioxide to sulphuric acid. Alberta Environment, Research Secretariat Report No. 1978/5. 144 pp.

Briggs, G.A. 1975. Plume rise predictions. Lectures on air pollution and environmental impact analyses, 59-104. Am. Meteor 1. Soc.

Carpenter, S.B., T.L. Montgomery, J.M. Leavitt, W.C. Colbaugh, and F.W. Thomas. 1971. Principal plume dispersion models TVA power plants. J. Air Pollut. Control Assoc. 21:491-495.

Cawse, P.A. 1974. A survey of atmospheric trace elements in the U.K. (1972-1973). AERE report #R-7669, Harwell, England.

Chamberlain, A. 1966. Transport of Lycopodium spores and other small particles to rough surfaces, Proc. R. Soc. A. 296:45-70.

Clough, W.S. 1973. Transport of particles to surfaces. Aerosol Sci. 4:227-234.

Cramer, H.E. 1957. A practical method for estimating the dispersal of atmospheric contaminants. Proceedings of the Conference on Applied Meteorology. Am. Meteorol. Soc.

Csanady, G.T. 1973. Turbulent diffusion in the environment. Geophysics and Astrophysics Monographs, D. Reidel Publishing Company, Dordrecht-Holland. pp 248.

Dams, R., and J. de Jonge. 1976. Chemical composition of Swiss aerosols from the jungfraujoch. Atmos. Environ. 10:1079-1084.

Danson, R.L., D.F.S. Natusch, J.R. Wallace, and C.A.E. Evans. 1974. Trace elements in fly ash--dependence of concentration on particle size. Environ. Sci. Techno. 8:1107-1113.

Davis, D.D., G.Smith, and J. Klauber. 1974. Trace gas analysis of power plant plumes via aircraft measurements: O_3, NO_x and SO_2 chemistry. Sci. 186:733-736.

Department of Environment. 1976. Criteria for national air quality objectives: Report to the Federal-Provincial Committee on Air Pollution by the Sub-Committee on Air Quality Objectives, Nov. 1976.

Duce, R.A., and G.L. Hoffman. 1976. Atmospheric vanadium transport to the ocean. Atmos. Environ. 10:089-996.

Fanaki, F.H. (Compiler). 1978. A meteorology and air quality winter field study in the AOSERP study area, March 1976. Prep. for the Alberta Oil Sands Environmental Research Program by Fisheries and Environment Canada, Atmospheric Environment Service. AOSERP Report 27. 249 pp.

Fanaki, F.H., and G. Lesins. 1975. Photographic measurements of smoke plume heights from industrial stacks. SMPTE 84:77-81.

Fanaki, F.H., R. Mickle, M. Lusis, J. Kovalick, J. Markes, F. Froude, J. Arnold, A. Gallant, S. Melnichuk, D. Brymer, A. Gaudenzi, A. Moser, and D. Bagg. 1979. Air system winter field study in the AOSERP study area, February 1977. Prep. for the Alberta Oil Sands Environmental Research Program by Atmospheric Environment Service. AOSERP Report 24. 182 pp.

Forrest, J., and L. Newman. 1977. Further studies in the oxidation of sulphur dioxide in coal-fired power plant plumes. Atmos. Environ. 11:465-474.

Foster, P.M. 1969. The oxidation of sulphur dioxide in power station plumes. Atmos. Environ. 3:157-175.

Freiberg, J. 1974. Effects of relative humidity and temperature on iron-catalysed oxidation of SO_2 in atmospheric aerosols. Environ. Sci. Technol. 8:731-734.

Garland, J.A. 1978. Dry and wet removal of sulphur from the atmosphere. International Symposium on Sulphur in the Atmosphere, Sept. 7-14, Dubrovnik, Yugoslavia. Atmos. Environ. 12:349-362.

Gifford, F.A. 1960. Some recent atmospheric dispersion observations. Nucl. Saf. 1:56-62.

Gifford, F.A. 1976. Turbulent diffusion--typing schemes; a review. Nucl. Saf. 17:25-43.

Gillani, N.V., R.B. Husar, J.D. Husar, D.E. Patterson, and W.E. Wilson. 1978. Project MISST: Kinetics of particulate sulphur formation in a power plant plume out to 300 km. International Symposium on Sulphur in the Atmosphere, Sept. 7-14, Dubrovnik, Yugoslavia. Atmos. Environ. 12:589-598.

Gladney, E.S., J.A. Small, G.E. Gordon, and W.H. Foller. 1976. Composition and site distribution of in-stack particulate material at a coal-fired power plant. Atmos. Environ. 10:1071-1077.

Halitsky, T. 1961. Single-camera measurement of smoke plumes. Int. J. Air Water Pollut. 4:185-198.

Hay, J.S., and F. Pasquill. 1959. Diffusion from a continuous source in relation to the spectrum of turbulence. Geophys. 6:345-365.

Husar, R.B., D.E. Patterson, J.D. Husar, N.V. Gillani, and W.E. Wilson. 1978. Project MISST: Sulphur budget in large plumes. International Symposium on Sulphur in the Atmosphere, Sept. 7-14, Dubrovnik, Yugoslavia. Atmos Environ 12:549-568.

Junge, C.E., and T.G. Ryan. 1958. Study of the SO_2 oxidation in solution and its role in atmospheric chemistry. Quart. J. R. Meteorol. Soc. 84:46-55.

Klockow, D., and Denzinger. 1976. Determination of sulphate by substoichiometric isotopic dilution analysis. European Monitoring Programme Manual for Sampling and Chemical Analysis Procedures, Norwegian Institute for Air Research, P.O. Box 130, N-2001, Lillestrom, Norway.

Koczkur, E. 1968. Plume rise and dispersion in a lake breeze. Ph.D. Thesis, Department of Mechanical Engineering, University of Toronto, Toronto, Canada. 123 pp.

Ludwick, J.D., T.D. Fox, and S.R. Garcia. 1977. Elemental concentrations of northern hemispheric air at Quillayute, Washington. Atmos. Environ. 11:1083-1088.

Lusis, M., K.G. Anlauf, L.A. Barrie, and H.A. Wiebe. 1977a. Plume chemistry studies at a northern Alberta power plant. Proceedures of Alberta Sulphur Gas Research Workshop III, Nov. 1977, University of Edmonton, Alberta.

Lusis, M.A., L.A. Barrie, H.A. Wiebe, K.G. Anlauf. 1977b. Development and testing of a filter pack for simultaneous sampling of gaseous and particulate compounds in the atmosphere. Atmos Environ Service, ARDA report 49-77, Downsview, Ontario, Canada.

Lusis, M.A., and C.R. Phillips. 1977. The oxidation of SO_2 to sulphates in dispersing plumes. Atmos. Environ. 11:239-241.

Mason, B. 1966. Principles of geochemistry. 3rd. ed. Wiley and Sons, Inc., New York.

Millan, M.M. 1976. A note on the geometry of plume diffusion measurements. Atmos. Environ. 10:655-658.

Montgomery, T.L., S.B. Carpenter, W.C. Colbaugh, and F.W. Thomas. 1971. Full scale study of plume rise at large electric generating station - Bull Run supplement. Air Quality Supplement, Air Quality Branch, Tennessee Valley Authority, Muscle Shoals, Ala. 58 pp.

Munn, R.E. 1964. Turbulence statistics at Douglas Point. Appl. Meteorol. 3:771-779.

Newman, L., J. Forrest, and B. Manowitz. 1975. The application of atmospheric oxidation of sulphur dioxide in the plume from a coal fired power plant. Atmos. Environ. 9:969-977.

Nieboer, H., W.P.L. Carter, A.C. Lloyd, and J.N. Pitts, Jr. 1976. The effect of latitude on the potential for formation of photochemical smog. Atmos. Environ. 10:731.

Pasquill, F. 1961. The estimation of dispersion of windborne material. Meteorol. Mag. 90:33.

Pasquill, F. 1976. Atmospheric dispersion parameters in Gaussian plume modelling, EPA-600/4-76-030b, Research Triangle Park, U.S.A.

Peterson, J.T. 1976. Calculated activic fluxes (290-700 nm) for air pollution photochemistry applications. Report EPA-600/4-76-025, U.S. Environmental Protection Agency, Research Triangle Park, N.C., NTIS PB. 255819.

Peterson, J.T., and K.L. Demerjian. 1976. The sensitivity of computed ozone concentrations to U.V. radiation in the Los Angeles Area. Atmos. Environ. 10:459.

Peterson, J.T., and E.C. Flowers. 1974. Urban-rural solar radiation and aerosol measurements in St. Louis and Los Angeles. Symposium on Atmospheric Diffusion and Air Pollution, Santa Barbara, Calif., Sept. 9-13, 1974 (published by Am. Meteor. Soc., Boston, Mass.).

Portelli, R.V. 1977. User's guide to three interactive point source dispersion models. Report ARQT-7-77, Atmospheric Environment Service, 4905 Dufferin St., Downsview, Ontario.

Puttock, J.S., and L.A. Barrie. 1978. A study of the deposition of atmospheric particulate matter to various collectors in relation to ambient concentrations and size distributions. ARQT Report, Atmospheric Environment Service, 4905 Dufferin St., Downsview, Ontario.

Rahn, K. 1976. Silicon and aluminum atmospheric aerosol crust-air fractionation. Atmos. Environ. 10:597-601.

Rahn, K.A., L. Schutz, and R. Jaenicke. 1976. The crustal component of background aerosols: its importance in interpreting heavy metal data. Proc. of W.M.O. Techn. Conf. on Atmos. Poll. Mgmt. Tech. Gothenburg, Sweden, Oct. 1976. Special Env. Report 10. W.M.O. 460.

Shen, T.T., R.L. Cheng, V.A. Mohnen, M. Current, and J.B. Hudson. 1977. Characterization of differences between oil-fired and coal-fired power plant emissions. Fourth International Clean Air Congress, Tokyo, May 16-20.

SNC Tottrup Services Ltd. 1978. Sources and emissions inventory for the Alberta Oil Sands area--Interim Report. AOSERP Contracted Report under Project ME 2.2.

Stevens, R.K., T.G. Dzubay, G. Russwurm, and D. Rickel. 1978. Sampling and analysis of atmospheric sulphates and related species. International Symposium on Sulphur in the Atmosphere, Dubrovnik, Yugoslavia. Atmos. Environ. 12:55-68.

Turner, D.B. 1964. A diffusion model for an urban area. J. Appl. Meteorol. 3:83-91.

Turner, D.B. 1967. Workbook of atmospheric dispersion estimates. Public Health Service Publication 999-AP-26, U.S. Department of Health, Education and Welfare. 84 pp.

Turner, H.E., and J. Markes. 1974. A minisonde system for atmospheric profiles. Report ARQT-1-74, Atmos. Environ. Service.

Whitby, K. 1978. The physical characteristic of sulphur aerosols. International Symposium on Sulphur in the Atmosphere. Dubrovnik, Yugoslavia. Atmos. Environ. 12:

USAEC. 1972. Regulatory guide 1.23 on-site meteorology programs. Washington, D.C., U.S.A.

Whiteman, C.D., and T.B. McKee. 1977. Observations of vertical atmospheric structure in a deep mountain valley. Arch. Meteorol. Geoph. Biokl. Ser. A, 26:39-50.

11. APPENDICES

11.1 POWER HOUSE STACK EMISSION DATA FOR JUNE 1977

Table 26. Powerhouse stack emission data for June 1977.

Date	Time	SO_2 Emissions ($kg \cdot s^{-1}$)	Effluent ($m^3 \cdot s^{-1}$)	Exit Velocity ($m \cdot s^{-1}$)	Gas Temp. (^oC)
June 16	0400	---	406	15.4	269
	0500		419	15.9	271
	0600	---	419	15.9	274
	0700	---	---	---	---
	0800	---	---	---	---
	0900	---	---	---	---
	1000	---	414	15.7	282
	1100	---	414	15.7	282
	1200	---	420	16.0	291
	1300	2.15	397	15.1	285
	1400	2.19	407	15.5	288
	1500	2.25	422	16.0	293
	1600	2.28	428	16.2	293
June 17	0400	2.31	423	16.1	280
	0500	2.33	423	16.1	277
	0600	2.27	413	15.7	277
	0700	2.25	422	15.6	280
	0800	2.25	422	15.6	280
	0900	---	422	16.0	282
	1000	---	413	15.7	274
	1100	---	415	15.7	280
	1200	---	423	16.1	277
	1300	---	449	17.0	288
	1400	---	454	17.2	288
	1500	---	499	17.0	288
	1600	---	436	16.6	282
June 18	0500	2.45	443	16.8	274
	0600	2.45	459	17.4	277
	0700	2.45	459	17.4	277
	0800	2.46	452	17.2	282
	0900	2.52	466	17.7	285
	1000	2.55	471	17.9	285
	1100	2.52	459	17.4	277
	1200	2.52	461	17.5	280
	1300	2.49	458	17.4	282
	1400	2.51	461	17.5	282
	1500	2.49	458	17.4	282

Continued . . .

Table 26. Continued.

Date	Time	SO_2 Emissions ($kg \cdot s^{-1}$)	Effluent ($m^3 \cdot s^{-1}$)	Exit Velocity ($m \cdot s^{-1}$)	Gas Temp. (^oC)
June 19	0500	2.49	456	17.3	280
	0600	2.49	453	17.2	277
	0700	2.51	458	17.4	280
	0800	2.48	453	17.2	280
	0900	2.52	468	17.8	288
	1000	2.52	463	17.6	282
	1100	2.55	467	17.7	280
	1200	2.60	474	18.0	280
	1300	2.63	485	18.4	285
	1400	2.58	481	18.3	291
	1500	2.57	472	17.9	282
June 20	0500	2.58	472	17.9	282
	0600	2.51	463	17.6	285
	0700	2.52	463	17.6	282
	0800	2.48	453	17.2	280
	0900	2.55	471	17.9	285
	1000	2.54	466	19.7	282
	1100	2.72	509	19.3	294
	1200	2.69	503	19.1	294
	1300	2.66	493	18.7	288
June 21	0500	2.57	465	17.6	274
	0600	2.54	457	17.3	271
	0700	2.42	438	16.6	274
	0800	2.46	441	16.7	269
	0900	2.51	454	17.2	274
	1000	2.51	464	17.6	271
	1100	2.63	460	17.4	271
	1200	2.55	464	17.6	277
	1300	2.51	454	16.6	271
	1400	2.48	448	17	274
	1500	2.54	464	17.6	280
	1600	2.54	466	17.7	282
June 22	1300	2.31	408	15.5	260
	1400	2.36	416	15.8	260
	1500	2.45	441	16.7	271
	1600	2.40	433	16.4	271
	1700	2.37	423	16.1	266
	1800	2.37	427	16.2	271
	1900	2.34	422	16.0	271

Continued . . .

Table 26. Concluded.

Date	Time	SO_2 Emissions ($kg \cdot s^{-1}$)	Effluent ($m^3 \cdot s^{-1}$)	Exit Velocity ($m \cdot s^{-1}$)	Gas Temp. (^oC)
June 22 (cont.)	2000	2.33	413	15.7	263
	2100	2.37	419	15.9	260
	2200	2.37	425	16.1	269
June 23	0500	2.58	467	17.7	274
	0600	2.58	474	18.0	282
	0700	2.54	461	17.5	277
	0800	2.51	456	17.3	277
	0900	2.37	427	16.2	271
	1000	2.28	403	15.3	260
	1100	2.31	412	15.7	266
	1200	2.34	413	15.7	260
	1300	2.39	430	16.3	271
	1400	2.36	420	16.0	266
	1500	2.36	420	16.0	266
June 24	0500	2.42	440	16.7	277
	0600	2.39	428	16.2	269
	0700	2.39	430	16.3	271
	0800	2.42	438	16.6	274
	0900	2.43	442	16.8	277
	1000	2.49	456	17.3	280
	1100	2.55	467	17.7	280
	1200	2.54	468	17.8	285
June 25	2000	2.75	505	19.2	282
	2100	2.78	510	19.4	282
	2200	2.69	496	18.8	285
	2300	---	477	18.1	282
June 26	1300	2.63	475	18.0	274
	1400	2.75	510	19.3	288
	1500	2.69	498	18.9	288
	1600	2.60	477	18.1	282
	1700	2.58	474	18.0	282
	1800	2.52	463	17.6	282
	1900	2.46	443	16.8	271
	2000	2.49	449	17.0	271
	2100	---	454	17.2	274
	2200	---	448	17.0	274

11.2 SYNOPTIC CONDITIONS

11.2.1 16 June 1977

As an occlusion linked to an Aluetian Low intensified off the coast of B.C., the massive high pressure advancing in front of it pushed into southern B.C. and Alberta. A weak cold front, associated with a low in the Northwest Territories, hovered over Great Slave Lake. A second Arctic ridge developed over the Yukon behind this cold front.

Relatively clear weather associated with the nearby ridge persisted until mid-morning when a nocturnal surface inversion disintegrated. Towering stratocumulus based at 1371 m covered four tenths of the sky. By late morning the stratocumulus became topped by thick altocumulus and localized shower activity occurred in the area during the afternoon. Visibility remained about 15 nautical miles throughout this period.

Winds were calm throughout the morning and afternoon hours in the Oil Sands.

11.2.2 17 June 1977

Yesterday's massive high pressure ridge over southern Alberta had intensified further while linking up with the Arctic high north of the cold front over the Northwest Territories. The disintegration of the cold front between these above highs occurred with migration of the closed Arctic low to Baffin Island.

Yesterday morning's mostly clear, stable conditions returned to the oil sands again overnight. As cloud cover was restricted to altocumulus and cirrus covering four tenths of the sky, the nocturnal surface inversion disintegrated by mid-morning. By mid-afternoon overcast, unstable weather returned with cumulonimbus and towering cumulus clouds based at the 1676 m elevation level. Very light showers were sighted during mid-afternoon in the area. Visibility was extended to 28 nautical miles during the morning but receded to 15 nautical miles by afternoon.

Winds were light southwesterly at 2 to 4 $m \cdot s^{-1}$ before dawn but veered around to the northwest by mid-afternoon at the same speed.

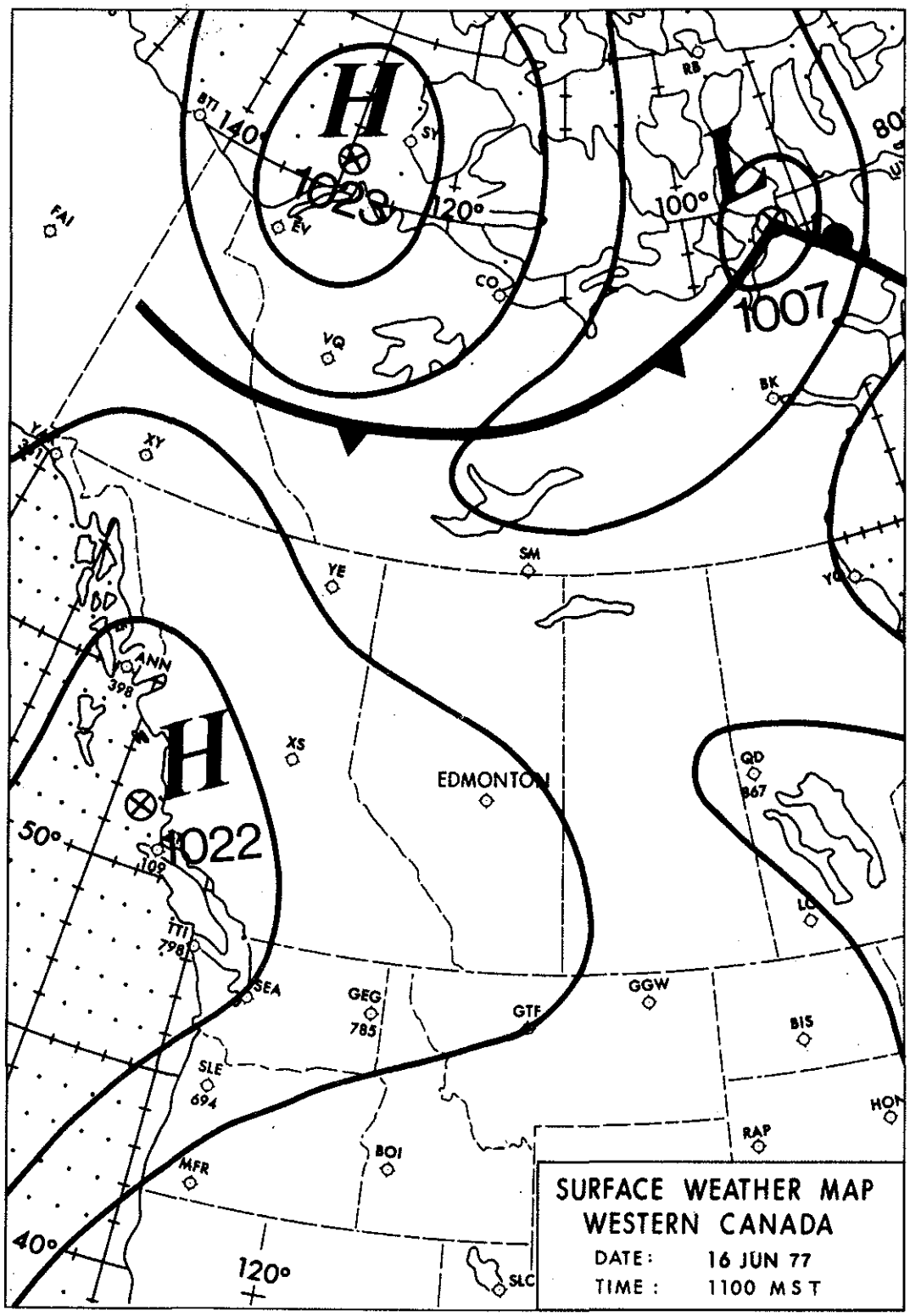

Figure 99. Surface weather map.

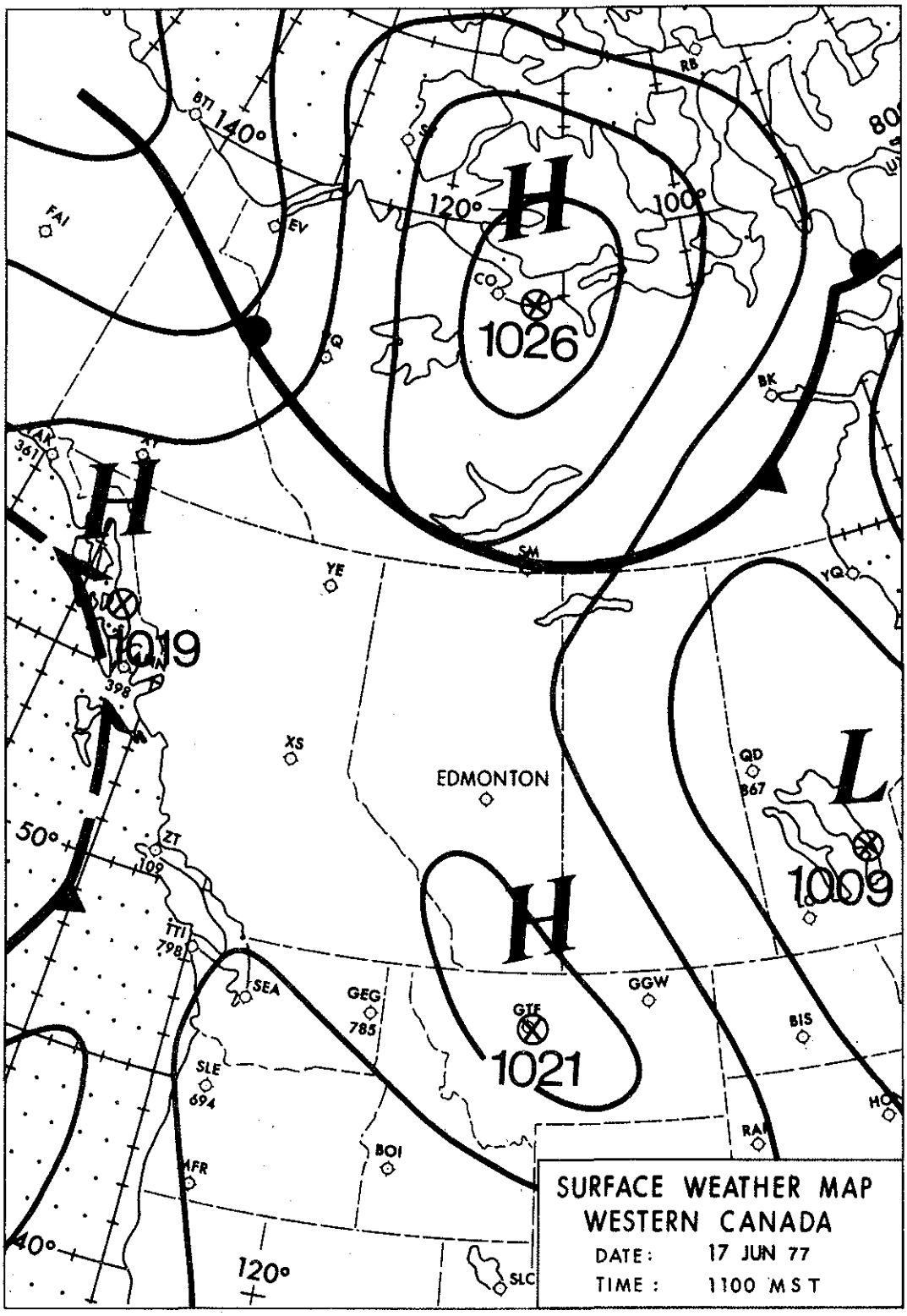

Figure 100. Surface weather map.

11.2.3 18 June 1977

The two high pressure ridges centered over the Northwest Territories and southern Alberta continued to intensify. A new low disturbance appearing over Alaska led to the formation of a new quasi-stationary front between the ridges. This front hovered directly over the study area at sunrise, but was pushed southwest during the early morning as the northern ridge intensified.

Clear, sunny weather conditions continued to dominate the weather pattern in the area. A weak frontal inversion aloft at 1500 m disappeared by mid-morning. Thin cumulofractus and altocumulus with bases at 1700 m covered two tenths of the sky shortly after dawn, but by mid-afternoon skies had cleared after passage of the ridge north of the quasi-stationary front. Visibility remained at about 15 nautical miles all day and no precipitation was reported.

Winds were calm in the early dawn hours and briefly picked up to 1 to 2 $m \cdot s^{-1}$ in the late morning before calming in the afternoon.

11.2.4 19 June 1977

The southern tongue-extension of yesterday's ridge over the Northwest Territories had developed into a separate ridge over northern Saskatchewan. The larger ridge had migrated slightly northeast towards Baffin Island while intensifying further. The quasi-stationary frontal network which had remained immediately west of the oil sands during morning hours, passed over the area during the late afternoon.

Clear dry weather conditions continued to dominate in the region. A nocturnal surface inversion lasted until mid-morning. Thin, scattered altocumulus based at 2700 m with a trace of cumulus gradually built up during morning hours to cover most of the sky. By late afternoon only cumulofractus clouds covering about seven tenths of the sky remained as the warm front passed to the east of the islands. Visibility remained at about 15 nautical miles throughout the day and no precipitation was reported.

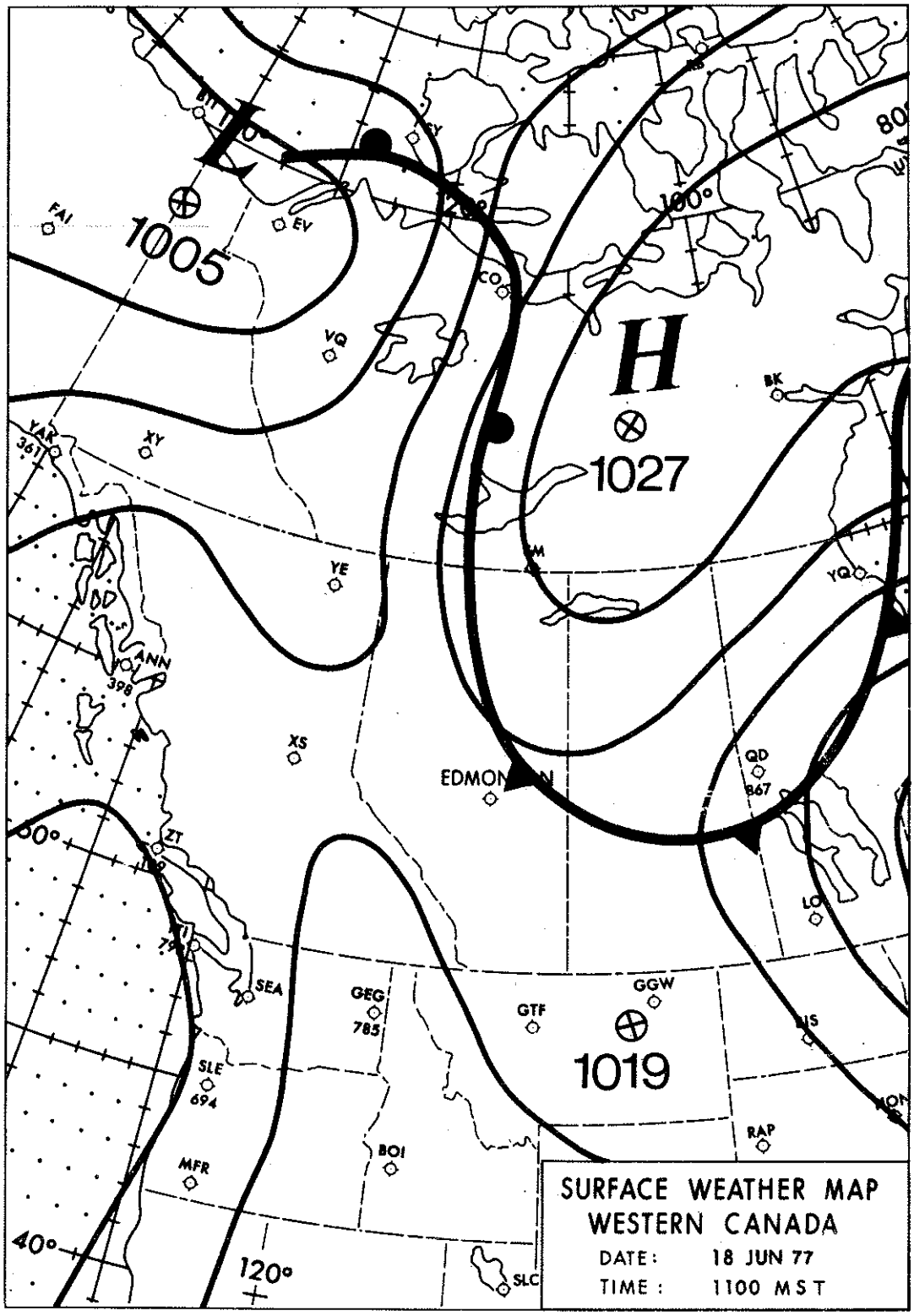

Figure 101. Surface weather map.

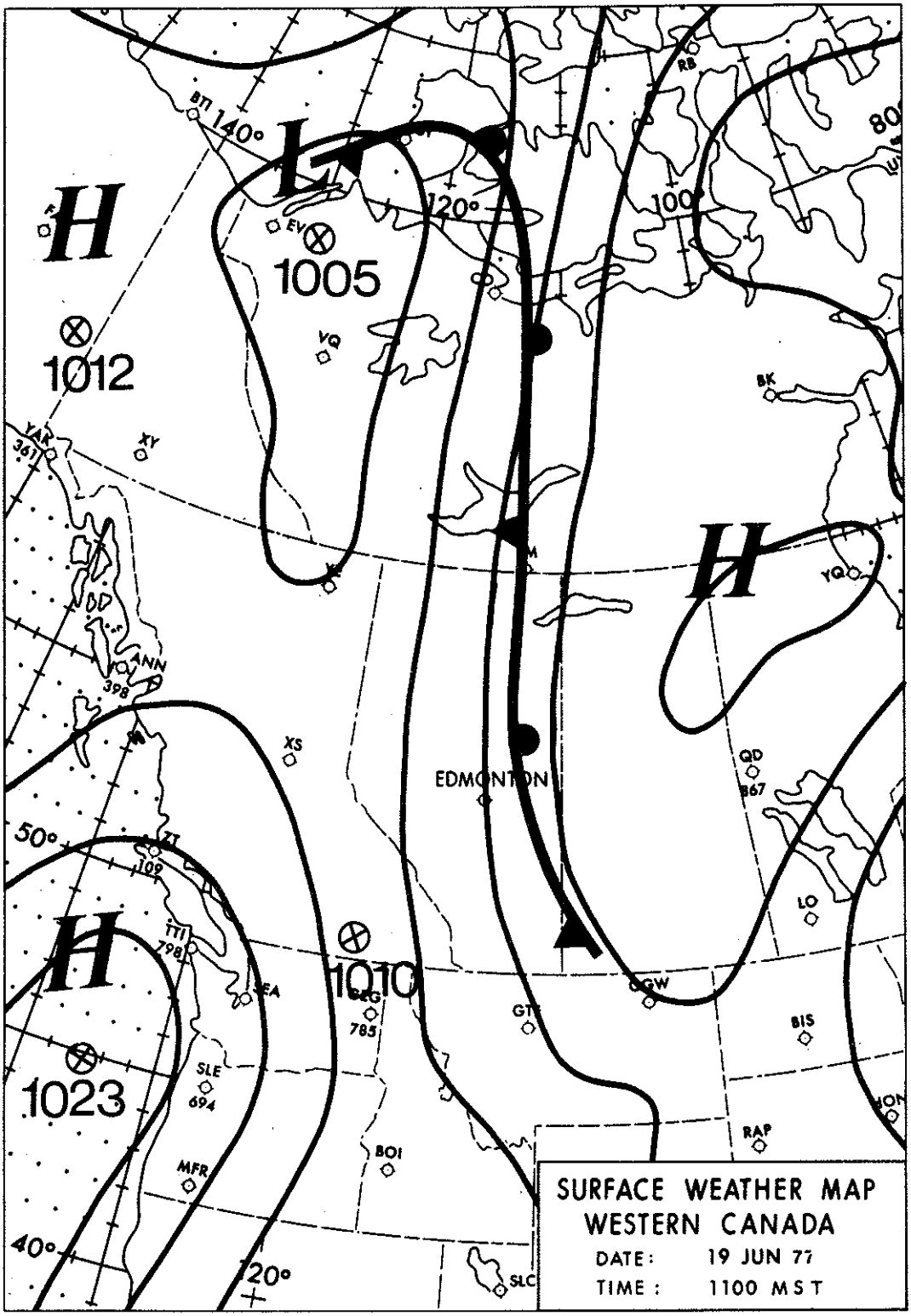

Figure 102. Surface weather map.

Winds were light east southeasterly at 2 to 4 $m \cdot s^{-1}$ at dawn but veered to south southeasterly by afternoon as the front passed through the oil sands.

11.2.5 20 June 1977

A closed low over the Yukon linked to a Pacific frontal network penetrated into the western Northwest Territories. An elevated cold frontal trough associated with this low entered Alberta in the early morning, reached the surface by midday, but remained about 500 km west of the oil sands during the afternoon. A second frontal system over the Arctic Archipelago had linked up with the Yukon closed low to bring strong cyclonic flow northward.

Warm, dry cyclonic flow returned to the oil sands region. The associated nocturnal inversion persisted until mid-morning when a strong frontal inversion based at 1 km occurred until noon. Towering cumulus and high altocumulus based at about 2700 m covered about four tenths of the sky during morning hours but changed to cumulofractus based at about 3600 m covering about seven tenths of the sky by mid-afternoon.

Visibility remained at about 15 nautical miles and no rainfall occurred during the period.

Winds were light southwesterly at 2 to 4 $m \cdot s^{-1}$ but veered around to south-southwesterly at about the same speed by mid-afternoon.

11.2.6 21 June 1977

Yesterday's closed low which had coupled with the Arctic Archipelago frontal system further intensified over the Northwest Territories. The cold frontal trough passed through the oil sands before sunrise, to be followed by another weak, occluded Pacific low entering B.C.

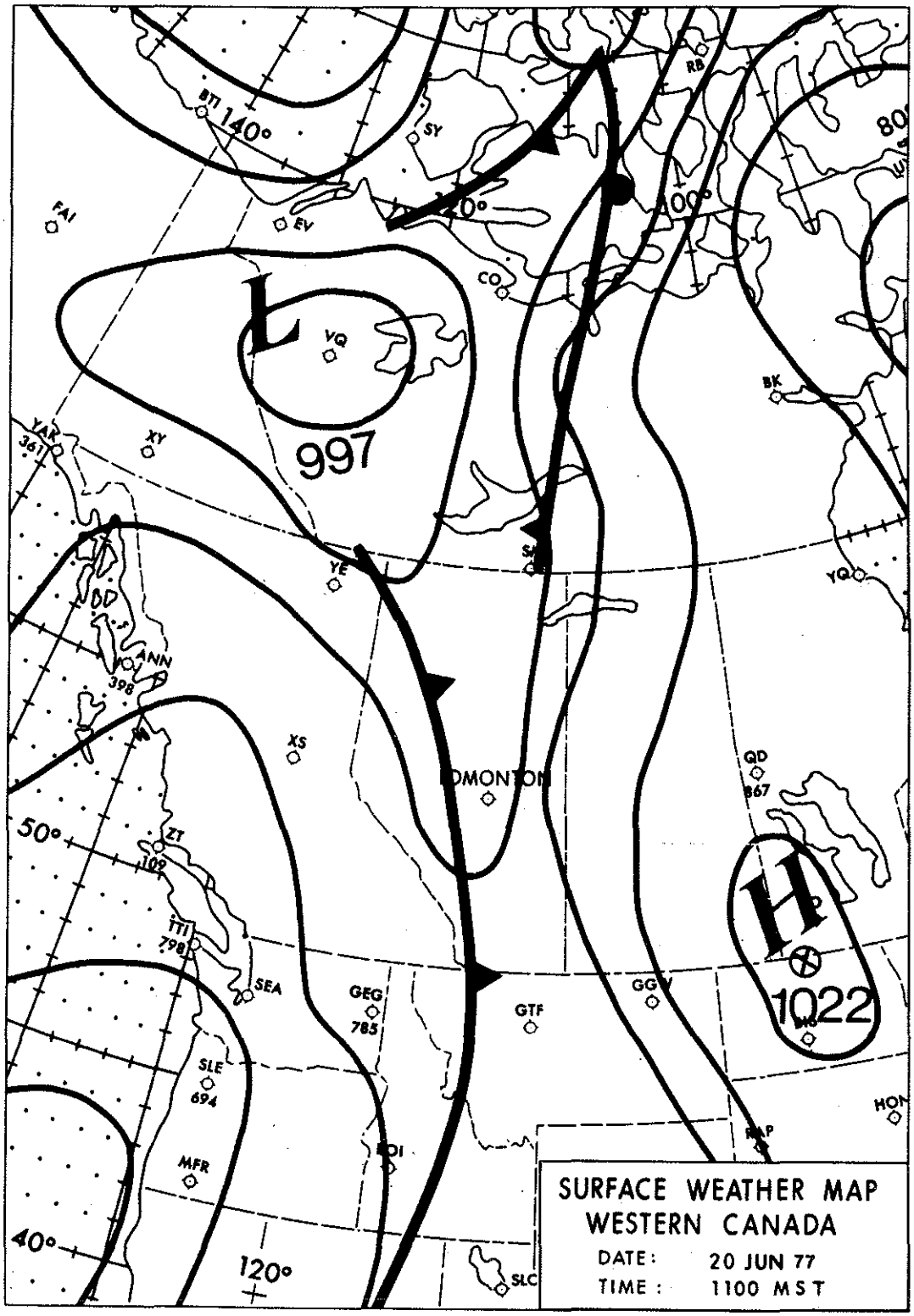

Figure 103. Surface weather map.

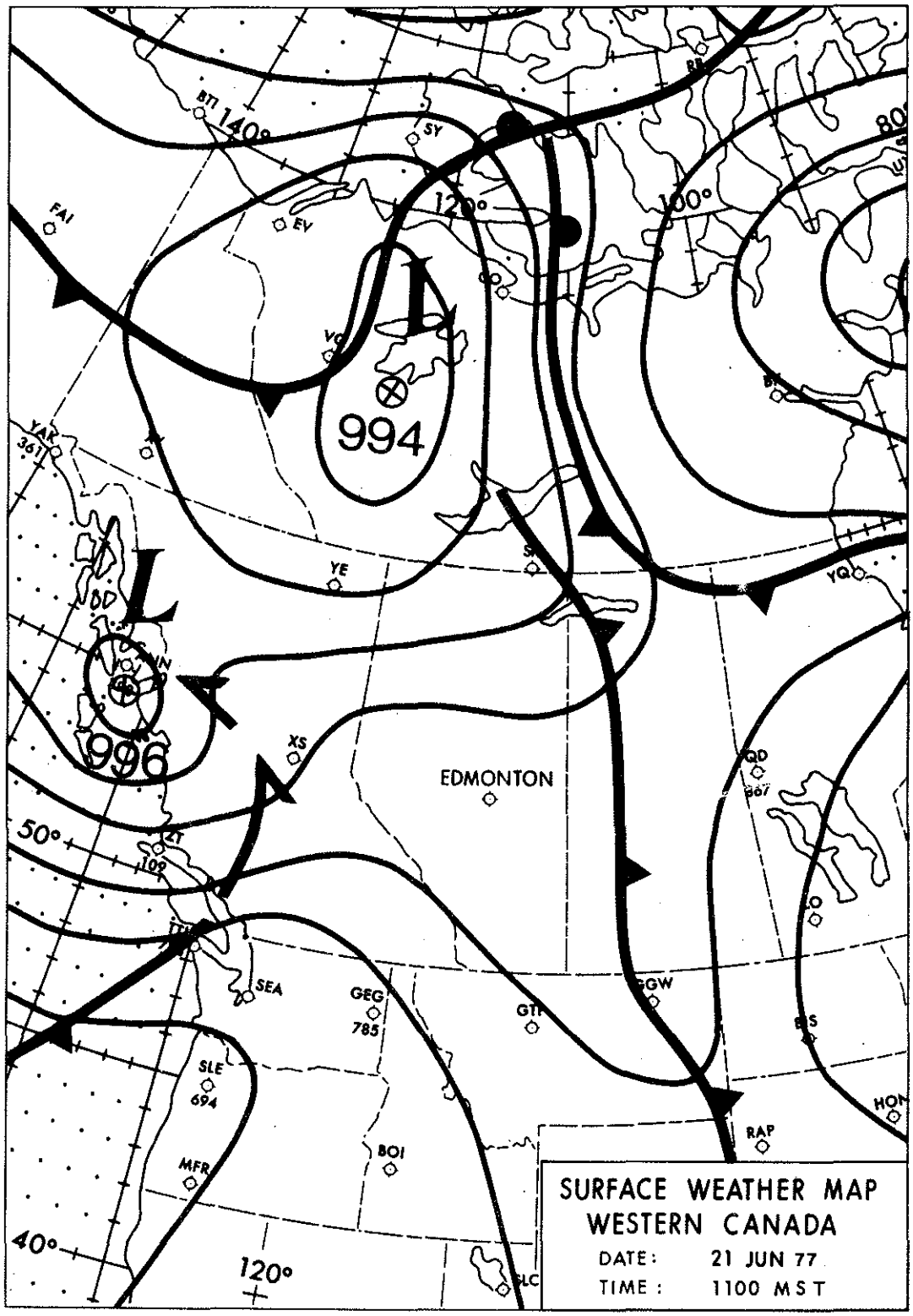

Figure 104. Surface weather map.

Cooler, moist conditions returned to the oil sands region in the morning after passage of the isolated cold front overhead. Thick altocumulus based at about 2100 m and covering nine tenths of the sky preced passage of the front. War, dry isothermal lapse conditions were replaced by cool, moist unstable air in the oil sands by early afternoon. Traces of altocumulus based at 1371 m covered three tenths of the sky at this time. Visibility remained about 15 nautical miles and no rainfall occurred.

Winds were calm in the early morning hours but increased to 2 to 4 $m \cdot s^{-1}$ from the northeast by early afternoon after passage of the cold front.

11.2.7 22 June 1977

A separate frontal wave had broken off from yesterday's coupled frontal wave network and migrated down to northern Manitoba. The occluded low over B.C. yesterday had died, leaving a new low developing over north-central Alberta and a cold front which passed through the oil sands shortly after sunrise. The remaining frontal network and closed low was quasi-stationary over the Northwest Territories.

Yesterday's relatively cooler, moist air mass continued to dominate the weather in the sands throughout the day. Traces of stratocumulus and cumulus mixed with thick altocumulus covered nine tenths of the sky and had a low base of about 1500 m during the early morning hours immediately after the front passed overhead. Late afternoon breakup of altocumulus clouds reduced the sky cover to about three tenths. Visibility remained the same and no precipitation was recorded.

Winds were calm during early morning hours but picked up to 4 to 6 $m \cdot s^{-1}$ from the west by early afternoon as the front passed through the area.

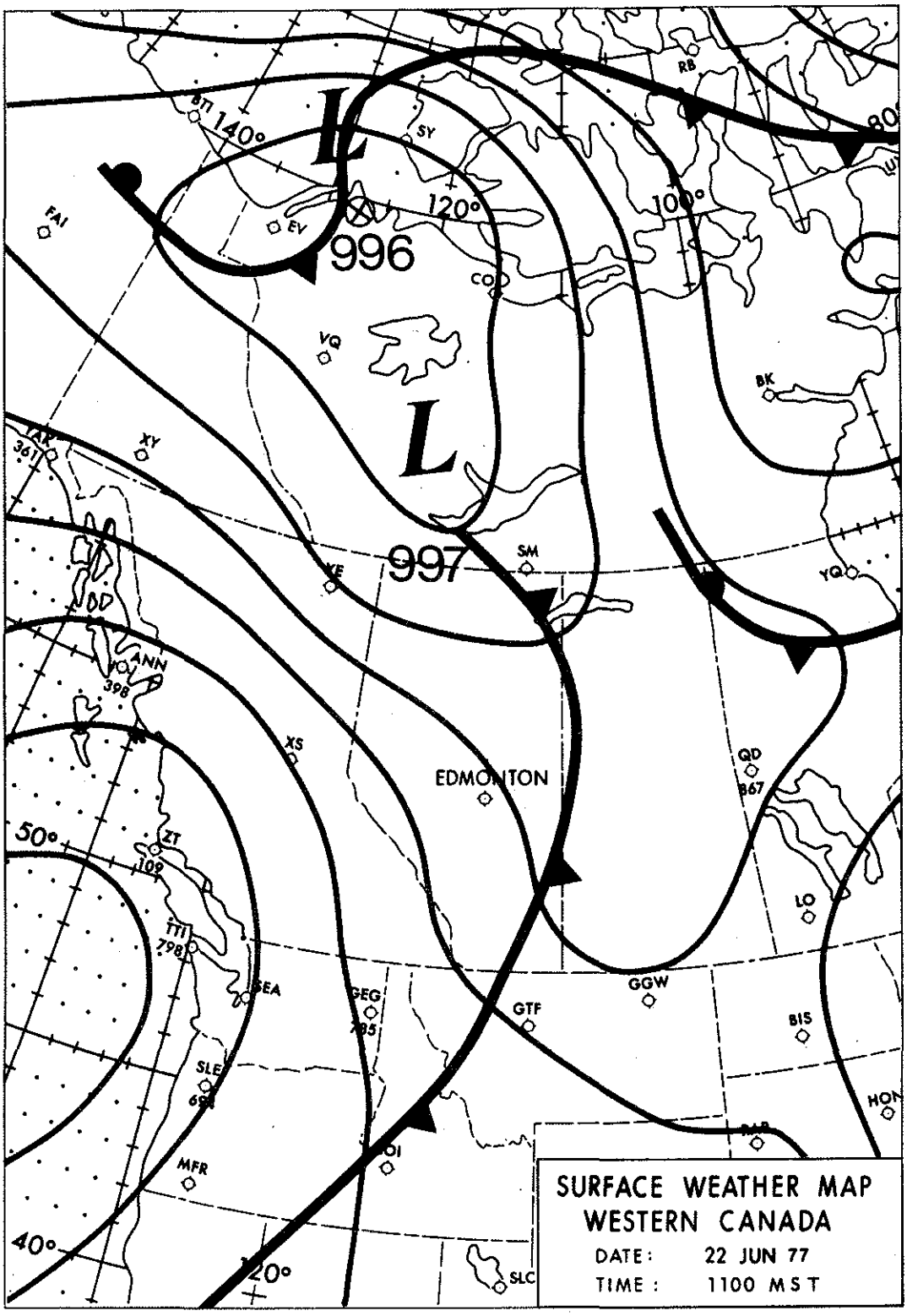

Figure 105. Surface weather map.

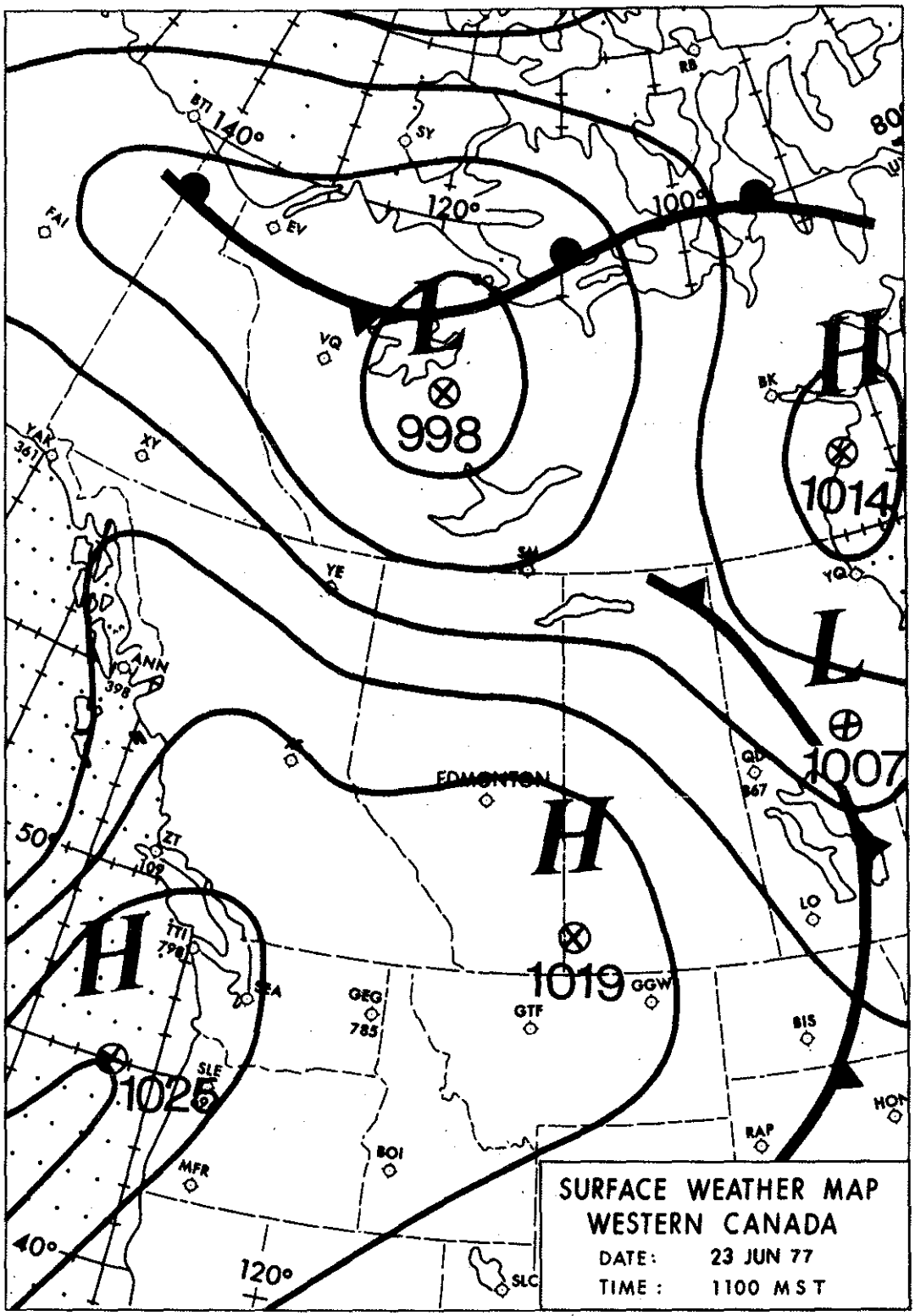

Figure 106. Surface weather map.

11.2.8 23 June 1977

Yesterday's closed low and frontal network remained quasi-stationary over Lake Athabasca and vicinity. The north-south cold front had migrated into Manitoba. A strong high-pressure ridge pushed into the B.C. hinterland from the Pacific and by late afternoon covered most of the southern half of Alberta. Another occluded front linked to an Aleutian low upstream followed behind the ridge off the B.C. coast.

Cold, very dry, weather again entered the region to dominate weather throughout the day. A weak surface nocturnal inversion lasted until shortly after dawn. Traces of stratocumulus and cirrus covered one tenth of the sky during morning. Towering stratocumulus based at 2400 m gradually developed in the afternoon to cover two or three tenths of the sky. Visibility remained at about 15 nautical miles throughout the day, and no rainfall occurred.

Winds were calm shortly after dawn before increasing to 6 to 10 $m \cdot s^{-1}$ from the west as anti-cyclonic flow from the ridge south of the oil sands began to influence the region.

11.2.9 24 June 1977

Yesterday's occluded front linked to an elongated Aleutian low wave pattern had pushed into Alberta and had coupled with the quasi-stationary low over the Northwest Territories. Another closed low immediately upstream from the occluded front migrated through northern B.C. to merge with the above quasi-stationary low system by afternoon.

Moist, slightly more unstable weather dominated weather in the oil sands as the occluded front passed through during late morning and early afternoon hours. A weak, elevated frontal inversion based at 200 m lasted until mid-morning. Thick cumulus based at about 900 m combined with thick altocumulus to create overcast conditions throughout the morning. Localized morning drizzle

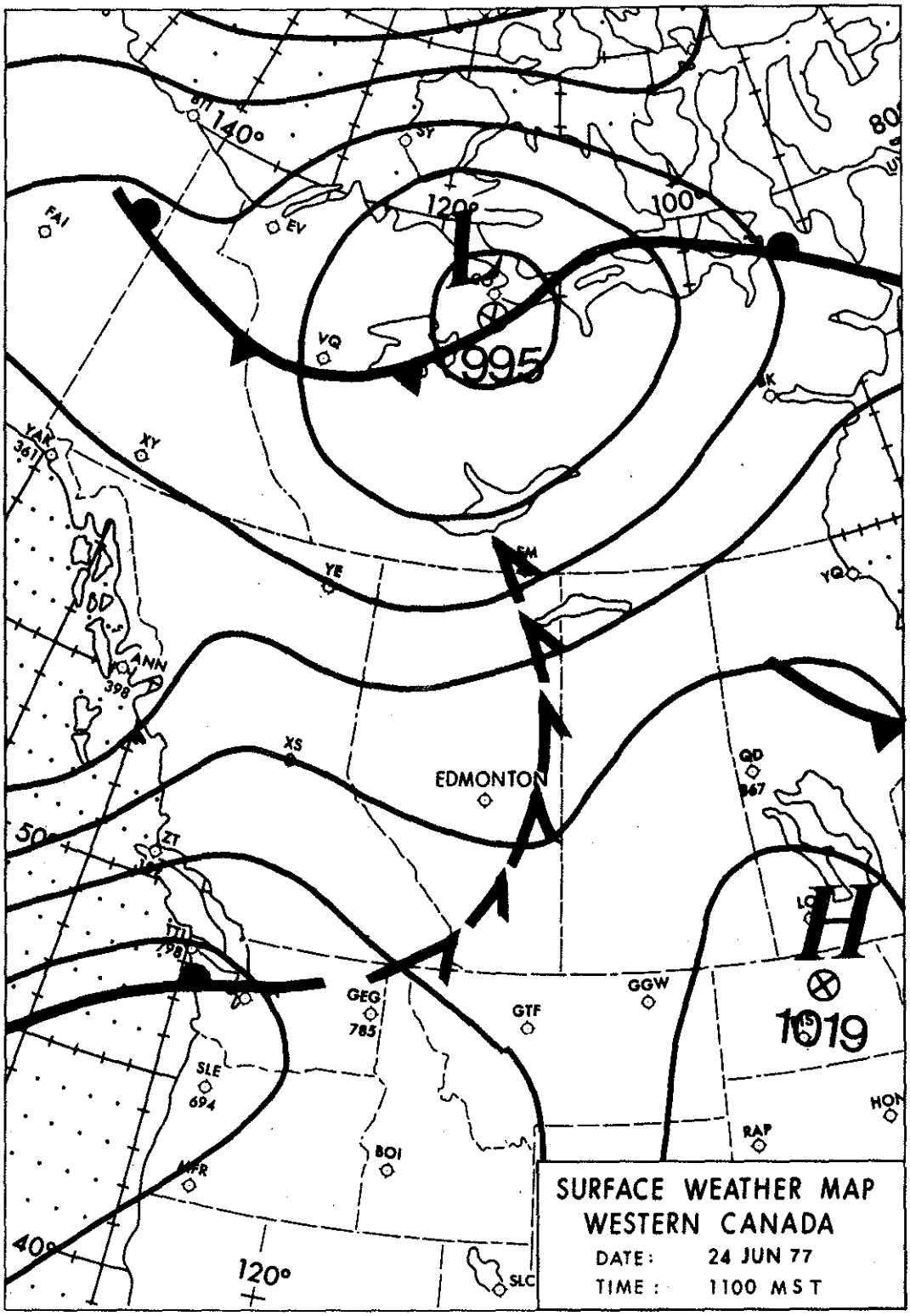

Figure 107. Surface weather map.

resulted in the area, but evaporation before precipitation reached the ground was widespread. Streaking altocumulus castellanus developed in a very unstable layer aloft shortly before light evening showers invaded the area. Visibility remained at 15 nautical miles.

Winds were calm during the early morning hours. However, by mid-afternoon they had picked up to 1 to 2 $m \cdot s^{-1}$ from the west-northwest as the occluded front passed through the area.

11.2.10 25 June 1977

Both the quasi-stationary closed low frontal system over the Territories and the occluded low over the Prairies linked to it moved negligibly westward during the day. By early afternoon another high pressure ridge had begun to penetrate the B.C. hinterland.

Cool, unstable weather remained in the area for another day. High stratocumulus and cumulus based at about 2400 m covered eight tenths of the sky during the morning. By mid-afternoon these cloud types had been replaced by cumulo nimbus as scattered moderate thunderstorms hit the oil sands area. These clouds were based at about 1500 m but became elevated to 2700 m during evening hours as the storm dissipated. Visibility remained at about 15 nautical miles.

Moderate south westerly winds at 2 to 4 $m \cdot s^{-1}$ in the early morning hours gave way to brisk north westerly flow at 6 to 11 $m \cdot s^{-1}$ as the occlusion's cyclonic circulation continued to dominate over the area.

11.2.11 26 June 1977

As the previously quasi-stationary closed low migrated towards Baffin Island during the day, the trailing cold front developed upstream into Alaska as a quasi-stationary frontal network. The cold front portion pushed down over the northern part

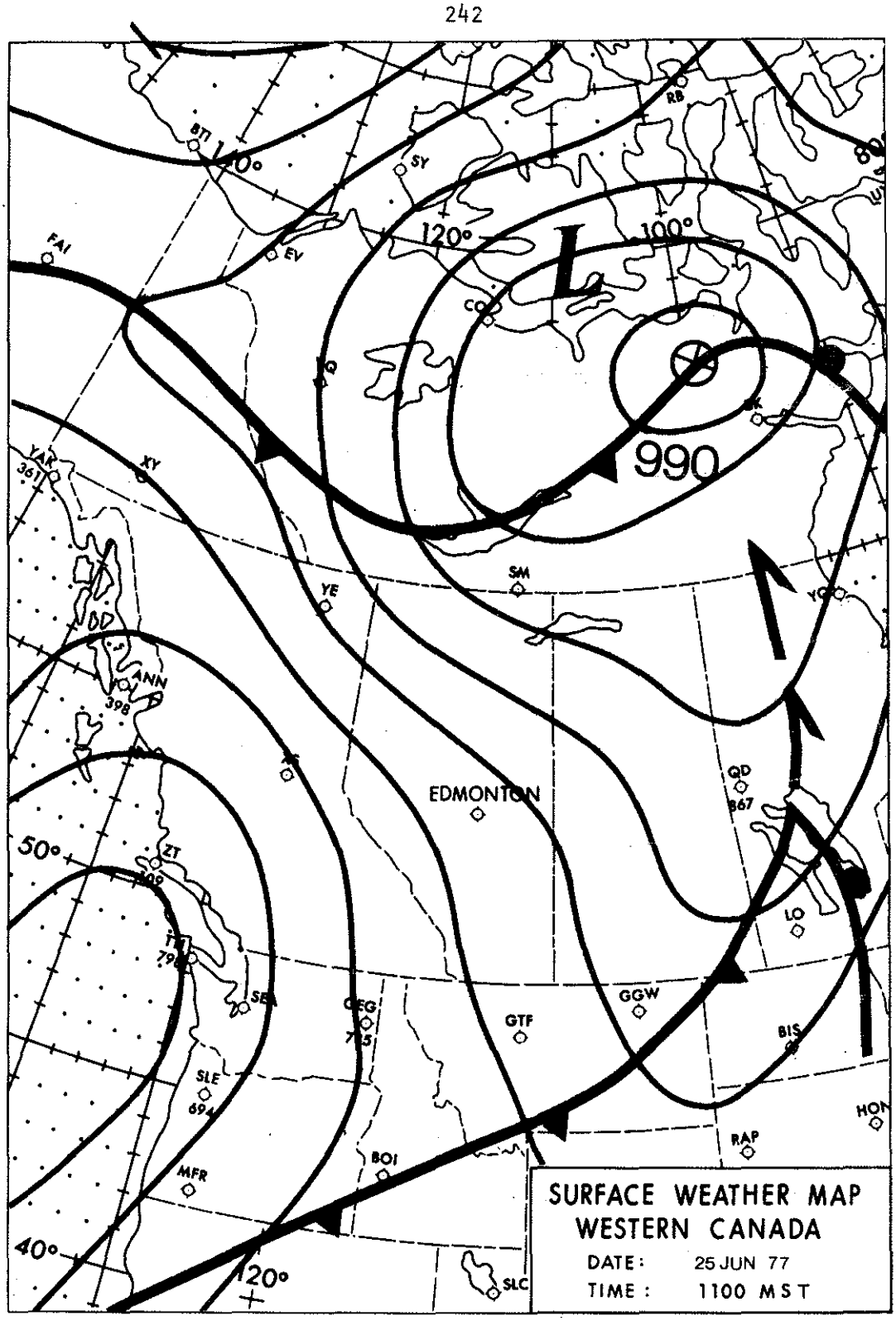

Figure 108. Surface weather map.

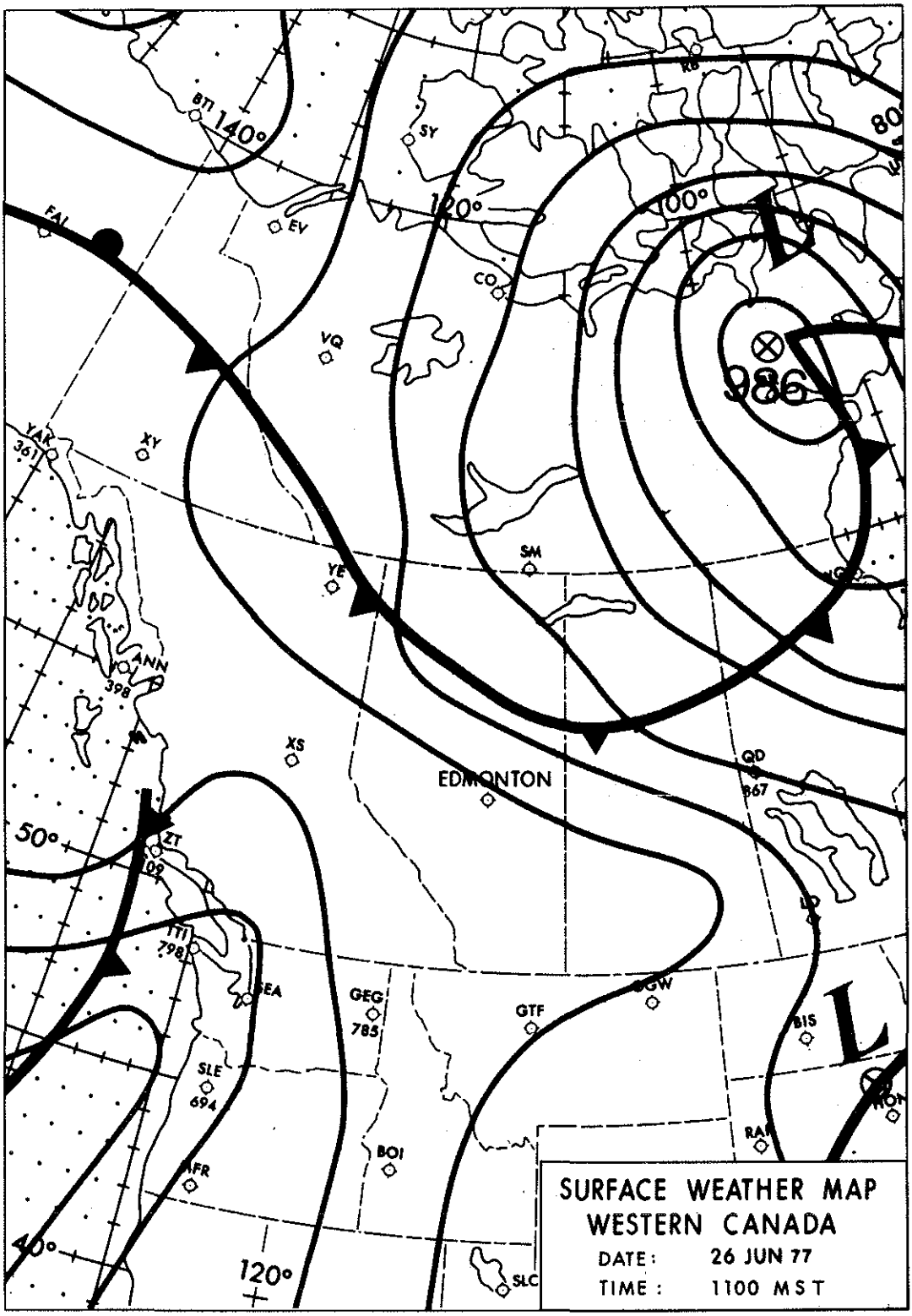

Figure 109. Surface weather map.

of the oil sands after sunrise. Yesterday's ridge moved into central Alberta shortly afterwards, causing the frontal network to recede back into the Northwest Territories during the morning.

Drier, cooler more stable weather had returned to the oil sands by late morning. A tongue from the costal ridge penetrated into central Alberta bringing northerly, anti-cyclonic flow into the Sands area. High-level altocumulus covering three tenths of the sky in the morning soon developed into cumulonimbus based at 1300 m. Light showers occurred in the southern portion of the oil sands during mid-afternoon and visibility remained at about 15 nautical miles.

Relatively light west southwesterly winds at 2 to 4 $m \cdot s^{-1}$ during the early morning hours under cyclonic flow conditions linked to the closed low gave way to light anti-cyclonic flow with northwest winds at 2 to 4 $m \cdot s^{-1}$ by mid-afternoon.

12. AOSERP RESEARCH REPORTS

1.		AOSERP First Annual Report, 1975
2.	AF 4.1.1	Walleye and Goldeye Fisheries Investigations in the Peace-Athabasca Delta--1975
3.	HE 1.1.1	Structure of a Traditional Baseline Data System
4.	VE 2.2	A Preliminary Vegetation Survey of the Alberta Oil Sands Environmental Research Program Study Area
5.	HY 3.1	The Evaluation of Wastewaters from an Oil Sand Extraction Plant
6.		Housing for the North--The Stackwall System
7.	AF 3.1.1	A Synopsis of the Physical and Biological Limnology and Fisheries Programs within the Alberta Oil Sands Area
8.	AF 1.2.1	The Impact of Saline Waters upon Freshwater Biota (A Literature Review and Bibliography)
9.	ME 3.3	Preliminary Investigations into the Magnitude of Fog Occurrence and Associated Problems in the Oil Sands Area
10.	HE 2.1	Development of a Research Design Related to Archaeological Studies in the Athabasca Oil Sands Area
11.	AF 2.2.1	Life Cycles of Some Common Aquatic Insects of the Athabasca River, Alberta
12.	ME 1.7	Very High Resolution Meteorological Satellite Study of Oil Sands Weather: "a Feasibility Study"
13.	ME 2.3.1	Plume Dispersion Measurements from an Oil Sands Extraction Plant, March 1976
15.	ME 3.4	A Climatology of Low Level Air Trajectories in the Alberta Oil Sands Area
16.	ME 1.6	The Feasibility of a Weather Radar near Fort McMurray, Alberta
17.	AF 2.1.1	A Survey of Baseline Levels of Contaminants in Aquatic Biota of the AOSERP Study Area
18.	HY 1.1	Interim Compilation of Stream Gauging Data to December 1976 for the Alberta Oil Sands Environmental Research Program
19.	ME 4.1	Calculations of Annual Averaged Sulphur Dioxide Concentrations at Ground Level in the AOSERP Study Area
20.	HY 3.1.1	Characterization of Organic Constituents in Waters and Wastewaters of the Athabasca Oil Sands Mining Area

21.		AOSERP Second Annual Report, 1976-77
22.	HE 2.3	Maximization of Technical Training and Involvement of Area Manpower
23.	AF 1.1.2	Acute Lethality of Mine Depressurization Water on Trout Perch and Rainbow Trout
24.	ME 4.2.1	Air System Winter Field Study in the AOSERP Study Area, February 1977.
25.	ME 3.5.1	Review of Pollutant Transformation Processes Relevant to the Alberta Oil Sands Area
26.	AF 4.5.1	Interim Report on an Intensive Study of the Fish Fauna of the Muskeg River Watershed of Northeastern Alberta
27.	ME 1.5.1	Meteorology and Air Quality Winter Field Study in the AOSERP Study Area, March 1976
28.	VE 2.1	Interim Report on a Soils Inventory in the Athabasca Oil Sands Area
29.	ME 2.2	An Inventory System for Atmospheric Emissions in the AOSERP Study Area
30.	ME 2.1	Ambient Air Quality in the AOSERP Study Area, 1977
31.	VE 2.3	Ecological Habitat Mapping of the AOSERP Study Area: Phase I
32.		AOSERP Third Annual Report, 1977-78
33.	TF 1.2	Relationships Between Habitats, Forages, and Carrying Capacity of Moose Range in northern Alberta. Part I: Moose Preferences for Habitat Strata and Forages.
34.	HY 2.4	Heavy Metals in Bottom Sediments of the Mainstem Athabasca River System in the AOSERP Study Area
35.	AF 4.9.1	The Effects of Sedimentation on the Aquatic Biota
36.	AF 4.8.1	Fall Fisheries Investigations in the Athabasca and Clearwater Rivers Upstream of Fort McMurray: Volume I
37.	HE 2.2.2	Community Studies: Fort McMurray, Anzac, Fort MacKay
38.	VE 7.1.1	Techniques for the Control of Small Mammals: A Review
39.	ME 1.0	The Climatology of the Alberta Oil Sands Environmental Research Program Study Area
40.	WS 3.3	Mixing Characteristics of the Athabasca River below Fort McMurray - Winter Conditions
41.	AF 3.5.1	Acute and Chronic Toxicity of Vanadium to Fish
42.	TF 1.1.4	Analysis of Fish Production Records for Registered Traplines in the AOSERP Study Area, 1970-75
43.	TF 6.1	A Socioeconomic Evaluation of the Recreational Fish and Wildlife Resources in Alberta, with Particular Reference to the AOSERP Study Area. Volume I: Summary and Conclusions
44.	VE 3.1	Interim Report on Symptomology and Threshold Levels of Air Pollutant Injury to Vegetation, 1975 to 1978
45.	VE 3.3	Interim Report on Physiology and Mechanisms of Air-Borne Pollutant Injury to Vegetation, 1975 to 1978

46. VE 3.4 Interim Report on Ecological Benchmarking and Biomonitoring for Detection of Air-Borne Pollutant
47. TF 1.1.1 A Visibility Bias Model for Aerial Surveys of Moose on the AOSERP Study Area
48. HG 1.1 Interim Report on a Hydrogeological Investigation of the Muskeg River Basin, Alberta
49. WS 1.3.3 The Ecology of Macrobenthic Invertebrate Communities in Hartley Creek, Northeastern Alberta
50. ME 3.6 Literature Review on Pollution Deposition Processes
51. HY 1.3 Interim Compilation of 1976 Suspended Sediment Data in the AOSERP Study Area
52. ME 2.3.2 Plume Dispersion Measurements from an Oil Sands Extraction Plant, June 1977
53. HY 3.1.2 Baseline States of Organic Constituents in the Athabasca River System Upstream of Fort McMurray
54. WS 2.3 A Preliminary Study of Chemical and Microbial Characteristics of the Athabasca River in the Athabasca Oil Sands Area of Northeastern Alberta.
55. HY 2.6 Microbial Populations in the Athabasca River
56. AF 3.2.1 The Acute Toxicity of Saline Groundwater and of Vanadium to Fish and Aquatic Invertebrates
57. LS 2.3.1 Ecological Habitat Mapping of the AOSERP Study Area (Supplement): Phase I
58. AF 2.0.2 Interim Report on Ecological Studies on the Lower Trophic Levels of Muskeg Rivers Within the Alberta Oil Sands Environmental Research Program Study Area
59. TF 3.1 Self-Aquatic Mammals. Annotated Bibliography
60. WS 1.1.1 Synthesis of Surface Water Hydrology
61. AF 4.5.2 An Intensive Study of the Fish Fauna of the Steepbank River Watershed of Northeastern Alberta.
62. TF 5.1 Amphibians and Reptiles in the AOSERP Study Area
63. An Overview Assessment of <u>In Situ</u> Development in the Athabasca Deposit
64. LS 21.6.1 A Review of the Baseline Data Relevant to the Impacts of Oil Sands Development on Large Mammals in the AOSERP Study Area
65. LS 21.6.2 A Review of the Baseline Data Relevant to the Impacts of Oil Sands Development on Black Bears in the AOSERP Study Area
66. AS 4.3.2 An Assessment of the Models LIRAQ and ADPIC for Application to the Athabasca Oil Sands Area

67. WS 1.3.2 Aquatic Biological Investigations of the Muskeg River Watershed

68. AS 1.5.3, AS 3.5.2 Air Study Summer Field Study in the AOSERP Study Area, June 1977

69. HS 40.1 Native Employment Patterns in Alberta's Athabasca Oil Sands region

70. LS 28.1.2 An Interim Report on the Insectivorous Animals in the AOSERP Study Area

71. HY 2.2 Lake Acidification Potential in the Alberta Oil Sands Environmental Research Program Study Area

These reports are not available upon request. For further information about availability and location of depositories, please contact:

Alberta Oil Sands Environmental Research Program
15th Floor, Oxbridge Place
9820 - 106 Street
Edmonton, Alberta
T5K 2J6